

**Carnegie Mellon University**  
**MELLON COLLEGE OF SCIENCE**

**THESIS**

SUBMITTED IN PARTIAL FULFILLMENT OF THE REQUIREMENTS  
FOR THE DEGREE OF

**DOCTOR OF PHILOSOPHY IN THE FIELD OF PHYSICS**

TITLE: "Geometry, Mechanics, and Biology: Applications for membranes and filaments"

PRESENTED BY: Zachary McDargh

ACCEPTED BY THE DEPARTMENT OF PHYSICS

Markus Deserno 7/25/17  
\_\_\_\_\_  
MARKUS DESERNO, CHAIR PROFESSOR DATE

Stephen Garoff 7/25/17  
\_\_\_\_\_  
STEPHEN GAROFF, DEPT HEAD DATE

APPROVED BY THE COLLEGE COUNCIL

Rebecca Doerge 08/04/17  
\_\_\_\_\_  
REBECCA DOERGE, DEAN DATE

Geometry, Mechanics, and Biology  
Applications for Membranes and Filaments  
Carnegie Mellon University

Zachary A. McDargh

July 25, 2017

# Abstract

Nature displays a vast array of geometrically ordered systems, at nearly every length scale. This is especially true in soft matter and biological physics, where geometric considerations help us understand problems from the assembly of helical proteins to the morphogenesis of flower petals. In many cases, this geometric ordering is mechanical in origin: energy must be expended for objects to stretch, bend, and deform. This thesis explores some of the conclusions that can be drawn from this simple observation.

First, we conduct a brief review of the geometry and mechanics of curves and surfaces in three dimensional space. This review explains how to identify and quantify the properties of these low-dimensional continua that can be considered geometric, and shows how these quantities can be used to construct energy functionals for filaments and sheets. Once these tools have been introduced, they are applied first to surfaces, and then to filaments.

In the first section of the chapter on surfaces, an extension of the Helfrich model of membrane elasticity is used to investigate the buckling of membranes in the gel phase. Measuring the stress-strain relation for buckled membranes provides access to the membrane's bending modulus, as well as a length scale used to construct the model. Remarkably, though, gel-phase buckles do not follow the classical stress-strain relation of Euler elastica, which works very well for fluid membranes. Rather, they exhibit an exotic mechanical property called “curvature softening”, uncommon for most ordinary materials, but exhibited by certain meta-materials. These properties are well captured by an extended Helfrich model we propose, which goes beyond quadratic order in the membrane curvature, but, unlike other theories of curvature softening, has the further advantage of being analytically tractable.

A discussion of helicoidally symmetric surfaces follows in the next section. There, a powerful method of parametrizing helicoidally symmetric surfaces is explicitly constructed, and its properties are investigated in detail. This parametrization makes it possible to prove many interesting and useful geometric relations, including the existence of an equivalence between helicoidal and axisymmetric soap films. Our analysis also illustrates the relationship between helicoidal symmetry and conservation laws, both for geodesics on the surface and for the surface itself.

Now equipped with a useful parametrization, an analysis of helicoidally symmetric membranes becomes simple. An especially interesting application, treated in Section 3.2.4, is the case of dynamin-mediated membrane fission, in which a protein called dynamin self-assembles into helical scaffolds around the membrane necks of budding vesicles, a process which then somehow induces fission. There has been considerable debate in the biological community surrounding whether this process occurs *catalytically* or *mechanically*. In the catalytic model, the membrane breaks when thermal fluctuations take it from a metastable state to a stable “hemi-fission”

state, which is then followed by fission. By contrast, in the mechanical model, the membrane is destabilized directly by dynamin. In contrast to previous claims, which rest upon a simplified and incomplete solution to the membrane shape problem, and which suggest the possibility of a dynamin-triggered membrane-breakdown, our full analysis here shows that such an instability does not exist, lending credence to the catalytic model.

Chapters 4 and 5 consider the confinement of elastic rods to curved surfaces. This analysis aims towards building a theory of dynamin-mediated fission from another perspective, in which the membrane is represented by a fixed surface, and the dynamin protein is a continuous elastic filament. Chapter 4 introduces a mathematical theory of confined elastic rods, expanding on work by Guven, Valencia, and Vázquez-Montejo [GVM12, GVVM14]. This formalism shows how to find, in a transparent and systematic way, the Euler-Lagrange equations for confined rods as well as the appropriate boundary conditions for various physical scenarios.

Chapter 5 then applies the theory to two systems: first, to Euler rods confined to cylinders, and then to helical rods of variable length confined to cylinders and catenoids. The cylindrically confined Euler rods serve as a demonstration of the surprising complexity of this problem, as even this very simple case turns out to be unexpectedly difficult and mathematically rich. Elastic filaments are then used as a simplified mathematical model to study dynamin's self-assembly on curved surfaces. To make our model more biologically relevant, we need to expand the Hamiltonian from Section 5.1 to include spontaneous curvature, spontaneous twist, and twist rigidity. Our subsequent analysis leads to predictions of dynamin's polymerization behavior on cylinders and catenoids, including whether and where the polymer prefers to form on the neck. Furthermore, a natural competition between binding energy and elastic deformations of the polymer emerges, resulting in the fact that pre-curving a narrow neck can serve as a *geometric* (as opposed to biochemical) trigger for dynamin to assemble there, and not on other parts of the membrane. On the other hand, our theory also predicts that dynamin can only constrict membrane necks by a limited amount (about ten percent) when relying exclusively on equilibrium processes; this suggests that dynamin-mediated fission is an active process by necessity.

# Dedication

To Anna, the GTP to my dynamin, whose support, patience, wisdom, and motivation have driven the creation of this thesis. Thank you for keeping me going on the many occasions when I didn't feel like grad school would ever end.

# Acknowledgements

I want to thank Mike Staib, Matthew Daniels, Nora Swisher, Brad Treece, Will Levine, Brian Josey, Amy Stetten, Mert Terzi, Chasen Ranger, and Patrick Mende, for cooking, drinking coffee and beer, going to shows, camping, climbing, talking, driving to New York, lifting weights, street fighting, and exploring Pittsburgh and the world with me. I'm a happier and smarter person for having known you all.

Thanks to my parents, Tiffany and Larry Cacciatore, and my brother, Patrick Cacciatore, for listening to my endless gripes, bringing some extra home to Pittsburgh, and always saving a place for me in Tampa.

Thanks to Patrick Diggins, Pablo Vázquez-Montejo, Jemal Guven, and Zhanchun Tu for crucial research advice and assistance. Thanks to my committee, John Nagle, Tina Lee, and Kaushik Daiyal for advice on this thesis, and throughout my graduate career.

I am especially happy to thank my advisor, Markus Deserno, who has taught me how to do research, how to write, and, most importantly, how to be a scientist.

# Contents

<b>1</b>	<b>Introduction</b>	<b>8</b>
<b>2</b>	<b>Essential geometry and elasticity</b>	<b>10</b>
2.1	Theory of curves . . . . .	11
2.1.1	Frenet-Serret frame . . . . .	11
2.1.2	Material frame . . . . .	13
2.1.3	Spontaneous curvature . . . . .	16
2.1.4	Darboux frame . . . . .	17
2.1.5	Compression and stretching . . . . .	19
2.2	Theory of surfaces . . . . .	19
2.2.1	Metric tensor . . . . .	20
2.2.2	Coordinate changes . . . . .	22
2.2.3	Curvature tensor . . . . .	23
2.2.4	Covariant derivatives . . . . .	27
<b>3</b>	<b>Surface elasticity</b>	<b>30</b>
3.1	Gel phase buckling . . . . .	30
3.1.1	Finding the shape of the buckle . . . . .	32
3.1.2	Stress-strain relation . . . . .	35
3.1.3	Conclusions . . . . .	38
3.2	Helicoidal surfaces . . . . .	39
3.2.1	Parametrization . . . . .	40
3.2.2	Symmetries and conservation laws . . . . .	43
3.2.3	Soap films . . . . .	49
3.2.4	Membranes . . . . .	52
<b>4</b>	<b>Surface-bound elastic filaments: theory</b>	<b>62</b>
4.1	Unconfined filament . . . . .	64
4.1.1	Bernoulli-Euler rod . . . . .	64
4.1.2	General rod . . . . .	67
4.2	Surface confinement with free cross section . . . . .	70
4.2.1	Boundary conditions . . . . .	73
4.3	Surface confinement with fixed cross section . . . . .	76
4.3.1	Boundary conditions . . . . .	80
4.4	Surface symmetries . . . . .	80

<b>5</b>	<b>Surface-bound elastic filaments: applications</b>	<b>82</b>
5.1	Bernoulli-Euler rods on cylinders . . . . .	82
5.1.1	Boundary conditions . . . . .	85
5.1.2	Free endpoints . . . . .	86
5.1.3	Closed curves . . . . .	90
5.2	Dynammin as a surface-confined Kirchhoff rod . . . . .	96
5.2.1	Cylindrical substrate . . . . .	101
5.2.2	Catenoidal substrate . . . . .	104
5.2.3	Conclusions . . . . .	113
<b>6</b>	<b>Conclusion and summary</b>	<b>116</b>
<b>A</b>	<b>Illustration of numerical methods</b>	<b>119</b>
A.1	Finding the differential equations . . . . .	120
A.2	Making a good guess . . . . .	121
A.3	Implementation . . . . .	123
A.4	Example scripts . . . . .	124

# Chapter 1

## Introduction

Science is often portrayed as a hierarchy, with mathematics at the bottom (the most prestigious position), followed by physics, chemistry, and onward, with some social science at the top. In this picture, mathematicians do the most fundamental work, discovering theorems that can be applied in essentially any pursuit, being derived from pure logic. Physicists use these theorems to study the fundamental constituents of the universe, quarks, leptons, and so on. Since everything else is simply a composite of these objects, at the end of the day, the entire natural world can be reduced to physics. Next in the hierarchy, chemistry uses these laws of physics to study matter a larger scale, focusing atoms, molecules, and how they interact with each other. Finally within the natural sciences comes biology. The framework sees biology as aggregated chemistry, so that life is simply many chemical reactions occurring in concert.

We take a somewhat different view, represented by an alleged quotation from Johannes Kepler: “Where there is matter, there is geometry”. Indeed, within biological cells, many objects take diverse and interesting shapes. Consider, for example, the folds and spirals of the endoplasmic reticulum [TSK<sup>+</sup>13], the polytopes of viral capsids, and the intricate twists and turns of DNA molecules. While many of these shapes are merely the transient result of thermal fluctuations, others are more persistent. These enduring configurations have mechanical origins. Just as gravity and tension determine the shape of a suspended electrical cable, the shapes of cellular components are determined by the external forces acting on them and their own mechanical constitutive relations. At the length scales at which this geometry is relevant, these objects can be regarded as continuous one dimensional or two dimensional objects. For example, DNA is approximately linear over lengths on the order of 50 nm, hundreds of times longer than atomic length scales. All of this is to say, this biological geometry and mechanics is *emergent*: it appears when one considers the DNA molecule or lipid membrane as a distinct object. The mechanical, geometric description becomes meaningful and informative far above the scales where chemistry dominates.

This picture, in some sense, subverts the previously discussed hierarchy. The constitutive relations for a given material body emerge from the details of its composition. Physics no longer comes “from below” to explain chemistry, which then explains biology. Rather, physics approaches horizontally: mechanics, like chemistry, geometry, and biology itself, is simply one of the many necessary tools to understanding a given biological system.

In this thesis, we will explore the applications of mechanics and geometry to a selection of biological and biologically inspired problems. These investigations will lead us to deep insights and fascinating results in both areas. In particular, we are interested in membrane fission, the process by which cell membranes divide. This will require us to understand the elasticity of both one and two dimensional continua, i.e. curves and surfaces. In addition to attempting to directly address biological questions, we will also pursue a few problems that interesting from a theoretical physics perspective, though they are inspired by biology, including the buckling of membranes and the physics of surfaces with helicoidal symmetry.

We will begin with a summary of the relevant geometry and elasticity theory in Chapter 2. Then, we apply the theory to surfaces, with a particular emphasis on membranes in chapter 3. In Chapter 4, we will discuss the theory of elastic filaments confined to surfaces, which we then apply to a few systems of interest in Chapter 5.

# Chapter 2

## Essential geometry and elasticity

This thesis will rely heavily on the tools of differential geometry, which applies the methods of analytical calculus to geometry. Differential geometry is essential for understanding curved generalizations of Euclidean space.

It may be surprising that the toolset for understanding abstract curved spaces is useful for our purposes. But it turns out that these generalizations are precisely the ones needed to describe the mechanical deformations we are interested in. Such deformations necessarily change the geometry of the object in question. When we say “geometry”, we refer to properties of the shape of an object that are independent of how the object is situated in space, and how we choose to label points on the object. For example, we will later study lipid membranes confined to a box that is shorter than the total length of the membrane. As a result, they will have to buckle, differing dramatically from their flat ground state. In ways that we will quantify in this chapter, the membrane is now curved, where it was previously flat. That curvature is a *geometric* quantity: regardless of whether we turn the membrane upside down, or put it somewhere else, or parameterize it differently, the curvature should remain constant. Geometry is traditionally focused on the local properties of an object (e.g. how it is curved), while global properties (e.g. how many holes it has) are the realm of topology. However, as we will see, the boundary between the two fields is often blurred.

In this chapter, we therefore present a minimal review of the differential geometry necessary to navigate this thesis. Since we are concerned with the elasticity of polymers and membranes, which, for our purposes, can be accurately approximated as one- and two-dimensional objects, we will restrict this review to the geometry of curves and surfaces in three dimensional Euclidean space. Along the way, we will introduce common geometrically defined energy functionals.

Accessible sources on these subjects include reviews by Kamien [Kam02], Deserno [Des15], and Singer [Sin08]. Deserno puts special emphasis on surfaces, while Singer emphasizes the elasticity of rods. Kamien discusses both, but puts a greater emphasis on topology than the others. Much of our presentation will follow these lectures, the differential geometry texts by Frankel [Fra11] and Kreyszig [Kre68], and Landau and Lifshitz’s *Theory of Elasticity* [LL59]. For a history of the study of elastic filaments, see Levien [Lev08].

## 2.1 Theory of curves

Many objects in the biological realm are much thinner than they are long. These exist over many length scales, from  $\sim 0.5$  nm thick for DNA to  $\sim 100$   $\mu\text{m}$  thick for human hair [SH94, HYZC99, BM00, GWB12, MLAR14]. For mechanical purposes, these can often be accurately considered as mathematical curves. We therefore turn towards the theory of elastic filaments or rods, a subject that has been studied for hundreds of years [Lev08]. In particular, we will focus on rods that are *hyperelastic*, that is, those for which the mechanical properties are derived from an energy density [Ant05].

In this section, there are many sign conventions that vary in the literature. In particular, the signs of many vectors, and the curvatures in the corresponding directions, are all somewhat variable between publications. Unfortunately, there is neither a single consistent framework nor a rational criterion for how to choose these signs.

### 2.1.1 Frenet-Serret frame

The simplest mechanical theory of rods considers only one mode of deformation: bending. In order to quantify how a rod bends, we must first understand the geometry of the curve it traces through space.

Let us therefore consider a rod as a curve in three space,  $\mathbf{Y}(s)$ . Without loss of generality, we will assume  $s$  is the arc-length along the curve. The first step in quantifying the geometry of the curve is to define the curve's *Frenet-Serret frame*. This is an orthonormal vector frame, pinned to the curve, that varies along its length. The motions of this frame naturally give rise to appropriate invariant descriptions of the filament's curvature. We will see throughout this section that many such vector frames can be defined, and that they are foundational to any understanding of the geometry of curves.

The first component of the Frenet-Serret frame is the curve's tangent vector  $\mathbf{T}$ ,

$$\mathbf{T} = \mathbf{Y}'(s). \quad (2.1)$$

By our assumption that  $s$  is the arc-length along the curve,  $|\mathbf{T}| = 1$ . The second vector in our frame is obtained by differentiating the tangent vector, which is guaranteed to result in a vector perpendicular to  $\mathbf{T}$  by virtue of the fact that  $\mathbf{T}$  has unit length. However,  $\mathbf{T}'$  need not itself be of unit magnitude. In fact, the magnitude of  $\mathbf{T}'$  defines the *curvature*  $\kappa$  of the space-curve, while the direction defines the *principal normal*  $\mathbf{N}$ , so that

$$\mathbf{T}'(s) = \kappa \mathbf{N}. \quad (2.2)$$

Notice that this definition of  $\mathbf{N}$  fails at points where  $\mathbf{T}' = 0$ . Thus there is no well-defined principal normal wherever  $\kappa$  vanishes.

The curvature  $\kappa$  is our first geometric invariant of the curve: it is preserved by isometric transformations of the curve, such as translations and rotations. It also has a simple geometric interpretation: the “radius of curvature”  $r = 1/\kappa$  is the radius of a hypothetical circle, called the *osculating circle* (“kissing” circle). The osculating circle lies in the  $\mathbf{TN}$ -plane, touching the curve at the point  $\mathbf{Y}(s)$  such that both the first and second arc-length derivative of the circle match that of the curve, as in figure 2.1.

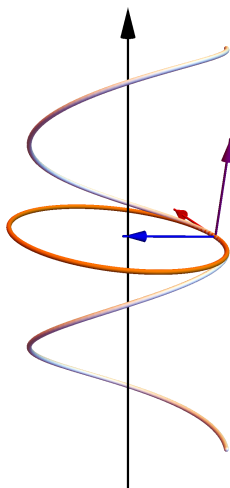


**Figure 2.1:** The osculating circle for a helical curve is shown here in orange. The radius of this circle is the curvature at the point of contact,  $r = 1/\kappa$ . The red, blue, and purple arrows are the tangent, normal, and binormal vectors, respectively.

Lastly, a third unit vector, called the binormal vector  $\mathbf{B}$  can be defined naturally as the cross product of the first two,

$$\mathbf{B} = \mathbf{T} \times \mathbf{N}. \quad (2.3)$$

The binormal  $\mathbf{B}$  is of course perpendicular to the osculating plane. Thus as the osculating circle rotates around the curve,  $\mathbf{B}$  keeps track of its orientation, and its derivative  $\mathbf{B}'$  will tell us the rate of the rotation. To compute  $\mathbf{B}'$ , first note that because the binormal has unit magnitude,  $|\mathbf{B}| = 1$ , its derivative must be perpendicular to  $\mathbf{B}$ . Furthermore, because  $\mathbf{T}$  and  $\mathbf{B}$  are orthogonal,

$$\begin{aligned} 0 &= (\mathbf{T} \cdot \mathbf{B})' = \mathbf{T}' \cdot \mathbf{B} + \mathbf{T} \cdot \mathbf{B}' \\ \implies \mathbf{B}' \cdot \mathbf{T} &= -\mathbf{T}' \cdot \mathbf{B} = -\kappa \mathbf{N} \cdot \mathbf{B} = 0. \end{aligned} \quad (2.4)$$

This implies that  $\mathbf{B}'$  is parallel to the principal normal  $\mathbf{N}$ . Defining the *torsion*  $\tau$ , we write

$$\mathbf{B}' = -\tau \mathbf{N}. \quad (2.5)$$

Note that for a planar curve (i.e. one that is entirely contained in a plane),  $\tau = 0$ . We can therefore consider  $\tau$  a local measurement of how much a curve deviates from being planar.

Since we have calculated the derivatives of  $\mathbf{T}$  and  $\mathbf{B}$  in detail, let us now consider how the principal normal  $\mathbf{N}$  changes along the filament. Because  $\mathbf{T}$  and  $\mathbf{N}$  are orthogonal, we see that  $\mathbf{N}' \cdot \mathbf{T} = -\mathbf{T}' \cdot \mathbf{N} = -\kappa$ . By the same logic,  $\mathbf{N}' \cdot \mathbf{B} = -\mathbf{B}' \cdot \mathbf{N} = \tau$ . This completes the set of identities known as the Frenet-Serret relations, which can be compactly written

$$\frac{d}{ds} \begin{pmatrix} \mathbf{N} \\ \mathbf{B} \\ \mathbf{T} \end{pmatrix} = \begin{pmatrix} 0 & \tau & -\kappa \\ -\tau & 0 & 0 \\ \kappa & 0 & 0 \end{pmatrix} \begin{pmatrix} \mathbf{N} \\ \mathbf{B} \\ \mathbf{T} \end{pmatrix}. \quad (2.6)$$

An alternative method of writing down the same statement is the following:

$$\mathbf{N}' = \boldsymbol{\omega} \times \mathbf{N}, \quad (2.7a)$$

$$\mathbf{B}' = \boldsymbol{\omega} \times \mathbf{B}, \quad (2.7b)$$

$$\mathbf{T}' = \boldsymbol{\omega} \times \mathbf{T}, \quad (2.7c)$$

where

$$\boldsymbol{\omega} = \kappa \mathbf{B} + \tau \mathbf{T}. \quad (2.8)$$

The vector  $\boldsymbol{\omega}$  is called the “angular velocity” vector, which describes the rotation of the Frenet-Serret frame: it rotates about  $\mathbf{T}$  at a rate  $\tau$ , and about  $\mathbf{B}$  and a rate  $\kappa$ . The nomenclature originates from an analogy to the rotation of a rigid body.

With these definitions, we have enough tools at our disposal to consider the simplest model of an elastic filament, for which the energy is proportional to the total squared curvature

$$E_{\text{BE}} = \frac{\alpha}{2} \int_0^L ds \kappa^2. \quad (2.9)$$

The parameter  $\alpha$  is the bending rigidity. This model is called the Euler rod, or sometimes the Bernoulli-Euler rod.

### 2.1.2 Material frame

However, the Bernoulli-Euler rod is far from a complete model. We can easily see that something is lacking in this description if we wish to apply it to real elastic rods and filaments. This can be demonstrated easily with a few moments of playing around with a wire (grab one if it’s handy!). Pinching one end in each hand and keeping the wire straight, we feel resistance as we twist it. This obviously requires information about the wire that *is not contained in its description as a space curve!*

Specifically, we need to keep track of the rotation of the actual physical cross section of the wire about the wire’s tangent, rather than that of an abstract vector frame. We therefore must define a new orthonormal frame, called the *material frame*,  $\{\mathbf{T}, \mathbf{m}_1, \mathbf{m}_2\}$  [Sin08]. This frame carries internal degrees of freedom of the rod through the vectors  $\mathbf{m}_i$ .

Defining the material frame turns out to be surprisingly subtle. The reason for this is that it can only be defined relative to some *reference configuration*,  $\mathbf{Y}^\circ(s)$ ,  $\mathbf{m}_1^\circ$ ,  $\mathbf{m}_2^\circ$ . That is, we imagine having the rod in a configuration  $\mathbf{Y}^\circ(s)$ , and painting a set of lines along it indicating the directions of  $\mathbf{m}_1^\circ$  and  $\mathbf{m}_2^\circ$ . Then, when the rod is deformed, we can use our painted lines to determine the new configuration of the material frame. In principle, the reference configuration can be chosen arbitrarily. The most obvious and natural choice is the *stress-free* configuration of the rod, that is, the configuration the rod takes when no forces are applied to it. However, this still leaves open the question of how to best paint our material lines on the rod.

Just as the Frenet-Serret equations (2.6) describe the rotation of the Frenet-Serret frame as it moves along the rod, we have a matrix relation that describes the rotation of the material frame:

$$\frac{d}{ds} \begin{pmatrix} \mathbf{m}_1 \\ \mathbf{m}_2 \\ \mathbf{T} \end{pmatrix} = \begin{pmatrix} 0 & \kappa_t & -\kappa_1 \\ -\kappa_t & 0 & -\kappa_2 \\ \kappa_1 & \kappa_2 & 0 \end{pmatrix} \begin{pmatrix} \mathbf{m}_1 \\ \mathbf{m}_2 \\ \mathbf{T} \end{pmatrix}, \quad (2.10)$$

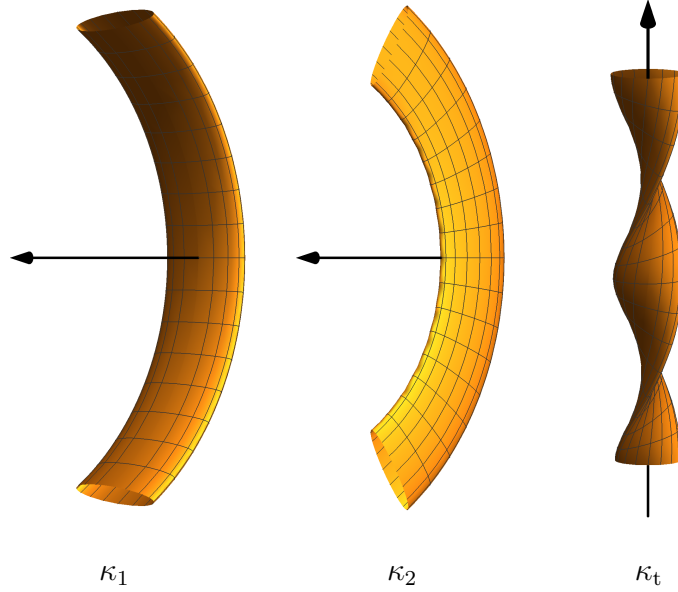


**Figure 2.2:** Different material curvatures and twist of a ribbon-like filament.

where  $\kappa_1$  and  $\kappa_2$  are called the *material curvatures* of the rod, and  $\kappa_t = \mathbf{m}'_1 \cdot \mathbf{m}_2$  is called the *twist*. As the torsion describes the rotation of the Frenet-Serret frame about  $\mathbf{T}$ , the twist describes the rotation of the material frame about  $\mathbf{T}$ . Again, we could equivalently write this equation using an angular velocity vector,

$$\mathbf{m}'_1 = \boldsymbol{\omega} \times \mathbf{m}_1, \quad (2.11a)$$

$$\mathbf{m}'_2 = \boldsymbol{\omega} \times \mathbf{m}_2, \quad (2.11b)$$

$$\mathbf{T}' = \boldsymbol{\omega} \times \mathbf{T}, \quad (2.11c)$$

where

$$\boldsymbol{\omega} = -\kappa_2 \mathbf{m}_1 + \kappa_1 \mathbf{m}_2 + \kappa_t \mathbf{T}. \quad (2.12)$$

The components of the angular velocity vector are often denoted differently. A common notation is to define the material curvatures so that  $\boldsymbol{\omega} = \kappa_t \mathbf{T} + \kappa_1 \mathbf{m}_1 + \kappa_2 \mathbf{m}_2$ , so that each curvature is the rate of rotation of the material frame about an axis. We instead define them to refer to how the filament bends in a given direction.

The quantities  $\kappa_1$  and  $\kappa_2$  are illustrated in figure 2.2. It should come as no surprise that the material curvatures, quantifying bending in different directions, can be related to the Frenet curvature  $\kappa$ , quantifying the overall bending. To do so, we introduce the angle  $\theta(s)$  between  $\mathbf{m}_1$  and  $\mathbf{N}$ . The curvature vector is then given by

$$\mathbf{T}' = \kappa \mathbf{N} = \kappa (\cos \theta \mathbf{m}_1 - \sin \theta \mathbf{m}_2) = \kappa_1 \mathbf{m}_1 + \kappa_2 \mathbf{m}_2, \quad (2.13)$$

leading to the identities

$$\kappa_1 = \kappa \cos \theta \quad (2.14)$$

$$\kappa_2 = -\kappa \sin \theta \quad (2.15)$$

$$\kappa^2 = \kappa_1^2 + \kappa_2^2. \quad (2.16)$$

By distinguishing curvature in different directions, the material frame allows us to model rods that have anisotropic bending rigidities. In fact, quantifying this anisotropy incidentally suggests a choice for the reference configuration of the material frame. The bending rigidity of an anisotropic rod is described by a  $2 \times 2$  symmetric matrix  $I_{ij}$  defined at each point along the filament, called the *inertia tensor* (again by analogy to the rigid rotor) [LL59]. In principle,  $I_{ij}$  need not be a constant function of  $s$ . This depends both on our choice of the material frame and the uniformity of the rod. For example, consider a rod with a circular cross section that gets wider along the rod's length. It should be obvious that the rod will be harder to bend at the thicker end than the thinner one, and thus there is no way to choose the material frame such that  $I_{ij}$  is constant. On the other hand, consider a rod much wider in one direction than the other, as depicted in figure 2.2. If we paint our material lines spiraling around such a filament, then  $I_{ij}$  will not be constant. But by painting straight lines up the side of the filament, we can guarantee that  $I_{ij}$  is constant. In fact, we can do even better: because  $I_{ij}$  is symmetric, its eigenvectors are orthogonal, implying that we can choose the material frame to *diagonalize*  $I_{ij}$ . This argument shows that the material frame is inextricable from the mechanical properties of the rod.

Constructing the material frame to diagonalize the inertia tensor fails in only one case: when it is proportional to the identity,  $I_{ij} \propto \delta_{ij}$ . Then, any pair of orthogonal vectors diagonalizes  $I_{ij}$ ; the most obvious solution is to choose the reference frame to have zero twist,  $\kappa_t = 0$ .

We can therefore define a natural generalization of the Euler elastic model, called the Kirchhoff elastic rod, for which the energy is [LS96, Sin08]

$$E_K = \frac{1}{2} \int_0^L ds (\alpha_1 \kappa_1^2 + \alpha_2 \kappa_2^2 + \beta \kappa_t^2), \quad (2.17)$$

where  $\alpha_i$  are the eigenvalues of  $I_{ij}$ . Terms proportional to  $\kappa_i \kappa_t$  are traditionally omitted because they break the  $s \mapsto -s$  symmetry of the filament [LL59]. The constant  $\beta$  defines the twist rigidity of the rod. The inertia tensor  $I_{ij}$  can be calculated in terms of the rod's Young modulus and the shape of its cross section, while calculating the twist rigidity  $\beta$  also requires the Poisson ratio [LL59].

Let us make the analogy to rigid body motion more rigorous. The energy in equation (2.17) is quadratic in the components of the angular velocity vector  $\boldsymbol{\omega}$ , which describes the rotation of the material frame. But the Lagrangian of a rigid rotor is simply quadratic in the components of the angular velocity vector of the rigid body, which describes the material rotation of the body [GPS02]. The analogy maps the material curvatures and twist to the components of the physical angular velocity. Both the elasticity and nonlinear dynamics literature have made fruitful use of this connection [MH88, DM93, NG99, GPL05].

The exact meaning of the twist  $\kappa_t$  for a complexly bending curve is not clear. After all, given the somewhat arbitrary definition of the material frame, how can its rotation quantify anything meaningful? In order to find a more digestible geometric interpretation, we define a curve's *natural frame* (or inertial frame), which has the special property of not rotating about the tangent vector. As a result, the angular velocity vector  $\boldsymbol{\omega}$  has no tangential component [Sin08]. Let the normal vectors to the filament in the natural frame be given by  $\mathbf{u}$  and  $\mathbf{v}$ . Then the vanishing tangential component of the angular velocity vector is equivalent to  $\mathbf{u}' \cdot \mathbf{v} = 0$ . Similar "parallel

transport” laws are in fact ubiquitous, for example governing the polarization of the electromagnetic waves in fiber-optic cables [Ber90].

Let us define the angle  $\psi$  between the natural and material frames. Then we can write  $\mathbf{m}_1$  and  $\mathbf{m}_2$  of the material frame in terms of  $\mathbf{u}$  and  $\mathbf{v}$ ,

$$\mathbf{m}_1 = \cos \psi \mathbf{u} + \sin \psi \mathbf{v} \quad (2.18)$$

$$\mathbf{m}_2 = -\sin \psi \mathbf{u} + \cos \psi \mathbf{v}. \quad (2.19)$$

Differentiating  $\mathbf{m}_1$ , one finds

$$\psi'(s) = \mathbf{m}'_1 \cdot \mathbf{m}_2 = \kappa_t. \quad (2.20)$$

Thus we have identified what it is that  $\kappa_t$  measures twist relative to: the natural frame of the rod. Although the natural frame coincides with the material frame in the case  $\kappa_t = 0$ , it is important to note that the natural frame *does not require information about the material of the rod*. It is fixed (up to an overall constant rotation) by the space curve the rod traces.

With this fact in mind, let us return for a moment to the Kirchhoff elastic rod, in particular the special case when  $\alpha_1 = \alpha_2$ , called the isotropic case. The energy is then

$$E_{\text{iso}} = \frac{1}{2} \int_0^L ds (\alpha [\kappa_1^2 + \kappa_2^2] + \beta \kappa_t^2) = \frac{1}{2} \int_0^L ds (\alpha \kappa^2 + \beta \psi'^2), \quad (2.21)$$

where we have used the identities (2.16) and (2.20). Recall that  $\kappa$  is a geometric property of the filament’s centerline, and is thus independent of the orientation of the material frame. Therefore this orientation only appears in the energy functional in the  $\psi'$  term and can be varied independently. Performing a functional variation of  $\psi$ , the change in energy is

$$\delta_\psi E_{\text{iso}} = - \int_0^L ds \delta\psi \psi'' + [\psi' \delta\psi]_0^L. \quad (2.22)$$

In order for the first term to vanish, we must have that the twist rate  $\psi' = \kappa_t$  is constant. Put another way,  $\kappa_t$  is the conserved quantity associated with isotropy of the rod.

One case of particular interest occurs when the angle  $\psi$  is free at the endpoints (i.e.  $\delta\psi$  is arbitrary). Then, the boundary term vanishes only if  $\kappa_t = \psi' = 0$ . This offers a mechanical justification for the definition of the natural frame: given a spatial configuration of a filament, the natural frame is equivalent to the material frame of an isotropic filament in that same configuration when the material cross-section is able to relax.

This decouples the material and geometric degrees of freedom, so that the energy functional of the isotropic Kirchhoff rod ultimately becomes identical to that of the Euler elastic rod [LS96]. We can restore the coupling between the internal and geometric degrees of freedom by breaking the isotropy of the rod. Then  $\kappa_t$  will not necessarily be constant.

### 2.1.3 Spontaneous curvature

For both the Kirchhoff and Bernoulli-Euler rods, the relaxed state of the rod is a straight line, with  $\kappa = 0$ . We further assumed in the case of the Kirchhoff rod that

the stress-free state is untwisted,  $\kappa_t = 0$ . It is not uncommon, though, for rods to have some spontaneous shape, i.e. for their relaxed state to be something other than a straight line. For example, the wire making up a coil spring is relaxed when it forms a helix with a certain pitch and radius; these could be described by a rod with some constant spontaneous curvature and twist. Dynamins filaments and human hairs as well form helical structures [MLAR14, SDS00a, FPG<sup>+</sup>11, FJN11].

Suppose the filament has some preferred curvature vector  $\mathbf{c}$ , and preferred twist  $c_t$ , such that, when no force is applied onto it,  $\kappa\mathbf{N} = \mathbf{c}$  and  $\kappa_t = c_t$ . This is incorporated into the Kirchhoff model by writing the energy as

$$E_{\text{gen}} = \frac{1}{2} \int_0^L ds \left( \alpha_1(\kappa_1 - c_1)^2 + \alpha_2(\kappa_2 - c_2)^2 + \beta(\kappa_t - c_t)^2 \right), \quad (2.23)$$

where  $c_i = \mathbf{c} \cdot \mathbf{m}_i$  are the components of the spontaneous curvature vector along the basis vectors of the material frame. Note that the spontaneous curvature vector  $\mathbf{c}$  defines a preferred direction. In general, this direction does not align with one of the eigenvectors of  $I_{ij}$ , and so there is a spontaneous curvature along both material directions (that is, both eigenvectors of the inertial tensor  $I_{ij}$ ).

We must be very careful about when it is appropriate to include a spontaneous twist. Firstly, introducing a spontaneous twist creates a term in the energy functional proportional to the twist  $\kappa_t$ , thus breaking the  $s \mapsto -s$  symmetry of the filament. In this sense, such filaments are somewhat anomalous. Secondly, the connection between a filament's (internal) twist and its (external) geometry is very subtle. For example, a filament with a rotating elliptic cross section and an unstressed state as in the right panel of figure 2.2 could be very reasonably said to have spontaneous twist: the natural choice for the material frame is along the principal axes of the ellipse, which choice leads to a non-zero twist in the unstressed state. However, the most natural energy functional for a filament *square* cross section that “twists” similarly *need not have any spontaneous twist!* In that case, the inertia tensor  $I_{ij}$  is proportional to the identity, and so is diagonal in any orthonormal basis. We can therefore choose a reference configuration for the material frame with  $\kappa_t = 0$ , as discussed above.

### 2.1.4 Darboux frame

We will also be interested in filaments that are confined to curved surfaces, e.g. dynamins on membranes or DNA on histones [BMS99, SDS00a]. In order to discuss the confinement of rods to surfaces, it will be convenient to introduce what is called the “Darboux frame”, which is often convenient for describing surface curves. This frame takes the normal vector  $\mathbf{n}$  to the surface as one of its elements.<sup>1</sup> The last vector in this frame is again defined using the cross product to complete an orthonormal triad,  $\mathbf{L} = \mathbf{T} \times \mathbf{n}$ , called the *conormal vector* or the *transverse vector* because it is tangential to the surface, but normal to the rod. See figure 2.3 for an illustration.

The Darboux relations describe the rotation of this frame,

$$\frac{d}{ds} \begin{pmatrix} \mathbf{T} \\ \mathbf{n} \\ \mathbf{L} \end{pmatrix} = \begin{pmatrix} 0 & \kappa_n & \kappa_g \\ -\kappa_n & 0 & \tau_g \\ -\kappa_g & -\tau_g & 0 \end{pmatrix} \begin{pmatrix} \mathbf{T} \\ \mathbf{n} \\ \mathbf{L} \end{pmatrix}, \quad (2.24)$$

<sup>1</sup>The surface normal is written lowercase to distinguish it as a surface vector, a convention we will do our best to adhere to throughout the thesis.

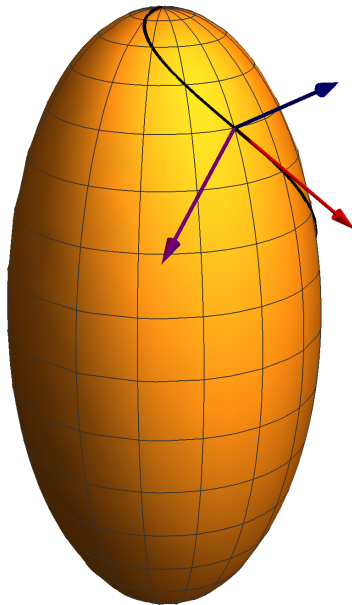


**Figure 2.3:** The Darboux frame for a curve on an ellipsoid. The red, blue, and purple arrows are the tangent, surface normal, and conormal vectors, respectively.

where  $\kappa_g$  is called the geodesic curvature,  $\kappa_n$  the normal curvature, and  $\tau_g$  the geodesic torsion. The equivalent identity in terms of an angular velocity vector is

$$\mathbf{T}' = \boldsymbol{\omega} \times \mathbf{T}, \quad (2.25a)$$

$$\mathbf{n}' = \boldsymbol{\omega} \times \mathbf{n}, \quad (2.25b)$$

$$\mathbf{L}' = \boldsymbol{\omega} \times \mathbf{L}, \quad (2.25c)$$

where

$$\boldsymbol{\omega} = \tau_g \mathbf{T} - \kappa_g \mathbf{n} + \kappa_n \mathbf{L}. \quad (2.26)$$

The normal curvature  $\kappa_n$  and geodesic torsion  $\tau_g$  are especially interesting because they are properties that are intrinsic to the surface: at a given point on the surface, and a given direction for the tangent vector  $\mathbf{T}$ ,  $\kappa_n$  and  $\tau_g$  are given. On the other hand, the geodesic curvature  $\kappa_g$  in that situation is still not prescribed. We will return to these quantities in the next section on the geometry of surfaces.

Let us introduce the angle  $\theta$  between the Frenet-Serret normal  $\mathbf{N}$  and the surface normal  $\mathbf{n}$ , so that

$$\kappa_n = \kappa \cos \theta \quad (2.27a)$$

$$\kappa_g = \kappa \sin \theta \quad (2.27b)$$

$$\kappa^2 = \kappa_g^2 + \kappa_n^2. \quad (2.27c)$$

When  $\theta = 0$ , the normal curvature is equal to the Frenet curvature,  $\kappa_n = \kappa$ , and the geodesic curvature vanishes,  $\kappa_g = 0$ . Curves for which  $\theta = 0$  everywhere are called

geodesics. When  $\theta = \pm\pi/2$  everywhere, so that  $\kappa_n = 0$  and  $\kappa = \pm\kappa_g$ , the curve is called an “asymptote”. We can also relate the geodesic torsion and Frenet-Serret torsion by writing the principal normal and binormal vectors as

$$\mathbf{N} = \cos\theta \mathbf{n} + \sin\theta \mathbf{L} \quad (2.28)$$

$$\mathbf{B} = -\sin\theta \mathbf{n} + \cos\theta \mathbf{L}. \quad (2.29)$$

Differentiating, we find that

$$\mathbf{N}' \cdot \mathbf{B} = \tau = \tau_g + \theta'. \quad (2.30)$$

This identity is the origin of the unfortunate name “geodesic torsion”: for geodesics, it is identical to the Frenet-Serret torsion. Note that the reason  $\tau_g = \tau$  for geodesics is really just that  $\theta$  is constant for geodesics. Any other curve with  $\theta = \text{constant}$  (for example, an asymptote) would of course also satisfy  $\tau_g = \tau$ .

### 2.1.5 Compression and stretching

In biological contexts, most of the energy deforming a rod goes into bending it, rather than compressing or stretching; thus most literature on elastic rods as a model of polymers or proteins focuses on the incompressible limit. But in certain cases, such as rubber bands, certain ropes, and structural columns, the length of the filament can be easily changed without adding or subtracting any material. This is especially important when studying the buckling of columns [Hud78]. In such cases, we must introduce an additional internal degree of freedom to keep track of the compression relative to the relaxed length called the compressive (or axial) strain

$$\gamma = \frac{d\hat{s}}{ds}, \quad (2.31)$$

where  $\hat{s}$  is the compressed arc-length, and  $s$  is the relaxed arc-length. The Kirchhoff rod model was extended to include compression in reference [Ant74]. This degree of freedom can substantially change the behavior of elastic rods, and lead to interesting non-linearities. For example, while the planar Bernoulli-Euler elastic rod has the same Euler-Lagrange equation as a classical pendulum, a compressible planar elastic rod has the Euler-Lagrange equation of a *relativistic* pendulum [OD16]. However, we will not need these considerations in the analysis presented in this thesis, and so we will not discuss the matter in depth.

## 2.2 Theory of surfaces

We would like to describe surfaces in terms of some kind of geometric invariants, as we have used for curves. Unfortunately, this increase in dimensionality leads to a substantial increase in difficulty. Curves are essentially defined by how they move through ambient space. Outside of this embedding, there is not much to say about a curve. Imagine living in a one dimensional space, where we can only go forwards and backwards. In this world, curvature becomes meaningless. How could we begin to measure it without something to curve relative to? The only interesting questions we can ask are global rather than local, such as is whether we ever return to our starting point if we walk in a straight line.

In contrast, a two-dimensional space can have many more properties that are defined without reference to the space in which the surface lives. It is perfectly sensible to talk about “the sphere” purely as a space without embedding it anywhere because the sphere has certain *intrinsic* properties. The most obvious property is a global one: if you walk “straight” in any direction for long enough, you’ll end up back where you were. However, we can also detect the geometry at a local level. If you look at a triangle on the sphere, the interior angles of that triangle would add up to more than  $\pi$ ; in fact, the sum of those angles would depend on the area of the triangle. It would even be possible to walk around in a “bi-angle”, a closed curve composed of two straight lines. These are abstract geometric properties that exist independent of where you put the sphere!

On the other hand, other properties *do* require reference to the ambient space. The normal curvature  $\kappa_n$  and geodesic torsion  $\tau_g$  of a surface curve, for example, were calculated using the surface’s normal vector,  $\mathbf{n}$ . Such a vector simply does not exist without an embedding space. Quantities that are defined in terms of the normal vector are said to be “extrinsic”.

Defining the geometric properties of a surface without reference to an ambient space can be somewhat difficult. Thankfully, we have the great advantage that we are only interested in real physical surfaces, representing objects such as membranes and soap films. We therefore consider embedding the surface in Euclidean three-dimensional space, making it possible to access all of the surface’s geometric properties easily.

Mathematically, we represent surfaces as maps that take coordinates  $(u^1, u^2)$  to a point in three dimensional Euclidean space  $\mathbf{X}(u^1, u^2) \in \mathbb{R}^3$ , called an “embedding” (note that the superscript in  $u^a$  is an index, not an exponent). This is called an *explicit* or parametric representation of the surface, in contrast to an *implicit* representation, which is defined by an equation of the form  $F(\mathbf{x}) = 0$ , where  $\mathbf{x} \in \mathbb{R}^3$ . We can derive everything we need to know about the surface from the map  $\mathbf{X}(u^1, u^2)$ .

### 2.2.1 Metric tensor

Perhaps the most important property of a surface is the metric tensor, which is used to measure the distance between points on the surface. This is so fundamental that the intrinsic properties of the surface are just those that are derived from the metric. For an abstract consideration of two-dimensional spaces, one could for instance take the metric as given. With an embedding, however, we can derive the distance between points on the surface in terms of the ambient space, so that the metric is “inherited”. Consider two close-by points on the surface with coordinates  $u^a$  and  $u^a + \delta u^a$ , where  $a$  is an index ranging from one to two. The distance between these two points is (to lowest order in  $\delta u^a$ )

$$|\mathbf{X}(u^a + \delta u^a) - \mathbf{X}(u^a)|^2 \approx \left( \delta u^a \frac{\partial \mathbf{X}}{\partial u^a} \right) \cdot \left( \delta u^b \frac{\partial \mathbf{X}}{\partial u^b} \right) = g_{ab} \delta u^a \delta u^b, \quad (2.32)$$

where repeated indices, one superscript and its counterpart subscript, are implicitly summed over. Here, we have defined the metric tensor, or “first fundamental form”,  $g_{ab}$  as

$$g_{ab} = \frac{\partial \mathbf{X}}{\partial u^a} \cdot \frac{\partial \mathbf{X}}{\partial u^b}, \quad (2.33)$$

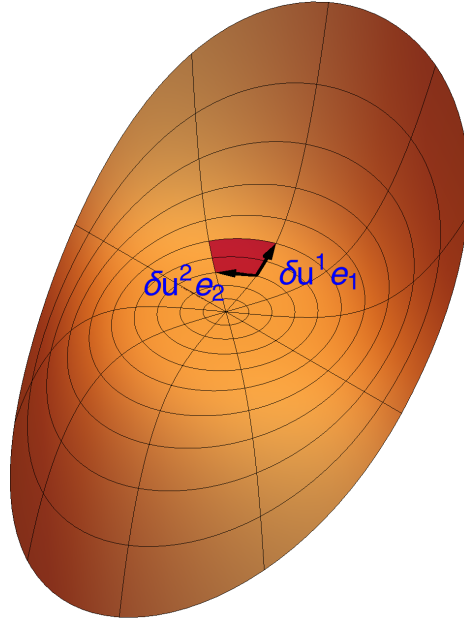


**Figure 2.4:** The the patch shown in red can be approximated as a parallelogram for small  $\delta u^1$  and  $\delta u^2$ . This approximation gives area of the patch using the metric tensor.

which is manifestly symmetric in its indices. We will also find it convenient to introduce the surface's tangent vectors  $\mathbf{e}_a$ ,

$$\mathbf{e}_a = \frac{\partial \mathbf{X}}{\partial u^a}. \quad (2.34)$$

These two vectors form a basis for the plane tangent to the surface at any given point.

The metric is also the natural tool to measure areas on the surface. Consider a small patch of surface bounded by coordinate curves, as shown in figure 2.4. For sufficiently small  $\delta u^1$  and  $\delta u^2$ , this patch can be well approximated by a parallelogram, and will thus have area

$$\begin{aligned} \delta u^1 \delta u^2 |\mathbf{e}_1 \times \mathbf{e}_2| &= \delta u^1 \delta u^2 |\mathbf{e}_1| |\mathbf{e}_2| \sin \theta \\ &= \delta u^1 \delta u^2 |\mathbf{e}_1| |\mathbf{e}_2| \sqrt{1 - \cos^2 \theta} \\ &= \delta u^1 \delta u^2 \sqrt{|\mathbf{e}_1|^2 |\mathbf{e}_2|^2 - (\mathbf{e}_1 \cdot \mathbf{e}_2)^2} \\ &= \delta u^1 \delta u^2 \sqrt{g}, \end{aligned} \quad (2.35)$$

where  $g = \det(g_{ab}) = g_{11}g_{22} - g_{12}^2$  is the determinant of the metric tensor. This defines the area element  $dA$  for the surface,

$$dA = \sqrt{g} du^1 du^2. \quad (2.36)$$

The area element is our first geometric invariant of the surface. With it, we can define a simple energy functional that is proportional to the surface's area. This

is commonly used to model soap films and fluid interfaces, which have a constant surface tension  $\sigma$ , so that the energy is

$$E_{\text{soap}} = \int dA \sigma. \quad (2.37)$$

The metric tensor also defines an inner product for vectors tangential to the surface. Let us write two vectors  $\mathbf{p}$  and  $\mathbf{q}$  in the basis of the surface tangent vectors,

$$\mathbf{p} = p^a \mathbf{e}_a, \quad \mathbf{q} = q^a \mathbf{e}_a \quad (2.38)$$

Their inner product is given by

$$\mathbf{p} \cdot \mathbf{q} = (p^a \mathbf{e}_a) \cdot (q^b \mathbf{e}_b) = g_{ab} p^a q^b. \quad (2.39)$$

Once again, the surface has inherited an inner product structure from the ambient space.

## 2.2.2 Coordinate changes

As we stated in the introduction, geometric properties of the surface should be independent of how we label the points on the surface. Therefore, it is important to consider how the quantities we have defined change when we change their labels, i.e. under a change of coordinates. Those that do change under coordinate transformations are not necessarily less valuable. They simply must be recognized as contingent upon the chosen coordinate system, and this fact must inform how we use such objects.

Coordinate transformations can always be represented by an invertible map  $(u^1, u^2) \mapsto (u'^1, u'^2)$ . We can express the new tangent vectors to the surface by simply applying the chain rule to the definition of the tangent vectors,

$$\mathbf{e}'_a = \frac{\partial \mathbf{X}}{\partial u'^a} = \frac{\partial u^b}{\partial u'^a} \frac{\partial \mathbf{X}}{\partial u^b} = J_a^b \mathbf{e}_b, \quad (2.40)$$

where we have defined the Jacobian matrix of our transformation,

$$J_a^b = \frac{\partial u^b}{\partial u'^a}. \quad (2.41)$$

We can apply the same reasoning to find the metric in the new basis,

$$\begin{aligned} g'_{ab} &= \frac{\partial \mathbf{X}}{\partial u'^a} \cdot \frac{\partial \mathbf{X}}{\partial u'^b} \\ &= \frac{\partial \mathbf{X}}{\partial u^c} \cdot \frac{\partial \mathbf{X}}{\partial u^d} \frac{\partial u^c}{\partial u'^a} \frac{\partial u^d}{\partial u'^b} \\ &= g_{cd} J_a^c J_b^d. \end{aligned} \quad (2.42)$$

Note that equation (2.42) is a similarity transformation of the original metric at each point on the surface. As a result, it is always possible to choose coordinates so that the metric is *locally* diagonal. In fact, by rescaling the coordinates that diagonalize the metric, it is even possible to choose coordinates (called “conformal coordinates” or “isothermal coordinates”) that render the metric proportional to the

identity matrix, so that  $g_{ab} = \phi(u, v)\delta_{ab}$  [DC76]. Note that it is not generally possible to define coordinates for which this relation holds globally; it is only guaranteed locally.

In equations (2.40) and (2.42), the transformation behavior was such that each index necessitated a Jacobian matrix. The components of surface vectors transform differently. For a vector  $\mathbf{p}$ , we consider the vector itself to be invariant, an object that exists independent of any chosen description of the surface. With this assumption, the transformation properties follow naturally,

$$\begin{aligned}\mathbf{p} &= p^a \mathbf{e}_a = p^a \frac{\partial \mathbf{X}}{\partial u^a} \\ &= p^a \frac{\partial u'^b}{\partial u^a} \frac{\partial \mathbf{X}}{\partial u'^b} = p^a (J^{-1})^b_a \mathbf{e}'_b = p'^b \mathbf{e}'_b \\ \implies p'^b &= (J^{-1})^b_a p^a.\end{aligned}\tag{2.43}$$

Since the vector itself is invariant, its components must transform via the inverse of the Jacobian matrix. From these transformation laws, we can see the beginning of a pattern: each subscript index results in multiplication by the Jacobian matrix (such indices are called “covariant”), while superscript indices result in multiplication by the inverse Jacobian matrix (and are called “contravariant”).<sup>2</sup> Objects with no indices (scalars) are invariant under reparameterization.

Note that not all objects with indices necessarily transform as outlined. The coordinates  $u^a$  themselves are one example, as is the metric determinant  $g$ . Later on, we will encounter more cases that are most conveniently written down with index notation, but do not transform appropriately. This “rule” therefore must be used cautiously.

With a metric, no object needs to be considered fundamentally covariant or contravariant: the transformation properties of each index can be exchanged easily by multiplying by the metric or its inverse. The inverse metric is defined by

$$g^{ab} g_{bc} = \delta_c^a,\tag{2.44}$$

where  $\delta_b^a$  is the Kronecker-delta, which is by definition coordinate independent. This allows us to, for example, consider contravariant versions of the surface tangent vectors,  $g^{ab} \mathbf{e}_b = \mathbf{e}^a$ , or covariant versions of the components of a vector  $p_a = g_{ab} p^b$ . With this notation, the inner product of two vectors can be written

$$\mathbf{p} \cdot \mathbf{q} = g_{ab} p^a q^b = p_a q^a.\tag{2.45}$$

This reasoning allows us to “contract” any two indices, that is, to combine and sum over them. For example, we can write the trace of a tensor  $A_{ab}$  as

$$\text{Tr}(A) = g^{ab} A_{ab} = A^a_a.\tag{2.46}$$

### 2.2.3 Curvature tensor

So far, we have focused on the metric tensor, which measures distances and areas on our surface. The metric and quantities derived from it are exactly what we mean when we talk about “intrinsic” geometry.

<sup>2</sup>For a convenient mnemonic, remember the rhyme “co-, low, primes below”.

On the other hand, the surface's *curvature tensor* is emphatically not intrinsic. It is defined by explicit reference to the surface normal vector. Since this normal vector is fundamentally a product of embedding the surface in ambient space, the curvature tensor is necessarily extrinsic.

First, we define the unit normal to the surface  $\mathbf{n}$

$$\mathbf{n} = \frac{\mathbf{e}_1 \times \mathbf{e}_2}{|\mathbf{e}_1 \times \mathbf{e}_2|}. \quad (2.47)$$

Because  $\mathbf{n}$  has constant unit magnitude, derivatives of  $\mathbf{n}$  with respect to the surface coordinates are necessarily perpendicular to  $\mathbf{n}$ , and hence tangential to the surface. We therefore write the derivative of  $\mathbf{n}$  in the tangent vector basis,

$$\partial_a \mathbf{n} = -K_a^b \mathbf{e}_b, \quad (2.48)$$

or, equivalently,

$$K_{ab} = -\partial_a \mathbf{n} \cdot \mathbf{e}_b, \quad (2.49)$$

where  $\partial_a$  denotes differentiation with respect to  $u^a$ . This defines the curvature tensor, or “second fundamental form”,  $K_{ab}$ . That  $K_{ab}$  transforms appropriately for a rank two covariant tensor is easily verified.

The fact that  $\mathbf{n}$  and  $\mathbf{e}_a$  are orthogonal leads to an identity that will prove very useful later on,

$$\begin{aligned} \partial_a (\mathbf{n} \cdot \mathbf{e}_b) &= 0 = -K_{ab} + \mathbf{n} \cdot \partial_a \mathbf{e}_b \\ \implies K_{ab} &= \mathbf{n} \cdot \partial_a \mathbf{e}_b. \end{aligned} \quad (2.50)$$

Traditionally, this equation is taken as the definition of the curvature tensor, and equation (2.49) is known as the “Weingarten equation”. Though they are logically equivalent, we might favor equation (2.50) as the definition because it makes the symmetry of  $K_{ab}$  explicit: it follows from the commutativity of partial derivatives,  $\partial_a \mathbf{e}_b = \partial_a \partial_b \mathbf{X} = \partial_b \mathbf{e}_a$ .

To understand the utility of the curvature tensor, consider a surface curve  $\mathbf{Y}(s) = \mathbf{X}(u^1(s), u^2(s))$ , which we again assume is parameterized by arc-length. The tangent vector to the curve can be written in the basis of the surface tangent vectors as

$$\mathbf{T} = \dot{\mathbf{Y}} = \frac{du^a}{ds} \frac{\partial \mathbf{X}}{\partial u^a} = \dot{u}^a \mathbf{e}_a = t^a \mathbf{e}_a. \quad (2.51)$$

Recall that the normal curvature of a surface curve is defined as  $\kappa_n = \dot{\mathbf{T}} \cdot \mathbf{n}$ . We can express this in terms of the surface coordinates as

$$\kappa_n = \mathbf{n} \cdot \dot{\mathbf{T}} = \mathbf{n} \cdot (t^a \dot{\mathbf{e}}_a + \dot{t}^a \mathbf{e}_a) = t^a \dot{t}^b \mathbf{n} \cdot \partial_b \mathbf{e}_a = K_{ab} t^a \dot{t}^b. \quad (2.52)$$

Using the Weingarten equation (2.49), the curvature tensor can also tell us the geodesic torsion  $\tau_g = \dot{\mathbf{n}} \cdot \mathbf{L}$  of the curve. Let us write the transverse vector in the basis of the surface tangent vectors as  $\mathbf{L} = l^a \mathbf{e}_a$ . Then the geodesic torsion is given by

$$\tau_g = \dot{\mathbf{n}} \cdot \mathbf{L} = -K_a^b \dot{t}^a \mathbf{e}_b \cdot \mathbf{L} = -K_{ab} \dot{t}^a l^b. \quad (2.53)$$

Thus given a point on the surface and a vector located at that point, the curvature tensor gives the normal curvature and the geodesic torsion. This justifies our claim

in Section 2.1 that  $\kappa_n$  and  $\tau_g$  are not properties of curves, but local properties of surfaces. In fact, thinking of  $\kappa_n$  as a surface property will lead us to two key geometric scalars characterizing the surface.

It is often useful to write the curvature tensor in the basis of the a curve's tangent and transverse vectors  $t^a$  and  $l^a$ . Then it is traditionally written

$$K_b^a = \begin{pmatrix} K_{\parallel} & K_{\parallel\perp} \\ K_{\parallel\perp} & K_{\perp} \end{pmatrix}, \quad (2.54)$$

so that  $K_{\parallel} = \kappa_n$  and  $K_{\parallel\perp} = \tau_g$ . The remaining quantity  $K_{\perp}$  is the normal curvature along a curve perpendicular to ours.

At a given point, consider the directions in which the normal curvature is extremal, i.e. the extrema of  $\kappa_n = K_{ab}t^at^b$ , subject to the constraint  $g_{ab}t^at^b = 1$ . We can calculate these directions by differentiating  $\kappa_n$  with respect to  $t^a$ , using a Lagrange multiplier to fix the magnitude of  $t^a$ :

$$\begin{aligned} \kappa_n &= K_{ab}t^at^b - \lambda(g_{ab}t^at^b - 1) \\ \implies 0 &= K_{ab}t^b - \lambda g_{ab}t^b \\ \implies K_b^at^b &= \lambda t^a. \end{aligned} \quad (2.55)$$

The directions that maximize the normal curvature are eigenvectors of the matrix  $K_b^a$  with eigenvalue  $\lambda$ . Multiplying the above equation by  $t_a$ , we see in fact that

$$K_{ab}t^at^b = \kappa_n = \lambda, \quad (2.56)$$

so that the eigenvalues of  $K_b^a$  are the extrema of the normal curvature. These eigenvalues are traditionally called  $\kappa_1$  and  $\kappa_2$  (not to be confused with the natural curvatures of a filament). Because the curvature tensor is symmetric, the eigenvectors are guaranteed to be orthogonal as long as  $\kappa_1 \neq \kappa_2$ . In that case,  $K_b^a$  is proportional to the identity matrix, and the eigenvectors can be chosen to be orthogonal.

The eigenvalues of the curvature tensor can be used to define two quantities characterizing the curvature of the surface

$$K = \text{Tr}(K_b^a) = K_a^a = \kappa_1 + \kappa_2 \quad (2.57)$$

$$K_G = \det(K_b^a) = \kappa_1\kappa_2, \quad (2.58)$$

called the “extrinsic” and “Gaussian” curvature, respectively. The extrinsic curvature  $K$  is so called to distinguish it from the Gaussian curvature  $K_G$ , which is an intrinsic quantity, i.e. it can be defined in terms of the metric! This is surprising since we defined it using the normal vector  $\mathbf{n}$ . However, it turns out that we did not *need*  $\mathbf{n}$  to define  $K_G$ . This is so remarkable that it is referred to as Gauss’ “Theorema Egregium” [Fra11].

In the basis of a curve's tangent and transverse vectors  $t^a$  and  $l^a$ , the extrinsic and Gaussian curvature are given by

$$K = K_{\parallel} + K_{\perp} = \kappa_n + K_{\perp} \quad (2.59a)$$

$$K_G = K_{\parallel}K_{\perp} - K_{\parallel\perp}^2 = \kappa_n(K - \kappa_n) - \tau_g^2, \quad (2.59b)$$

where we have replaced  $K_{\perp} = K - \kappa_n$  on the second line.

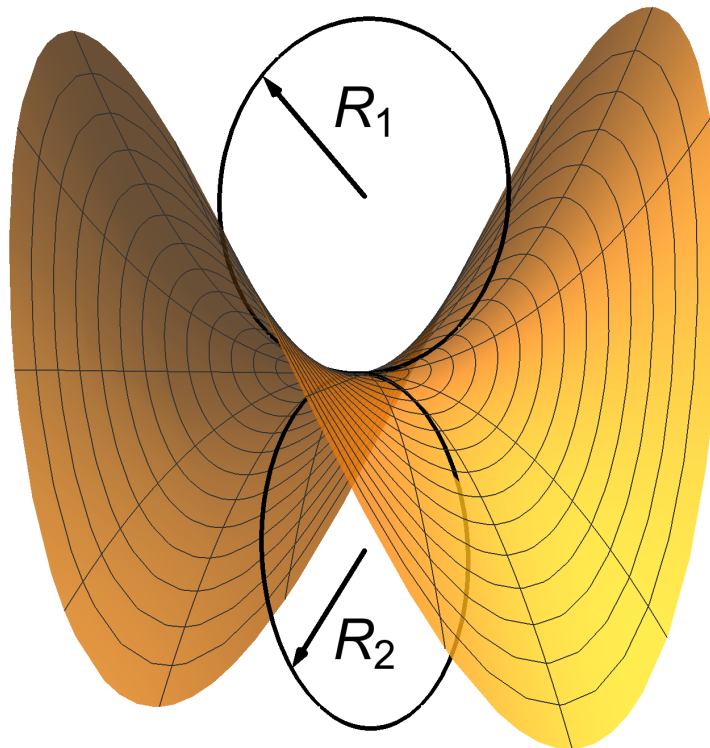


**Figure 2.5:** At a saddle point, the principal curvatures have the same magnitude but opposite sign, so that  $K = 0$ .

The extrinsic curvature and Gaussian curvature lead us to a few other important functionals for surfaces. One example is the Willmore functional [Wil65],

$$E_{\text{Willmore}} = \int dA K^2. \quad (2.60)$$

Note that the Willmore functional is invariant under rescaling: if all lengths are rescaled by a factor  $\lambda$ ,  $K^2 \mapsto \lambda^{-2}K^2$ , and  $dA \mapsto \lambda^2 dA$ , leaving the energy unchanged. In fact, the Willmore functional is invariant under the much larger group of conformal transformations of the ambient space [VDM14]. Because of its simplicity and deep mathematical structure, this functional has a long history and extensive literature, in fact having been proposed by Poisson [Poi14, LY82, B<sup>+</sup>84]. An equivalent model has even been introduced independently by Polyakov [Pol86] and Kleinert [Kle86] as an action functional for the string world sheet in string theory.

The Gaussian curvature of the surface also presents a scalar from which an energy functional could logically be defined,

$$E = \int dA K_G. \quad (2.61)$$

Remarkably, this is a topological invariant for closed surfaces (i.e. surfaces with no boundary). That is, for an arbitrary continuous deformation of the surface the integral (2.61) gives a fixed value. This is a result of the Gauss-Bonnet theorem, which states for a general surface  $S$  that

$$\int_S dA K_G + \int_{\partial S} ds \kappa_g = 2\pi\chi, \quad (2.62)$$

where  $\partial S$  is the boundary of  $S$ ,  $\kappa_g$  is the geodesic curvature of the boundary, and  $\chi$  is the Euler characteristic of the surface [Fra11]. The latter is a topological invariant of the surface. For a compact, orientable surface with no boundary,  $\chi = 2 - 2g$ , where  $g$  counts the number of holes in the surface. For example, this theorem states that the total Gaussian curvature of a sphere (or any topologically equivalent surface) is  $4\pi$ , and that the total Gaussian curvature of a torus (or any topologically equivalent surface) vanishes.

Just as we introduced spontaneous curvature for filaments above, it is also common to study surfaces with spontaneous curvature. The Helfrich functional<sup>3</sup> for lipid membranes includes such a term,

$$E_{\text{Helfrich}} = \int dA \left\{ \sigma + \frac{\kappa}{2}(K - K_s)^2 + \bar{\kappa}K_G \right\}, \quad (2.63)$$

where  $\kappa$  is the bending rigidity of the membrane (not to be mistake for the curvature of a space curve), and  $\bar{\kappa}$  is the Gaussian curvature modulus [Hel73]. The spontaneous extrinsic curvature  $K_s$  gives the extrinsic curvature of the surface in the stress-free state. Spontaneous extrinsic curvature arises from the asymmetry between the two membrane leaflets. This functional combines all of the possible terms we have discussed up to now.

## 2.2.4 Covariant derivatives

Curvature in surfaces also leads to changes in the way we evaluate derivatives. Consider differentiating a vector  $\mathbf{f} = f^a \mathbf{e}_a$ . The naive approach of simply taking  $\partial_a f^b$  unfortunately leads to a derivative that does not behave properly under change of coordinates, i.e. it is not a tensor. Under the coordinate change  $u^a \mapsto u'^a$ , we see

$$\begin{aligned} \partial'_a f'^b &= J_a^c \partial_c \left( (J^{-1})^b_d f^d \right) \\ &= J_a^c (J^{-1})^b_d \partial_c f^d + J_a^c f^d \partial_c (J^{-1})^b_d. \end{aligned} \quad (2.64)$$

If  $\partial_a f^b$  were a proper tensor, the latter term would not be present! We can define a proper tensorial derivative by considering the derivative of the full vector rather than its individual components,

$$\partial_a \mathbf{f} = \partial_a (f^b \mathbf{e}_b) = (\partial_a f^b) \mathbf{e}_b + f^b \partial_a \mathbf{e}_b = (\partial_a f^b + f^c \Gamma_{ac}^b) \mathbf{e}_b + f^b K_{ab} \mathbf{n}, \quad (2.65)$$

where we have defined the *Christoffel symbols of the second kind*  $\Gamma_{ab}^c$  via

$$\partial_a \mathbf{e}_b = \Gamma_{ab}^c \mathbf{e}_c + K_{ab} \mathbf{n}. \quad (2.66)$$

The Christoffel symbols (called “symbols” because they themselves are not tensors) are clearly symmetric in the two subscript indices. By lowering the last index, we obtain the Christoffel symbols of the first kind<sup>4</sup>,  $\Gamma_{abc} = g_{cd} \Gamma_{ab}^d = (\partial_a \mathbf{e}_b) \cdot \mathbf{e}_c$ .

<sup>3</sup>We will avoid using the word “Hamiltonian” when we mean “energy”, which we reserve for the Legendre transform of a Lagrangian.

<sup>4</sup>Note that there is an unfortunate notational ambiguity here. Some authors switch the placement of the upstairs index so that it comes *first*. We follow the convention used in Frankel’s [Fra11] and Kreyszig’s [Kre68] textbooks.

The Christoffel symbols define the *covariant derivative* of a vector,

$$\nabla_a f^b = \partial_a f^b + \Gamma_{ac}{}^b f^c. \quad (2.67)$$

It is crucial that the Christoffel symbols also do not transform like tensors under coordinate changes. This is by design: it must be true in order for them to cancel out the improper transformation terms of the partial derivative.

The covariant derivative can also be generalized to objects with covariant indices or multiple indices. For quantities with one covariant index (sometimes called “co-vectors”), the derivation works essentially the same way that it did for vectors, i.e. by differentiating  $\mathbf{A} = A_i \mathbf{e}^i$ . One finds

$$\nabla_i A_j = \partial_i A_j - \Gamma_{ij}{}^k A_k. \quad (2.68)$$

This definition allows us to take the covariant derivative of the surface tangent vectors  $\mathbf{e}_a$  themselves, leading to a set of identities known as the Gauss formulas

$$\nabla_a \mathbf{e}_b = \partial_a \mathbf{e}_b - \Gamma_{ac}{}^b \mathbf{e}^c = K_{ab} \mathbf{n}. \quad (2.69)$$

For tensors with multiple indices, the covariant derivative has a Christoffel symbol term for each index, with a sign determined by whether the index is covariant or contravariant. For example, the covariant derivative of a rank two covariant tensor is

$$\nabla_a B_{bc} = \partial_a B_{bc} - \Gamma_{ca}{}^d B_{bd} - \Gamma_{ba}{}^d B_{dc}. \quad (2.70)$$

An important consequence for the covariant derivative of the metric follows,

$$\begin{aligned} \nabla_a g_{bc} &= \nabla_a (\mathbf{e}_b \cdot \mathbf{e}_c) = \partial_a \mathbf{e}_b \cdot \mathbf{e}_c + \partial_a \mathbf{e}_c \cdot \mathbf{e}_b - g_{bd} \Gamma_{ca}{}^d - g_{dc} \Gamma_{ba}{}^d \\ &= \Gamma_{abc} + \Gamma_{acb} - \Gamma_{cab} - \Gamma_{bac} = 0. \end{aligned} \quad (2.71)$$

This is described as the metric being compatible with the Christoffel symbols.

The covariant derivative allows us to generalize many familiar ideas from flat space to curved surfaces. For example, we are able to define an analogue of the divergence theorem for curved surfaces. Consider a vector field  $f^a$  defined on a patch on such a surface. The quantity  $\nabla_a f^a$  is a scalar; it plays the role of the divergence in our analogy. Integrating this over a patch  $\Omega$  of the surface, it can be shown that [Fra11]

$$\int_{\Omega} dA \nabla_a f^a = \int_{\partial\Omega} ds \nu_a f^a, \quad (2.72)$$

where  $\boldsymbol{\nu} = \nu^a \mathbf{e}_a$  is the outward pointing unit normal to the patch of the surface.

Another instructive generalization is that of a straight line. In flat space, a straight line is defined by having a constant tangent vector. We can use the same rough idea to construct the surface analogue. Let  $u^a(s)$  describe a curve on the surface parametrized by arc-length, with  $t^a = \dot{u}^a$  the tangent vector to the curve. We would like to require that the tangent vector is constant in the sense that its covariant derivative *along itself* vanishes,

$$t^a \nabla_a t^b = \frac{\partial u^a}{\partial s} \frac{\partial t^b}{\partial u^a} + t^a \Gamma_{ac}{}^b t^c = \ddot{u}^b + \Gamma_{ac}{}^b \dot{u}^a \dot{u}^c = 0, \quad (2.73)$$

where we have used the chain rule to reach the second equality. This is apparently two equations, one for each value of the index  $b$ . However, the tangential projection is satisfied trivially because the length of the tangent vector is constant,

$$0 = t^a \nabla_a (g_{bc} t^b t^c) = 2g_{bc} t^c t^a \nabla_a t^b = 2t_b (t^a \nabla_a t^b). \quad (2.74)$$

The other equation comes from the projection onto the transverse vector  $\mathbf{L} = l^a \mathbf{e}_a$ ,

$$0 = l_b (\ddot{u}^b + \Gamma_{ac}{}^b \dot{u}^a \dot{u}^c) = \mathbf{L} \cdot t^a \nabla_a \mathbf{T} = \mathbf{L} \cdot \dot{\mathbf{T}} = \kappa_g. \quad (2.75)$$

We have identified the transverse projection of  $t^a \nabla_a t^b$  as the geodesic curvature  $\kappa_g = \dot{\mathbf{T}} \cdot \mathbf{L}$ . Thus the surface analogue of a straight line is a curve that satisfies  $\kappa_g = 0$ ; such curves are called “geodesics”. Geodesics are additionally analogous to straight lines in that they minimize the distance between points.

# Chapter 3

## Surface elasticity

In chapter 2, we discussed a few elastic models for surfaces. The present chapter will focus on applications and extensions of those models. In each case, we consider only surfaces having a continuous symmetry group. This is extremely important because it allows us to write the energy as an integral over only one variable; thus the shape equation will simplify to an *ordinary*, rather than a *partial*, differential equation.

First, in section 3.1, we discuss a simple extension of the Helfrich model, which we use to study simulated membranes. In section 3.2, we focus broadly on surfaces possessing helicoidal symmetry, including their parametrization, conservation laws, and mechanics. After finding some interesting mathematical results along the way, our study of helicoidal surfaces culminates in a mechanical model of dynamin-mediated membrane fission.

### 3.1 Gel phase buckling

Lipid membranes form the boundaries of different compartments and organelles in the cell, preventing the uncontrolled diffusion of matter. In many situations, the shape, stress, and stability of these membranes can be predicted from elasticity theory. Classic examples include the shape of red blood cells [Can70, HWM02] and vesicles [DH76], and the tension in tubules [RT95]. Membranes are often studied using coarse-grained molecular dynamics simulations, for which various coarse-grained models of lipids have been developed [MRY<sup>+</sup>07, CD05, BWD14]. It is important to know the elastic parameters of these coarse-grained membranes both for interpreting those simulations and so that we can compare them to real experiments.

The elastic parameters of a simulated membrane are usually either measured passively—for example, by measuring the membrane’s fluctuation spectrum—or actively, in which case one measures the energetic response of the membrane to applied deformations. One useful active method is to buckle the membrane [Nog11, KNNS13, HDID13, WD15, WD16]. In these simulations, an initially planar membrane is confined to a box that is shorter than the membrane is long. As a result, the membrane is forced to buckle, as in figure 3.1. These simulations can be compared to theory in two distinct ways. First, theory predicts a specific shape for the buckle. Second, theory predicts a *stress-strain relation* for the buckle. This gives the stress necessary to buckle the membrane by a given amount (see figure 3.2 for examples). Heuristically, the stress is a measure of the force that one part of the

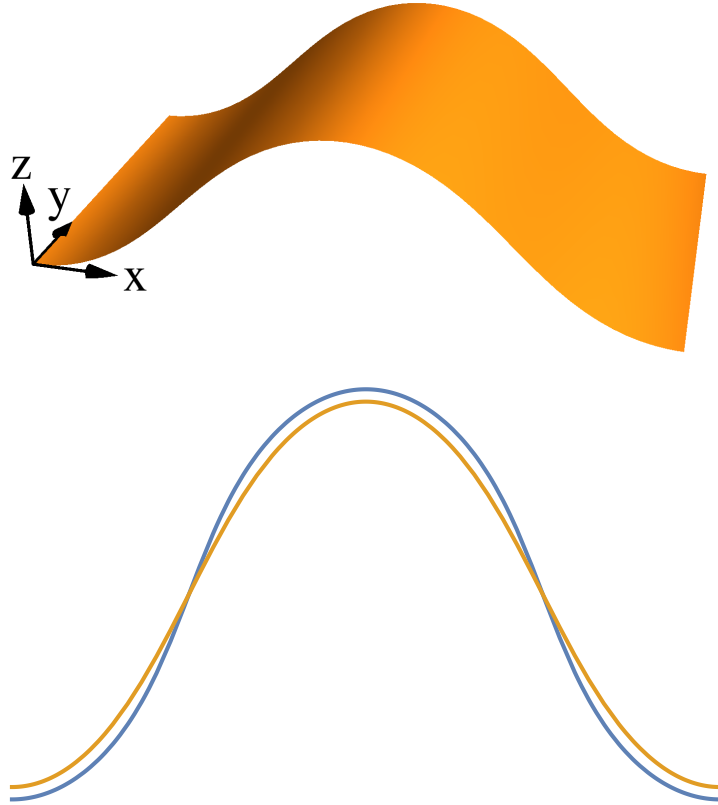


**Figure 3.1:** Example of a fluid phase membrane buckle confined in the  $x$ -direction (top), and comparison of a profile curve to that of the gel phase buckle (right). The blue curve represents a buckled membrane in the gel phase.

membrane imposes on its neighbors. Since the force and the extent of buckling can be measured in the simulation, this gives us a method of directly comparing theory and simulation.

Such simulations have been performed previously for membranes in the fluid phase [HDID13]. Active methods for determining the bending modulus become increasingly suitable both as  $\kappa$  increases and the temperature decreases because the amplitude of the fluctuations scales as  $\sim k_B T / \kappa$ . Such methods are therefore obviously useful at lower temperatures, where the membrane enters the stiffer and more ordered gel phase [DIMD15]. Although it is not common in biology, the gel phase has fascinating mechanical properties, as we will see here. These properties are highly sought after in the field of meta-materials [COL<sup>+</sup>15].

In the fluid case, the bending energy is given by the familiar Helfrich model,

$$E = \int dA \frac{\kappa}{2} K^2, \quad (3.1)$$

where we take the spontaneous curvature  $K_s = 0$  because the two leaflets are identical. Because of the symmetry of the buckle, this energy functional is identical to the Bernoulli-Euler model of an elastic rod in two dimensions; the shapes predicted by the model are thus well known.

Surprisingly, the results of the simulations disagree with these predictions [DIMD15]. Relative to the shapes of Euler buckles, the curvature of the gel phase membranes

is more localized, indicating that the membrane becomes softer as the curvature increases (see figure 3.1). This phenomenon is known as *curvature softening*, which has indeed been observed in gel phase membrane vesicles [BG79, QQF<sup>+</sup>12]. Curvature softening also occurs in DNA rings [YKM05], and has been proposed as an explanation for anomalous measurements of carbon nanotube rigidity [TOY08] and faceted edges in membrane vesicles [SdlC12]. Some meta-materials are in fact designed to harness this phenomenon [COL<sup>+</sup>15]

The simplest model of curvature softening uses an energy density that is defined piece-wise as a function of the curvature [TOY08]. In that model, the bending energy is quadratic at low curvature, but becomes linear at a critical curvature  $K_c$ ,

$$\mathcal{E} = \begin{cases} \frac{1}{2}\kappa K^2 & K < K_c \\ \frac{1}{2}\kappa K_c(2K - K_c) & K > K_c. \end{cases} \quad (3.2)$$

We would prefer, however, to write down a curvature softening energy functional that is analytic. The hope is that we could then more easily solve the shape equation, which we could compare with our simulated buckles.

A simple way to modify the Helfrich energy density to reflect softening (while still respecting the symmetries of the model) would be to add a term  $E_{\text{add}} \propto -K^4$ , where the softening is reflected by the negative coefficient on the term. However, the resulting energy functional suffers from a severe problem: it is not bounded below. Therefore, at very large curvatures, the energy density can be arbitrarily negative. We could introduce a positive term proportional to  $K^6$  to restore boundedness, but this introduces new problems. Firstly, the energy is not guaranteed to be convex. Secondly, it creates an additional free parameter; as the number of parameters proliferates, the model becomes less predictive. One candidate energy density with only one parameter that is guaranteed to be convex and bounded below is the following:

$$\mathcal{E} = \int dA \left\{ \frac{\kappa^2}{\kappa_4} \left( \sqrt{1 + \frac{\kappa_4}{\kappa} K^2} - 1 \right) \right\}, \quad (3.3)$$

where we assume  $\kappa_4 > 0$ . This is reminiscent of the curvature softening energy functional in equation (3.2), but it goes smoothly from quadratic to linear, rather than piece-wise. In the limit of small bending, this function becomes

$$\begin{aligned} \mathcal{E} &= \int dA \left\{ \frac{\kappa^2}{\kappa_4} \left( 1 + \frac{\kappa_4}{2\kappa} K^2 - \frac{\kappa_4^2}{8\kappa^2} K^4 + \mathcal{O}(K^6) \right) - \frac{\kappa^2}{\kappa_4} \right\} \\ &= \int dA \left\{ \frac{\kappa}{2} K^2 - \frac{\kappa_4}{8} K^4 + \mathcal{O}(K^6) \right\}. \end{aligned} \quad (3.4)$$

The coefficient on the  $K^4$  term is negative, implying that we have captured the effect of a negative fourth order correction without sacrificing boundedness or introducing too many new parameters. Note that in order for the second term under the square root to be dimensionless,  $\kappa_4/\kappa$  must have dimensions of (length)<sup>2</sup>. We therefore define  $\ell := \sqrt{\kappa_4/\kappa}$  as the crossover length from Helfrich-like behavior to the behavior of the new model.

### 3.1.1 Finding the shape of the buckle

Now let us consider the specific case of a membrane of length  $L$  confined to a box of length  $L_x$ , with the membrane totally flat in the  $y$ -direction. Following previous

work on buckling [Nog11], we parametrize the membrane by

$$\mathbf{X}(s, y) = \begin{pmatrix} x(s) \\ y \\ z(s) \end{pmatrix}, \quad (3.5)$$

where  $s$  is arc-length along the direction perpendicular to the  $y$ -axis. In this parametrization, the functions  $x(s)$  and  $z(s)$  must satisfy

$$\dot{x}^2 + \dot{z}^2 = 1, \quad (3.6)$$

where a dot indicates differentiation with respect to arc-length  $s$ . Let us define the angle  $\psi$  between the  $x$ -axis and the tangent vector  $\dot{\mathbf{X}}$ . Then,  $\dot{x} = \cos \psi$  and  $\dot{z} = \sin \psi$ , so equation (3.6) is satisfied automatically. This angle is also useful in that the extrinsic curvature of the surface is given by the very simple expression  $K = -\dot{\psi}$ .

To enforce the constraint that the buckle fit inside a box of length  $L_x$ , we introduce a Lagrange-multiplier  $f_x$  which we identify as the stress in the  $x$ -direction,

$$\begin{aligned} \frac{\mathcal{E}}{\kappa} &= \int dA \left\{ \frac{1}{\ell^2} \left( \sqrt{1 + \ell^2 K^2} - 1 \right) + \frac{f_x}{\kappa} \left( \cos \psi - \frac{L_x}{L} \right) \right\} \\ &= L_y \int ds \left\{ \frac{1}{\ell^2} \left( \sqrt{1 + \ell^2 \dot{\psi}^2} - 1 \right) + \frac{f_x}{\kappa} \left( \cos \psi - \frac{L_x}{L} \right) \right\}, \end{aligned} \quad (3.7)$$

where we have used the symmetry along the  $y$ -direction to perform the integral over  $y$ . Since  $f_x/\kappa$  has dimensions of length<sup>-2</sup>, we define a constant  $\lambda^2 := \kappa/f_x$ . For a buckle,  $f_x \geq 0$ , that is, the stress is compressive.

Performing the variation with respect to  $\psi$ , we see

$$\begin{aligned} \frac{\delta \mathcal{E}}{\kappa} &= L_y \int ds \left\{ \frac{\dot{\psi}}{\sqrt{1 + \ell^2 \dot{\psi}^2}} \delta \dot{\psi} - \lambda^{-2} \sin \psi \delta \psi \right\} \\ &= L_y \int ds \left\{ -\frac{d}{ds} \left( \frac{\dot{\psi}}{\sqrt{1 + \ell^2 \dot{\psi}^2}} \right) - \lambda^{-2} \sin \psi \right\} \delta \psi + \left[ \frac{\dot{\psi}}{\sqrt{1 + \ell^2 \dot{\psi}^2}} \delta \psi \right]_0^L. \end{aligned} \quad (3.8)$$

Thus the buckle is in equilibrium when  $\psi$  satisfies the Euler-Lagrange equation

$$-\lambda^{-2} \sin \psi = \frac{\ddot{\psi}}{\sqrt{1 + \ell^2 \dot{\psi}^2}^3}. \quad (3.9)$$

The simulations use periodic boundary conditions, so the points  $s = 0$  and  $s = L$  are identified. The boundary terms therefore vanish automatically. For convenience, we will measure the arc-length  $s$  from the inflection point, so that  $\dot{\psi}(s = 0) = 0$ . The equivalence between flexible rods and rigid rotators is manifested here in the fact that, when  $\ell = 0$ , equation (3.9) is the equation of motion for a pendulum. Interestingly, for finite  $\ell$ , equation (3.9) is equivalent to the Euler-Lagrange equation for a *relativistic* pendulum [OD16].

Equation (3.9) can be integrated using the integrating factor  $\dot{\psi}$ . Defining the inflection angle  $\psi_i = \psi(0)$ , the left-hand side gives  $\lambda^{-2}(\cos \psi(s) - \cos \psi_i)$ , while the right-hand side gives

$$\begin{aligned} \int_0^s ds \frac{\ddot{\psi}\dot{\psi}}{\sqrt{1 + \ell^2\dot{\psi}^2}^3} &= \left[ \frac{-1}{\ell^2 \sqrt{1 + \ell^2\dot{\psi}^2}} \right]_0^s \\ &= \frac{1}{\ell^2} \left( 1 - \frac{1}{\sqrt{1 + \ell^2\dot{\psi}^2}} \right). \end{aligned} \quad (3.10)$$

The integrated equation thus simplifies to

$$1 - \frac{1}{\sqrt{1 + \ell^2\dot{\psi}^2}} = \phi(\cos \psi - \cos \psi_i), \quad (3.11)$$

where we have introduced the dimensionless force on the buckle  $\phi := \ell^2/\lambda^2 = f_x \kappa_4/\kappa^2$ .

We have now put the Euler-Lagrange equation (3.9) into a form that can be solved easily by separation of variables. First, solve equation (3.11) for  $\dot{\psi}$ ,

$$\dot{\psi} = \frac{\sqrt{\phi(\cos \psi - \cos \psi_i)[2 - \phi(\cos \psi - \cos \psi_i)]}}{\ell(1 - \phi(\cos \psi - \cos \psi_i))}. \quad (3.12)$$

By formally considering  $\dot{\psi} = d\psi/ds$  a fraction, we can rearrange this equation so that  $d\psi$  and  $ds$  are on opposite sides of the equality. Collecting all terms containing  $\psi$ , we can then integrate both sides, leading to

$$\frac{s}{\ell} = \int_{\psi_i}^{\psi(s)} d\psi \frac{1 - \phi(\cos \psi - \cos \psi_i)}{\sqrt{\phi(\cos \psi - \cos \psi_i)(2 - \phi(\cos \psi - \cos \psi_i))}}. \quad (3.13)$$

This method of solution is known as a *quadrature*, and implicitly solves equation (3.9). The full embedding of the buckle in space is given by

$$\begin{aligned} \frac{x(s)}{\ell} &= \int ds \cos \psi = \int_{\psi_i}^{\psi(s)} d\psi \frac{\cos \psi}{\dot{\psi}} \\ &= \int_{\psi_i}^{\psi(s)} \cos \psi \frac{1 - \phi(\cos \psi - \cos \psi_i)}{\sqrt{\phi(\cos \psi - \cos \psi_i)(2 - \phi(\cos \psi - \cos \psi_i))}} \end{aligned} \quad (3.14a)$$

$$\begin{aligned} \frac{z(s)}{\ell} &= \int ds \sin \psi = \int_{\psi_i}^{\psi(s)} d\psi \frac{\sin \psi}{\dot{\psi}} \\ &= \int_{\psi_i}^{\psi(s)} \sin \psi \frac{1 - \phi(\cos \psi - \cos \psi_i)}{\sqrt{\phi(\cos \psi - \cos \psi_i)(2 - \phi(\cos \psi - \cos \psi_i))}}, \end{aligned} \quad (3.14b)$$

where in equation (3.15b) we have replaced  $ds = d\psi/\dot{\psi}$ , using equation (3.12) for  $\dot{\psi}$ . It is now easy to generate membrane shapes numerically, which can then be compared to the shapes obtained in simulations. Treating  $\phi = \ell^2 f_x/\kappa$  as a fit parameter, and using the measured value of  $f_x$  from the simulation, we can determine

the material parameter  $\ell$  for our membranes. We find that the simulated shapes agree much more with this model than with the Helfrich theory: the root-mean-square deviation between simulated shapes and the predictions of the extended model is about an order of magnitude smaller than that between simulated shapes and the Helfrich theory [DIMD15].

### 3.1.2 Stress-strain relation

Our implicit solution for the buckle's shape is sufficient for calculating the stress-strain relation, which we can also compare with results from simulations. The stress-strain relation provides the force  $f_x$  necessary to induce a strain  $\gamma = 1 - L_x/L$ , given the material parameters  $\kappa$  and  $\ell$ . We begin by writing  $L$  and  $L_x$  in terms of our quadrature by integrating equations (3.13) and (3.14a) over a quarter period of the buckle,

$$\frac{L}{4\ell} = \int_0^{\psi_i} d\psi \frac{1 - \phi(\cos \psi - \cos \psi_i)}{\sqrt{\phi(\cos \psi - \cos \psi_i)[2 - \phi(\cos \psi - \cos \psi_i)]}}, \quad (3.15a)$$

$$\frac{L_x}{4\ell} = \int_0^{\psi_i} d\psi \cos \psi \frac{1 - \phi(\cos \psi - \cos \psi_i)}{\sqrt{\phi(\cos \psi - \cos \psi_i)[2 - \phi(\cos \psi - \cos \psi_i)]}}, \quad (3.15b)$$

Note that our expressions for both  $L_x$  and  $L$  are proportional to  $\ell$ , but otherwise depend only on  $\phi$  and  $\psi_i$ . We can therefore easily write the strain  $\gamma(\phi, \psi_i) = 1 - L_x/L$  in terms of those variables. However, this is not very useful for comparison to simulations: we are not interested in the strain at a given force  $\phi$  and inflection angle  $\psi_i$ . The inflection angle of our buckle is free to change. If we increase the force, we expect  $\gamma$  and  $\psi_i$  to both change together. Instead, we seek the strain  $\gamma$  at fixed force  $\phi$  and fixed length  $L$ .

Our strategy for this task is as follows. First, we will compute  $\gamma$  as a series expansion in powers of  $\phi$ , which we will be able to invert to find  $\psi_i$  as a function of  $\gamma$  and  $\phi$ . We can then insert this relation into equation (3.15a), giving us  $L$  as a function of  $\gamma$  and  $\phi$ . Lastly, we will invert this for  $\phi$  as a function of  $L$  and  $\gamma$ .

To find our series expansion of  $\gamma$ , first note that the integrands in equations (3.15a) and (3.15b) both contain a factor of the form  $1/\sqrt{x(2-x)}$ , where  $x = \phi(\cos \psi - \cos \psi_i)$ . This can be expanded as

$$\frac{1}{\sqrt{x(2-x)}} = \frac{1}{2} \sum_{n=0}^{\infty} \frac{(2n-1)!!}{2^n n!} \left(\frac{x}{2}\right)^{n-1/2}. \quad (3.16)$$

Note that this series converges absolutely if and only if  $|x|/2 < 1$ . This is a critical point: in order to evaluate the integral as a series expansion, we will have to switch the order of the sum with that of the integral, which is only allowed if the series is absolutely convergent. Doing so, we integrate this series term by term, giving [GR14]

$$\int_0^{\psi_i} d\psi \left(\frac{\cos \psi - \cos \psi_i}{2}\right)^{n-1/2} = \frac{(2n-1)!!\pi}{4^n} \sin^n(\psi_i) P_{-1/2}^{-n}(\cos \psi_i), \quad (3.17)$$

$$\int_0^{\psi_i} d\psi \cos \psi \left(\frac{\cos \psi - \cos \psi_i}{2}\right)^{n-1/2} = \frac{(2n-1)!!\pi}{4^n} \sin^n(\psi_i) P_{1/2}^{-n}(\cos \psi_i), \quad (3.18)$$

where  $P_l^m(x)$  are the associated Legendre functions. Inserting these expressions into equations (3.15a) and (3.15b), we find

$$L = 2\pi\ell \sum_{n=0}^{\infty} \frac{((2n-1)!!)^2 \phi^{n-1/2}}{8^n n!} \sin^n \psi_i \left( P_{-1/2}^{-n}(\cos \psi_i) - \frac{2n-1}{2} \phi \sin \psi_i P_{-1/2}^{-n-1}(\cos \psi_i) \right), \quad (3.19)$$

$$L_x = 2\pi\ell \sum_{n=0}^{\infty} \frac{((2n-1)!!)^2 \phi^{n-1/2}}{8^n n!} \sin^n \psi_i \left( P_{1/2}^{-n}(\cos \psi_i) - \frac{2n-1}{2} \phi \sin \psi_i P_{1/2}^{-n-1}(\cos \psi_i) \right). \quad (3.20)$$

These expressions naturally lead to an expansion for  $\gamma = 1 - L_x/L$  in powers of  $\phi$ . In light of the exact solution for the Bernoulli-Euler buckles [HDID13], it is convenient at this point to make a small change of variables: let us introduce the elliptic parameter  $m = \sin^2(\psi_i/2)$ . Rather than obtain  $\psi_i$  directly in terms of  $\gamma$  and  $\phi$ , we will solve for  $m$ .

Following reference [HDID13], let us assume that we can write  $m$  as a series<sup>1</sup> in  $\gamma$ , i.e.

$$m = \sum_{n=0}^{\infty} a_n(\phi) \gamma^n. \quad (3.21)$$

We now insert this series into our equation for  $\gamma$ . Then we can find the coefficients  $a_n(\phi)$  by equating like powers of  $\gamma$  from each side of the equation. The coefficients are presented up to order  $n = 6$  in Table 3.1. Since this calculation has already been performed in the Bernoulli-Euler case in reference [HDID13], we can compare our coefficients with  $\phi = 0$  to theirs as a sanity check, finding that they agree.

Now, we can insert our formula for  $m(\gamma, \phi)$  into equation (3.15a). Let us define  $\delta := 2\pi\ell/L$  as a dimensionless measure of how much the buckle differs from the Eulerian buckle. Then, again assuming the series is well-defined, we write

$$\phi = \delta^2 \sum_{n=0}^{\infty} b_n(\delta) \gamma^n. \quad (3.22)$$

As we did to find the coefficients of  $m$ , we can equate the coefficients on like powers of  $\gamma$  to find the  $b_n(\delta)$ , which are shown up to order  $n = 6$  (though our calculations go up to order  $n = 10$ ) in Table 3.2.

Amidst all the redefinitions, series expansions, and inversions, it is easy to lose sight of the forest for the trees. After some rearranging and re-expressing in terms of the original variables, equation (3.22) gives

$$f_x = \kappa \left( \frac{2\pi}{L} \right)^2 \sum_n b_n(\delta) \gamma^n. \quad (3.23)$$

As expected, we see in Table 3.2 that when  $\delta \rightarrow 0$ , we recover the coefficients for Euler buckling found in [HDID13]. The stress-strain relation is shown for a few values of  $\delta$  in figure 3.2.

<sup>1</sup>This would not be possible if  $m$  is not a well-defined function of  $\gamma$  and  $\phi$ , e.g. if one set of values  $(\gamma, \phi)$  led to two possible values for  $m$ .

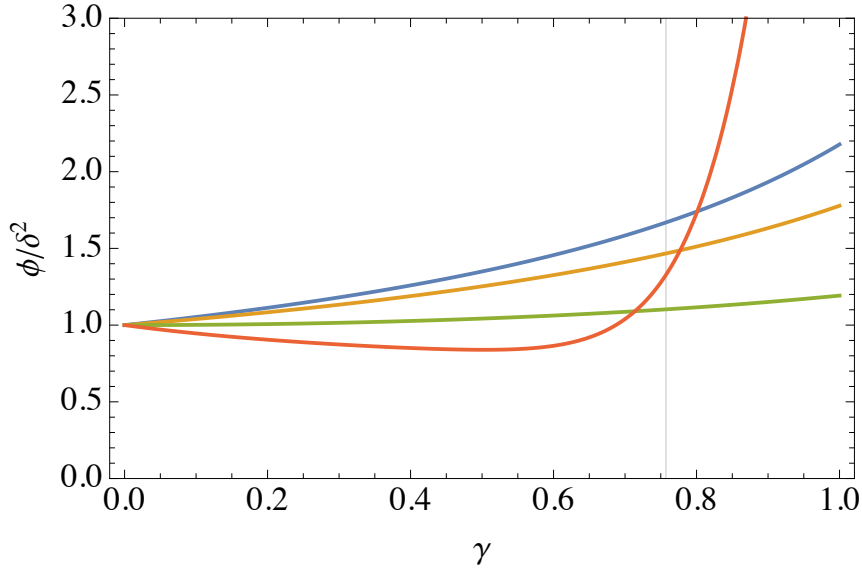


**Figure 3.2:** The dimensionless stress-strain relations for  $\delta = 0, \sqrt{3}/6, 1/\sqrt{3}, \sqrt{3}/2$  are shown in blue, orange, green, and red, respectively. All stresses have been scaled by the critical buckling force. At  $\delta = 0$ , we recover the Euler buckling case; at  $\delta = 1/\sqrt{3}$ , the stress-strain relation becomes non-monotonic. The vertical line shows the strain at which a kink forms with  $\delta = \sqrt{3}/2$ .

One of the hallmarks of buckling is that in the limit  $\gamma \rightarrow 0$ , the force  $f_x \rightarrow \kappa(2\pi/L)^2$  does not vanish. This indicates that there is a critical buckling force: the membrane will not buckle unless a force greater than this is applied. Interestingly, the critical force does not depend on  $\ell$ , and so is identical to the critical force for an Euler buckle,

$$f_0 = \kappa \left( \frac{2\pi}{L} \right)^2. \quad (3.24)$$

However, this theory differs from the Helfrich model at first order in  $\gamma$ , i.e. in the *slope* of the stress-strain relation at  $\gamma = 0$ . In fact, when  $\delta > 1/\sqrt{3} \approx 0.577$ , the slope at  $\gamma = 0$  becomes *negative*, so that the stress is no longer monotonic in the strain. This non-monotonicity represents an instability. To see how, consider a planar membrane, to which we apply an increasingly large force. Before we reach the critical buckling force  $f_0$ , there are two configurations with finite  $\gamma$  with the appropriate value of  $f_x$ . The membrane can therefore discontinuously jump to one of these configurations!

This is more than just a theoretical novelty: simulations measured  $\ell = 27.5 \pm 2.2$  nm for the Cooke lipid model, and  $\ell = 13.9 \pm 0.5$  nm for the MARTINI model [DIMD15]. These correspond to  $\delta = 2.9$  and  $\delta = 2.0$ , respectively, far beyond the critical value. This theory has also been applied to the same model membranes in the fluid phase, finding  $\ell = 10.1 \pm 40$  nm for the Cooke model, and  $\ell = 8.1 \pm 0.8$  nm for MARTINI, corresponding to  $\delta = 0.95$  and  $\delta = 1.1$  respectively [DI16]. Thus, in the fluid phase, these membranes are in the negative compressibility regime.

Recall that our series expansions are only convergent when the quantity  $x = \phi(\cos\psi - \cos\psi_i)$  satisfies  $|x| < 2$ . In order for our calculations to be valid, this inequality must be satisfied *for the whole buckle*. We should therefore consider the

	$a_n(\phi)$
$n = 0$	0
$n = 1$	1
$n = 2$	$-\frac{1}{8}(3\phi + 1)$
$n = 3$	$\frac{1}{32}(-5\phi^2 + 6\phi - 1)$
$n = 4$	$\frac{1}{1024}(39\phi^3 + 51\phi^2 + 33\phi - 11)$
$n = 5$	$\frac{1}{4096}(435\phi^4 - 420\phi^3 + 30\phi^2 + 36\phi - 17)$
$n = 6$	$\frac{1}{32768}(1499\phi^5 - 3795\phi^4 + 462\phi^3 + 74\phi^2 + 87\phi - 55)$

**Table 3.1:** Coefficients of  $m(\gamma, \phi)$  series expansion.

	$b_n(\delta)$
$n = 0$	1
$n = 1$	$\frac{1}{2}(1 - 3\delta^2)$
$n = 2$	$\frac{3}{32}(31\delta^4 - 14\delta^2 + 3)$
$n = 3$	$\frac{1}{128}(-779\delta^6 + 447\delta^4 - 129\delta^2 + 21)$
$n = 4$	$\frac{5}{8192}(21687\delta^8 - 15116\delta^6 + 5346\delta^4 - 1212\delta^2 + 159)$
$n = 5$	$\frac{3}{16384}(160804\delta^{10} - 131947\delta^8 + 54972\delta^6 - 15154\delta^4 + 2888\delta^2 - 315)$
$n = 6$	$\frac{7}{131072}(1244807\delta^{12} - 1175367\delta^{10} + 562848\delta^8 - 180206\delta^6 + 41991\delta^4 - 6939\delta^2 + 642)$

**Table 3.2:** Coefficients of  $\phi(\gamma, \delta)$  series expansion.

point where  $x$  is maximized, which occurs at points where  $\psi = 0$ . We conclude that the series converges as long as

$$\phi < \frac{1}{1 - \cos \psi_i} = \frac{1}{2m}. \quad (3.25)$$

Comparing this with equation (3.12), we see that the failure of our series expansion to converge coincides with the divergence of  $\psi$ . This indicates that a *kink* has formed in the buckle. This is a natural consequence of curvature softening; some examples are discussed in references [YKM05, TOY08, SdlC12, EHA14]. Interestingly, we also see kinks form in simulations, though they occur at lower strain than theory predicts. It is worth noting that we obtain such strange pathological behavior from a totally innocuous energy functional: unlike the piecewise constructions discussed above, our energy density is both convex and infinitely differentiable.

Using our previously calculated series expansions for  $\phi$  and  $m$ , we can establish inequality (3.25) as a relation between  $\gamma$  and  $\delta$ , so that for a given  $\delta$ , we can find the strain  $\gamma^*$  at which it will kink, plotted in figure 3.3. We find that  $\gamma^* = 1$  at  $\delta \approx 0.763930$ , implying that below this value of  $\delta$ , the membrane will never kink. Conversely,  $\gamma^* \rightarrow 0$  asymptotically as  $\delta \rightarrow \infty$ ; thus for very large  $\delta$ , any strain at all will result in a kink.

### 3.1.3 Conclusions

Our extension of the Helfrich model successfully predicted appropriate shapes and stress-strain relations for curvature-softening membrane buckles. We found that for sufficiently large values of  $\delta = 2\pi\ell/L$ , the stress-strain relation is in fact non-monotonic. Increasing  $\delta$  even further, we reach a phase in which it is possible for

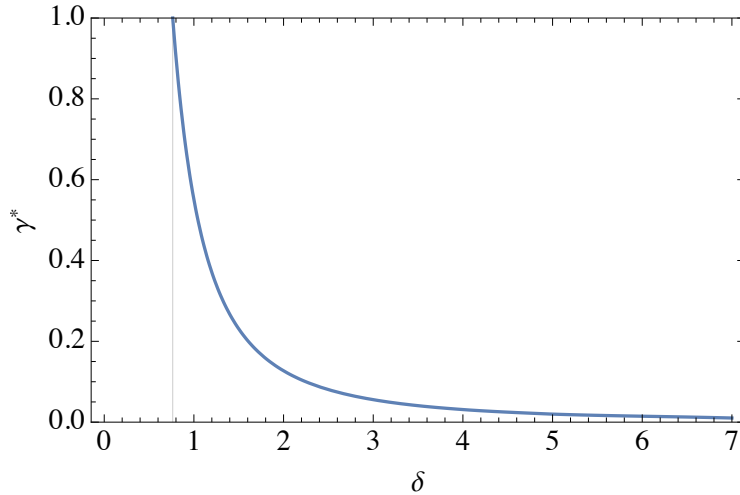


**Figure 3.3:** The strain  $\gamma^*$  at which a membrane with a given value of  $\delta$  will kink. If  $\delta < 0.763930$  (i.e. left of the vertical line), no amount of strain will create a kink.

the curvature  $\dot{\psi}$  to diverge, so that the buckle forms a kink. It is interesting to wonder whether this model correctly predicts when kinks occur for our buckles, and whether it could also explain faceting of vesicles in the gel phase, which has indeed been observed [BG79, QQF<sup>+</sup>12].

## 3.2 Helicoidal surfaces

Helicoidal symmetry is interesting for both practical and theoretical reasons. From a practical perspective, helical objects are abundant in nature. For example, regions of the endoplasmic reticulum called Terasaki junctions have been proposed to be locally helicoidal [TSK<sup>+</sup>13]. Chromatin assembles into helices known as “30 nm fibers” [FM86]. Helical symmetry is also common in engineering applications because helical objects have the virtue of allowing material to flow along their axis. This principle motivates the design of the Archimedean pump, used in the Antarctic for retrieving ice cores [KB04, SS85], as well as spiral stairs. Not to mention, corkscrew designs can be very aesthetically pleasing, as in the Solomonic columns in St. Peter’s Basilica.

From a mathematical perspective, helicoidal symmetry is interesting because it can be considered a generalization of axial symmetry. Whereas axially symmetric objects are symmetric under rotations about an axis, helically symmetric objects are symmetric under a simultaneous rotation and translation. This relationship results in certain properties of axially symmetric objects mapping cleanly to helicoidally symmetric analogues. Since axially symmetric surfaces are very well studied, including constant extrinsic curvature surfaces [RBN83], Willmore surfaces [JSL93, DDG08], and membranes [Lip91], it is natural to ask which results of those studies also can be generalized to helicoidally symmetric surfaces.

Here, we will consider helicoidally symmetric surfaces generally before restricting our focus to certain mechanical theories of surfaces. Before we consider these physical problems, though, let us make a digression on how best to parametrize the surface. The parametrization explored here will prove very useful both for understanding conservation laws emerging from helicoidal symmetry and variational

problems. These tools will facilitate an analysis of the stability of helicoidal soap films and membranes, the latter serving as a mechanical model of dynamin-mediated membrane fission.

### 3.2.1 Parametrization

In Section 3.1, we represented the buckle by a single profile curve, parametrized by arc-length, which, when traced along the  $y$ -axis, generated the full surface. Similar parametrizations are also useful for axially symmetric surfaces: one traces rotations of a profile curve, known as the *generatrix*<sup>2</sup>, about some axis, generating a surface that is symmetric about that axis. See references [DH76, JS94, DEK<sup>+</sup>97, Tu11] for applications of such parametrizations to membrane mechanics. We would like to apply this same reasoning to helicoidally symmetric surfaces; that is, we want to parametrize our surface by a single curve, that, when traced along a helix, generates a helicoidally symmetric surface. Such a parametrization was in fact considered by Do Carmo in reference [DCD82].

There are in principle many equivalent ways to choose which surface curve to use as the generatrix. We will choose one whose tangent vector is always perpendicular to the generator of the helical symmetry. Even though enforcing this condition will require some extra effort, it will prove well worth it. As an additional constraint, we will choose our coordinates such that the generatrix itself is parametrized by arc-length.

We write our parametrization in the form

$$\mathbf{X} = \begin{pmatrix} r(v) \cos(u + \varphi(v)) \\ r(v) \sin(u + \varphi(v)) \\ cu + \zeta(v) \end{pmatrix}, \quad (3.26)$$

where  $2\pi c$  is the pitch of the surface. This form guarantees that  $u$  parametrizes motion along the symmetry generator, and that  $v$  parametrizes motion along a generatrix. As  $u$  goes from zero to  $2\pi$ , the generatrix traces a full rotation about the  $z$  axis, and a vertical motion of  $2\pi c$  along the axis. The conditions for the parametrization discussed above restrict how the functions  $r$ ,  $\varphi$ , and  $\zeta$  may depend on  $v$ . The first such restriction is the requirement that the tangent vector to the generatrix (given by  $\mathbf{e}_v = \partial_v \mathbf{X}$ ) and the generator of the symmetry (given by  $\mathbf{e}_u = \partial_u \mathbf{X}$ ) be perpendicular; this translates to

$$\mathbf{X}_u \cdot \mathbf{X}_v = r^2 \varphi' + c \zeta' = 0. \quad (3.27)$$

The second condition is that  $v$  measure arc-length along the generatrix, that is, that  $(\partial_v \mathbf{X})^2 = 1$ ; this translates to

$$\mathbf{X}_v^2 = r'^2 + r^2 \varphi'^2 + \zeta'^2 = 1. \quad (3.28)$$

For the planar buckles in section 3.1, it was useful to define the angle  $\psi$  between the profile curve's tangent vector and the  $x$ -axis. For axially symmetric surfaces, one might similarly define  $\psi$  as the angle between the tangent vector of the generatrix

---

<sup>2</sup>For axially symmetric surfaces, the generatrices are the meridians, i.e. curves for which the cylindrical coordinate  $\phi$  is constant.

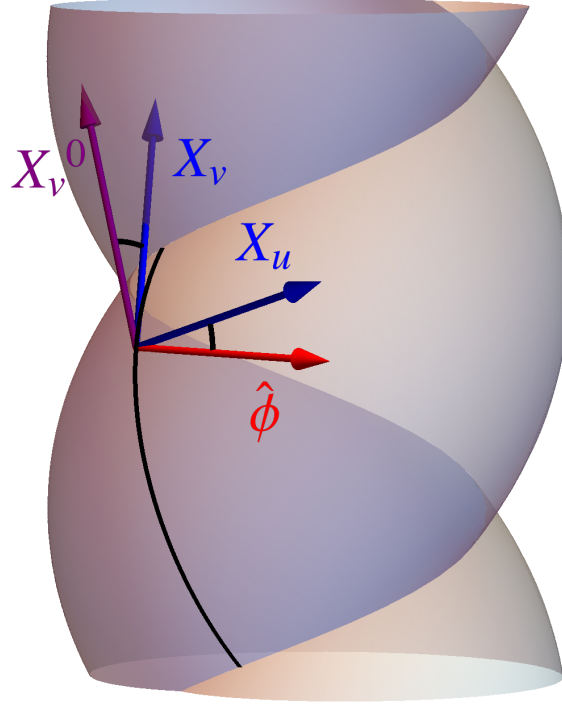


**Figure 3.4:** The two tangent vectors to the surface are shown in blue. The red vector is  $\hat{\phi}$ . The vector  $\mathbf{X}_v^0 = \hat{\mathbf{r}} \times \mathbf{X}_u$  is the tangent to a helix perpendicular to the generator  $\mathbf{X}_u$ . The angle  $\psi$  is measured between  $\mathbf{X}_v$  and  $\mathbf{X}_v^0$ .

and the  $z$ -axis. This is called an *angle-arc-length* parametrization. Analogously, we will define an angle  $\psi$  such that the following relations hold:

$$r' = \sin \psi \quad (3.29)$$

$$\varphi' = -\frac{c \cos \psi}{r \sqrt{r^2 + c^2}} \quad (3.30)$$

$$\zeta' = \frac{r \cos \psi}{\sqrt{r^2 + c^2}}. \quad (3.31)$$

Like in the axially or translationally symmetric angle-arc-length parametrizations, these relations make it possible to describe the surface by a single function  $\psi(v)$ . The coordinates  $r$ ,  $\varphi$ , and  $\zeta$  are then obtained by integration. In this case,  $\psi$  has a subtler geometric meaning, which we will address shortly.

It is convenient to define the local pitch angle of the helix  $\alpha = \arctan(c/r)$ . The tangent and normal vectors are then given by

$$\mathbf{X}_u = \sqrt{r^2 + c^2} \left( \cos \alpha \hat{\phi} + \sin \alpha \hat{\mathbf{z}} \right) \quad (3.32)$$

$$\mathbf{X}_v = \sin \psi \hat{\mathbf{r}} - \cos \psi \left( \sin \alpha \hat{\phi} - \cos \alpha \hat{\mathbf{z}} \right) \quad (3.33)$$

$$\mathbf{n} = \cos \psi \hat{\mathbf{r}} + \sin \psi \left( \sin \alpha \hat{\phi} - \cos \alpha \hat{\mathbf{z}} \right). \quad (3.34)$$

In this form, both the requirements  $|\mathbf{X}_v| = 1$  and  $|\mathbf{n}| = 1$  are manifestly satisfied. Equation (3.33) clarifies the geometric meaning of  $\psi$ : it is the angle the tangent to the generatrix  $\mathbf{X}_v$  makes with the  $\phi z$ -plane. When  $\psi = 0$ ,  $\mathbf{X}_v$  is given by

$\mathbf{X}_v^0 = \hat{\mathbf{r}} \times \mathbf{X}_u$ , which points along a helix perpendicular to  $\mathbf{X}_u$ . This is illustrated in figure 3.4.

The resulting metric and curvature tensor are

$$g_{ab} = \begin{pmatrix} r^2 + c^2 & 0 \\ 0 & 1 \end{pmatrix}, \quad \sqrt{g} = \sqrt{r^2 + c^2} \quad (3.35)$$

$$K_{ab} = \begin{pmatrix} r \cos \psi & -\frac{c}{\sqrt{r^2 + c^2}} \\ -\frac{c}{\sqrt{r^2 + c^2}} & \frac{c^2 \cos \psi}{r(r^2 + c^2)} - \psi' \end{pmatrix}. \quad (3.36)$$

Because we chose  $u$  to parametrize the helical symmetry, none of the geometric invariants of the surface depend on  $u$ . Taking the eigenvalues of  $K_b^a$ , we see that the principal curvatures are

$$\kappa_{\pm} = \frac{1}{2} \left( \frac{\cos \psi}{r} - \psi' \pm \sqrt{\frac{4c^2}{(c^2 + r^2)^2} + \left( \psi' + \frac{\cos \psi}{r} \frac{r^2 - c^2}{r^2 + c^2} \right)^2} \right). \quad (3.37)$$

Interestingly, this implies that the total curvature is independent of  $c$ , [Koz99]

$$K = \kappa_+ + \kappa_- = \frac{\cos \psi}{r} - \psi'. \quad (3.38)$$

An important consequence of  $K$  being independent of  $c$  is that it does not change in the  $c \rightarrow 0$  limit, i.e. for the case of axial symmetry. As mentioned above, in that case,  $\psi$  measures the angle between the generatrix's tangent vector and the  $z$ -axis. This is a remarkable result that will prove useful when we discuss soap films. Our choice of generatrix has manifested a connection between helicoidally and axially symmetric surfaces that is not otherwise visible.

Would another choice of generatrix have made our parametrization even simpler? For example, in the axially symmetric angle-arc-length parametrization, the curvature tensor is diagonal. Could we set up our parametrization so that this property holds as well? It turns out the answer is no. To see why, consider the metric and the curvature tensor as two-by-two matrices at each point on the surface. Each matrix is uniquely diagonalized by one orthogonal basis. But we have already found the basis that diagonalizes the metric at all points: it is the surface tangent vectors in our current parametrization. However, in this basis, the off-diagonal part of the curvature tensor vanishes *if and only if*  $c = 0$ . We conclude when  $c \neq 0$  (i.e. except for axially symmetric surfaces) one cannot simultaneously diagonalize the curvature tensor and the metric of a helicoidal surface.

Recall from Chapter 2 that the off-diagonal components of  $K_b^a$  are proportional to the geodesic torsion  $\tau_g$  of the basis vectors. We therefore see that the generatrices of helicoidally symmetric surfaces always have non-zero  $\tau_g$ , and are therefore not planar.

Consider a curve on our surface, parametrized by arc-length, given by  $(u(s), v(s))$ , whose tangent vector makes an angle  $\theta(s)$  with the local  $\mathbf{e}_u$ -direction. A formula from Liouville states that, given locally orthogonal coordinates  $u$  and  $v$ , the geodesic curvature can be decomposed as [DC76],

$$\kappa_g = \frac{d\theta}{ds} + \kappa_u \cos \theta + \kappa_v \sin \theta, \quad (3.39)$$

where  $\kappa_u$  and  $\kappa_v$  are the geodesic curvature of the  $u$ -curves and  $v$ -curves, respectively. These can be calculated easily

$$\kappa_u = -\frac{r \sin \psi}{r^2 + c^2} \quad (3.40a)$$

$$\kappa_v = 0. \quad (3.40b)$$

Inserting these, we find that the geodesic curvature for any curve on the surface is given by

$$\kappa_g = \frac{d\theta}{ds} - \frac{r \sin \psi}{r^2 + c^2} \cos \theta. \quad (3.41)$$

As a result of the helicoidal symmetry of the surface, the geodesic equation  $\kappa_g = 0$  has a first integral. This is analogous to Clairaut's relation, which states that  $\mathcal{I} = r \cos \theta$  is conserved along geodesics on axially symmetric surfaces [Fra11, DC76]. Indeed, multiplying  $\kappa_g$  by the integrating factor  $\sqrt{r^2 + c^2} \sin \theta$  and taking the anti-derivative with respect to  $s$ , we find that the first integral is given by

$$\sqrt{r^2 + c^2} \cos \theta = \mathcal{I} = \text{const}. \quad (3.42)$$

When  $c = 0$ , we recover Clairaut's relation. This is a necessary but not sufficient condition for a curve to be a geodesic; for example, when  $\theta = 0$ ,  $\mathcal{I} = \sqrt{r^2 + c^2}$  is constant, but the geodesic curvature in general does not vanish. In fact, in general for a curve with  $\theta = \text{const}$ ,  $\kappa_g$  only vanishes in two cases: if  $\sin \psi = 0$  everywhere, i.e. the surface is a cylinder; or if  $\theta = \pm\pi/2$ , i.e. the curve is a generatrix.

Equation (3.42) is in fact result of a more general theorem stating that the projection of the unit tangent vector to a geodesic onto a Killing field is conserved along the geodesic [Fra11]. A Killing field is a vector field on a surface that generates an isometry of that surface; for example, translations along the  $z$ -axis are isometries of the cylinder, so  $\hat{z}$  is a Killing field on the cylinder. Since motion along  $u$  obviously generates isometries of our surface, the tangent vector  $\mathbf{X}_u$  forms a Killing field. Let us consider a geodesic with unit tangent vector  $\mathbf{T} = \cos \theta \mathbf{X}_u / \sqrt{r^2 + c^2} + \sin \theta \mathbf{X}_v$ . Taking the inner product with the Killing field, we find

$$\mathbf{T} \cdot \mathbf{X}_u = \sqrt{r^2 + c^2} \cos \theta = \mathcal{I}. \quad (3.43)$$

The left hand side of equation (3.42) is precisely the inner product between the unit tangent vector of a curve and this Killing field.

### 3.2.2 Symmetries and conservation laws

For helicoidal surfaces that minimize some energy functional, Noether's theorem tells us that there should be conserved quantities associated with the helicoidal symmetry of the surfaces we have considered. It turns out that these conservation laws are most naturally expressed in terms of the the *stress tensor*  $\mathbf{f}^a$  of the surface, where  $a$  is an index ranging from one to two, introduced by Capovilla and Guven in reference [CG02]. The parametrization described in the last section will be especially useful for extracting conserved scalars from the stress tensor.

The stress tensor for a surface in three-dimensional space is somewhat unusual in that it is not "square": instead, it gives a three-dimensional space vector for each

value of the index  $a$ . This is a result of the physical meaning of the stress tensor: imagine cutting the surface along a line perpendicular to the tangent vector  $\mathbf{e}_a$ . The force per unit length that must be applied to the cut in order to hold the surface in the same configuration is  $\mathbf{f}^a$ . In other words,  $\mathbf{f}^a$  describes the internal forces that parts of the surface apply to each other. A detailed exploration of the utility of the membrane stress tensor is discussed in reference [Mül07]. For our purposes, the most important property of the stress tensor is that it provides the force per unit area on the surface at every point [CG02, Guv04],

$$\nabla_a \mathbf{f}^a = P \mathbf{n}, \quad (3.44)$$

where  $\nabla_a$  is the covariant derivative on the surface, and  $P$  is the local pressure across the surface, which in general is not constant. The interpretation of equation (3.44) is that the force transmitted outward from each point on the surface (i.e. the divergence of the stress tensor  $\nabla_a \mathbf{f}^a$ ) is equal to the external force per unit area applied at that point (i.e.  $P \mathbf{n}$ ). For surfaces with energy functionals that only depend on geometric invariants of the surface (such as the Helfrich, Willmore, and soap film energy functionals we have discussed), the stress tensor can be expressed entirely in terms of surface geometry. Crucially, this implies that the stress tensor inherits the symmetries of the surface.

Equation (3.44) is equivalent to the shape equation of the surface, as it describes the conditions for mechanical equilibrium. For example, recall from Chapter 2 that the soap film energy functional is given by

$$E = \int dA \sigma, \quad (3.45)$$

where  $\sigma$  is the surface tension. The soap film stress tensor is given by [Guv04]

$$\mathbf{f}^a = \sigma \mathbf{e}^a. \quad (3.46)$$

This has a simple interpretation: the force per unit length transmitted across any curve is a constant, independent of the curve. The direction of the force is always along the transverse vector to the cut. Taking the divergence and applying the Gauss formulas (2.69), we recover the Euler-Lagrange equation of a soap film,

$$\begin{aligned} \nabla_a \mathbf{f}^a &= \sigma \nabla_a \mathbf{e}^a = \sigma K_a^a \mathbf{n} = \sigma K \mathbf{n} = P \mathbf{n} \\ \implies K &= \frac{P}{\sigma}. \end{aligned} \quad (3.47)$$

This well-studied equation is known as the Young-Laplace equation [DHKW92, DGBWQ13, Fra11].

To see how the stress tensor can lead to a conservation law, consider the total force on a patch  $\Omega$  of an *axially* symmetric surface. Assuming that the surface is not subject to any external forces, e.g. from contact with another object or osmotic pressure, the pressure vanishes everywhere:  $P = 0$ . Then the total force on any patch is guaranteed to vanish, so that

$$\int_{\Omega} dA \nabla_a \mathbf{f}^a = 0 = \int_{\partial\Omega} ds \ell_a \mathbf{f}^a, \quad (3.48)$$

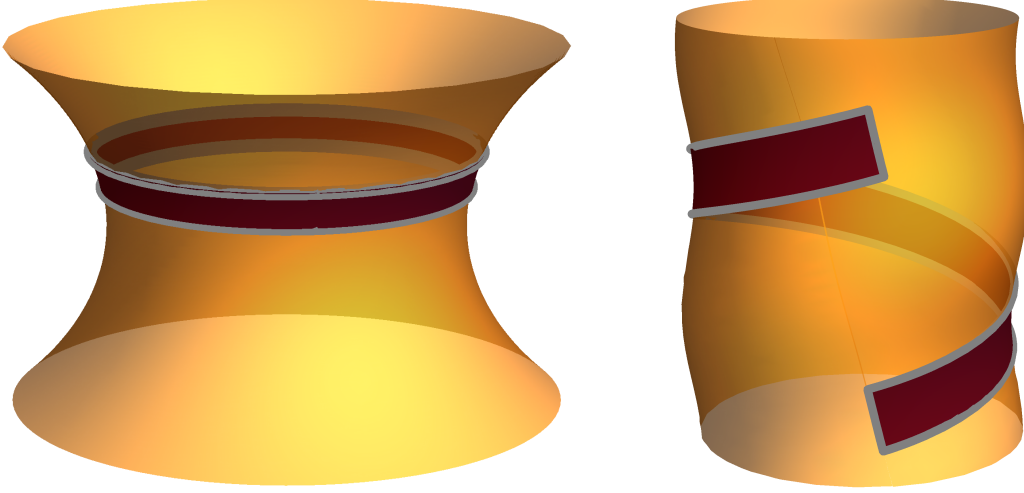


**Figure 3.5:** The patch  $\Omega$  is shown in red. In both cases, it is bounded by coordinate curves.

where  $s$  is arc-length along the boundary of  $\Omega$ ,  $\ell = \ell^a \mathbf{e}_a$  is the outward pointing unit normal to  $\Omega$  (transverse to the boundary curve), and we have used the divergence theorem from equation (2.72).

Let us now restrict to the case when the patch  $\Omega$  has the same symmetry as the surface, as shown on the left in figure 3.5. The boundary of  $\Omega$  is two disjoint circular rings  $\mathcal{C}_1$  and  $\mathcal{C}_2$ . Let the tangent vector to the meridians be given by  $\boldsymbol{\mu} = \mu^a \mathbf{e}_a$ . Because  $\ell$  is the *outward* pointing normal, it is parallel to  $\boldsymbol{\mu}$  on  $\mathcal{C}_1$ , while it is antiparallel on  $\mathcal{C}_2$ . The boundary integral in equation (3.48) can therefore be written

$$\int_{\partial\Omega} ds \ell_a \mathbf{f}^a = \int_{\mathcal{C}_1} ds \mu_a \mathbf{f}^a - \int_{\mathcal{C}_2} ds \mu_a \mathbf{f}^a = 0. \quad (3.49)$$

Recall that the patch  $\Omega$  is arbitrary except for the fact that it is symmetric about the axis. Thus, the equality above holds for any two rings  $\mathcal{C}_1$  and  $\mathcal{C}_2$  on the surface, implying that the integral

$$\int_{\mathcal{C}} ds \mu_a \mathbf{f}^a \quad (3.50)$$

does not depend on our choice of  $\mathcal{C}$ ! This integral represents the total of the internal forces transmitted across the curve  $\mathcal{C}$ . This this force is the same for every ring on the surface. We can write this constant in closed form by exploiting the symmetry of the surface, which is of course inherited by the stress tensor. The arc-length element is given by  $ds = r d\phi$ , where  $r$  and  $\phi$  are the radial and axial cylindrical coordinates, respectively. Integrating over the loop, the  $\hat{\mathbf{r}}$  and  $\hat{\boldsymbol{\phi}}$  components of the vector  $\mu_a \mathbf{f}^a$  give zero, leaving only the component along  $\hat{\mathbf{z}}$ . Our constant is therefore given by

$$f_z = \int_{\mathcal{C}} d\phi r \mu_a \mathbf{f}^a = 2\pi r \mu_a \mathbf{f}^a \cdot \hat{\mathbf{z}}. \quad (3.51)$$

For an example, let us return to soap films. We can describe an axially symmetric surface using our parametrization for helicoidally symmetric surfaces with vanishing pitch,  $c = 0$ . Then the generatrix is given by a meridian, and  $\psi$  is the angle between

the tangent to the meridians  $\boldsymbol{\mu}$  and the symmetry axis  $\hat{\mathbf{z}}$ . The constant  $f_z$  is then given by

$$\frac{f_z}{2\pi} = r\boldsymbol{\mu}_a \mathbf{f}^a \cdot \hat{\mathbf{z}} = r\sigma\boldsymbol{\mu}_a \mathbf{e}^a \cdot \hat{\mathbf{z}} = r\sigma\boldsymbol{\mu} \cdot \hat{\mathbf{z}} = r\sigma \cos \psi. \quad (3.52)$$

Differentiating with respect to arc-length along the meridian  $v$ , we find

$$\begin{aligned} \partial_v(r\sigma \cos \psi) &= \sigma(\sin \psi \cos \psi - r \sin \psi \psi') \\ &= r\sigma \sin \psi \left( \frac{\cos \psi}{r} - \psi' \right) \\ &= r \sin \psi \sigma K = 0, \end{aligned} \quad (3.53)$$

where we have used  $\partial_v r = \sin \psi$  on the first line. Going to the third line, we recognize the quantity in parentheses as the extrinsic curvature  $K$ . Since the shape equation for soap films in the absence of pressure is identically  $K = 0$ , confirming that  $f_z = 2\pi r\sigma \cos \psi$  is conserved.

We can apply the same reasoning for helicoidally symmetric surfaces. Consider a patch  $\Omega$  that winds around exactly one period of the helix as shown on the right in figure 3.5. Let  $\Omega$  be bounded on all sides by coordinate curves from the parametrization we developed in subsection 3.2.1, so that two of its sides are segments of generatrices, and the other two are helices. Again, it follows from the absence of external forces that

$$\int_{\Omega} dA \nabla_a \mathbf{f}^a = \int_{\partial\Omega} ds \ell_a \mathbf{f}^a = 0. \quad (3.54)$$

In this case, the boundary of  $\Omega$  is connected. Consider first the two sides of the boundary described by segments of generatrices (the short segments in figure 3.5). Because our patch winds exactly one full turn around the helix, the contribution to the integral from these sides is identical up to a sign difference, which emerges because the outward-pointing normal points in the opposite direction along the two curves. These contributions therefore cancel out, and we need only consider the terms arising from integrating over helices. We dub these curves  $\mathcal{H}_1$  and  $\mathcal{H}_2$  for the upper and lower helix, respectively. Along these curves, the outward normal is given by  $\boldsymbol{\ell} = \mathbf{X}_v = \ell^a \mathbf{e}_a$  on  $\mathcal{H}_1$  and  $\boldsymbol{\ell} = -\mathbf{X}_v = -\ell^a \mathbf{e}_a$  on  $\mathcal{H}_2$ . The force integral therefore gives

$$\begin{aligned} \int_{\partial\Omega} ds \ell_a \mathbf{f}^a &= \int_{\mathcal{H}_1} du \sqrt{r^2 + c^2} \ell_a \mathbf{f}^a - \int_{\mathcal{H}_2} du \sqrt{r^2 + c^2} \ell_a \mathbf{f}^a \\ &= 2\pi \hat{\mathbf{z}} \left( \sqrt{r^2 + c^2} \ell_a \mathbf{f}^a \Big|_{\mathcal{H}_1} - \sqrt{r^2 + c^2} \ell_a \mathbf{f}^a \Big|_{\mathcal{H}_1} \right) = 0. \end{aligned} \quad (3.55)$$

Just as for axially symmetric surfaces, the patch  $\Omega$  was chosen arbitrarily, implying that the equality holds for any two helices  $\mathcal{H}_1$  and  $\mathcal{H}_2$ , and therefore that

$$f_z = \hat{\mathbf{z}} \cdot \sqrt{r^2 + c^2} \ell_a \mathbf{f}^a \quad (3.56)$$

is constant on helicoidally symmetric surfaces. In this case,  $f_z$  represents the total of the internal forces transmitted across one helical of the surface.

For soap films, we again find  $f_z \propto \sigma r \cos \psi$ . We will encounter this constant again later on in this chapter when we discuss helicoidal membranes.

### Scale invariance

So far in this section, we have examined conserved quantities arising from the helicoidal symmetry of our surface. These conservation laws exist because we have focused on energy functionals that are symmetric under translations and rotations of the surface in its embedding space. Thus when the surface exhibits linear combinations of those symmetries, a conserved scalar arises. Recall from Chapter 2 that the Willmore functional (2.60) is also invariant under rescaling. This invariance can also lead to a conservation law, which we explore here.

The Willmore functional is given by

$$E = \int dA \frac{\kappa}{2} K^2. \quad (3.57)$$

Imagine rescaling the surface so that all lengths  $\lambda$  are multiplied by a factor  $(1 + \epsilon)$ ,  $\lambda \mapsto (1 + \epsilon)\lambda$ , where  $\epsilon$  is assumed to be small. Then the area element is mapped to  $dA \mapsto (1 + 2\epsilon + \mathcal{O}(\epsilon^2))dA$ , and the extrinsic curvature goes to  $K \mapsto (1 - \epsilon + \mathcal{O}(\epsilon^2))K$ . So the rescaled energy is

$$E = \int dA \left( \frac{\kappa}{2} (1 + 2\epsilon)(1 - 2\epsilon)K^2 + \mathcal{O}(\epsilon^2) \right) = \int dA \left( \frac{\kappa}{2} K^2 + \mathcal{O}(\epsilon^2) \right). \quad (3.58)$$

Under rescaling, the Willmore energy does not change at all! In fact, the Willmore functional is invariant under the entire group of conformal transformations of the embedding space, which includes scale transformations [LY82, JSL93, VDM14]. Again, we will find a conserved quantity associated with this symmetry from the stress tensor.

Following Guven [CG02], we divide the stress tensor into a normal part  $f^a$  and a tangential part  $f^{ab}$ , where the indices  $a$  and  $b$  range from one to two. For the Willmore functional, the stress tensor is then given by [Mül07]

$$\mathbf{f}^a = f^{ab} \mathbf{e}_b + f^a \mathbf{n}, \quad \text{where} \quad (3.59a)$$

$$f^a = -\kappa \nabla^a K, \quad (3.59b)$$

$$f^{ab} = \kappa K^{ab} K - g^{ab} \frac{\kappa}{2} K^2. \quad (3.59c)$$

Note that the tangential part of the stress tensor is traceless:

$$g_{ab} f^{ab} = \kappa \left( K_a^a K - \delta_a^a \frac{K^2}{2} \right) = \kappa (K^2 - K^2) = 0. \quad (3.60)$$

This fact is known to be a result of the conformal invariance of the energy functional [Guv05, RC05]. A key step towards obtaining a conservation law is observing that the vanishing of the trace of the stress tensor can be written as a divergence:

$$\nabla_a (\mathbf{f}^a \cdot \mathbf{X}) = (\nabla_a \mathbf{f}^a) \cdot \mathbf{X} + \mathbf{f}^a \cdot \nabla_a \mathbf{X} = \mathbf{f}^a \cdot \mathbf{e}_a = f^{ab} g_{ab} = 0, \quad (3.61)$$

where we have assumed the surface is in equilibrium, so that  $\nabla_a \mathbf{f}^a = 0$ . In the terminology of field theory, we have identified  $\mathbf{f}^a \cdot \mathbf{X}$  as the *Noether current* associated with scale invariance.

This Noether current can lead us to a conservation law just as the vanishing divergence of  $\mathbf{f}^a$  did. Let us return to the case of axially symmetric surfaces. Integrating  $\nabla_a(\mathbf{f}^a \cdot \mathbf{X})$  over the strip  $\Omega$  shown in figure 3.5, we can again use the divergence theorem find a conserved quantity,

$$\int_{\Omega} dA \nabla_a(\mathbf{f}^a \cdot \mathbf{X}) = \int_{c_1} d\phi r \mathbf{f}^a \cdot \mathbf{X} \mu_a - \int_{c_2} dr r \mathbf{f}^a \cdot \mathbf{X} \mu_a = 0. \quad (3.62)$$

Since the patch of membrane was chosen arbitrarily, we conclude that the integral

$$\int_{\mathcal{C}} d\phi r \mathbf{f}^a \cdot \mathbf{X} \mu_a = 2\pi r \mathbf{f}^a \cdot \mathbf{X} \mu_a \quad (3.63)$$

is conserved. Inserting  $\mathbf{X} = (r(s) \cos \phi, r(s) \sin \phi, z(s))^T$  as the embedding of the surface, we find that the conserved quantity is given by [ZMT17]

$$\mathcal{I} = r \mathbf{f}^a \cdot \mathbf{X} \mu_a = \pi \kappa (r^2 \psi'^2 \cos \psi - \tan \psi (\sin \psi - 2r f_z) - 2f_z z). \quad (3.64)$$

Interestingly, this conservation law *does not* extend to helicoidally symmetric surfaces. Of course  $\nabla_a(\mathbf{f}^a \cdot \mathbf{X}) = 0$ , as we have shown generally. But it turns out that use this fact does not lead to a conserved scalar on helicoidal surfaces. Again we can integrate  $\nabla_a(\mathbf{f}^a \cdot \mathbf{X})$  over the patch  $\Omega$  and use the divergence theorem to transform this into an integral over  $\partial\Omega$ ,

$$\int_{\Omega} dA \nabla_a(\mathbf{f}^a \cdot \mathbf{X}) = \int_{\partial\Omega} ds \ell_a \mathbf{f}^a \cdot \mathbf{X}. \quad (3.65)$$

But this time, we are not able to cancel the contributions from the parts of the boundary that are  $v$ -curves: the factor  $\mathbf{X}$  differs at the two ends, so that those terms do not cancel. Let the upper and lower  $v$ -curves bounding  $\Omega$  be denoted  $\mathcal{G}_1$  and  $\mathcal{G}_2$ , respectively. The embedding function  $\mathbf{X}$  differs at the two  $v$ -curves by the pitch of the helix,  $\mathbf{X}|_{\mathcal{G}_1} = \mathbf{X}|_{\mathcal{G}_2} + 2\pi c \hat{\mathbf{z}}$ . Noting that the outward normal now points along the helical generators,  $\ell = \mathbf{X}_u / |\mathbf{X}_u| = \nu^a \mathbf{e}_a$ , we see that the sum of the contributions from these curves to the integral in equation (3.65) is

$$\begin{aligned} \int_{\mathcal{G}_1} ds \nu_a \mathbf{f}^a \cdot \mathbf{X} - \int_{\mathcal{G}_2} ds \nu_a \mathbf{f}^a \cdot \mathbf{X} &= 2\pi c \int dv \mathbf{f}^a \cdot \hat{\mathbf{z}} \nu_a \\ &= \pi \kappa \int dv \frac{c^2 K^2}{\sqrt{r^2 + c^2}}. \end{aligned} \quad (3.66)$$

In general, this integral does not vanish, so that there is no constant analogous to  $\mathcal{I}$  for helicoidal surfaces. Evidently, we instead have

$$\frac{\partial \mathcal{I}}{\partial v} = \pi \kappa \frac{c^2 K^2}{\sqrt{r^2 + c^2}}. \quad (3.67)$$

So why is  $\mathcal{I}$  not conserved on helicoidal Willmore surfaces? It seems we have shown quite generally that it is conserved for surfaces minimizing scale invariant functionals, and that the Willmore functional is indeed scale invariant. However, recall the symmetry we have imposed on the surface *has a built in length scale*, that is, the pitch  $c$ . It should come as little surprise that this breaks the conservation

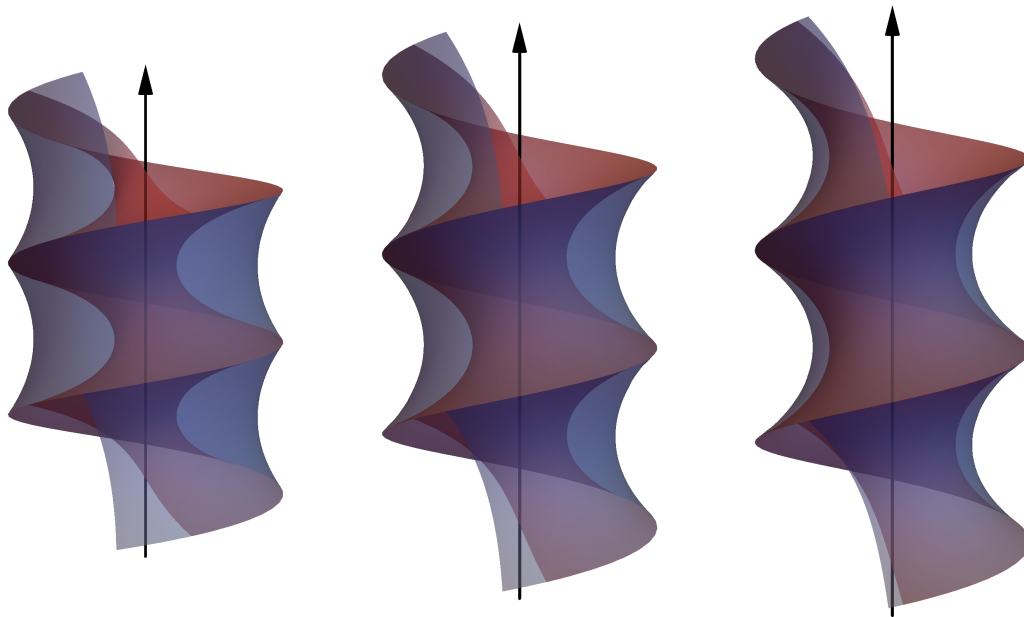


**Figure 3.6:** At low pitch, there are two minimal surfaces spanning a given helix; increasing the pitch beyond a critical value  $c^*/R = 0.223\,019$ , there are none.

law associated with scale invariance. We can see exactly how this symmetry breaking comes about by considering the energy per helical turn of a Willmore surface, explicitly restricting our focus to the helicoidal case,

$$E = \int dA \frac{\kappa}{2} K^2 = \int du \int dv \sqrt{r^2 + c^2} \frac{\kappa}{2} K^2 = 2\pi \int dv \sqrt{r^2 + c^2} \frac{\kappa}{2} K^2. \quad (3.68)$$

Upon rescaling, the quantities  $v$ ,  $r$ , and  $K$  change so that  $v \mapsto (1 + \epsilon)v$ ,  $r \mapsto (1 + \epsilon)r$ , and  $K \mapsto (1 - \epsilon)K$ . But, crucially,  $c$  should be seen as fixed. This is because when we focus on surfaces with a certain helical symmetry, we must specify a pitch in advance; changing  $c$  is actually changing the symmetry of the surface. To first order in  $\epsilon$ , the energy becomes

$$\begin{aligned} E &= 2\pi \frac{\kappa}{2} \int dv (1 + \epsilon) \sqrt{(1 + \epsilon)^2 r^2 + c^2} (1 - \epsilon)^2 K^2 \\ &= \pi \kappa \int dv \sqrt{r^2 + c^2} \frac{\kappa}{2} K^2 - \epsilon \pi \kappa \int dv \frac{c^2 K^2}{\sqrt{r^2 + c^2}} + \mathcal{O}(\epsilon^2). \end{aligned} \quad (3.69)$$

We should recognize the integrand of the second term: it is minus the anomalous rate of change of  $\mathcal{I}$  in equation (3.67)! Because of the fixed pitch  $c$ , the energy is no longer scale invariant, confirming our assertion.

### 3.2.3 Soap films

The parametrization discussed in above is also especially useful for finding surfaces that minimize a given energy functional, because it allows us to replace the surface's shape equation (ordinarily a partial differential equation) with an ordinary differential equation. Let us consider a soap film as a simple example with some

surprisingly interesting properties. It is common for the surface to enclose a fixed volume, in which case the energy is augmented with a Lagrange multiplier term,

$$E = \int dA \sigma + P \int dV. \quad (3.70)$$

where  $P$  admits the interpretation of pressure across the surface. As discussed in section 3.2.2, the Euler-Lagrange equation for soap films is [DHKW92, DGBWQ13, Fra11]

$$K = \frac{P}{\sigma}, \quad (3.71)$$

that is, the extrinsic curvature is a constant, given by  $P/\sigma$ . Surfaces with  $K = 0$  are called *minimal surfaces*, because they minimize the area functional, while those with  $K \neq 0$  are called *constant mean curvature* (CMC) surfaces. There is an extensive mathematical literature on the subject of such surfaces, containing many beautiful theorems [DCD82, DHKW92, BPA99]. They are also well-studied in soft matter physics, because they accurately represent tension dominated surfaces in general, especially fluid interfaces in the absence of gravity [RBN83, DGBWQ13].

Let us investigate a soap film spanning a helical wire. We assume that it will inherit the symmetry of the wire (though this is not necessarily so [MAGP16]), so that the surface can be described by the parametrization constructed in section 3.2.1. Recall that we have shown that  $K$  takes the same functional form for helicoidally symmetric surfaces as for axially symmetric ones. As a result, it follows immediately that *for every axially symmetric soap film, there is a corresponding helicoidally symmetric one!* The map from axially symmetric soap films to helicoidally symmetric ones was constructed more rigorously and in detail by Do Carmo using the same parametrization [DCD82].<sup>3</sup> Since axially symmetric soap films are very well studied, this is a valuable observation. All that remains is to evaluate the boundary conditions; however, these differ from the conditions on axially symmetric surfaces in physically meaningful ways.

The generatrix spans the separation between rungs of a helix with radius  $R$  and pitch  $2\pi c$ . Let the arc-length  $s$  be measured from the center of the generatrix, so that  $v \in (-L/2, L/2)$ , where  $L$  is the total arc-length of the generatrix. First, we consider the case with  $P = 0$ . The soap film equation is satisfied by

$$r(v) = \sqrt{a^2 + v^2}, \quad (3.72a)$$

$$\psi(v) = \arcsin\left(\frac{v}{\sqrt{a^2 + v^2}}\right), \quad (3.72b)$$

where  $a$  is a free parameter that is determined by the boundary conditions. At  $v = \pm L/2$ , the radial coordinate must be the radius of the helix  $R$ , i.e.  $r(\pm L/2) = R$ , implying that  $L = 2\sqrt{R^2 - a^2}$ . In the axially symmetric case, these equations describe a catenoid.

The condition that the generatrix connects one rung to the next determines  $a$ . To express this condition mathematically, we consider the vertical distance traversed

---

<sup>3</sup>This is an interesting example of the cultural differences between physicists and mathematicians. Where our proof is essentially Feynman's adage "The same equations have the same solutions", Do Carmo painstakingly constructed the correspondence explicitly.

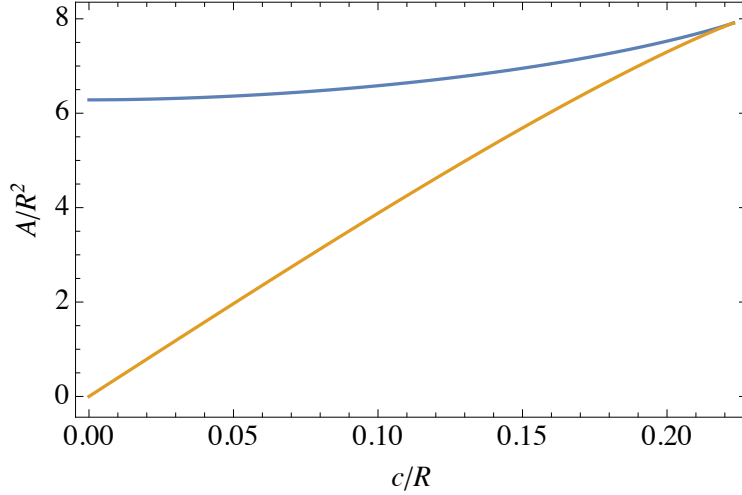


**Figure 3.7:** The energies of the two surfaces satisfying  $K = 0$  merge at the critical point. The stable branch of the solution is shown in orange.

by a meridian of the surface over one period. This is by definition the pitch of the helix  $2\pi c$ . Recall that meridians are defined as curves for which the axial cylindrical coordinate  $\phi$  is constant, or equivalently, the differential of  $\phi$  vanishes,  $d\phi = 0$ . Express this in terms of the surface coordinates  $u$  and  $v$ , we find

$$d\phi = -\frac{c \cos \psi}{r\sqrt{r^2 + c^2}} dv + du = 0. \quad (3.73)$$

This can be understood as a relation between the differentials  $du$  and  $dv$  characterizing the meridians. By solving equation (3.73) for  $du$ , we can write  $dz$  in terms of only  $dv$ ,

$$dz = \frac{r \cos \psi}{\sqrt{r^2 + c^2}} dv + c du = \frac{\sqrt{r^2 + c^2}}{r} \cos \psi dv. \quad (3.74)$$

Note that this relation only holds along the meridians. Integrating  $dz$  over one period of the meridian gives the pitch of the helix,

$$\int dz = 2\pi c = \int_{-L/2}^{L/2} dv \frac{\sqrt{r^2 + c^2}}{r} \cos \psi. \quad (3.75)$$

Inserting our expressions for  $r(v)$ ,  $\psi(v)$ , and  $L$ , this leads to a transcendental equation for  $a$ ,

$$\begin{aligned} 2\pi c &= \int_{-\sqrt{R^2 - a^2}}^{\sqrt{R^2 - a^2}} dv \sqrt{\frac{a^2 + v^2 + c^2}{a^2 + v^2}} \frac{a}{\sqrt{a^2 + v^2}} \\ &= 2 \left[ c \arctan \left( \frac{c}{a} \sqrt{\frac{R^2 - a^2}{R^2 + c^2}} \right) + a \operatorname{artanh} \left( \sqrt{\frac{R^2 - a^2}{R^2 + c^2}} \right) \right]. \end{aligned} \quad (3.76)$$

This equation can only be solved numerically. Let us proceed in terms of dimensionless variables  $a/R$  and  $c/R$ . We find that at low pitch, there are two solutions  $a/R$ , leading to the red and blue surfaces shown in figure 3.6. As  $c/R$  increases, we reach a point  $c^*/R = 0.223\,019$  where there is only one solution. Above this critical value, there are no solutions.

In figure 3.7 we plot the surface area of each of the two solutions as a function of  $c/R$ . The upper branch is higher in area and, by implication, higher in energy. It is thus at best meta-stable.

When  $K = P/\sigma \neq 0$ , the generatrix is described by

$$r(v) = \sqrt{\frac{2(1 - Ka)(1 - \cos(Kv)) + K^2a^2}{K^2}}. \quad (3.77)$$

As in the case  $K = 0$ ,  $a$  is a parameter setting the radius of the surface at the midpoint between rungs, and there is a critical pitch  $c^*/R$  above which there are no soap films satisfying the boundary conditions. However, that critical pitch now depends on the extrinsic curvature  $K$ . We will return to this issue in the following section, where we treat it numerically.

### 3.2.4 Membranes

One interesting biological application of these considerations is dynamin-mediated membrane fission. Dynamin mediates the final fission step in the formation of clathrin coated vesicles during endocytosis [SDS00b, MR13b, ABDC<sup>+</sup>16]. During the early years of dynamin research, there was some debate as to whether dynamin functions as a “molecular switch” [SMS99, Sev02] or as a “mechano-chemical enzyme” [DMH04b, BAE<sup>+</sup>08b, Ram11]. The latter mechanical model relies on the fact that dynamin undergoes a conformational change upon GTP hydrolysis, wherein the radius and pitch of the helix decrease; [DMH04b, RUFDC06b] in the model, the resulting deformation of the underlying membrane neck then lead to fission through an unspecified mechanism (said mechanism will be the subject of this paper). It is now widely agreed that the means through which dynamin induces membrane fission are indeed mechanical [MR13b, ABDC<sup>+</sup>16, SF11b, Rou14].

However, the question of how dynamin’s conformational change leads to the ultimate fission step remains open. A few proposals have been discussed in the literature. Firstly, there is the *catalytic model* [Ram11, SF11b, FLDB<sup>+</sup>03, KK03, SBA<sup>+</sup>13]. In this model, the membrane has two possible equilibrium states: first, that of an approximately cylindrical tubule; and second, what is known as the *hemi-fused* state, wherein the membrane’s inner leaflets merge, forming a short stretch of cylindrical micelle. Dynamin’s conformational change increases the energy of the tubular state, increasing the probability that a thermal fluctuation will push the membrane into the hemi-fission state. This would imply that membrane fission is itself a stochastic process that may or may not succeed after dynamin’s constriction and disassembly, depending on the state of the membrane when the dynamin scaffold disassembles.

In contrast, the *instability model* posits that the membrane neck becomes intrinsically unstable when the dynamin scaffold goes into its constricted configuration [Ram11]. This instability could arise through an increase in the pitch of the dynamin helix [SDS00b, SMWM99, MSV<sup>+</sup>01, Koz01, RAL<sup>+</sup>11], or a decrease in its radius [HS95, WS96, Koz99, Koz01, SDS00b, Rou14]. The possibility that the induction of spontaneous curvature in the membrane (for example by wedge-like inclusions [FEAS15] or changes in lipid composition [SWT<sup>+</sup>99, RGL<sup>+</sup>99, KCdKB03, MMTK04]) is related to this instability is also often suggested [Ram11, Koz01,

MGL<sup>+</sup>11, CIFC<sup>+</sup>11]. These proposals sometimes resemble Leibler’s idea of a curvature instability, where a protein creates spontaneous curvature in the membrane, which recruits more of the protein, leading to a positive feedback loop [Lei86].

The instability model has significant appeal from a theoretical perspective because it attempts to explain fission at a very abstract level, leading to a mechanism that is potentially universal. Indeed, the model requires no information about the membrane beyond its representation as a curvature elastic sheet. In particular, no discussion of leaflet merger or hemifission intermediate states is required. Furthermore, it closely echoes the instability of helicoidal soap films discussed in Section 3.2.3. Note that the soap film can be pushed across the collapse transition by either of the deformation modes that are proposed to destabilize dynamin, i.e. by decreasing the radius of the helix or by increasing its pitch.

So far, theoretical studies looking for such an instability in membranes have either restricted their focus to small deformations of the membrane (assuming it is approximately cylindrical)[Koz99, FJK<sup>+</sup>16a] or used indirect methods to minimize the membrane energy[Koz01]. In particular, we will discuss reference [Koz01], and how our analysis differs from it. However, this problem is well-defined, and can be solved without approximations. Here we will use numerical methods to solve the exact membrane shape equation, finding that such an instability in helicoidal membranes does not, in fact, exist.

Considering the overall geometry of a membrane constricted by a dynamin helix, we seek helicoidal surfaces minimizing the Helfrich energy functional

$$E = \int dA \left\{ \sigma + \frac{\kappa}{2} (K - K_s)^2 \right\}. \quad (3.78)$$

where  $K_s$  is the spontaneous curvature,  $\sigma$  is the tension in the membrane. We can evaluate the relevance of the surface tension  $\sigma$  by noting that there is a length scale associated with it: typically,  $\sqrt{\kappa/\sigma} \sim 30\text{-}100$  nm in the plasma membrane [HSDS96, DSWM98, MH01]. Since we are interested in smaller length scales (the pitch and radius of the dynamin helix are both on the order of 10 nm), we can assume that the effects of the tension can be considered a small correction relative to those of the bending term  $\kappa(K - K_s)^2/2$ . The  $\sigma = 0$  case is also convenient for comparison with Kozlov[Koz01], who takes the tension to vanish as well.

In that case, it is obvious that the energy vanishes if the curvature at all points on the membrane satisfies

$$K = K_s. \quad (3.79)$$

Evidently, since the total energy  $E \geq 0$ , this is lowest energy state for our membrane. In Kozlov’s previous study of helicoidally symmetric membranes [Koz01], he considers equation (3.79), finding that there are no solutions for certain values of the dimensionless combinations  $c/R$  and  $RK_s$ , concluding that the membrane is unstable in this regime. But as we have shown, CMC surfaces minimize the *soap film* energy functional, not that of membranes.

The membrane is in static equilibrium rather when the functional variation of the energy vanishes, given by [ZCH87, CG02]

$$\nabla^2 K - \frac{1}{2}(K - K_s) [(K - K_s)K - 2K^2 + 4K_G] = 0 \quad (3.80)$$

where  $K_G$  is the surface's Gaussian curvature, and  $\nabla^2$  is the surface Laplace-Beltrami operator. Naturally, the shape equation is satisfied when  $K = K_s$ . However, not all surfaces satisfying equation (3.80) will also satisfy equation (3.79). This distinction is why our results disagree with those of Kozlov: he solves equation (3.79) to find the shape of the membrane, not accounting for the fact that it is only a sufficient condition for equilibrium, not a necessary one.

Because the shape equation of membranes is more complicated and less well studied than that of soap films, in the present section we will use a slightly different method that is more amenable to numerical analysis. Specifically, we would prefer to write the shape equation as a system of first order equations rather than one higher order equation. These can then be solved easily using the Matlab routine BVP4C<sup>4</sup>.

While it is always possible to represent a higher order differential equation as a system of first order ones, some ways of doing so are better than others. We use a method that leads to equations and boundary conditions that often have clear physical interpretations; as a bonus, these equations are also (relatively) simple. First, we write the energy per helical turn of the membrane in our parametrization,

$$\begin{aligned} E &= \int dA \frac{\kappa}{2} (K - K_s)^2 = \int_0^{2\pi} du \int_0^L dv \sqrt{r^2 + c^2} \frac{\kappa}{2} (K - K_s)^2 \\ &= 2\pi \int_0^L dv \sqrt{r^2 + c^2} \frac{\kappa}{2} (K - K_s)^2, \end{aligned} \quad (3.81)$$

where  $L$  is the length of the generatrix, which is *a priori* unknown. By integrating over  $u$ , we reduce the problem to that of a one dimensional Lagrangian system. To our energy we add a system of Lagrange multipliers enforcing the relations of our parametrization; these will allow us to treat  $r$ ,  $\psi$ , and  $K$  as independent variables. The augmented energy functional is given by

$$\begin{aligned} E &= 2\pi \int_0^L dv \left\{ \sqrt{r^2 + c^2} \frac{\kappa}{2} (K - K_s)^2 + f_r (r' - \sin \psi) + f_z \left( \bar{z}' - \cos \psi \frac{\sqrt{r^2 + c^2}}{r} \right) \right. \\ &\quad \left. - \lambda_K \left( \psi' - \frac{\cos \psi}{r} + K \right) \right\}, \end{aligned} \quad (3.82)$$

where  $\bar{z}$  is a placeholder variable used to represent the constraint in equation (3.75): by enforcing the boundary conditions  $\bar{z}(0) = 0$  and  $\bar{z}(L) = 2\pi c$ , equation (3.75) is automatically satisfied.

The Lagrange multiplier  $f_r$  fixes the relationship between  $r$  and  $\psi$ , providing the first in our system of first order equations,

$$r'(v) = \sin \psi. \quad (3.83)$$

Similarly,  $f_z$  gives us the differential equation for  $\bar{z}$ ,

$$\bar{z}'(v) = \cos \psi \frac{\sqrt{r^2 + c^2}}{r}. \quad (3.84)$$

---

<sup>4</sup>See the appendix for a demonstration of how we use BVP4C

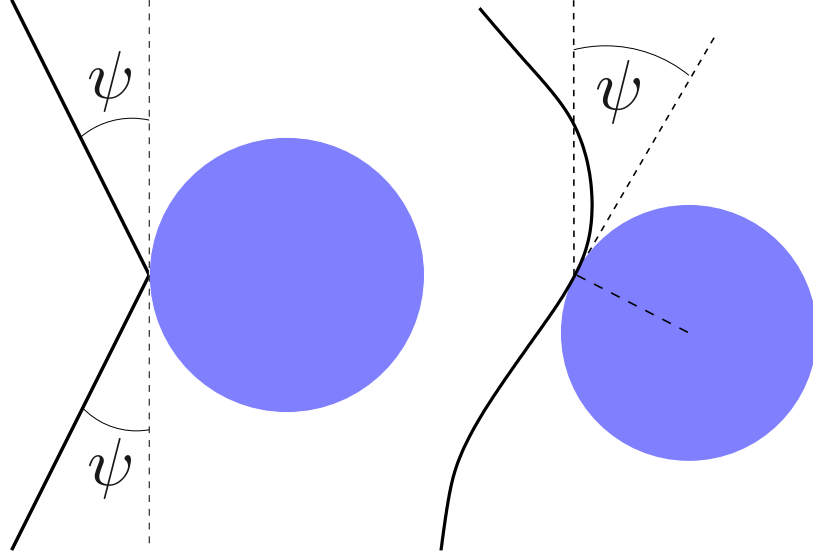


**Figure 3.8:** The geometry and mechanics of membranes with kinked (left) and smooth (right) boundary conditions at the dynamin contact line are significantly different. The blue circles represent idealized cross sections of the dynamin protein, and the black curves represent cross sections of the membrane.

Lastly,  $\lambda_K$  fixes the definition of the extrinsic curvature, giving a differential equation for  $\psi$

$$\psi'(v) = \frac{\cos \psi}{r} - K. \quad (3.85)$$

The other Euler-Lagrange equations of this system come from variations with respect to  $r$ ,  $\bar{z}$ , and  $\psi$ . Varying with respect to  $\bar{z}$  gives

$$0 \stackrel{!}{=} \delta_{\bar{z}} E = 2\pi \int ds f_z \delta \bar{z}' = 2\pi \left( - \int ds f_z' \delta \bar{z} + [\delta \bar{z} f_z] \right), \quad (3.86)$$

implying that  $f_z$  is a constant. Since  $\delta \bar{z}|_0 = \delta \bar{z}|_L = 0$ , the boundary term vanishes trivially. Varying with respect to  $K$ , we find an algebraic equation identifying  $\lambda_K$ ,

$$\delta_K E = 2\pi \int dv \delta K \left\{ \kappa \sqrt{r^2 + c^2} (K - K_s) - \lambda_K \right\} \quad (3.87)$$

$$\implies \lambda_K = \kappa \sqrt{r^2 + c^2} (K - K_s). \quad (3.88)$$

Varying with respect to  $\psi$  gives

$$\begin{aligned} \delta_\psi E &= 2\pi \int dv \left\{ \delta \psi \left( -f_r \cos \psi + f_z \sin \psi \frac{\sqrt{r^2 + c^2}}{r} \right) - \lambda_K \delta \psi' \right\} \\ &= 2\pi \int dv \left\{ \delta \psi \left( -f_r \cos \psi + f_z \sin \psi \frac{\sqrt{r^2 + c^2}}{r} + \lambda_K' \right) \right\} + 2\pi [\lambda_K \delta \psi]_{v=0}^{v=L} \end{aligned} \quad (3.89)$$

$$\implies \lambda_K' = f_r \cos \psi - f_z \sin \psi \frac{\sqrt{r^2 + c^2}}{r}, \quad (3.90)$$

where we have used integration by parts to reach the second line. The requirement that the boundary term vanishes determines the membrane's boundary conditions. In this case, we can either fix  $\psi$  (so that  $\delta\psi = 0$ ), or we can require that  $\lambda_K = 0$  (equivalently, that  $K = K_s$ ) at the point where the generatrix meets the helical support.

Which case is appropriate depends on the microscopic details of the dynamin-membrane interaction. Dynamin binds to the membrane via its pleckstrin homology (PH) domain, which has a small hydrophobic loop that inserts into the membrane [ZCL<sup>+</sup>96, SBQ<sup>+</sup>96, RS08], sometimes characterized as a wedge[SBA<sup>+</sup>13, FEAS15, RPL<sup>+</sup>09]. It is possible (though, perhaps unlikely, given that the loop is only a few amino acids long [ALSP97]) that this insertion of the PH domain into the bilayer disrupts the membrane bilayer's integrity, allowing the creation of a kink. However, since the PH domain does not penetrate very far into the membrane [RS08, RPL<sup>+</sup>09], one might also suppose that the surface is smooth across the contact line. Our geometric conception of these two possibilities at the level of continuum theory are illustrated in figure 3.8.

In the smooth case,  $\psi$  is not free to take whatever value minimizes the bending energy, but instead is fixed by the protein; we are therefore not free to vary it at all, so  $\delta\psi = 0$  at the boundary, thereby guaranteeing in a different way that the boundary term in equation (3.90) vanishes. The protein can impose any value for  $\psi$  by applying a torque to the membrane. This has been discussed in the case of small deformations in reference [FJK<sup>+</sup>16a]. In this thesis, we will assume that  $\psi = 0$ , not only for simplicity, but also based on the apparent symmetry of the dynamin's structure [FPG<sup>+</sup>11, FJN11, SFH<sup>+</sup>14].

To our knowledge, there is no sufficiently high resolution data on the membrane-dynamin interaction to resolve the question of whether kinked or smooth boundary conditions are more appropriate. We will therefore present both cases. The implications of our results will turn out not to depend significantly on which boundary conditions we use.

Lastly, the variation with respect to  $r$  gives

$$\begin{aligned} \delta_r E &= 2\pi \int dv \left\{ \delta r \left( -f_z \frac{c^2}{r^2 \sqrt{r^2 + c^2}} - \lambda_K \frac{\cos \psi}{r^2} \right) + f_r \delta r' \right\} \\ &= 2\pi \int dv \left\{ \delta r \left( -f_z \frac{c^2}{r^2 \sqrt{r^2 + c^2}} - \lambda_K \frac{\cos \psi}{r^2} - f_r' \right) \right\} + 2\pi [f_r \delta r]_{v=0}^{v=L} \end{aligned} \quad (3.91)$$

$$\implies f_r' = -f_z \frac{c^2}{r^2 \sqrt{r^2 + c^2}} - \lambda_K \frac{\cos \psi}{r^2}. \quad (3.92)$$

To maintain contact with the helix, we require  $r|_{s=0} = r|_{s=L} = R$ , so  $\delta r = 0$  at the contact line. If we wanted to allow the radius of the helix to vary, we would require  $f_r$  to vanish at the contact line.

These Euler-Lagrange equations make up a coupled set of first order equations

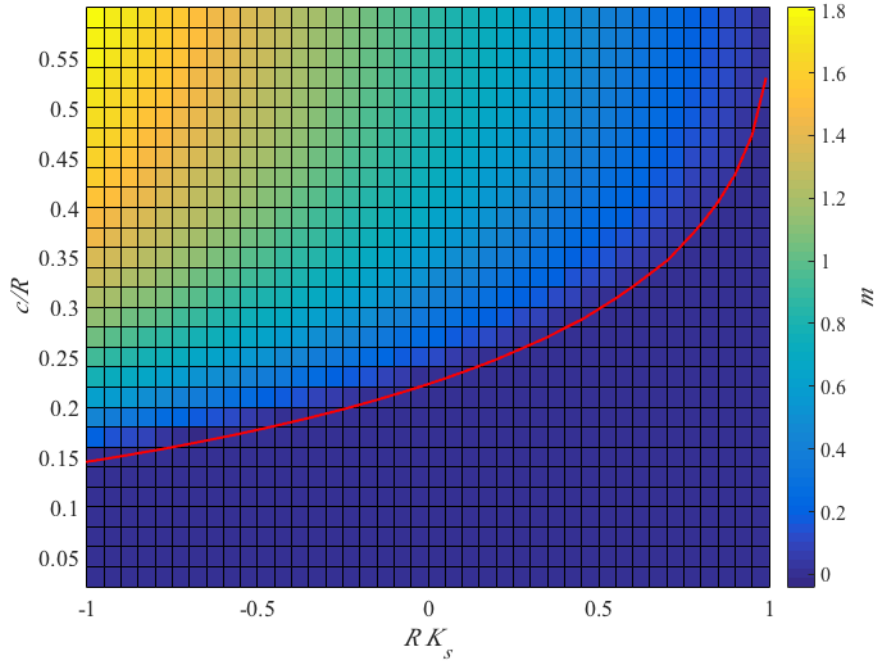


**Figure 3.9:** Phase diagram for membranes with kinked boundary conditions. Below the red line, there are CMC solutions to the shape equation, so  $m = 0$ , while it is non-zero above the red line.

that are equivalent to the membrane shape equation,

$$r' = \sin \psi \quad (3.93a)$$

$$\psi' = \frac{\cos \psi}{r} - K \quad (3.93b)$$

$$\bar{z}' = \cos \psi \frac{\sqrt{r^2 + c^2}}{r} \quad (3.93c)$$

$$K' = \frac{f_r \cos \psi}{\kappa \sqrt{r^2 + c^2}} - \frac{f_z \sin \psi}{\kappa r} - \frac{K - K_s}{r^2 + c^2} r \sin \psi \quad (3.93d)$$

$$f_z' = 0 \quad (3.93e)$$

$$f_r' = -f_z \frac{c^2}{r^2 \sqrt{r^2 + c^2}} - \kappa \sqrt{r^2 + c^2} (K - K_s) \frac{\cos \psi}{r^2}. \quad (3.93f)$$

As mentioned above, we solve these equations using the Matlab program BVP4C, a relaxation routine well suited to solving boundary value problems of this sort.

### Kinked boundary conditions

First, we consider the surfaces with kinked boundary conditions, so that  $K = K_s$  at the dynamin contact line. This case will be ideal for comparison with Kozlov, since he allows his surfaces to be kinked. Example solutions to the shape equation are shown in figure 3.10. At low pitch, we indeed find that CMC surfaces are the lowest energy solutions, agreeing with Kozlov's result; we call this regime the CMC region. These solutions of course have exactly zero bending energy. Recall that these special surfaces in fact solve the soap film shape equation (3.79); thus, above the critical pitch where soap films become unstable, solutions of this type no longer

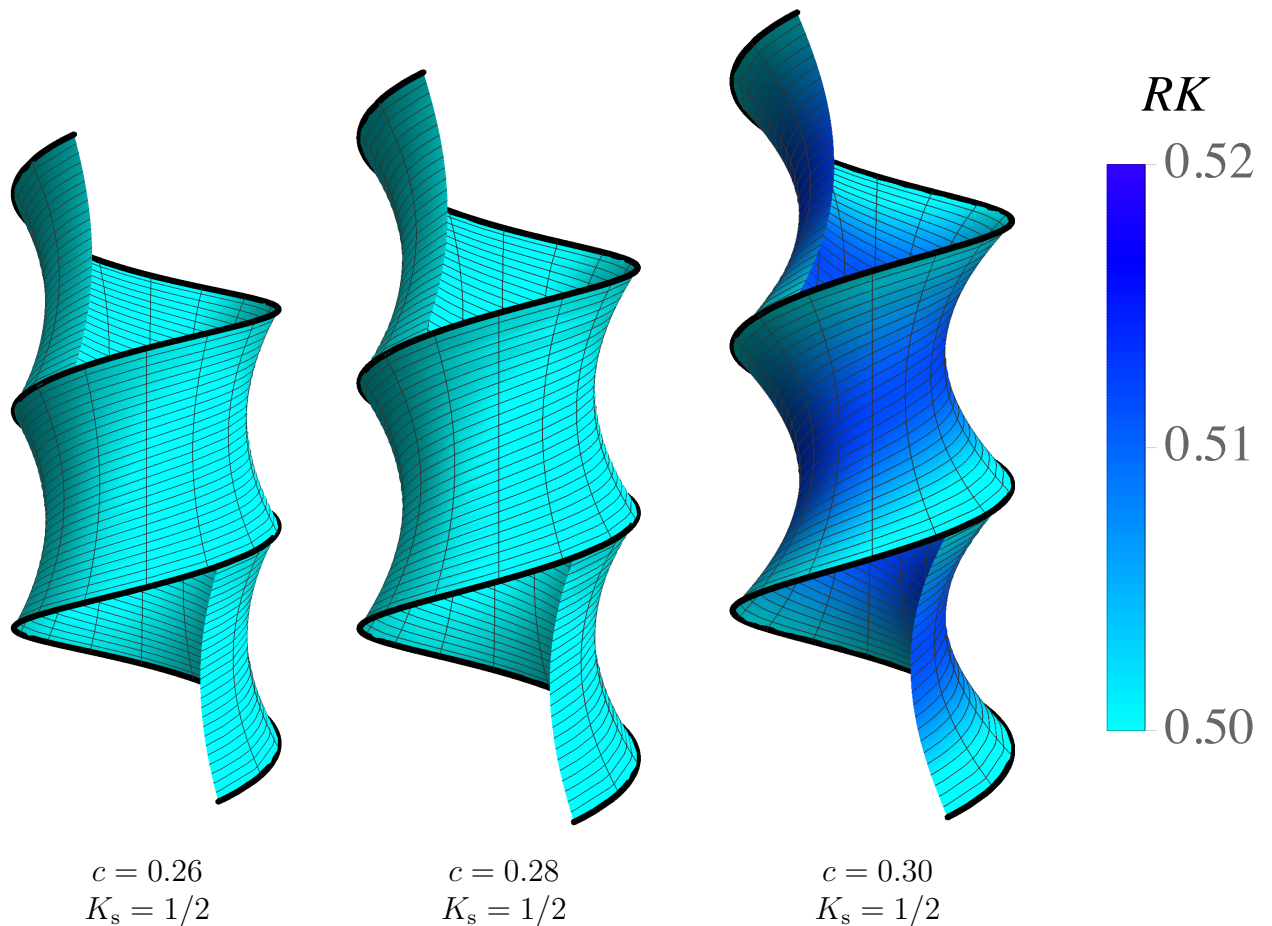


**Figure 3.10:** Example membrane configurations. The coloring indicates the local scaled extrinsic curvature  $RK$ . The dynamin contact line is illustrated in black.

exist, and the membrane cannot have constant extrinsic curvature. However, we *still* find solutions to the membrane shape equation (3.80). In that regime, the extrinsic curvature  $K$  is not equal to  $K_s$ ; in fact, it is not even constant. We call this regime the non-CMC region.

To quantify a surface's deviation from equation (3.79), we define the order parameter  $m = \langle R(K - K_s) \rangle$ , where  $\langle \cdot \rangle$  indicates averaging over the membrane. This order parameter of course vanishes in the CMC region, but increases continuously going into the non-CMC region, as shown in figure 5.17. This transition is precisely the instability of the soap film equation: in the non-CMC region, there are no solutions to equation (3.79), and so the membrane must go into a configuration with non-zero energy. Examples of CMC and non-CMC surfaces are shown in figure 3.10.

From our numerical results, it appears that the transition from  $m = 0$  to  $m > 0$  occurs continuously, so that a small change in the parameters  $R$ ,  $c$ , or  $K_s$  leads to a small change in the surface. If the membrane underwent a *discontinuous* transition, it would have to be temporarily out of equilibrium, potentially destabilizing the membrane and leading to breakage. The transition we observe, however, can be performed adiabatically, so that the membrane is always in equilibrium.

Of course, configurations with  $m \neq 0$  will also have non-zero energy. The dynamin helix must therefore do work to deform the membrane out of the CMC region. This energy can be provided by GTP hydrolysis.

### Smooth boundary conditions

We also solve equation (3.80) with boundary conditions requiring the surface to be smooth at the contact line. Examples of such solutions are shown in figure 3.2.4. In this case, the membrane only has constant mean curvature when  $RK_s = 1$ , in which case it is exactly cylindrical. That is, with these boundary conditions, solutions to equation (3.79) are almost never solutions to equation (3.80). As a result, there is no significant transition in the order parameter  $m$ , or in the shape of the surface. Once again, small changes in the parameters  $R$ ,  $c$ , and  $K_s$  seem to always lead to small changes in the membrane's shape, so that any change can be performed adiabatically.

Furthermore, we find no set of parameters for which a solution does not exist. Even at very large pitch-radius ratios  $c/R \sim 10$ , our numerical solver is able to find shapes satisfying the shape equation.

### Conclusions

Using the full membrane shape equation, we have found that there are equilibrium membrane configurations possessing helicoidal symmetry at all relevant values of the pitch and spontaneous curvature. This is true whether one requires smooth surfaces or allows kinks at the helical contact line.

As we have shown, Kozlov's analysis of helicoidal membranes considered only a subset of the solutions to the membrane shape equation, namely, CMC surfaces. The omission of other solutions led to the conclusion that no solutions exist in a certain regime. On the contrary, the membrane continuously transitions from a CMC state to a non-CMC state as the helical pitch increases, the helical radius decreases, or the membrane spontaneous curvature decreases. Non-CMC surfaces are of course higher in energy than their counterparts, requiring the dynamin protein to do work in order to drive the membrane across the transition from CMC to non-CMC.

Perhaps more importantly, the lower order equation considered by Kozlov permits fewer boundary conditions. This makes it impossible to consider membranes that are differentiable across the dynamin contact line. Using the higher order equation and applying these smooth boundary conditions we find that the membrane has no instability or shape transition of any sort.

Although we have found that solutions to the shape equation exist for seemingly any boundary conditions, we must point out that there is a stricter sense of the word "stability" that one encounters primarily in the mathematical literature and which we have not analyzed here. This meaning distinguishes local minima of the energy functional, which are stable, from saddle points, which are unstable. To guarantee our solutions' stability in this sense requires the technically challenging framework of the second variation, the functional analogue of the second derivative. In order to evaluate the stability of a membrane configuration in this sense, one must calculate the spectrum of eigenvalues of a differential operator for each solution of the shape equation; this operator was calculated for membranes in references [ZCH89, CGS03]. For an example of such a calculation applied to helicoidal soap films, see reference [BPA99].

If the membrane does not possess such an instability, the analysis presented here suggests the Helfrich model cannot explain why the membrane undergoes fission. This is not entirely surprising; after all, the Helfrich model only describes the mem-

brane approximately, and is not guaranteed to be valid at length scales on the order of a few nanometers. Higher order terms or internal degrees of freedom such as tilt or membrane compressibility may be essential for understanding how dynamin's conformational change induces fission.

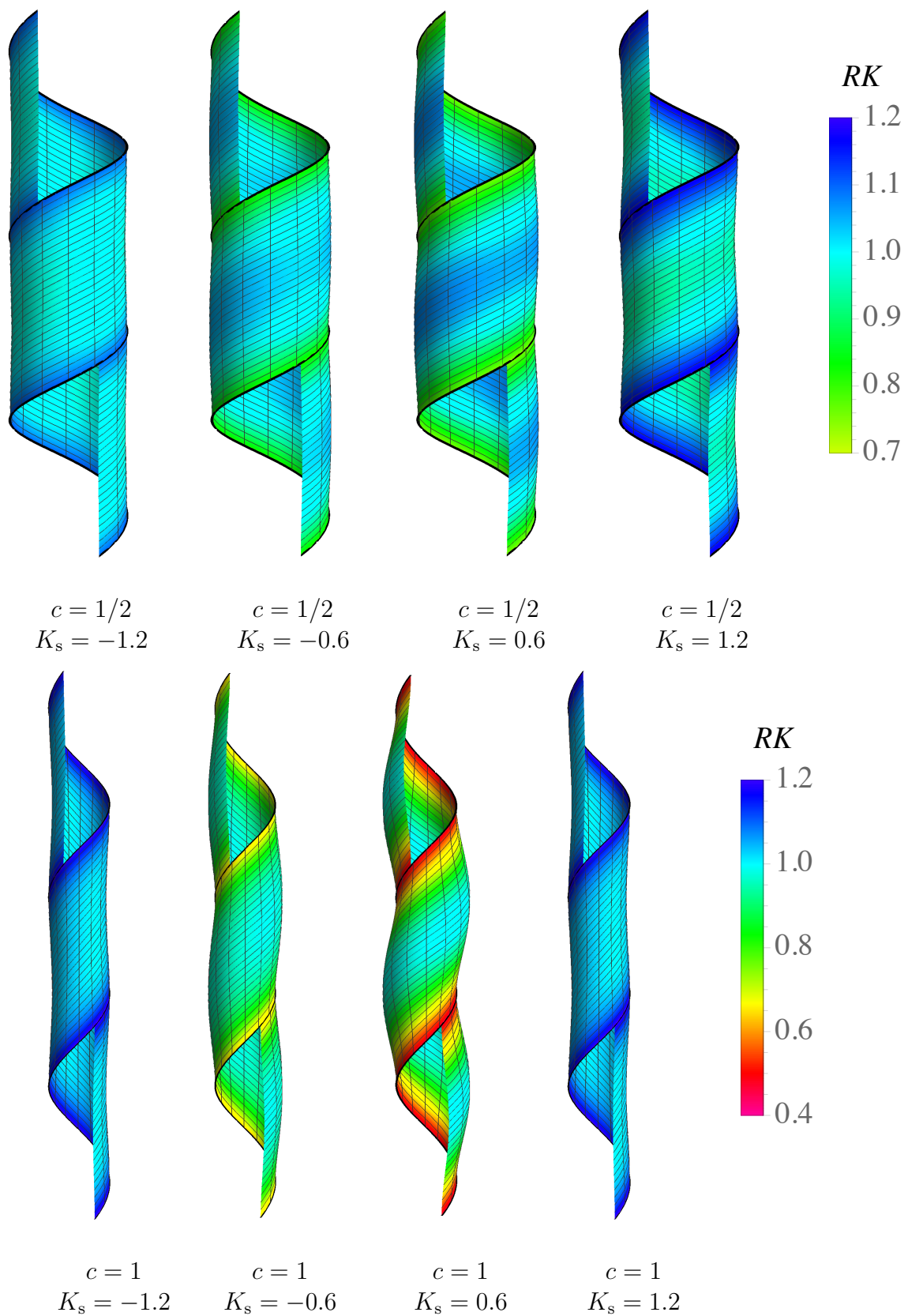


**Figure 3.11:** (Top) Example membrane configurations with smooth boundary conditions  $c = 1/2$ . (Bottom) Example configurations with  $c = 1$ .

# Chapter 4

## Surface-bound elastic filaments: theory

Now that we have the geometric tools available, we can begin to investigate the elastic behavior of filaments. Before we attempt this study, though, we will first need to review the theory of their mechanics more generally, which has a history dating back to Galileo [Lev08]. We take a particular interest in the confinement of elastic rods to curved surfaces, a problem with many applications to biology, but also important in engineering. In particular, we seek to build a continuum model of dynamin mediated membrane fission, to which we have already made a few references in this thesis [SDS00a, MR13b, ABDC<sup>+</sup>16]. Another system that could be modeled as a surface bound elastic rod is chromatin, which is assembled from chains of DNA wrapping around small spheres called histones [OO74, FM86]. In fact, DNA's binding to histones differs from dynamin's membrane binding in a mechanically crucial way. This distinction between different types of surface binding will be discussed in depth in this chapter. Outside of the biological realm, the elastic theory of rods was applied to the buckling of drill strings inside a cylindrical hole [VdH01]. In comparison to the general elastic filament, the confined elastic filament is very young: David Hilbert once famously (and incorrectly) assumed that surface-confined elastic filaments lie along geodesics, creating a rare opportunity for mathematicians and physicists with more conventionally human intellects to favorably pit theirs against his [HCV52]. This very system was also studied more recently by Nickerson and Manning in reference [NM88]. The formalism was significantly improved even more recently by Guven and Vázquez-Montejo in references [GVM12, GVVM14]. In particular, reference [GVVM14] discusses surface confined filaments fairly generally, and overlaps to a large degree with section 4.3. We review their work here firstly because many of their results will be needed in future chapters, but also because this chapter will include an expansion upon their discoveries.

In many cases, the chemical details of polymers and proteins is indispensable for understanding their functioning. For example, actin is not simply an inert rod in the cell; it is constantly polymerizing and being actively pushed around by myosin motors. Dynamin does not only bind to the membrane during endocytosis, but can also bind to itself and to other proteins that can affect the membrane composition [SWT<sup>+</sup>99]. However, the mechanics of these objects is as indispensable as their chemistry. As we will see in this chapter and the next, a mechanical study of surface bound elastic rods will provide us with insights that are often surprising,

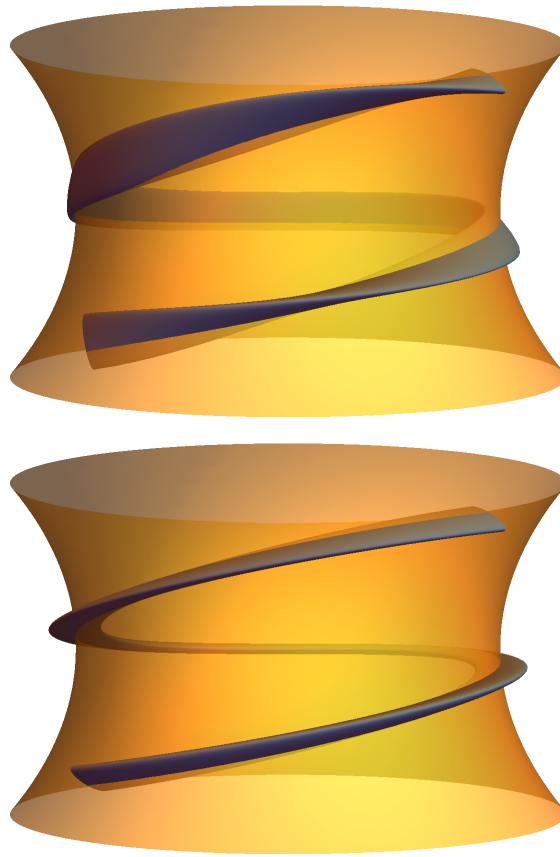


**Figure 4.1:** Examples of filaments with rotating (top) and fixed (bottom) cross sectional orientations.

non-trivial, and, most importantly, useful.

To begin, we will find the Euler-Lagrange equations of an elastic filament in three dimensional Euclidean space in section 4.1. These calculations will illustrate the basic mechanics of such rods, and introduce some of our methods of analysis. Then we can consider confining the filament to a curved surface. The details of this confinement are profoundly important. Namely, certain binding mechanisms will constrain the orientation of the filament's cross section relative to the surface normal. In more mathematically language, the details of the binding mechanism determine the relationship between the Darboux frame and the material frame. As alluded to above, DNA binds to histones via electrostatic attraction. The attraction between the oppositely charged DNA molecule and the histone is the same regardless of the DNA's orientation. On the other hand, dynamin binds to membranes via its pleckstrin homology (PH) domain, and thus maintains a fixed material orientation relative to the surface. Figure 4.1 illustrates the different constraints implied by these mechanisms, showing one filament with a freely twisting cross section, and one with a fixed cross section. It is a theory of surface confinement with fixed cross sections that was developed in reference [GVVM14]. Our contribution is to generalize their results to include filaments with freely twisting cross sections. We will first discuss confinement of filaments with free cross sections in section 4.2, and then review the results of Guven et al. in section 4.3. This sequence of presentation is of course ahistorical, but we believe it will be clearer than the alternative.

## 4.1 Unconfined filament

### 4.1.1 Bernoulli-Euler rod

Let us begin with an analysis of the simplest model of an elastic filament, the Bernoulli-Euler rod,

$$E_{\text{BE}} = \int ds \alpha \frac{\kappa^2}{2}. \quad (4.1)$$

We parametrize the filament by the function  $\mathbf{Y}(s)$  (where  $s$  is assumed to be arc-length). Following references [GVM12, GVVM14], we will add Lagrange multiplier terms to this energy functional defining the tangent vector and material curvatures, and ensuring the orthogonality of the material frame vectors. These will allow us to treat the various quantities in the energy functional as independent, making the process of finding the Euler-Lagrange equation for the filament much easier. As we will see, the filament is in equilibrium when the forces on it are balanced at every point. This physical condition must be expressed in terms of the geometry of the filament in order for the Euler-Lagrange equation to meaningfully describe the shape of the filament.

With the Lagrange multipliers, the energy functional becomes

$$E_{\text{BE}} = \int_0^L ds \left\{ \frac{\alpha}{2} \mathbf{T}'^2 + \mathbf{F} \cdot (\mathbf{T} - \mathbf{Y}') + \frac{\Lambda}{2} (\mathbf{T}^2 - 1) \right\}. \quad (4.2)$$

The multiplier  $\mathbf{F}$  enforces the definition of  $\mathbf{T}$ , and the multiplier  $\Lambda$  ensures that  $\mathbf{T}$  is a unit vector (or, equivalently, that  $s$  is arc-length). Varying with respect to  $\mathbf{Y}$ , we find

$$\delta_{\mathbf{Y}} E_{\text{BE}} = \int_0^L ds \mathbf{F}' \cdot \delta \mathbf{Y} - [\mathbf{F} \cdot \delta \mathbf{Y}]_0^L, \quad (4.3)$$

implying that, in equilibrium,

$$\mathbf{F}' = 0. \quad (4.4)$$

Thus, the vector  $\mathbf{F}$  is conserved along the filament. In fact, it is the constant associated with translational invariance. The boundary conditions require that either  $\delta \mathbf{Y} = 0$  or  $\mathbf{F} = 0$  at the endpoints. Varying with respect to  $\mathbf{T}$  gives

$$\delta_{\mathbf{T}} E_{\text{BE}} = \int_0^L ds (-\alpha \mathbf{T}''' + \mathbf{F} + \Lambda \mathbf{T}) \cdot \delta \mathbf{T} + \alpha [\kappa \mathbf{N} \cdot \delta \mathbf{T}]_0^L. \quad (4.5)$$

In equilibrium, we therefore get

$$\mathbf{F} = \alpha \mathbf{T}'' - \Lambda \mathbf{T} = -(\alpha \kappa^2 + \Lambda) \mathbf{T} + \alpha \kappa' \mathbf{N} + \alpha \kappa \tau \mathbf{B}, \quad (4.6)$$

where we have used the Frenet equations (2.6) to evaluate  $\mathbf{T}''$ . The vanishing of the boundary term requires that either the tangent vector is either clamped fixed,  $\delta \mathbf{T} = 0$ , or free to vary, in which case  $\kappa = 0$ .

Together, equations (4.4) and (4.6) give the Euler-Lagrange equations for the filament. However, the function  $\Lambda$  is still unknown. To find a meaningful equilibrium

condition, we must find  $\Lambda$  in terms of the geometry of the filament, e.g. in terms of  $\kappa$  and  $\tau$ . Let us label the components of  $\mathbf{F}$  in the Frenet-Serret basis as  $\mathbf{F} = F_T\mathbf{T} + F_N\mathbf{N} + F_B\mathbf{B}$ . Then the tangential projection of equation (4.4) gives

$$0 = \mathbf{F}' \cdot \mathbf{T} = (\mathbf{F} \cdot \mathbf{T})' - \mathbf{F} \cdot \mathbf{T}' = -3\alpha\kappa\kappa' - \Lambda', \quad (4.7)$$

where we have used the Frenet-Serret equations (2.6) to evaluate  $\mathbf{T}' = \kappa\mathbf{N}$ . This can be integrated to obtain  $\Lambda(s)$ ,

$$\Lambda = -\frac{3}{2}\alpha\kappa^2 + \mathcal{H}, \quad (4.8)$$

where  $\mathcal{H}$  is a constant of integration. This quantity is analogous to the surface tension  $\sigma$  of a surface; just as  $\sigma$  can serve as a Lagrange multiplier fixing the area of the surface, it turns out that  $\mathcal{H}$  controls the length of the filament.

We could also have obtained this equation by noting that the integrand in equation (4.2) does not depend explicitly on  $s$ . We can consider equation (4.2) as a Lagrangian system with arc-length  $s$  playing the role of time. But a time-independent Lagrangian implies that the system's Hamiltonian must be conserved [GPS02]. Similarly, we will in fact show that  $\mathcal{H}$  is the constant of motion associated with arc-length-independence!

To see this explicitly, recall that for a Lagrangian system with coordinates  $q^i$ , the Hamiltonian is given by the Legendre transform of the Lagrangian, that is

$$q'^i p_i - \mathcal{L} = \mathcal{H}, \quad (4.9)$$

where the  $p_i = \partial\mathcal{L}/\partial q'^i$  are called the ‘‘canonical momenta’’ conjugate to coordinates  $q^i$ . The energy density plays the role of the Lagrangian  $\mathcal{L}$ . In this case, ‘‘coordinates’’ are  $\mathbf{Y}$  and  $\mathbf{T}$ , with conjugate momenta

$$\mathbf{P}_Y = \frac{\partial\mathcal{L}}{\partial\mathbf{Y}'} = -\mathbf{F} \quad (4.10)$$

$$\mathbf{P}_T = \frac{\partial\mathcal{L}}{\partial\mathbf{T}'} = \alpha\kappa\mathbf{N}. \quad (4.11)$$

The Hamiltonian is therefore

$$\begin{aligned} \mathcal{H} &= \mathbf{P}_Y \cdot \mathbf{Y}' + \mathbf{P}_T \cdot \mathbf{T}' - \mathcal{L} \\ &= -F_T + \alpha\kappa^2 - \frac{\alpha}{2}\kappa^2 \\ &= \alpha\kappa^2 + \Lambda + \frac{\alpha}{2}\kappa^2 \\ &= \frac{3\alpha}{2}\kappa^2 + \Lambda, \end{aligned} \quad (4.12)$$

which agrees with equation (4.8).

The normal and binormal projections of equation (4.4) can now be written as

$$\mathbf{F}' \cdot \mathbf{N} = \alpha \left[ \kappa'' + \kappa \left( \frac{\kappa^2}{2} - \tau^2 - \mathcal{H} \right) \right] = 0 \quad (4.13a)$$

$$\mathbf{F}' \cdot \mathbf{B} = \alpha [2\kappa'\tau + \kappa\tau'] = \alpha \frac{(\kappa^2\tau)'}{\kappa} = 0. \quad (4.13b)$$

These conditions describe the equilibrium of the filament.

How can we interpret these equations physically? One informative picture emerges from considering a uniform translation of the filament. Let us therefore displace the filament by a constant  $\delta\mathbf{Y} = \mathbf{a}$ , leaving the tangent vector unchanged  $\delta\mathbf{T} = 0$ . During this displacement, we imagine the bulk of the filament to be in equilibrium, though the ends may be clamped or held in some way. As a result of the displacement, the energy changes by

$$\delta E_{\text{BE}} = \int_0^L ds \mathbf{F}' \cdot \mathbf{a} - [\mathbf{F} \cdot \mathbf{a}]_0^L = -\mathbf{a} \cdot [\mathbf{F}]_0^L. \quad (4.14)$$

Since the change in energy is minus the displacement  $\mathbf{a}$  times the force, we identify

$$[\mathbf{F}]_0^L = \int_0^L ds \mathbf{F}' \quad (4.15)$$

as the force on the filament.

The fact that  $\mathbf{F}'$  is the force per unit length on the filament also offers an explanation for  $\mathbf{F}$  itself. Just as equilibrium for a surface is achieved when the divergence of the stress vanishes, equilibrium for the filament is defined by the derivative of  $\mathbf{F}$  vanishing. We therefore conclude that  $\mathbf{F}$  is the stress in the filament: if we make a cut across the filament at point  $s$ , then  $\mathbf{F}(s)$  is the force we will have to apply to keep the filament in the same configuration. This also suggests an interpretation for  $\mathcal{H}$ , which appears as a constant in the tangential component of the stress tensor. This behavior is reminiscent of the surface tension  $\sigma$  in a surface. We conclude that  $\mathcal{H}$  represents a constant isotropic tension in the filament: when  $\mathcal{H} > 0$ , the filament is under tension, and when  $\mathcal{H} < 0$ , it is under compression.

A similar calculation can identify the torque on the filament. Consider performing a constant rotation by an amount  $\theta$  about an axis  $\mathbf{w}$ , so that  $\delta\mathbf{Y} = \theta\mathbf{w} \times \mathbf{Y}$  and  $\delta\mathbf{T} = \theta\mathbf{w} \times \mathbf{T}$ . Assuming the filament is in equilibrium, the resulting change in energy is

$$\delta E_{\text{BE}} = [-\mathbf{F} \cdot (\theta\mathbf{w} \times \mathbf{Y}) + \alpha\kappa\mathbf{N} \cdot (\mathbf{w} \times \mathbf{T})]_0^L = -\theta\mathbf{w} \cdot [\mathbf{Y} \times \mathbf{F} - \alpha\kappa\mathbf{B}]_0^L. \quad (4.16)$$

This identifies the quantity in brackets,

$$\mathbf{M} = \mathbf{Y} \times \mathbf{F} - \alpha\kappa\mathbf{B} \quad (4.17)$$

as the moment of the filament. As  $\mathbf{F}$  describes the force necessary to hold the filament in place after cutting it,  $\mathbf{M}$  describes the *torque* necessary to do so. The first term is the torque due to external stresses, i.e.  $\mathbf{F}$ . The second term  $\mathbf{S} = -\alpha\kappa\mathbf{B}$  is known as the *bending moment* of the filament. Because the filament only bends about the  $\mathbf{B}$  axis,  $\mathbf{S}$  only has components in the  $\mathbf{B}$  direction.

Consider the derivative of the moment  $\mathbf{M}'$ . Using equation (4.4), this is given by

$$\begin{aligned} \mathbf{M}' &= \mathbf{T} \times \mathbf{F} + \mathbf{Y} \times \mathbf{F}' - \alpha(\kappa\mathbf{B})' \\ &= \alpha\kappa'\mathbf{B} - \alpha\kappa\tau\mathbf{N} - \alpha\kappa'\mathbf{B} + \alpha\kappa\tau\mathbf{N} = 0. \end{aligned} \quad (4.18)$$

Thus the moment  $\mathbf{M}$  is the conserved quantity associated with rotational symmetry.

### 4.1.2 General rod

As we discussed in Chapter 2, the energy of the Bernoulli-Euler rod can be augmented in a number of ways to make it more realistic. Namely, we could consider anisotropy between different types of bending, include penalties for twist, and allow for the possibility of spontaneous curvature. Including these quantities will not change the physical meaning of the Euler-Lagrange equations; it will only change their appearance.

Let us consider a filament whose energy density is defined by an arbitrary function  $\mathcal{E}(\kappa_1, \kappa_2, \kappa_t)$ , which depends only on the material curvatures and the twist of the rod,

$$E = \int_0^L ds \mathcal{E}(\kappa_1, \kappa_2, \kappa_t). \quad (4.19)$$

The energy density  $\mathcal{E}$  could take a large variety of forms, such as that in the Kirchhoff model of the elastic rod (see equation (2.17)). Again, we will use Guven's method [GVM12, GVVM14] and add a system of Lagrange multipliers to the energy functional. However, this time, we will need additional Lagrange multipliers to enforce the orthonormality of every vector in the material frame and to define the material curvatures and twist in terms of the material frame. The final energy functional is given by

$$E = \int_0^L ds \left\{ \mathcal{E}(\kappa_1, \kappa_2, t) + \mathbf{F} \cdot (\mathbf{T} - \mathbf{Y}'(s)) + \frac{1}{2} \gamma_{ij} (\mathbf{f}_i \cdot \mathbf{f}_j - \delta_{ij}) + \frac{1}{2} \Gamma_{ij} (\mathbf{f}'_i(s) \cdot \mathbf{f}_j - M_{ij}) \right\}, \quad (4.20)$$

where the  $\mathbf{f}_i$  are the basis vectors of the material frame with  $\mathbf{f}_1 = \mathbf{m}_1$ ,  $\mathbf{f}_2 = \mathbf{m}_2$ ,  $\mathbf{f}_3 = \mathbf{T}$  and  $M_{ij}$  are the components of the material frame connection matrix<sup>1</sup>, given by

$$M = \begin{pmatrix} 0 & \kappa_t & -\kappa_1 \\ -\kappa_t & 0 & -\kappa_2 \\ \kappa_1 & \kappa_2 & 0 \end{pmatrix}. \quad (4.21)$$

Because the constraint enforced by  $\gamma_{ij}$  is symmetric in the indices  $i$  and  $j$ , we assume without loss of generality that  $\gamma_{ij}$  is symmetric. Similarly, we assume that  $\Gamma_{ij}$  is antisymmetric.

In this case, the stress  $\mathbf{F}$  will not be given by equation (4.6). Instead, we must calculate the appropriate stress function for the new energy density. However, as in the case of the Bernoulli-Euler rod, we see immediately by varying with respect to  $\mathbf{Y}$  that

$$\mathbf{F}' = 0. \quad (4.22)$$

Thus we should still expect that the force at each point on the filament vanishes.

<sup>1</sup>In this section, we will mostly not bother with distinguishing between covariant and contravariant indices. This is because all the indices here are in an orthonormal cartesian basis, where the metric is simply  $g_{ij} = \delta_{ij}$ . There is therefore no difference between the two types of indices.

Because we have enforced their definition through Lagrange multipliers, we can also vary with respect to the curvatures of the filament independently. We find

$$0 = \frac{\partial \mathcal{E}}{\partial \kappa_1} + \Gamma_{13} \quad (4.23a)$$

$$0 = \frac{\partial \mathcal{E}}{\partial \kappa_2} + \Gamma_{23} \quad (4.23b)$$

$$0 = \frac{\partial \mathcal{E}}{\partial t} - \Gamma_{12}, \quad (4.23c)$$

and therefore that

$$\Gamma = \begin{pmatrix} 0 & \mathcal{F}_t & -\mathcal{F}_1 \\ -\mathcal{F}_t & 0 & -\mathcal{F}_2 \\ \mathcal{F}_1 & \mathcal{F}_2 & 0 \end{pmatrix}, \quad (4.24)$$

where  $\mathcal{F}_i = \partial \mathcal{E} / \partial \kappa_i$  for  $i = 1, 2$  and  $\mathcal{F}_t = \partial \mathcal{E} / \partial t$ .

Lastly, we vary with respect to the  $\mathbf{f}_i$  to find

$$0 = F_j \delta_{i3} + \gamma_{ij} - \left( \frac{1}{2} \Gamma'_{ij} + \Gamma_{ik} M_{kj} \right). \quad (4.25)$$

The unusual term  $\delta_{i3}$  arises because the  $F_j$  term only appears when varying with respect to  $\mathbf{T} = \mathbf{f}_3$ . Using our assumption that  $\gamma_{ij}$  is symmetric, we can eliminate the  $\gamma_{ij}$  term by antisymmetrizing in  $i$  and  $j$ ,

$$0 = F_j \delta_{i3} - F_i \delta_{j3} - \Gamma'_{ij} - \Gamma_{ik} M_{kj} + \Gamma_{jk} M_{ki}. \quad (4.26)$$

Taking  $i = 3, j = 1$  in equation (4.26), we find

$$F_1 = \mathcal{F}'_1 - \mathcal{F}_2 \kappa_t + \mathcal{F}_t \kappa_2. \quad (4.27)$$

Taking  $i = 3, j = 2$ , we find

$$F_2 = \mathcal{F}'_2 + \mathcal{F}_1 \kappa_t - \mathcal{F}_t \kappa_1. \quad (4.28)$$

Lastly, we take  $i = 1, j = 2$ , leading to

$$\mathcal{F}'_t = \mathcal{F}_1 \kappa_2 - \mathcal{F}_2 \kappa_1. \quad (4.29)$$

This last equation actually has very different information content from the two preceding it. In fact, it provides the Euler-Lagrange equation for the cross section of the filament! For example, using the Kirchhoff energy functional with spontaneous curvature defined in equation (2.23), it becomes

$$\beta \kappa'_t(s) = -\alpha_2 (\kappa_2 - c_2) \kappa_1 + \alpha_1 (\kappa_1 - c_1) \kappa_2. \quad (4.30)$$

In the isotropic rod case  $c_1 = c_2 = 0$ ,  $\alpha_1 = \alpha_2$ , and equation (4.29) reduces to

$$\kappa'_t(s) = 0. \quad (4.31)$$

For the Bernoulli-Euler rod,  $\mathcal{F}_t$  vanishes, so equation (4.29) is satisfied trivially.

The only physically significant quantity we have not determined is  $F_T$ . As for the Bernoulli-Euler rod, we cannot algebraically solve the above equations simultaneously for  $F_T$  and  $\gamma_{33}$ , where  $\gamma_{33}$  plays the role that  $\Lambda$  did for the Bernoulli-Euler rod. However, we can again exploit that fact that the energy density does not depend explicitly on  $s$  to find  $F_T$  up to an additive constant  $\mathcal{H}$ . In this case, the functions  $\mathbf{Y}$  and  $\mathbf{f}_i$  have conjugate momenta given by

$$\mathbf{P}_{\mathbf{Y}} = -\mathbf{F} \quad (4.32)$$

$$\mathbf{P}_{\mathbf{f}_i} = \frac{1}{2}\Gamma_{ij}\mathbf{f}_j. \quad (4.33)$$

The Hamiltonian is therefore given by

$$\begin{aligned} \mathcal{H} &= -\mathbf{F} \cdot \mathbf{Y}' + \frac{1}{2}\Gamma_{ij}\mathbf{f}_j \cdot \mathbf{f}'_i - \mathcal{E} \\ &= -F_T + \frac{1}{2}\Gamma_{ij}\mathbf{f}_j \cdot (M_{ik}\mathbf{f}_k) - \mathcal{E} \\ &= -F_T + \frac{1}{2}\Gamma_{ij}M_{ij} - \mathcal{E}. \\ \implies F_T &= \kappa_1\mathcal{F}_1 + \kappa_2\mathcal{F}_2 + \kappa_t\mathcal{F}_t - \mathcal{E} - \mathcal{H}. \end{aligned} \quad (4.34)$$

We now have the ingredients to write (4.22) explicitly. The tangential component is satisfied trivially:

$$\begin{aligned} \mathbf{F}' \cdot \mathbf{T} &= (\mathbf{F} \cdot \mathbf{T})' - \mathbf{F} \cdot \mathbf{T}' \\ &= (\kappa_1\mathcal{F}_1 + \kappa_2\mathcal{F}_2 + \kappa_t\mathcal{F}_t - \mathcal{E} - \mathcal{H})' - \kappa_1(\mathcal{F}'_1 - \mathcal{F}_2\kappa_t + \mathcal{F}_t\kappa_2) - \kappa_2(\mathcal{F}'_2 + \mathcal{F}_1\kappa_t - \mathcal{F}_t\kappa_1) \\ &= \kappa'_1\mathcal{F}_1 + \kappa'_2\mathcal{F}_2 + \kappa'_t\mathcal{F}_t + \kappa_1\mathcal{F}'_1 + \kappa_2\mathcal{F}'_2 + \kappa_t\mathcal{F}'_t - \kappa'_i\frac{\partial\mathcal{E}}{\partial\kappa_i} - \kappa_t\frac{\partial\mathcal{E}}{\partial\kappa_t} \\ &\quad - \kappa_1\mathcal{F}'_1 - \kappa_2\mathcal{F}'_2 - \kappa_t(\kappa_2\mathcal{F}_1 - \kappa_1\mathcal{F}_2) = 0, \end{aligned} \quad (4.35)$$

where we have used the definition of the  $\mathcal{F}_i$  to eliminate the  $\kappa'_i$  terms, and equation (4.29) to eliminate the  $\mathcal{F}'_t$  term. The projections onto  $\mathbf{m}_1$  and  $\mathbf{m}_2$  give, respectively,

$$\begin{aligned} \mathbf{F}' \cdot \mathbf{m}_1 &= F'_2 + \kappa_1F_T - \kappa_tF_3 \\ &= \mathcal{F}''_1 - \mathcal{F}'_2\kappa_t - \mathcal{F}_2t' + \mathcal{F}'_t\kappa_2 + \mathcal{F}_t\kappa'_2 + \\ &\quad \kappa_1(\kappa_1\mathcal{F}_1 + \kappa_2\mathcal{F}_2 + \kappa_t\mathcal{F}_t - \mathcal{E} - \mathcal{H}) - \kappa_t(\mathcal{F}'_2 + \mathcal{F}_1\kappa_t - \mathcal{F}_t\kappa_1) \end{aligned} \quad (4.36)$$

$$\begin{aligned} \mathbf{F}' \cdot \mathbf{m}_2 &= F'_3 + \kappa_2F_T + \kappa_tF_2 \\ &= \mathcal{F}''_2 + \mathcal{F}'_1\kappa_t + \mathcal{F}_1t' - \mathcal{F}'_t\kappa_1 - \mathcal{F}_t\kappa'_1 + \\ &\quad \kappa_2(\kappa_1\mathcal{F}_1 + \kappa_2\mathcal{F}_2 + \kappa_t\mathcal{F}_t - \mathcal{E} - \mathcal{H}) + \kappa_t(\mathcal{F}'_1 - \mathcal{F}_2\kappa_t + \mathcal{F}_t\kappa_2). \end{aligned} \quad (4.37)$$

We have already remarked that, as the conserved quantity associated with translation invariance,  $\mathbf{F}$  still defines the stress in the filament. We can again find the moment  $\mathbf{M}$  by considering a uniform rotation of the filament by an angle  $\theta$  about the  $\mathbf{w}$  axis. Then, the changes in the position  $\mathbf{Y}$  and material frame elements  $\mathbf{f}_i$  are given by  $\delta\mathbf{Y} = \theta\mathbf{w} \times \mathbf{Y}$  and  $\delta\mathbf{f}_i = \theta\mathbf{w} \times \mathbf{f}_i$ . The resulting change in energy,

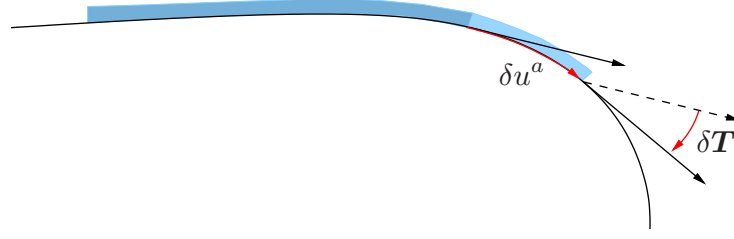


**Figure 4.2:** The blue bars represent a surface-confined filament before and after a small translation  $\delta u^a$ . The surface confinement couples the translation with rotation  $\delta \mathbf{T}$  of the filament's tangent vector.

assuming the filament is in equilibrium, is

$$\begin{aligned} \delta E &= \left[ -\mathbf{F} \cdot (\theta \boldsymbol{\omega} \times \mathbf{Y}) + \frac{1}{2} \Gamma_{ij} \mathbf{f}_j \cdot (\theta \boldsymbol{\omega} \times \mathbf{f}_i) \right]_0^L \\ &= -\theta \boldsymbol{\omega} \cdot \left[ \mathbf{Y} \times \mathbf{F} + \frac{1}{2} \Gamma_{ij} \mathbf{f}_i \times \mathbf{f}_j \right]_0^L \\ &= -\theta \boldsymbol{\omega} \cdot \left[ \mathbf{Y} \times \mathbf{F} + \frac{1}{2} \Gamma_{ij} \varepsilon_{ijk} \mathbf{f}_k \right]_0^L \end{aligned} \quad (4.38)$$

$$\implies \mathbf{M} = \mathbf{Y} \times \mathbf{F} + \frac{1}{2} \Gamma_{ij} \varepsilon_{ijk} \mathbf{f}_k. \quad (4.39)$$

The term in the moment due to external stresses  $\mathbf{Y} \times \mathbf{F}$  is unchanged in form. The bending moment of the rod, though, is now given by

$$\mathbf{S} = \frac{1}{2} \Gamma_{ij} \varepsilon_{ijk} \mathbf{f}_k = -\mathcal{F}_2 \mathbf{m}_1 + \mathcal{F}_1 \mathbf{m}_2 + \mathcal{F}_t \mathbf{T}, \quad (4.40)$$

which, we note, is very similar in form to the angular velocity vector  $\boldsymbol{\omega}$  given in equation (2.12). For the Bernoulli-Euler rod, the structure of  $\mathbf{F}$  and  $\mathbf{S}$  guaranteed that  $\mathbf{M}' = 0$ ; it simply turned out to be an identity. In this case, that is only true for the components of  $\mathbf{M}'$  that are perpendicular to the rod. The tangential projection of  $\mathbf{M}'$ , though, contains additional physical information: it is identically equation (4.29)! Thus equation (4.29) tells us that the rod's material cross section is relaxed when the torque about the tangent vector is conserved.

## 4.2 Surface confinement with free cross section

As we confine the filament to a surface, much of the physics remains unchanged. The Lagrange multiplier  $\mathbf{F}$  which defines the tangent vector will still represent the stress in the filament. The equilibrium conditions are still determined by force and torque balance. However, except in special cases, confinement to a surface breaks the translational and rotational symmetries that were present before. As a result, the stress  $\mathbf{F}$  and torque  $\mathbf{M}$  are no longer conserved. Surface confinement will also couple certain variables that were independent before: whereas translation and bending are unrelated when the filament is free, translation along a surface may put the filament in a region where the surface is itself more strongly curved, necessitating increased bending in the filament (see figure 4.2). In particular, this coupling makes the evaluation of boundary conditions much subtler.

We describe the surface by  $\mathbf{X}(u^1, u^2)$ , where the  $u^a$  are generic surface coordinates. Because the filament is confined to the surface, it also has a natural parametrization as a surface curve  $u^a(s)$ , embedded in space as  $\mathbf{X}(u^1(s), u^2(s))$ . We therefore add an additional Lagrange multiplier  $\boldsymbol{\lambda}$  to our previous energy functional, identifying the surface curve  $u^a(s)$  and the space curve  $\mathbf{Y}(s)$ . This leads to

$$E = \int_0^L ds \left\{ \mathcal{E}(\kappa_1, \kappa_2, \kappa_t) + \mathbf{F} \cdot (\mathbf{T} - \mathbf{Y}'(s)) + \boldsymbol{\lambda} \cdot (\mathbf{X}(u^1(s), u^2(s)) - \mathbf{Y}) + \frac{1}{2} \gamma_{ij} (\mathbf{f}_i \cdot \mathbf{f}_j - \delta_{ij}) + \frac{1}{2} \Gamma_{ij} (\mathbf{f}'_i(s) \cdot \mathbf{f}_j - M_{ij}) \right\}, \quad (4.41)$$

where  $\mathcal{E}$  is again a generic energy density depending only on the material curvatures and twist. Note that if the energy does not depend on twist, it is still important to distinguish whether the cross section is free or fixed, because the energy may not be symmetric in the two material curvatures  $\kappa_1$  and  $\kappa_2$ .

The stress  $\mathbf{F}$  is still determined by variation with respect to the  $\mathbf{f}_i$ , and has the same form it did in the absence of surface confinement. Similarly, the analysis leading to equations (4.24), (4.34) and (4.29) still holds. Thus  $\Gamma$  and  $\mathbf{F}$  take the same form they did for the unconfined filament, and we still find that

$$\mathcal{F}'_t = \mathcal{F}_1 \kappa_2 - \mathcal{F}_2 \kappa_1, \quad (4.42)$$

providing the Euler-Lagrange equation for the filament's cross section. However,  $\mathbf{F}$  is apparently no longer conserved. Now, the variation with respect to  $\mathbf{Y}$  gives

$$\begin{aligned} \delta_{\mathbf{Y}} E &= \int ds (-\mathbf{F} \cdot \delta \mathbf{Y}' - \boldsymbol{\lambda} \cdot \delta \mathbf{Y}) \\ &= \int ds (\mathbf{F}' - \boldsymbol{\lambda}) \cdot \delta \mathbf{Y} - [\mathbf{F} \cdot \delta \mathbf{Y}]_0^L \\ &\implies \mathbf{F}' = \boldsymbol{\lambda}. \end{aligned} \quad (4.43)$$

Thus *the surface must exert a force on the filament to maintain confinement*. From Newton's third law, we therefore conclude that the filament exerts an opposing force in equilibrium. This is the mechanism by which filaments are able to deform surfaces. Varying with respect to the coordinates of the surface curve  $u^a(s)$  leads to

$$\begin{aligned} \delta_{u^a} E &= \int ds (\boldsymbol{\lambda} \cdot \partial_a \mathbf{X} \delta u^a) \\ &\implies \boldsymbol{\lambda} \cdot \mathbf{e}_a = 0 \end{aligned} \quad (4.44)$$

where  $\mathbf{e}_a = \partial_a \mathbf{X}$  are the surface tangent vectors. Together, equations (4.43) and (4.44) imply that

$$\mathbf{F}' = \boldsymbol{\lambda} = \lambda \mathbf{n}, \quad (4.45)$$

where  $\mathbf{n}$  is the surface unit normal vector, and  $\lambda$  is the normal component of the force density. Equation (4.45) implies that the force on the filament is entirely perpendicular to the surface. Whereas for the unconfined filament equilibrium required that all forces on the filament vanish, in this case, *only the forces that are in the tangent plane of the surface must vanish*.

Since the Lagrange multipliers take the same form they did for the unconfined filament, most of our work is done. What remains is to write the Euler-Lagrange equation for the filament's centerline explicitly in terms of geometry. To do so, we must consider the projections of  $\mathbf{F}'$  onto the Darboux frame, rather than the material frame. In the Darboux basis, we see

$$\mathbf{F}' = (F'_a \mathbf{d}_a + F_a \mathbf{d}'_a) = (F'_a \mathbf{d}_a + F_a D_{ab} \mathbf{d}_b) = (F'_a - D_{ab} F_b) \mathbf{d}_a, \quad (4.46)$$

where  $\mathbf{d}_i$  are the basis vectors of the Darboux frame, so that  $\mathbf{d}_1 = \mathbf{n}$ ,  $\mathbf{d}_2 = \mathbf{L}$ ,  $\mathbf{d}_3 = \mathbf{T}$ , and  $D_{ab}$  are the components of the Darboux matrix

$$D = \begin{pmatrix} 0 & \tau_g & -\kappa_n \\ -\tau_g & 0 & -\kappa_g \\ \kappa_n & \kappa_g & 0 \end{pmatrix}. \quad (4.47)$$

Thus the Darboux frame components of the stress  $\mathbf{F}$  must satisfy

$$F'_N + \kappa_n F_T - \tau_g F_L = \lambda \quad (4.48a)$$

$$F'_L + \kappa_g F_T + \tau_g F_N = 0. \quad (4.48b)$$

$$F'_T - \kappa_n F_N - \kappa_g F_L = 0 \quad (4.48c)$$

The condition (4.48c) will turn out to be trivial; it is identically satisfied given the form of  $\mathbf{F}$ . Equation (4.48a) will give an explicit form for the force on the filament, and equation (4.48b) will be the Euler-Lagrange equation for the filament's centerline.

To calculate the transverse force density of equation (4.48b), we must write out the basis vectors  $\mathbf{n}$  and  $\mathbf{L}$  in terms of the material frame. Using the change of basis formulas

$$\mathbf{n} = \cos \phi \mathbf{f}_1 + \sin \phi \mathbf{f}_2 \quad (4.49a)$$

$$\mathbf{L} = -\sin \phi \mathbf{f}_1 + \cos \phi \mathbf{f}_2, \quad (4.49b)$$

we can write the curvatures, the  $\mathcal{F}_i$ , and the components of  $\mathbf{F}$  as

$$\kappa_n = \mathbf{T}' \cdot \mathbf{n} = \cos \phi \kappa_1 + \sin \phi \kappa_2 \quad (4.50a)$$

$$\kappa_g = \mathbf{T}' \cdot \mathbf{L} = -\sin \phi \kappa_1 + \cos \phi \kappa_2 \quad (4.50b)$$

$$\mathcal{F}_n = \frac{\partial \mathcal{E}}{\partial \kappa_n} = \cos \phi \mathcal{F}_1 + \sin \phi \mathcal{F}_2 \quad (4.50c)$$

$$\mathcal{F}_g = \frac{\partial \mathcal{E}}{\partial \kappa_g} = -\sin \phi \mathcal{F}_1 + \cos \phi \mathcal{F}_2 \quad (4.50d)$$

$$\begin{aligned} F_T &= \kappa_1 \mathcal{F}_1 + \kappa_2 \mathcal{F}_2 + \kappa_t \mathcal{F}_t - \mathcal{E} - \mathcal{H} \\ &= \kappa_g \mathcal{F}_g + \kappa_n \mathcal{F}_n + \kappa_t \mathcal{F}_t - \mathcal{E} - \mathcal{H} \end{aligned} \quad (4.50e)$$

$$F_N = \cos \phi F_1 + \sin \phi F_2 = \mathcal{F}'_n + \kappa_g \mathcal{F}_t - (\phi' + t) \mathcal{F}_g \quad (4.50f)$$

$$F_L = -\sin \phi F_1 + \cos \phi F_2 = \mathcal{F}'_g - \kappa_n \mathcal{F}_t + (\phi' + t) \mathcal{F}_n. \quad (4.50g)$$

We can simplify this by noting that

$$\tau_g = \mathbf{n}' \cdot \mathbf{L} = \phi' + \mathbf{f}'_1 \cdot \mathbf{f}_2 \cos^2 \phi - \mathbf{f}'_2 \cdot \mathbf{f}_1 \sin^2 \phi = \phi' + t. \quad (4.51)$$

Finally, we can write equations (4.48a) and (4.48b) explicitly as

$$\begin{aligned} \lambda = & \mathcal{F}_n'' + \kappa_g \mathcal{F}_t' - \tau_g \mathcal{F}_g' + \kappa_n' \mathcal{F}_t - \tau_g' \mathcal{F}_g \\ & + \kappa_n (\kappa_g \mathcal{F}_g + \kappa_n \mathcal{F}_n + \kappa_t \mathcal{F}_t - \mathcal{E} - \mathcal{H}) \\ & - \tau_g (\mathcal{F}_g' - \kappa_n \mathcal{F}_t + \tau_g \mathcal{F}_n) \end{aligned} \quad (4.52)$$

$$\begin{aligned} 0 = & \mathcal{F}_g'' - \kappa_n' \mathcal{F}_t + \tau_g' \mathcal{F}_n - \kappa_n \mathcal{F}_t' + \tau_g \mathcal{F}_n' \\ & + \kappa_g (\kappa_g \mathcal{F}_g + \kappa_n \mathcal{F}_n + \kappa_t \mathcal{F}_t - \mathcal{E} - \mathcal{H}) \\ & + \tau_g (\mathcal{F}_n' + \kappa_g \mathcal{F}_t - \tau_g \mathcal{F}_g) \end{aligned} \quad (4.53)$$

Combined with equation (4.29), we now have a complete set of differential equations describing the centerline and internal degrees of freedom of the filament. However, we do not know what boundary conditions are appropriate. This calculation will prove surprisingly subtle.

## 4.2.1 Boundary conditions

As we alluded to in the previous section, the calculation of boundary conditions is much more complicated for the confined filament. Specifically, this is because the  $\delta \mathbf{f}_i$  are no longer truly independent from  $\delta \mathbf{Y}$ : translations along the surface can create changes in the filament's material frame.

Each use of integration by parts leads in the calculation of the Euler-Lagrange equations leads to a boundary term, i.e. a term that is evaluated at the endpoints of the filament. The total boundary term, also called the *Noether current*, left over from all of our variations is

$$Q = -\mathbf{F} \cdot \delta \mathbf{Y} + \frac{1}{2} \Gamma_{ij} \delta \mathbf{f}_i \cdot \mathbf{f}_j. \quad (4.54)$$

In equilibrium,  $Q$  of course must vanish. But because  $\delta \mathbf{Y}$  and  $\delta \mathbf{f}_i$  are not linearly independent, we cannot determine the appropriate conditions when  $Q$  is in this form. After writing down  $Q$  in terms properly independent fields, we will be able to choose physical boundary conditions.

We need a total of three independent variation fields: two fields to vary the position of the filament on the surface,  $\Phi$  and  $\Psi$ , and one to vary the orientation of the filament's cross section relative to the Darboux frame,  $\delta \phi$ . We begin by writing the variation  $\delta \mathbf{Y}$  in terms of tangential and transverse variation fields

$$\delta \mathbf{Y} = \Phi \mathbf{T} + \Psi \mathbf{L}. \quad (4.55)$$

We can immediately see how this variation induces changes in  $\mathbf{T} = \mathbf{f}_3$  by differentiating  $\delta \mathbf{Y}$ . Because the variation and the arc-length derivative commute, we see

$$\delta \mathbf{T} = \delta \mathbf{Y}' = (\kappa_n \Phi - \tau_g \Psi) \mathbf{n} + (\Psi' + \kappa_g \Phi) \mathbf{L} + (\Phi' - \kappa_g \Psi) \mathbf{T}. \quad (4.56)$$

However, the magnitude of  $\mathbf{T}$  must be preserved by the variation. This implies that  $\delta(\mathbf{T} \cdot \mathbf{T}) = 2\mathbf{T} \cdot \delta \mathbf{T} = 0$ , leading to a constraint on the variation fields

$$\Phi' = \kappa_g \Psi, \quad (4.57)$$

so that

$$\delta \mathbf{T} = (\kappa_n \Phi - \tau_g \Psi) \mathbf{n} + (\Psi' + \kappa_g \Phi) \mathbf{L}. \quad (4.58)$$

Rather than determine the variations of the material frame basis vectors directly, we will first calculate the variations of the Darboux frame basis vectors. For the surface normal, we have

$$\delta \mathbf{n} = \frac{\partial \mathbf{n}}{\partial u^a} \delta u^a = -K_a^b \mathbf{e}_b \delta u^a, \quad (4.59)$$

where  $K_{ab}$  is the extrinsic curvature tensor of the surface, and we have used the Weingarten equation (2.49),  $\partial_a \mathbf{n} = -K_a^b \mathbf{e}_b$ . We can write  $\delta u^a$  in terms of  $\Phi$  and  $\Psi$  as

$$\delta u^a = \delta \mathbf{Y} \cdot \mathbf{e}^a = \Phi t^a + \Psi l^a, \quad (4.60)$$

where  $t^a$  and  $l^a$  are the components of  $\mathbf{T}$  and  $\mathbf{L}$  in the  $\mathbf{e}_a$  basis. Because  $\mathbf{T}$  and  $\mathbf{L}$  form a complete basis for the tangent plane to the surface, we can also write  $\mathbf{e}_b = t_b \mathbf{T} + l_b \mathbf{L}$ . Thus we find

$$\begin{aligned} \delta \mathbf{n} &= -K_a^b (t_b \mathbf{T} + l_b \mathbf{L}) (\Phi t^a + \Psi l^a) \\ &= -\mathbf{T} K_{ab} (t^a t^b \Phi + l^a t^b \Psi) - \mathbf{L} K_{ab} (t^a l^b \Phi + l^a l^b \Psi) \\ &= \mathbf{T} (-\kappa_n \Phi + \tau_g \Psi) + \mathbf{L} (\tau_g \Phi - (K - \kappa_n) \Psi), \end{aligned} \quad (4.61)$$

where  $K$  is the mean curvature of the surface. In the last line we have used the identities (2.52), (2.53) and the fact that  $K_{ab} l^a l^b = K_{\perp} = K - \kappa_n$ .

The fact that the basis vectors are orthogonal provides a set of identities which allows us to determine  $\delta \mathbf{L}$  from  $\delta \mathbf{T}$  and  $\delta \mathbf{n}$ :

$$\delta(\mathbf{n} \cdot \mathbf{L}) = \delta \mathbf{n} \cdot \mathbf{L} + \mathbf{n} \cdot \delta \mathbf{L} = 0 \quad (4.62a)$$

$$\delta(\mathbf{T} \cdot \mathbf{L}) = \delta \mathbf{T} \cdot \mathbf{L} + \mathbf{T} \cdot \delta \mathbf{L} = 0, \quad (4.62b)$$

so that

$$\delta \mathbf{L} = -\mathbf{T} (\delta \mathbf{T} \cdot \mathbf{L}) - \mathbf{n} (\delta \mathbf{n} \cdot \mathbf{L}) = -\mathbf{T} (\Psi' + \kappa_g \Phi) + \mathbf{n} (-\tau_g \Phi + (K - \kappa_n) \Psi). \quad (4.63)$$

Combining equations (4.49a) and (4.49b), we can write  $\mathbf{f}_1$  and  $\mathbf{f}_2$  in the Darboux basis,

$$\mathbf{f}_1 = \cos \phi \mathbf{n} - \sin \phi \mathbf{L}, \quad (4.64a)$$

$$\mathbf{f}_2 = \sin \phi \mathbf{n} + \cos \phi \mathbf{L}, \quad (4.64b)$$

leading to

$$\begin{aligned} \delta \mathbf{f}_1 \cdot \mathbf{f}_2 &= -\delta \phi + \cos^2 \phi \delta \mathbf{n} \cdot \mathbf{L} - \sin^2 \phi \delta \mathbf{L} \cdot \mathbf{n} \\ &= -\delta \phi + \tau_g \Phi - (K - \kappa_n) \Psi. \end{aligned} \quad (4.65)$$

We now have all the ingredients to express equation (4.54) in terms of properly distinct variation fields. We find

$$\begin{aligned} Q &= \Phi (-F_T + \mathcal{F}_n \kappa_n + \mathcal{F}_t \tau_g) + \Psi (-F_L + \mathcal{F}_g \kappa_g + \mathcal{F}_t (K - \kappa_n) - \mathcal{F}_n \tau_g) + \Psi' \mathcal{F}_g - \delta \phi \mathcal{F}_t \\ &= \Phi (-\mathcal{F}_g \kappa_g + \mathcal{H} + \mathcal{E}) - \Psi (\mathcal{F}'_g - \mathcal{F}_g \kappa_g + \mathcal{F}_t (K - 2\kappa_n) + 2\mathcal{F}_n \tau_g) + \Psi' \mathcal{F}_g - \delta \phi \mathcal{F}_t. \end{aligned} \quad (4.66)$$

The possible range of boundary conditions is summarized in table 4.1.

$\Phi = 0$	Tangential coordinate fixed	$-\mathcal{F}_g \kappa_g + \mathcal{H} + \mathcal{E} = 0$
$\Psi = 0$	Transverse coordinate fixed	$\mathcal{F}'_g - \mathcal{F}_g \kappa_g + \mathcal{F}_t (K - 2\kappa_n) + 2\mathcal{F}_n \tau_g = 0$
$\Psi' = 0$	Tangent vector fixed	$\mathcal{F}_g = 0$
$\delta\phi = 0$	Cross section fixed	$\mathcal{F}_t = 0$
$\delta L = 0$	Total length fixed	$\mathcal{H} = 0$

**Table 4.1:** At each endpoint ( $s = 0$  and  $s = L$ ), one boundary condition must be chosen from every row.

Consider a filament with completely free endpoints. That is, the location of the endpoints, the direction the filament is pointing, and the orientation of the filament's cross section are all unconstrained. This implies that  $\Phi$ ,  $\Psi$ ,  $\Psi'$ , and  $\delta\phi$  are all arbitrary. Thus, in order for the boundary term to vanish, the coefficients on the variation fields must be zero, so that

$$\mathcal{H} + \mathcal{E}|_{\text{endpoints}} = 0 \quad (4.67a)$$

$$\mathcal{F}'_g + 2\mathcal{F}_n \tau_g = 0 \quad (4.67b)$$

$$\mathcal{F}_g = 0 \quad (4.67c)$$

$$\mathcal{F}_t = 0. \quad (4.67d)$$

The last two of these has a natural physical interpretation in terms of the bending moment  $\mathbf{S}$ . Because  $\mathcal{F}_g$  is the component of the bending moment  $\mathbf{S}$  along the normal vector  $\mathbf{n}$ , the tangent  $\mathbf{T}$  is free to rotate about the normal when it vanishes. Because  $\mathcal{F}_t$  is the component of  $\mathbf{S}$  along the tangent vector  $\mathbf{T}$ , the cross section is free to rotate about  $\mathbf{T}$  when it vanishes.

Equation (4.66) offers an opportunity make a few useful interpretations. First,  $\Phi$  is the field corresponding to moving the endpoint of the filament along its tangent vector. We therefore see that the cost of moving the end of the filament along itself is  $\mathcal{H} + \mathcal{E}$ . The field  $\Psi'$  corresponds to varying the direction of the tangent vector within the tangent plane of the surface; therefore  $\mathcal{F}_g$  is the torque associated with that rotation. Lastly, because it couples directly to  $\delta\phi$ , we identify  $\mathcal{F}_t$  as the torque associated with rotating the filament's cross section.

## Length variation

In many biological systems, including dynamin, the filaments we are interested in actually freely polymerize on the surface of interest. This contrasts from the description we have given above, in which the length of the polymer is fixed. We should therefore consider  $L$  as a variable that can be varied just like the filament's overall configuration, effectively changing from the fixed  $L$  ensemble to a fixed chemical potential ensemble. Variations that change the overall interval of the arc-length  $s$  (or, in a classical mechanical Lagrangian system, the time  $t$ ) are called  $\Delta$ -variations; we follow the discussion presented in Goldstein's Classical Mechanics textbook [GPS02].

We consider a variation as in the above section, with  $\mathbf{Y} \mapsto \mathbf{Y} + \delta\mathbf{Y}$ ,  $\mathbf{f}_i \mapsto \mathbf{f}_i + \delta\mathbf{f}_i$ , but with the additional variation  $L \mapsto L + \delta L$ . Assuming that the Euler-

Lagrange conditions hold, the change in energy is

$$\begin{aligned}\delta E &= \int_0^{L+\delta L} ds \mathcal{E} - \int_0^L ds \mathcal{E} \\ &= \delta L \mathcal{E}|_{s=L} + \left[ -\mathbf{F} \cdot \delta \mathbf{Y} + \frac{1}{2} \Gamma_{ij} \delta \mathbf{f}_i \cdot \mathbf{f}_j \right]_{s=L}.\end{aligned}\quad (4.68)$$

The terms  $\delta \mathbf{Y}$  and  $\delta \mathbf{f}_i$  are evaluated at the original arc-length endpoints of the filament. But we need the variations at the *new* endpoints; we call these variation fields  $\Delta \mathbf{Y}$  and  $\Delta \mathbf{f}_i$ . To find these variations, we must include the change in the coordinates induced by the extension of the filament

$$\Delta \mathbf{Y} = \delta \mathbf{Y} + \delta L \mathbf{Y}' = \delta \mathbf{Y} + \mathbf{T} \delta L \quad (4.69)$$

$$\Delta \mathbf{f}_i = \delta \mathbf{f}_i + \delta L \mathbf{f}'_i = \delta \mathbf{f}_i + M_{ij} \mathbf{f}_j \delta L. \quad (4.70)$$

Inserting this into our expression for the total change in energy, we see

$$\delta E = -\mathbf{F} \cdot \Delta \mathbf{Y} + \frac{1}{2} \Gamma_{ij} \Delta \mathbf{f}_i \cdot \mathbf{f}_j - \delta L \left( -\mathcal{E} - \mathbf{F} \cdot \mathbf{T} + \frac{1}{2} \Gamma_{ij} M_{ij} \right). \quad (4.71)$$

The first two terms in this equation are analogous to the boundary terms considered above in this section. The term in parentheses represents the cost of additional polymerization: it is identically the Hamiltonian calculated in (4.34)! If we want the filament to be in equilibrium with respect to overall changes in its length, we therefore must require that the Hamiltonian vanish. Thus, for filaments with variable length, the boundary conditions calculated above must be augmented to include

$$\mathcal{H} = 0. \quad (4.72)$$

We can also consider adding a term to the energy

$$E_L = - \int_0^L ds \mu, \quad (4.73)$$

where  $\mu$  is a constant force driving polymerization of the filament onto the surface. Because it is a constant, it changes none of the Euler-Lagrange equations; however, it changes the boundary conditions in that the Hamiltonian should satisfy  $\mathcal{H} = -\mu$  rather than vanishing.

### 4.3 Surface confinement with fixed cross section

What if the material frame of the filament is constrained to make a fixed angle with the surface? As we discussed above, this would be the case if the filament's binding to the surface is localized to one "sticky side" of the filament, for instance in the PH domain of dynamin. An illustration of this idea is shown in figure 4.3.

In general, the cross sectional orientation relative to the surface is a third source of anisotropy for the filament (in addition to the eigenvectors of the inertia tensor and the direction of the spontaneous curvature). In general, these symmetry breaking effects need not align, so that a filament whose energy functional is diagonal in the material frame may not be so in the Darboux frame.

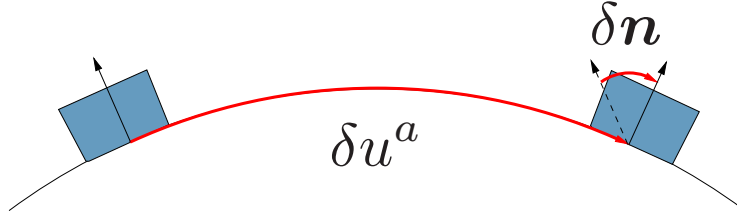


**Figure 4.3:** The blue polygons represent material cross-sections of a surface confined filament before and after a small translation  $\delta u^a$ . After the translation, a rotation of the material frame by  $\delta \mathbf{n}$  is necessary.

We assume that the constraint fixes the angle  $\phi$  between the material and Darboux frames to a constant value along the entire filament. Then, the material curvatures are given by

$$\kappa_1 = \kappa_n \cos \phi - \kappa_g \sin \phi \quad (4.74)$$

$$\kappa_2 = \kappa_n \sin \phi + \kappa_g \cos \phi \quad (4.75)$$

$$\kappa_t = \tau_g. \quad (4.76)$$

Only in the special case when  $\phi = 0$  are the material curvatures equivalent to their Darboux analogues. However, recall that the material frame can be chosen however we like: the only reason to make any particular selection is so as to diagonalize the inertia tensor  $I_{ij}$ . But since we write the energy density as an unspecified function of the material curvatures in twist in this section, we are free to redefine the material frame by rotating it by a constant  $\phi$ . Then, we can identify one component of the material frame, say  $\mathbf{m}_1$ , with the surface normal vector  $\mathbf{n}$ .

Regardless of what value it takes, when the angle  $\phi$  is constant, the material curvatures  $\kappa_1$  and  $\kappa_2$  can be written as functions of the Darboux curvatures. We can therefore write the energy density  $\mathcal{E}$  as depending only on the Darboux curvatures. To enforce the constraint, we amend the energy in equation (4.41) with a term ensuring that the material frame vector  $\mathbf{m}_1$  points along the surface normal vector  $\mathbf{n}$ . The energy becomes

$$E = \int_0^L ds \left\{ \mathcal{E}(\kappa_n, \kappa_g, \tau_g) + \mathbf{F} \cdot (\mathbf{T} - \mathbf{Y}'(s)) + \boldsymbol{\lambda} \cdot (\mathbf{X}(u^1(s), u^2(s)) - \mathbf{Y}) \right. \\ \left. - \mathbf{m} (\mathbf{f}_1(s) - \mathbf{n}(u^1(s), u^2(s))) + \frac{1}{2} \Lambda_{ij} (\mathbf{d}_i \cdot \mathbf{d}_j - \delta_{ij}) + \frac{1}{2} \Delta_{ij} (\mathbf{d}'_i(s) \cdot \mathbf{f}_j - D_{ij}) \right\}, \quad (4.77)$$

where the  $\mathbf{f}_i$  are the basis vectors of the material frame, and  $D_{ij}$  are the components of the Darboux matrix, given in equation (4.47). After the identification with the Darboux frame, the material frame vectors become  $\mathbf{f}_1 = \mathbf{n}$ ,  $\mathbf{f}_2 = \mathbf{L}$ ,  $\mathbf{f}_3 = \mathbf{T}$ . Because the constraints they enforce possess these symmetries, we assume without loss of generality that  $\Delta_{ij}$  is antisymmetric and that  $\Lambda_{ij}$  is symmetric. Note that  $\mathbf{m}$  has three components, but really only constrains two degrees of freedom: the fact that  $\mathbf{n}$  is a unit vector is enforced elsewhere.

Varying with respect to  $\mathbf{Y}$ , we again find that

$$\mathbf{F}' = \boldsymbol{\lambda}. \quad (4.78)$$

However, varying with respect to  $u^a$  gives a significantly different result because of the  $\mathbf{n}$  term:

$$\boldsymbol{\lambda} \cdot \mathbf{e}_a + K_a^b \mathbf{m} \cdot \mathbf{e}_b = \lambda_a + K_a^b m_b = 0, \quad (4.79)$$

where we have again used the Weingarten equations (2.49) to rewrite  $\partial_a \mathbf{n} = K_a^b \mathbf{e}_b$ .

In this case, we see that the local force applied to the filament is not purely along the surface normal. It also has components in the surface's tangent plane. In light of our physical interpretation of the Euler-Lagrange equation for the filament with a free cross section, this seems strange. We might expect that the transverse force on the filament should still vanish at every point. The reason it does not is that *by fixing the cross section relative to the surface normal, we have coupled translations of the filament to rotations of its cross section*. Thus the force on the filament can now be balanced by the filament's bending moment.

Although  $\boldsymbol{\lambda}$  now has components tangential to the surface, the component along the tangent to *the filament*,  $\boldsymbol{\lambda} \cdot \mathbf{T}$ , still must vanish because the energy density remains arc-length-independent. The vanishing of  $\boldsymbol{\lambda} \cdot \mathbf{T}$  is equivalent to the conservation of the Hamiltonian  $\mathcal{H}$ . Projecting equation (4.79) onto the tangent vector,

$$\lambda_T = t^a \lambda_a = -t^a K_a^b \mathbf{m} \cdot \mathbf{e}_b = 0. \quad (4.80)$$

We can then insert  $\mathbf{m} = m_T \mathbf{T} + m_N \mathbf{N} + m_L \mathbf{L}$ , leading to

$$-t^a K_{ab} (m_T \kappa_t^b + m_L l^b) = -\kappa_n m_T + \tau_g m_L = 0, \quad (4.81)$$

where we again used the identities in equations (2.52) and (2.53).

The transverse projection of the external force gives

$$\begin{aligned} \lambda_L = l^a \lambda_a &= -K_{ab} (m_T l^a t^b + m_L l^a l^b) \\ &= (\tau_g^2 - \kappa_n (K - \kappa_n)) \frac{m_L}{\kappa_n}, \end{aligned} \quad (4.82)$$

where we have again used the identities (2.52) and (2.53). We can simplify this further using the following identity for the surface's Gaussian curvature  $K_G$ ,

$$K_G = \kappa_n (K - \kappa_n) - \tau_g^2, \quad (4.83)$$

which follows from writing  $K_{ab}$  in the  $t^a$  and  $l^a$  basis and evaluating the determinant. Therefore, the Euler-Lagrange equation in the fixed cross section case is given by

$$\mathbf{F}' \cdot \mathbf{L} = -\frac{K_G m_L}{\kappa_n}. \quad (4.84)$$

In the free cross section case, the transverse force on the filament  $\lambda_L$  had to vanish. Here, it is not zero, but instead is balanced by a torque  $m_L$ , with lever arm  $\kappa_n/K_G$ .

The procedure for determining the Lagrange multipliers is very similar to that of the previous sections. We simply need to obtain the components of  $\mathbf{F}$  and  $\mathbf{m}$  in the Darboux frame basis. Varying with respect to the curvatures and geodesic torsion, we find

$$0 = \frac{\partial \mathcal{E}}{\partial \kappa_n} + \Delta_{13} \quad (4.85)$$

$$0 = \frac{\partial \mathcal{E}}{\partial \kappa_g} + \Delta_{23} \quad (4.86)$$

$$0 = \frac{\partial \mathcal{E}}{\partial \tau_g} - \Delta_{12}. \quad (4.87)$$

implying

$$\Delta = \begin{pmatrix} 0 & \mathcal{F}_t & -\mathcal{F}_n \\ -\mathcal{F}_t & 0 & -\mathcal{F}_g \\ \mathcal{F}_n & \mathcal{F}_g & 0 \end{pmatrix}, \quad (4.88)$$

where  $\mathcal{F}_n = \partial\mathcal{E}/\partial\kappa_n$ ,  $\mathcal{F}_g = \partial\mathcal{E}/\partial\kappa_g$  and  $\mathcal{F}_t = \partial\mathcal{E}/\partial\tau_g$ . Varying with respect to the material frame basis vectors  $\mathbf{f}_i$ , we find

$$0 = m_j\delta_{i1} + F_j\delta_{i3} + \Lambda_{ij} - \left( \frac{1}{2}\Delta'_{ij} + \Delta_{ik}D_{kj} \right). \quad (4.89)$$

As in section 4.1.2, the unusual terms  $\delta_{i1}$  and  $\delta_{i3}$  emerge from the fact that  $\mathbf{m}$  and  $\mathbf{F}$  only couple to  $\mathbf{f}_1$  and  $\mathbf{f}_3$ , respectively. Again, we consider the individual components of this  $3 \times 3$  matrix equation, as we did solving equation (4.25). We find that

$$m_L = \mathcal{F}'_t - \kappa_g\mathcal{F}_n + \kappa_n\mathcal{F}_g \quad (4.90)$$

$$F_N = \mathcal{F}'_n + \kappa_g\mathcal{F}_t + \frac{\tau_g}{\kappa_n}(\mathcal{F}'_t - \kappa_g\mathcal{F}_n) \quad (4.91)$$

$$F_L = \mathcal{F}'_g + \tau_g\mathcal{F}_n - \kappa_n\mathcal{F}_t. \quad (4.92)$$

Interestingly, it is not possible to solve these equations for  $m_N$ . This is a consequence of using a three-dimensional Lagrange multiplier to constrain two degrees of freedom, as discussed above. However,  $m_N$  does not appear in the Euler-Lagrange equations or boundary conditions, and therefore physically irrelevant.

It is also interesting to compare equation (4.90) with equation (4.29). After expressing equation (4.29) in the Darboux frame basis, it turns out that the Lagrange multiplier  $m_L = \mathbf{S}' \cdot \mathbf{T} = 0$  is the condition for the filament's cross section to be relaxed! We can therefore interpret  $m_L$  as the local torque per unit length due to twisting the filament about its axis.

We again find  $F_T$  through the filament's Hamiltonian. In this case,

$$F_T = \kappa_g\mathcal{F}_g + \kappa_n\mathcal{F}_n + \tau_g\mathcal{F}_t - \mathcal{E} - \mathcal{H}. \quad (4.93)$$

Note that the tangential components of the stress  $F_T$  and  $F_L$  are not altered by constraining the filament's cross section. This will be useful in our discussion of boundary conditions. We now have all the ingredients necessary to express the Euler-Lagrange equations in terms of geometric quantities:

$$\begin{aligned} -\frac{K_G}{\kappa_n}(\mathcal{F}'_t - \mathcal{F}_n\kappa_g + \mathcal{F}_g\kappa_n) &= \mathcal{F}''_g - \kappa'_n\mathcal{F}_t + \tau'_g\mathcal{F}_n - \kappa_n\mathcal{F}'_t + \tau_g\mathcal{F}'_n \\ &+ \kappa_g(\kappa_g\mathcal{F}_g + \kappa_n\mathcal{F}_n + \tau_g\mathcal{F}_t - \mathcal{E} - \mathcal{H}) \\ &+ \tau_g(\mathcal{F}'_n + \mathcal{F}_t\kappa_g + \frac{\tau_g}{\kappa_n}(\mathcal{F}'_t - \kappa_g\mathcal{F}_n)). \end{aligned} \quad (4.94)$$

The normal component of the force on the filament is given by

$$\begin{aligned} \lambda_N &= \left( \mathcal{F}'_n + \kappa_g\mathcal{F}_t + \frac{\tau_g}{\kappa_n}(\mathcal{F}'_t - \kappa_g\mathcal{F}_n) \right)' \\ &+ \kappa_n(\kappa_g\mathcal{F}_g + \kappa_n\mathcal{F}_n + \tau_g\mathcal{F}_t - \mathcal{E} - \mathcal{H}) - \tau_g(\mathcal{F}'_g + \tau_g\mathcal{F}_n - \kappa_n\mathcal{F}_t). \end{aligned} \quad (4.95)$$

$\Phi = 0$	Tangential coordinate fixed	$-\mathcal{F}_g \kappa_g + \mathcal{H} + \mathcal{E} = 0$
$\Psi = 0$	Transverse coordinate fixed	$\mathcal{F}'_g - \mathcal{F}_g \kappa_g + \mathcal{F}_t(K - 2\kappa_n) + 2\mathcal{F}_n \tau_g = 0$
$\Psi' = 0$	Tangent vector fixed	$\mathcal{F}_g = 0$
$\delta L = 0$	Total length fixed	$\mathcal{H} = 0$

**Table 4.2:** At each endpoint of the filament, a boundary condition must be chosen from every row.

### 4.3.1 Boundary conditions

The procedure for calculating the boundary conditions for filaments with fixed cross sections is nearly identical to that of the filaments with free cross sections at every step. The only difference is that the field varying the cross section orientation is not introduced—for obvious reasons. Because of this significant similarity, many steps in this calculation will be skipped.

The Noether charge is given by

$$Q = -\mathbf{F} \cdot \delta \mathbf{Y} + \frac{1}{2} \Delta_{ij} \delta \mathbf{f}_i \cdot \mathbf{f}_j. \quad (4.96)$$

Again, we vary  $\mathbf{Y}$  by introducing tangential and transverse variation fields,  $\delta \mathbf{Y} = \Phi \mathbf{T} + \Psi \mathbf{L}$ . Recall our earlier remark that the projections of the filament stress  $\mathbf{F}$  onto the tangent vector  $\mathbf{T}$  and transverse vector  $\mathbf{L}$  are unchanged by constraining the filament's cross section. Since the normal component of  $\mathbf{F}$  does not contribute to the Noether charge, the entire  $\mathbf{F} \cdot \delta \mathbf{Y}$  term is also unchanged from the free cross section case.

Because we already know  $\Delta_{ij}$  and  $\delta \mathbf{f}_i \cdot \mathbf{f}_j$ , we are now ready to write down the Noether charge in terms of our independent variation fields  $\Phi$  and  $\Psi$ , finding

$$Q = \Phi(-\mathcal{F}_g \kappa_g + \mathcal{H} + \mathcal{E}) - \Psi(\mathcal{F}'_g - \mathcal{F}_g \kappa_g + \mathcal{F}_t(K - 2\kappa_n) + 2\mathcal{F}_n \tau_g) + \Psi' \mathcal{F}_g, \quad (4.97)$$

that is,  $Q$  is identical to the free cross section case in equation (4.66), except for the missing  $-\delta \phi \mathcal{F}_t$  term corresponding to the variation of the cross section. Thus, for a filament with totally free endpoints,

$$\mathcal{H} + \mathcal{E}|_{\text{endpoints}} = 0 \quad (4.98)$$

$$\mathcal{F}'_g = \mathcal{F}_t(2\kappa_n - K) - 2\mathcal{F}_n \tau_g \quad (4.99)$$

$$\mathcal{F}_g = 0. \quad (4.100)$$

The full set of possible boundary conditions is summarized in table 4.2.

If we want to allow the filament's overall length to vary, the derivation from section 4.2.1 still applies. Again, we augment the boundary conditions with the requirement that  $\mathcal{H} = 0$ , or, if there is a non-zero polymerization force,

$$\mathcal{H} = -\mu. \quad (4.101)$$

## 4.4 Surface symmetries

In section 4.1 we found that the vectors  $\mathbf{F}$  and  $\mathbf{M}$  are conserved for an elastic filament that is not confined to a surface. These conservation laws are a result of

the translational and rotational symmetry of Euclidean space. When a filament is confined to a surface, this symmetry is in general broken. However, if the surface possesses its own symmetries, there will be corresponding conservation laws. Reference [GVVM14] includes a discussion of such laws.

For surfaces with translational symmetry, a uniform translation along the symmetry direction does not change the geometry of the filament at all. Obvious examples of surfaces with translational symmetry include the cylinder (which is symmetric with respect to translations along its axis), the plane (which is symmetric with respect to translations along any of its own tangent vectors), and the buckled membranes discussed in section 3.1 (which are symmetric under translation along the ridges). A uniform translation along the symmetry direction obviously does not change the shape of the filament, and hence does not change its energy. Noether's theorem tells us that if a system is invariant under a certain transformation, then the momentum conjugate to the coordinate representing that transformation is invariant [GPS02]. We have already seen that the momentum conjugate to  $\mathbf{Y}$  is  $\mathbf{P}_Y = -\mathbf{F}$ . Let us assume the surface is symmetric under translations along the  $z$ -axis. Then,

$$(\mathbf{F} \cdot \hat{\mathbf{z}})' = F'_z = 0. \quad (4.102)$$

This equation states that the stress along the direction of symmetry is conserved. For the cylinder, this means that the stress along the cylindrical axis is conserved. For the plane, it means that the stress in any tangential direction is conserved. Recall that the membrane buckles studied in section 3.1 were equivalent to planar elastic rods. This fact implies that the  $\hat{\mathbf{z}}$  and  $\hat{\mathbf{x}}$  components of the membrane stress are conserved in that system.

The other primary transformations of interest are rotations. Again, we have already calculated the momentum conjugate to rotation of the filament. It is the torque,

$$\mathbf{M} = \mathbf{Y} \times \mathbf{F} + \mathbf{S}, \quad (4.103)$$

where

$$\mathbf{S} = \mathcal{F}_t \mathbf{T} - \mathcal{F}_2 \mathbf{m}_1 + \mathcal{F}_1 \mathbf{m}_2 \quad (4.104)$$

$$= \mathcal{F}_t \mathbf{T} - \mathcal{F}_g \mathbf{N} + \mathcal{F}_n \mathbf{L}. \quad (4.105)$$

For example, consider a surface that is symmetric under rotations around the  $z$ -axis, such as the catenoid or the cylinder. Then Noether's theorem implies

$$(\mathbf{M} \cdot \hat{\mathbf{z}})' = M'_z = 0. \quad (4.106)$$

Just as the components of  $\mathbf{F}$  along directions of translational symmetry are conserved, the components of  $\mathbf{M}$  along axes of rotational symmetry are conserved. This is especially interesting on the sphere: since every axis is an axis of rotational symmetry, we recover the full rotational symmetry of Euclidean space, so that  $\mathbf{M}' = 0$  [GVM12].

# Chapter 5

## Surface-bound elastic filaments: applications

In this chapter, we will apply the findings of Chapter 4 to specific systems. In the first section, we consider one of the simplest possible cases of confinement of rods: the Bernoulli-Euler rod confined to a cylinder. This investigation will illustrate the rich mathematical structure that emerges in surface-confined rods. This work was published in reference [VMMDG15]. In the second section, we will consider the confinement of Kirchhoff rods to both cylinders and catenoids, with an eye towards modeling dynamin from the perspective of a flexible polymerizing filament. This work was published in reference [MVMGD16].

### 5.1 Bernoulli-Euler rods on cylinders

Analyzing the physical situation of the Bernoulli-Euler rod confined to the surface of a cylinder will illustrate the surprising complexity that surface bound elastic filaments can exhibit, especially with regards to the force density  $\lambda$  transmitted to the surface. Luckily, the symmetries of the cylinder make many calculations solvable analytically. We will focus on the shapes of filaments in equilibrium and the force that they exert on the surface.

Recall that for Bernoulli-Euler rods, the energy is given by

$$E = \int ds \frac{\alpha}{2} \kappa^2, \quad (5.1)$$

where  $\kappa$  is the Frenet curvature. Because it is the only energy scale present in this section, we will take  $\alpha = 1$  throughout what follows.

As we discussed in Chapter 4, in general, the appropriate conditions for equilibrium of the filament depend on whether we regard the cross section of the filament to be fixed relative to the surface. For filaments with freely rotating cross sections, equilibrium is achieved when the transverse force on the filament vanishes (equation (4.53)) and the twisting moment of the filament vanishes (equation (4.29)). For those with fixed cross sections, the twisting moment and transverse force become coupled, leaving only a single equilibrium condition given by equation (4.94). However, in the special case of the Bernoulli-Euler rod, we do not need to make the distinction between fixed and free cross sections. This equivalence holds only when two conditions are satisfied simultaneously. Firstly, the filament must be symmetric

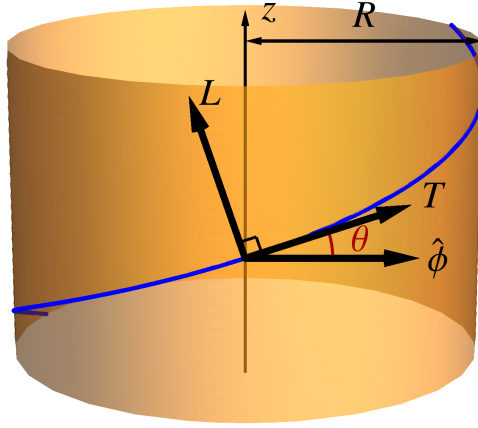


**Figure 5.1:** Illustration of parameters for cylindrically bound filaments.

under rotations of its cross section. Secondly, the energy must not punish twisting of the filament.

Let us write the energy in terms of the geodesic and normal curvatures as

$$E = \int ds \frac{\kappa_g^2 + \kappa_n^2}{2}. \quad (5.2)$$

The moments of the filament are therefore

$$\mathcal{F}_g = \frac{\partial \mathcal{E}}{\partial \kappa_g} = \kappa_g \quad (5.3a)$$

$$\mathcal{F}_n = \frac{\partial \mathcal{E}}{\partial \kappa_n} = \kappa_n \quad (5.3b)$$

$$\mathcal{F}_t = \frac{\partial \mathcal{E}}{\partial \tau_g} = 0 \quad (5.3c)$$

Inserting these into equation (4.53) or (4.94), the condition for mechanical equilibrium is given explicitly in terms of the geometry of the filament by

$$\kappa_g'' + \tau_g' \kappa_n + 2\tau_g \kappa_n' + \kappa_g \left( \frac{\kappa_g^2 + \kappa_n^2}{2} - \tau_g^2 - \mathcal{H} \right) = 0, \quad (5.4)$$

where a prime denotes differentiation with respect to arc-length. Using equation (4.52) or equation (4.95), the local normal force density exerted on the surface is given by

$$\lambda = \kappa_n'' - 2\tau_g \kappa_g' - \tau_g' \kappa_g + \kappa_n \left( \frac{\kappa_g^2 + \kappa_n^2}{2} - \tau_g^2 - \mathcal{H} \right). \quad (5.5)$$

On the cylinder, the geodesic curvature, normal curvature, and geodesic torsion are given by

$$\kappa_g = \theta', \quad (5.6a)$$

$$\kappa_n = \frac{\cos^2 \theta}{R}, \quad (5.6b)$$

$$\tau_g = \frac{\sin(2\theta)}{2R}, \quad (5.6c)$$

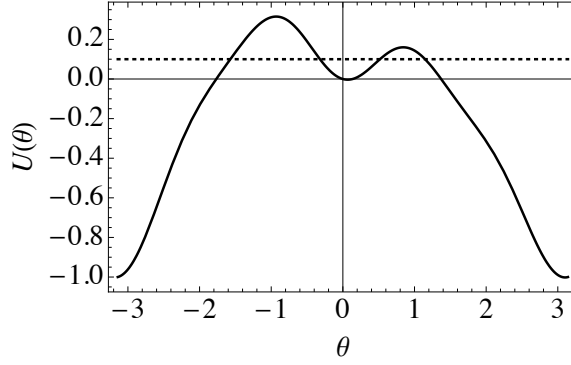


**Figure 5.2:** Illustration of the “particle in a potential” analogy. The role of the potential is played by  $U(\theta)$  (solid line), and the role of the total energy is played by  $\mathcal{H}$  (dotted line). In this case,  $f = 0.1$ ,  $m = -0.5$ ,  $\mathcal{H} = 0.1$ .

where  $\theta$  is the angle between the filament’s tangent vector  $\mathbf{T}$  and the local horizontal, and  $R$  is the radius of the cylinder.

Let us parametrize the surface with the usual cylindrical coordinates,  $\phi$  and  $z$ . With our definition of  $\theta$ , the coordinates of the filament satisfy

$$R\phi'(s) = \cos \theta, \quad z'(s) = \sin \theta, \quad (5.7)$$

The tangent vector is thus manifestly unit magnitude,  $|\mathbf{T}| = 1$ . Since it is the only length scale present in this problem, we can simply take  $R = 1$  in what follows. Doing so, and inserting equations (5.6a)-(5.6c), equation (5.4) becomes

$$0 = \theta' \frac{\theta'^2 - 3 \sin^2(2\theta) + 3 \cos^4 \theta - 2\mathcal{H}}{2} + \theta^{(3)}, \quad (5.8)$$

where  $\theta^{(3)}$  denotes the third derivative of  $\theta$  with respect to  $s$ .

Recall from Chapter 4.4 that surface confined filaments possess conserved quantities associated with translational and rotational symmetry of the surface [VMMDG15, GVVM14], both of which are present on the cylinder. Associated with the rotational symmetry, the torque  $m$  along the  $z$ -axis is conserved,

$$m = \mathbf{M} \cdot v\hat{s}z = \frac{1}{2} \cos \theta (-2\mathcal{H} - \cos^4 \theta + \theta'^2) - \sin \theta (2 \sin \theta \cos^3 \theta + \theta''). \quad (5.9)$$

Indeed, differentiating this equation and using  $m' = 0$ , we recover equation (5.4) with an overall pre-factor of  $\sin \theta$ . Similarly, the translational symmetry of the cylinder implies that the stress  $f$  along the  $z$ -axis is conserved,

$$f = \mathbf{F} \cdot v\hat{s}z = \frac{1}{2} \sin \theta (-2\mathcal{H} - \cos^4 \theta + \theta'^2) + \cos \theta (2 \sin \theta \cos^3 \theta + \theta''). \quad (5.10)$$

Again, by differentiating this equation and using  $f' = 0$ , we recover equation (5.4), this time with an overall pre-factor of  $\cos \theta$ .

We can take a linear combination of these constants to cancel the  $\theta''$  terms, leading to

$$f \sin \theta + m \cos \theta = \frac{1}{2} \theta'^2 - \frac{\cos^4 \theta}{2} - \mathcal{H}. \quad (5.11)$$

$\delta \mathbf{Y} \cdot \mathbf{T} = 0$	Tangential coordinate fixed	$\mathcal{H} + (\kappa_n^2 - \kappa_g^2)/2 = 0$
$\delta \mathbf{Y} \cdot \mathbf{L} = 0$	Transverse coordinate fixed	$\kappa_g' - \kappa_g^2 + 2\kappa_n \tau_g = 0$
$\delta \theta = 0$	Tangent vector fixed	$\kappa_g = 0$
$\delta L = 0$	Total length fixed	$\mathcal{H} = -\mu$

**Table 5.1:** At each endpoint of the filament, one boundary condition must be chosen from every row.

We have now reduced the problem to that of a particle in a potential with energy  $\mathcal{H}$  and position  $\theta$ , where the potential energy is given by

$$U(\theta) = -\frac{\cos^4 \theta}{2} - f \sin \theta - m \cos \theta. \quad (5.12)$$

An illustration of this idea is shown in figure 5.2. Note that only the  $f \sin \theta$  term breaks  $\theta \mapsto -\theta$  symmetry.

Equation (5.11) can of course be solved by separation of variables, just as we did for the buckled membranes in section 3.1. In this case, the quadrature is given by

$$s = \int d\theta \frac{1}{\sqrt{2(\mathcal{H} - U(\theta))}}. \quad (5.13)$$

We will only be able to evaluate the integral on the right hand side in special cases.

With equation (5.11), we can eliminate the derivatives of  $\theta$  from the equation for  $\lambda$  (5.5), so that  $\lambda$  becomes a function of only  $\theta$  and the constants  $f$ ,  $m$ , and  $\mathcal{H}$ :

$$\lambda = \frac{1}{8} [14f \sin \theta - 18f \sin(3\theta) - 2m(5 \cos \theta + 9 \cos(3\theta)) - 9 \cos(4\theta) - 3 \cos(6\theta) - (64\mathcal{H} + 9) \cos(2\theta) - 3]. \quad (5.14)$$

With this information, we can begin to solve the Euler-Lagrange equations for the filament in detail. But first, we will need to establish the appropriate boundary conditions.

### 5.1.1 Boundary conditions

In Chapter 4, we found that for a filament with endpoints that are free to rotate and slide along the surface, the appropriate boundary conditions are

$$\kappa_g = 0 \quad (5.15)$$

$$\mathcal{H} + \mathcal{E} = \mathcal{H} + \frac{\cos^4 \theta}{2} = 0 \quad (5.16)$$

$$\mathcal{F}_g' = \mathcal{F}_t(2\kappa_n - K) - 2\mathcal{F}_n \tau_g \implies \theta'' = -2 \cos^3 \theta \sin \theta, \quad (5.17)$$

where  $\mathcal{E} = (\kappa_g^2 + \kappa_n^2)/2$  is the energy density. Comparing these conditions with equations (5.9) and (5.10), we see that  $f = m = 0$  for free filaments. We will consider this case in more detail later. If we want to go from a fixed length ensemble to one in which the filament is free to polymerize, we would amend these equations to include

$$\mathcal{H} = -\mu, \quad (5.18)$$

where  $\mu$  is a constant force driving the polymerization of the filament.

Removing any degree of freedom at the endpoints requires removing one of the above boundary conditions. The full set of possible boundary conditions is summarized in Table 5.1. If we want to consider a filament with fixed endpoints, so that the curve goes from a point  $(\phi_1, z_1)$  to a point  $(\phi_2, z_2)$ , then we would not enforce boundary conditions (5.16) and (5.17). We can also consider a filament with *clamped* endpoints, so that the value of  $\theta$  is also fixed at the ends; then we would not enforce condition (5.15). For the sake of definiteness, we focus on filaments with free endpoints.

Another interesting possibility is that the filament is closed. This is mathematically equivalent to requiring that the filament begin and end at the same point with the same tangent vector. We will see that the mechanical behavior of closed filaments depends strongly on topological considerations, namely how many times the filament winds around the cylinder.

### 5.1.2 Free endpoints

Naïvely, we may think that the behavior of a filament with totally free endpoints is obvious: it should simply lie along a meridian of the surface, in which case it has exactly zero energy. While this is obviously the ground state (i.e. the lowest energy state), there is actually a whole family of solutions parameterized by the constant stress  $\mathcal{H}$ . Only in the case  $\mathcal{H} = 0$  does the filament lie along a meridian. On the other hand, when  $\mathcal{H} = -1/2$ , the filament lies along a ring with  $\theta = 0$ . Between these cases, the filament takes a trajectory on the cylinder over which the angle  $\theta$  is not constant. While in other cases the shape of the filament will have to be computed numerically, in this special case we can actually find analytical results.

Note that, although all filament configurations discussed in this section do satisfy the Euler-Lagrange equation of the filament, we cannot guarantee that they actually *minimize* the energy: they may be saddle points of the energy functional, in which case they would be unstable. Distinguishing such solutions from mechanically stable ones requires the framework of the second variation. Although the second variation for this system was calculated in reference [VMMDG15], actually applying it is incredibly difficult for all but the simplest configurations, and not a task that we undertake here.

We begin solving equation (5.11) by rewriting it as

$$\theta'^2 = \cos^4 \theta - \cos^4 \theta_i, \quad (5.19)$$

where we have made the replacement  $\mathcal{H} = -\cos^4 \theta_i/2$ , with  $\theta_i$  being the angle of the filament at the inflection point, i.e. the point where  $\theta' = 0$ . It is always possible to write  $\mathcal{H}$  in this form; if it were not, (namely, if  $\mathcal{H} > 0$  or  $\mathcal{H} < -1/2$ ), then there is no point at which  $\theta' = 0$ , and the boundary conditions cannot be satisfied. This implies that  $-1/2 \leq \mathcal{H} \leq 0$  for free filaments. Recall from the previous chapter that  $\mathcal{H}$  admits the interpretation of tension in the filament. Since these rods must have  $\mathcal{H} < 0$ , they are under compression.

The angle  $\theta$  will oscillate periodically between  $-\theta_i$  and  $\theta_i$ . The quadrature (5.13)

now becomes

$$s = \int ds = \int_0^{\theta(s)} \frac{d\theta}{\sqrt{\cos^4 \theta - \cos^4 \theta_i}}. \quad (5.20)$$

This integral can in fact be evaluated in terms of special functions:

$$s = \frac{1}{\sqrt{2} \cos \theta_i} F \left[ \arctan \left( \frac{\sin \theta \cos \theta_i}{\sqrt{2(\cos^2 \theta - \cos^2 \theta_i)(1 + \cos^2 \theta_i)}} \right) \middle| \frac{\sin^2 \theta_i}{2} \right], \quad (5.21)$$

where  $F(\phi|m)$  is the elliptic integral of the first kind. In this case,  $s$  is measured from the point where  $\theta = 0$ . Inserting  $\theta = \theta_i$ , we see that the period of oscillations of  $\theta(s)$  is

$$L = 4(s|_{\theta=\theta_i} - s|_{\theta=0}) = \frac{4}{\sqrt{2} \cos \theta_i} K \left( \frac{\sin^2 \theta_i}{2} \right), \quad (5.22)$$

where  $K(m) = F(\pi/2|m)$  is the complete elliptic integral of the first kind.

Equation (5.21) can in fact be inverted for  $\theta(s)$  using the Jacobi elliptic function  $\text{sc}(u|m)$ ,

$$\theta(s) = \arccos \sqrt{\frac{2 \cos^2 \theta_i - \cos^2 \theta_i (1 + \cos^2 \theta_i) \text{sc}(\sqrt{2} \cos \theta_i s | \sin^2 \theta_i / 2)}{2 \cos^2 \theta_i - (1 + \cos^2 \theta_i) \text{sc}(\sqrt{2} \cos \theta_i s | \sin^2 \theta_i / 2)}}. \quad (5.23)$$

With  $\theta(s)$ , we can find the coordinates  $\phi$  and  $z$  from equations (5.7). These are given analytically by

$$\begin{aligned} \phi &= \int ds \cos \theta = \int_{\theta_i}^{\theta(s)} d\theta \frac{\cos \theta}{\sqrt{\cos^4 \theta - \cos^4 \theta_i}} \\ &= \frac{1}{\sqrt{1 + \cos^2 \theta_i}} \left( F \left[ \arcsin \frac{\sin \theta}{\sin \theta_i} \middle| \frac{\sin^2 \theta_i}{1 + \cos^2 \theta_i} \right] - K \left[ \frac{\sin^2 \theta_i}{1 + \cos^2 \theta_i} \right] \right) \end{aligned} \quad (5.24)$$

$$\begin{aligned} z &= \int ds \sin \theta = \int_{\theta_i}^{\theta(s)} d\theta \frac{\sin \theta}{\sqrt{\cos^4 \theta - \cos^4 \theta_i}} \\ &= \frac{1}{\sqrt{2} \cos \theta_i} F \left[ \arccos \frac{\cos \theta_i}{\cos \theta} \middle| \frac{1}{2} \right]. \end{aligned} \quad (5.25)$$

Let us consider the overall extent and geometry of these solutions. Given one endpoint of the filament, where does it end up? First, we see from equation (5.25) that

$$z|_{\theta=\pm\theta_i} = \frac{1}{\sqrt{2} \cos \theta_i} F \left[ \arccos \frac{\cos \theta_i}{\cos(\pm\theta_i)} \middle| \frac{1}{2} \right] = \frac{1}{\sqrt{2} \cos \theta_i} F \left[ 0 \middle| \frac{1}{2} \right] = 0. \quad (5.26)$$

Over every half period, the filament returns to the ring  $z = 0$ . This is a result of the  $z \mapsto -z$  symmetry that occurs when  $f = 0$ . Over one full period of the filament's oscillation, the  $\phi$  coordinate changes by an amount

$$\Delta\phi = 4(\phi|_{\theta=\theta_i} - \phi|_{\theta=0}) = 4 \frac{1}{1 + \cos^2 \theta_i} K \left[ \frac{\sin^2 \theta_i}{1 + \cos^2 \theta_i} \right]. \quad (5.27)$$

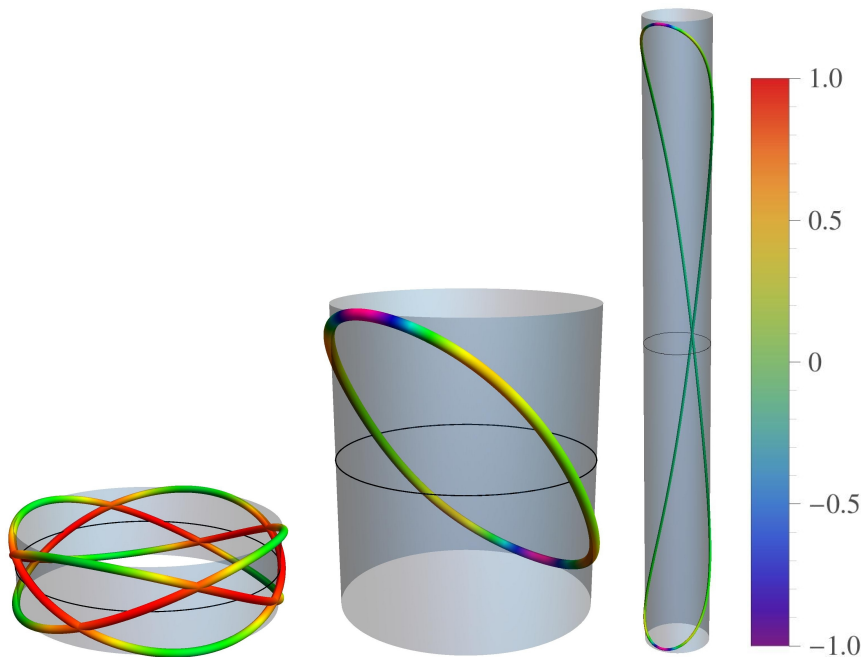


**Figure 5.3:** Closed curves with  $f = m = 0$ . From left to right, these curves have  $w/n = 3/4$ ,  $w/n = 1$ ,  $w/n = 2$ . The far right image has been scaled down by a factor of two relative to the others. Each curve is colored by its normalized local force density  $\lambda$ .

For certain values of  $\theta_i$ , the filament completes an integer number of full turns around the cylinder, so that  $\Delta\phi = 2\pi w$ , where  $w$  is an integer called the *winding number*. This implies that the filament actually closes back on itself. But it is also possible for the filament to close even if  $\Delta\phi \neq 2\pi w$  if we consider a filament that completes multiple oscillatory periods  $n$  before completing a full turn around the cylinder. Then, we write

$$\Delta\phi = \frac{2\pi w}{n}, \quad (5.28)$$

so that after  $n$  periods of the filament's oscillation, it winds  $w$  times around the cylinder. For example, if  $w/n = 3/4$ , four periods of the filament circumnavigate the cylinder three times. This and other cases of closed filaments are shown in figure 5.3.

Considering  $\Delta\phi$  as a function of the inflection angle  $\theta_i$ , it has a minimum at  $\theta_i = 0$ , where  $\Delta\phi = 1/\sqrt{2}$  (shown in figure 5.4). It is therefore impossible to have, for example,  $w/n = 1/2$  or  $w/n = 2/3$  when  $f = m = 0$ . On the other hand, the winding  $\Delta\phi \rightarrow \infty$  as the inflection angle  $\theta_i \rightarrow \pi/2$ , so there is no upper bound on  $w/n$ .

## Force

Let us turn our focus to the force  $\lambda$  a filament with free endpoints exerts on the surface, calculated in equation (5.14). Because we have calculated the shape of the filament analytically, we can determine the force it exerts exactly. For small inflection angles  $\theta_i$ , the force is uniformly positive, i.e. outward. If we imagine that the filament is on the interior of the cylinder, it would be in contact with the

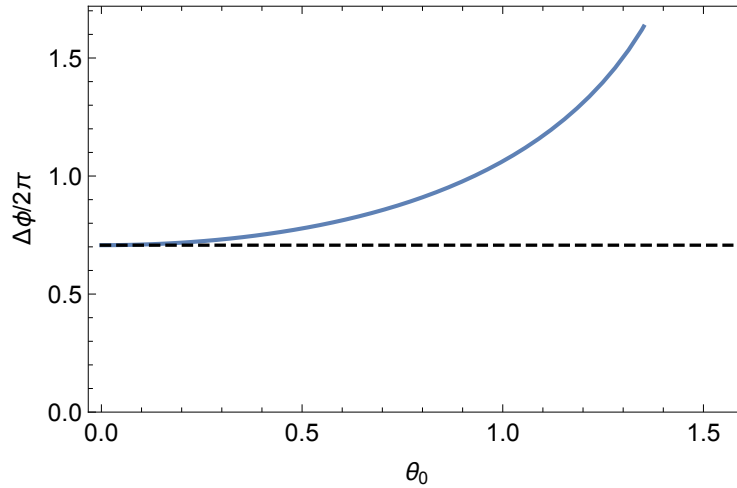


**Figure 5.4:** Extent of winding  $\Delta\phi/2\pi$  as a function of inflection angle  $\theta_i$ . The dotted line indicates  $1/\sqrt{2}$ .

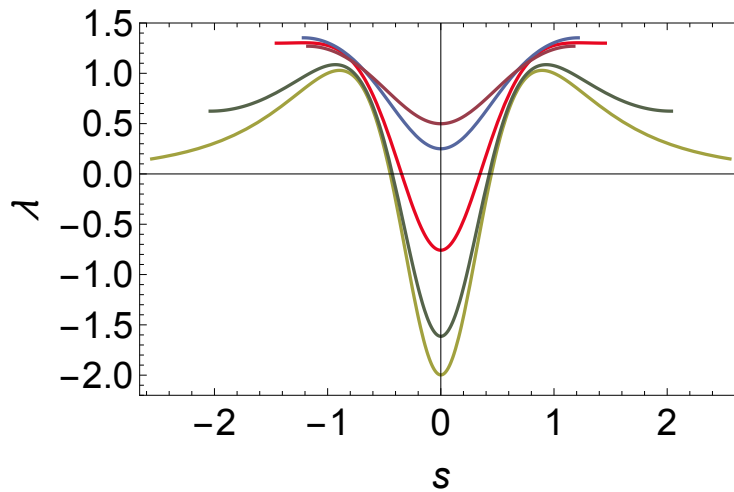


**Figure 5.5:** The force per unit length  $\lambda$  exerted on the cylinder over one period of the filament as a function of arc-length  $s$  for a few values of the inflection angle  $\theta_i$ ; from top to bottom,  $\theta_i = 0.3, 0.374734, 0.64, 0.93, 1.4$ .

cylinder at every point *even in the absence of any adhesion energy*. At  $\theta_i = 0.374734$  however, the force vanishes at the point where  $\theta = 0$ . For larger inflection angles, the force is in some places negative and other places positive. In this case, if there is no force of attraction between filament and surface, the filament loses contact with the surface at the points where  $\lambda < 0$ ; what would happen when the filament is only in partial contact with the surface is beyond the scope of this analysis. As the inflection angle approaches  $\pi/2$ , the force at the inflection point tends towards zero. This is shown in figure 5.5. In no case does the filament exert uniformly inward forces. *We therefore conclude that a Bernoulli-Euler rod with free endpoints cannot constrict a cylinder without, at some points, also dilating it.*

The preceding discussion illustrates the surprising subtlety of this problem. Even with the simplest boundary conditions on a highly symmetric surface, the filament can take a variety of shapes and exert non-uniform forces. This counter-intuitive behavior is a product of the boundary conditions and the forces exerted on the filament by the surface.

### 5.1.3 Closed curves

Let us now consider closed curves more generally. Closed filaments of course have no boundary; the boundary terms of the variation therefore vanish trivially.

However, there are certain conclusions that we can draw based on the closure of the curve. Firstly, the function  $\theta(s)$  is of course periodic, implying that  $\theta$  will oscillate between two angles  $\theta_a$  and  $\theta_b$ . We again characterize each closed equilibrium state by two integers: the winding number  $w$  and the number of periods  $n$ . We will label the set of solutions with winding number  $w$  and  $n$  periods  $L_{w,n}$ . Each such set has a continuum of solutions parametrized by the length  $L$  of the filament (or, equivalently, the curvature independent stress  $\mathcal{H}$ ), which we write as  $L = 2\pi(w + \Delta r)$ , where  $\Delta r \geq 0$  is the “excess radius” of the filament. Using equation (5.13), the length can be expressed in terms of the filament’s trajectory as

$$L = \int_0^L ds = 2n \int_{\theta_a}^{\theta_b} d\theta \frac{ds}{d\theta} = \int_{\theta_a}^{\theta_b} \frac{2n}{\sqrt{2(\mathcal{H} - U(\theta))}} d\theta = 2\pi(w + \Delta r). \quad (5.29)$$

The factor of  $2n$  comes from the fact that  $\theta$  goes from  $\theta_a$  to  $\theta_b$  and back each time per period.

Following similar reasoning, over the length of the filament, the coordinate  $z$  changes by an amount

$$\Delta z = \int_0^L ds \sin \theta = \int_{\theta_a}^{\theta_b} \frac{2n \sin \theta}{\sqrt{2(\mathcal{H} - U(\theta))}} d\theta = 0, \quad (5.30)$$

where we have used the quadrature in equation (5.13) and the relation between  $z$  and  $\theta$  in equation (5.7). It is of course necessary that  $\Delta z = 0$  for the filament to close. If  $f = 0$ , the potential  $U(\theta)$  is an even function, so  $\theta_a = -\theta_b$ . Because the integrand is odd, it is then guaranteed that  $\Delta z = 0$ . If  $f \neq 0$ , the  $z \mapsto -z$  symmetry is broken, and the filament in general does not close. Though we have no proof that  $f = 0$  is necessary to ensure that the filament closes, we will take  $f = 0$  for the rest of this section.

Lastly, we can calculate the winding number as

$$\Delta \phi = \int_0^L ds \cos \theta = 2n \int_{\theta_a}^{\theta_b} \frac{\cos \theta}{\sqrt{2(\mathcal{H} - U(\theta))}} d\theta = 2\pi w, \quad (5.31)$$

where we have used the quadrature (5.13) and the relation between  $\phi$  and  $\theta$  in equation (5.7).

Before we begin solving the Euler-Lagrange equations, there are a few conclusions we can already draw from the analogy to a particle in a potential. In the analogy, closed filaments correspond to bound states of the particle. When  $f = 0$ ,  $\theta$  oscillates about the ring with  $\theta = 0$ ; this requires that  $\theta = 0$  be a local minimum of the potential  $U(\theta)$ . Since the second derivative must be non-negative at a local minimum, we conclude that  $U''(0) = m + 2 \geq 0$ . The fact that  $\theta$  is oscillatory also tells us that the Hamiltonian  $\mathcal{H}$  cannot exceed the highest peak of the potential, given by

$$\mathcal{H} \leq \mathcal{H}_{\max} = \begin{cases} \frac{3}{4} \sqrt[3]{\frac{m^4}{2}} & m < 2 \\ m - \frac{1}{2} & m > 2 \end{cases}. \quad (5.32)$$

As  $\mathcal{H} \rightarrow \mathcal{H}_{\max}$ , the period of oscillations  $L/n \rightarrow \infty$ .

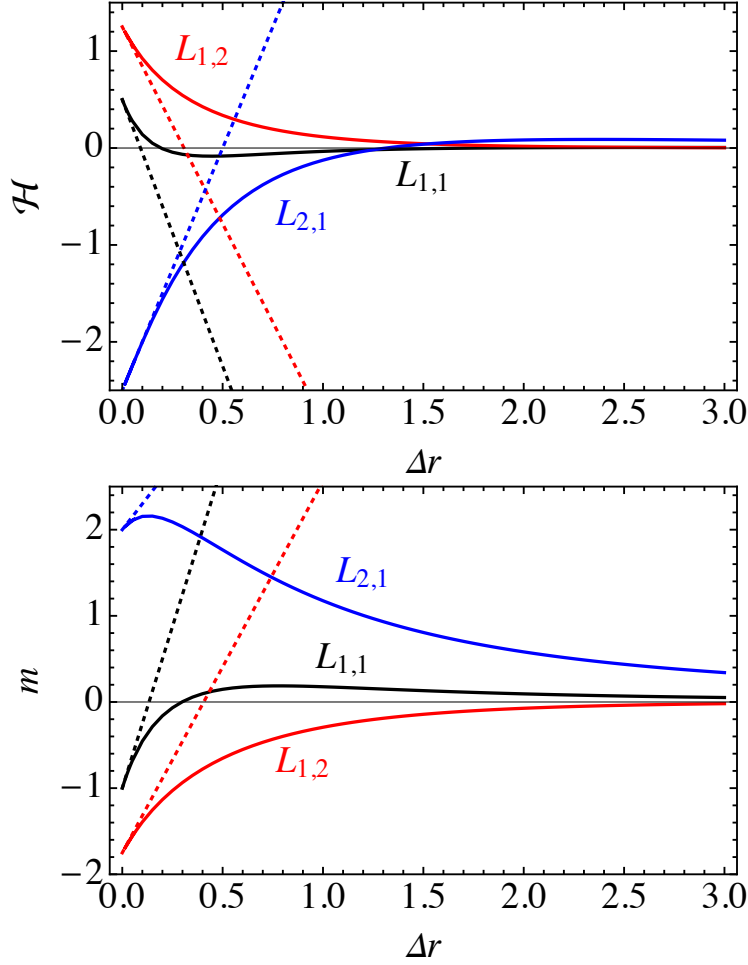


**Figure 5.6:** Perturbative calculations (dotted lines) give the values and slope of  $\mathcal{H}$  and  $m$  at  $\Delta r = 0$ , but the approximation does not hold at larger values of  $\Delta r$ .

### Perturbative regime

If  $\Delta r$  is small, the amplitude of oscillations is small, implying that the filament is approximately circular. We can therefore use perturbation theory to approximate the shape of filaments with small  $\Delta r$ . In this framework, we write each quantity in the model as a formal power series in some “smallness parameter”  $\epsilon$ . Because  $\epsilon$  is arbitrary, we can solve then equation (5.11) “order by order” in the parameter  $\epsilon$ .

First, we write  $\theta(s)$ ,  $m$ , and  $\mathcal{H}$  as

$$\theta = \epsilon \theta_1 + \epsilon^2 \theta_2 + \dots \quad (5.33a)$$

$$m = m_0 + \epsilon m_1 + \epsilon^2 m_2 + \dots \quad (5.33b)$$

$$\mathcal{H} = \mathcal{H}_0 + \epsilon \mathcal{H}_1 + \epsilon^2 \mathcal{H}_2 + \dots \quad (5.33c)$$

We now insert equations (5.33a)-(5.33c) into the Euler-Lagrange equation (5.11) and series expand the result. This leads to

$$-\left(\frac{1}{2} + m_0\right) - m_1 \epsilon + \frac{1}{2} \left( (m_0 + 2)q_1^2 + q_1^2 - 2m_2 \right) \epsilon^2 + \dots = H_0 + H_1 \epsilon + H_2 \epsilon^2 + \dots \quad (5.34)$$

The terms of each order in  $\epsilon$  on either side of the equality must match. At order zero, this implies

$$-\frac{1}{2} - m_0 = \mathcal{H}_0, \quad (5.35)$$

giving us a relation between  $m$  and  $\mathcal{H}$  for exactly circular rings. At next order, we obtain

$$-m_1 = \mathcal{H}_1. \quad (5.36)$$

It turns out that this is the only equation in which the parameter  $\mathcal{H}_1$  appears. We can therefore set  $m_1 = -\mathcal{H}_1 = 0$  without loss of generality.

At order  $\epsilon^2$  we obtain a differential equation describing the shape of the filament,

$$m_2 + \mathcal{H}_2 = \frac{1}{2}\theta_1'^2 + \frac{1}{2}(m_0 + 2)\theta_1^2. \quad (5.37)$$

This should look familiar: it is the equation of a harmonic oscillator with energy  $m_2 + \mathcal{H}_2$ , unit mass, and frequency  $\omega = \sqrt{m_0 + 2}$ ! Again invoking Feynman's aphorism "The same equations have the same solutions", the function  $\theta_1(s)$  is therefore given by

$$\theta_1(s) = \sqrt{\frac{2(\mathcal{H}_2 + m_2)}{m_0 + 2}} \cos(\sqrt{m_0 + 2} s). \quad (5.38)$$

All of the familiar results for the harmonic oscillator of course carry over to the present scenario. Since we expect the frequency to be a real number, this result fits nicely with our earlier conclusion that  $m \geq -2$ . As long as  $\omega$  is real, the angle oscillates sinusoidally with amplitude

$$\theta_a = \sqrt{\frac{2(\mathcal{H}_2 + m_2)}{m_0 + 2}}. \quad (5.39)$$

We can now begin to relate the geometric parameters of the filament,  $\Delta r$ ,  $n$ , and  $w$ , to the mechanical ones,  $m$  and  $\mathcal{H}$ . We begin by evaluating  $\Delta\phi$  using the integral in equation (5.31). We find

$$\begin{aligned} \Delta\phi &= \int_{-\theta_i}^{\theta_i} \frac{2n \cos \theta}{\sqrt{2(U(\theta_i) - U(\theta))}} d\theta \\ &= \int_{-\theta_a}^{\theta_a} \frac{2n}{\sqrt{m_0 + 2}\sqrt{\theta_a^2 - \theta^2}} d\theta - 2n\epsilon^2 \int_{-\theta_a}^{\theta_a} \frac{12m_2 + (4 + 11m_0)\theta^2 - (m_0 + 20)\theta_a^2}{24\sqrt{m_0 + 2}^3 \sqrt{\theta_a^2 - \theta^2}} d\theta + \dots \\ &= \frac{2\pi n}{\sqrt{m_0 + 2}} - \epsilon^2 \frac{2\pi n(8m_2 + 3(m_0 - 4)\theta_a^2)}{16\sqrt{m_0 + 2}^3} + \dots \end{aligned} \quad (5.40)$$

But we also know  $\Delta\phi$  through the closure condition  $\Delta\phi = 2\pi w$ . We can also solve this boundary condition order by order, so that it must be satisfied at order  $\epsilon^0$ , and all higher order terms in  $\Delta\phi$  must vanish identically. We therefore obtain the following equations for  $m_0$  and  $m_2$ :

$$m_0 = \left(\frac{n}{w}\right)^2 - 2 \quad (5.41a)$$

$$m_2 = -\frac{3\theta_a^2}{8} \left[ \left(\frac{n}{w}\right)^2 - 6 \right]. \quad (5.41b)$$

We follow similar reasoning to relate the total length  $L$  to the mechanical parameters. Using equation (5.29), we see

$$\begin{aligned}
 L &= \int_{-\theta_i}^{\theta_i} \frac{2n}{\sqrt{2(U(\theta_i) - U(\theta))}} d\theta \\
 &= \int_{-\theta_a}^{\theta_a} \frac{2n}{\sqrt{m_0 + 2}\sqrt{\theta_a^2 - \theta^2}} d\theta + 2n\epsilon^2 \int_{-\theta_a}^{\theta_a} \frac{(m_0 + 20)(\theta^2 + \theta_a^2) - 12m_2}{24\sqrt{m_0 + 2}^3 \sqrt{\theta_a^2 - \theta^2}} d\theta \\
 &= \frac{2n\pi}{\sqrt{m_0 + 2}} + 2n\epsilon^2 \frac{\theta_a^2(m_0 + 20) - 8m_2}{16\sqrt{m_0 + 2}^3} + \dots .
 \end{aligned} \tag{5.42}$$

Again, we already know  $L = 2\pi(w + \Delta r)$ . Recall that this discussion began with the assumption that  $\Delta r$  is small; we now formalize that statement by assuming that the lowest order term in  $\Delta r$  is at least order  $\epsilon^1$ . Then, at order  $\epsilon^0$ , equation (5.42) simply confirms equation (5.41a) for  $m_0$ . Inserting equations (5.41a) and (5.41b), the remaining term tells us

$$\Delta r = \epsilon^2 \frac{n}{\pi} \frac{\theta_a^2(m_0 + 20) - 8m_2}{16\sqrt{m_0 + 2}^3} + \dots = \epsilon^2 \frac{\theta_a^2 w}{4} + \dots . \tag{5.43}$$

Finally, we can combine equations (5.39), (5.41b), and (5.43) to write  $m_2$  and  $\mathcal{H}_2$  entirely in terms of geometric quantities

$$m_2 = \frac{3\Delta r}{w} \left( 3 - \frac{n^2}{2w^2} \right) \tag{5.44}$$

$$\mathcal{H}_2 = \frac{\Delta r}{w} \left( \frac{7n^2}{2w^2} - 9 \right). \tag{5.45}$$

Insert these into our power series and taking  $\epsilon = 1$ , this implies

$$m = \frac{n^2}{w^2} - 2 + \frac{3\Delta r}{w} \left( 3 - \frac{n^2}{2w^2} \right) \tag{5.46}$$

$$\mathcal{H} = \frac{3}{2} - \frac{n^2}{w^2} + \frac{\Delta r}{w} \left( \frac{7n^2}{2w^2} - 9 \right). \tag{5.47}$$

These are plotted, along with numerical calculations (which we will discuss in the next section) of  $m$  and  $\mathcal{H}$  in the non-linear regime in figure 5.6. For larger deformations (or filaments with a larger excess radius  $\Delta r$ ), these perturbative results do not approximate  $\mathcal{H}$  and  $m$  well.

These results also tell us the force exerted on the cylinder by approximately circular loops. Up to second order in  $\epsilon$ , the force density  $\lambda$  is given by

$$\lambda = \omega^2 - 1 + \Delta r \frac{(4 - 22\omega^2) \cos(2\omega s) - 5\omega^2 + 14}{2w}. \tag{5.48}$$

To lowest order, the force is given by  $\omega^2 - 1 = n^2/w^2 - 1$ . Thus for approximately circular filaments completing more loops around the cylinder than oscillatory periods, the force is negative (see figure 5.9), i.e. constrictive, while if there are more oscillatory periods than loops (see figure 5.8), the force would tend to dilate the cylinder. As  $\Delta r$  increases, the magnitude of the second term grows; if  $\Delta r$  is large enough, the force is no longer uniformly inward or outward.

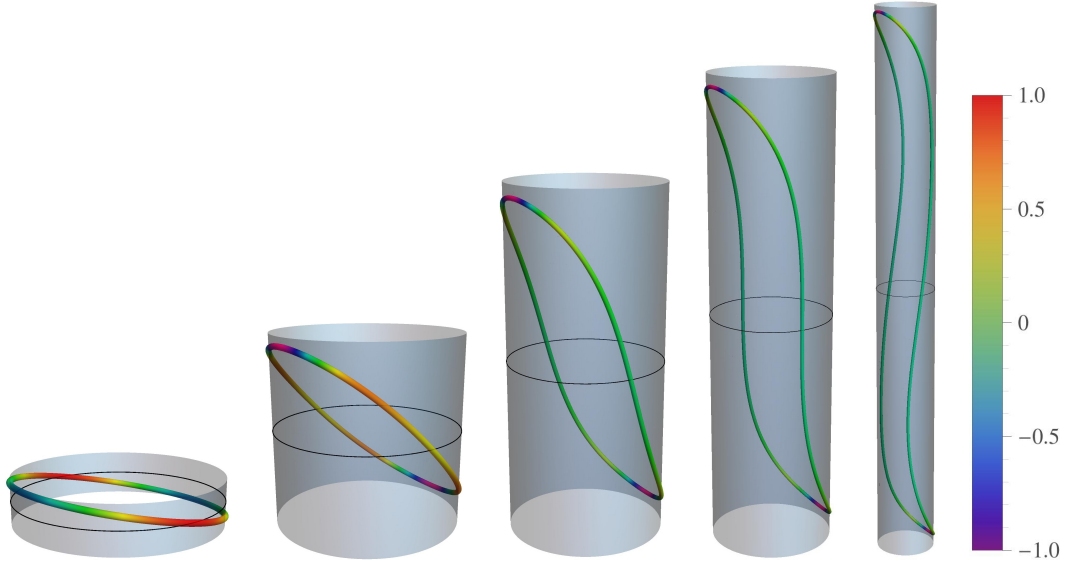


**Figure 5.7:** Closed curves in the  $L_{1,1}$  series. Each curve is colored by its normalized local force density  $\lambda$ .

### Nonlinear Regime

We could in principle take these calculations to higher orders in  $\epsilon$ , but simply finding numerical solutions to equation (5.11) is more practical. We perform these calculations using Matlab's built-in boundary value problem solving routine BVP4C, where our set of first order equations is given by

$$\phi' = \cos \theta \quad (5.49a)$$

$$z' = \sin \theta \quad (5.49b)$$

$$\theta' = \kappa_g \quad (5.49c)$$

$$\kappa_g' = f \cos \theta - m \sin \theta - 2 \sin \theta \cos^3 \theta. \quad (5.49d)$$

This enables us to go to very large deformations of the filament, as shown in figures 5.7, 5.8, and 5.9. In each figure, the filament is colored by the force density  $\lambda$  normalized by the maximum of its magnitude,  $\lambda/\max_s\{|\lambda|\}$ . This is because the sign of  $\lambda$  is more important than its overall magnitude, which has no significance without defining a rigidity for the surface or allowing it to respond.

Another useful quantity is the *net force* transmitted to the surface,

$$\Lambda = \int_0^L ds \lambda. \quad (5.50)$$

This will help us ascertain whether the filament tends to decrease or increase the cylinder's radius, overall. We will focus on the  $L_{1,1}$ ,  $L_{1,2}$ , and  $L_{2,1}$  series as a representative sample of the behavior of these filaments.

For each series  $L_{n,w}$  that we have considered, the inflection angle  $\theta_i$  increases as a function of  $\Delta r$  at small  $\Delta r$ . This pattern continues past the point when  $\theta_i = \pi/2$ , developing an overhang. Continuing to increase  $\Delta r$ , the inflection angle  $\theta_i$  increases only slightly beyond this point, eventually reaching a maximum. The angle then asymptotically decreases towards  $\theta_i = \pi/2$  as  $\Delta r \rightarrow \infty$ .

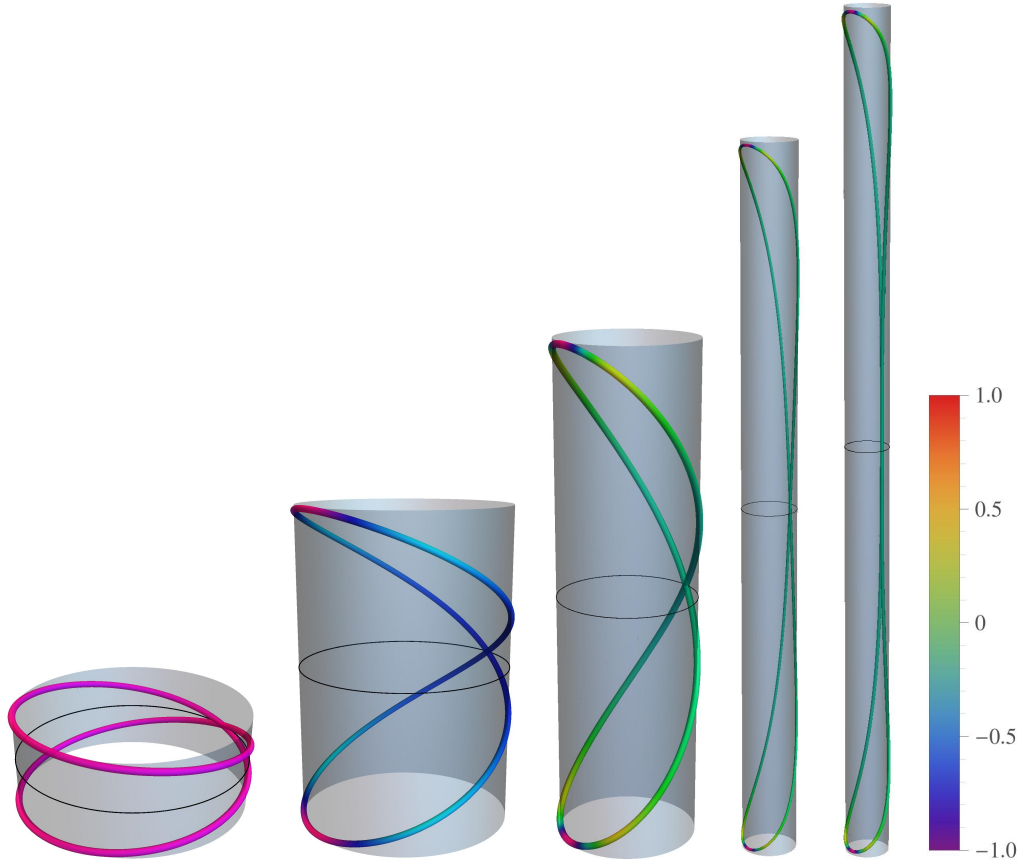


**Figure 5.8:** Closed curves in the  $L_{2,1}$  series. Each curve is colored by its normalized local force density  $\lambda$ .

To determine if the filament is uniformly constrictive or dilative, we calculate the maximum and minimum of  $\lambda(s)$  over the entire curve. We see numerically that the maximum and minimum force (plotted in figure 4.45) tend towards  $\lambda_{\max} \rightarrow 1$  and  $\lambda_{\min} \rightarrow -2$  as  $\Delta r \rightarrow \infty$ . This implies that, whether bound to the inside or the outside of the cylinder, very long filaments tend to detach. The net force  $\Lambda$  from long filaments on the surface though is always outward. In the limit  $\Delta r \rightarrow \infty$ ,  $\Lambda \rightarrow \pi n$ .

The behavior at low  $\Delta r$  accords well with our perturbative calculations. For all solutions in the  $L_{1,1}$  series, the force is neither uniformly constrictive nor dilative. In the  $L_{1,2}$  series, the force is uniformly dilative for small excess lengths, but becomes mixed at a finite length. In the  $L_{2,1}$  series, the force is uniformly constrictive for small excess lengths; this is a result of the fact that the ratio  $n/w < 1$ .

## Conclusions

In this section, we have seen that the behavior of even the simplest elastic filaments on highly symmetric surfaces can be surprisingly complex. Even filaments with free endpoints can take many different configurations depending on their length  $L$ , or, equivalently, the Hamiltonian  $\mathcal{H}$ . For short filaments, the sign of the force density  $\lambda$  is uniform, and matches the sign of  $n/w - 1$ . This shows that it is possible for the filaments to constrict the cylinder, even when the stress-free state of the filament is a straight line. For longer filaments, the force tends to constrict the cylinder in

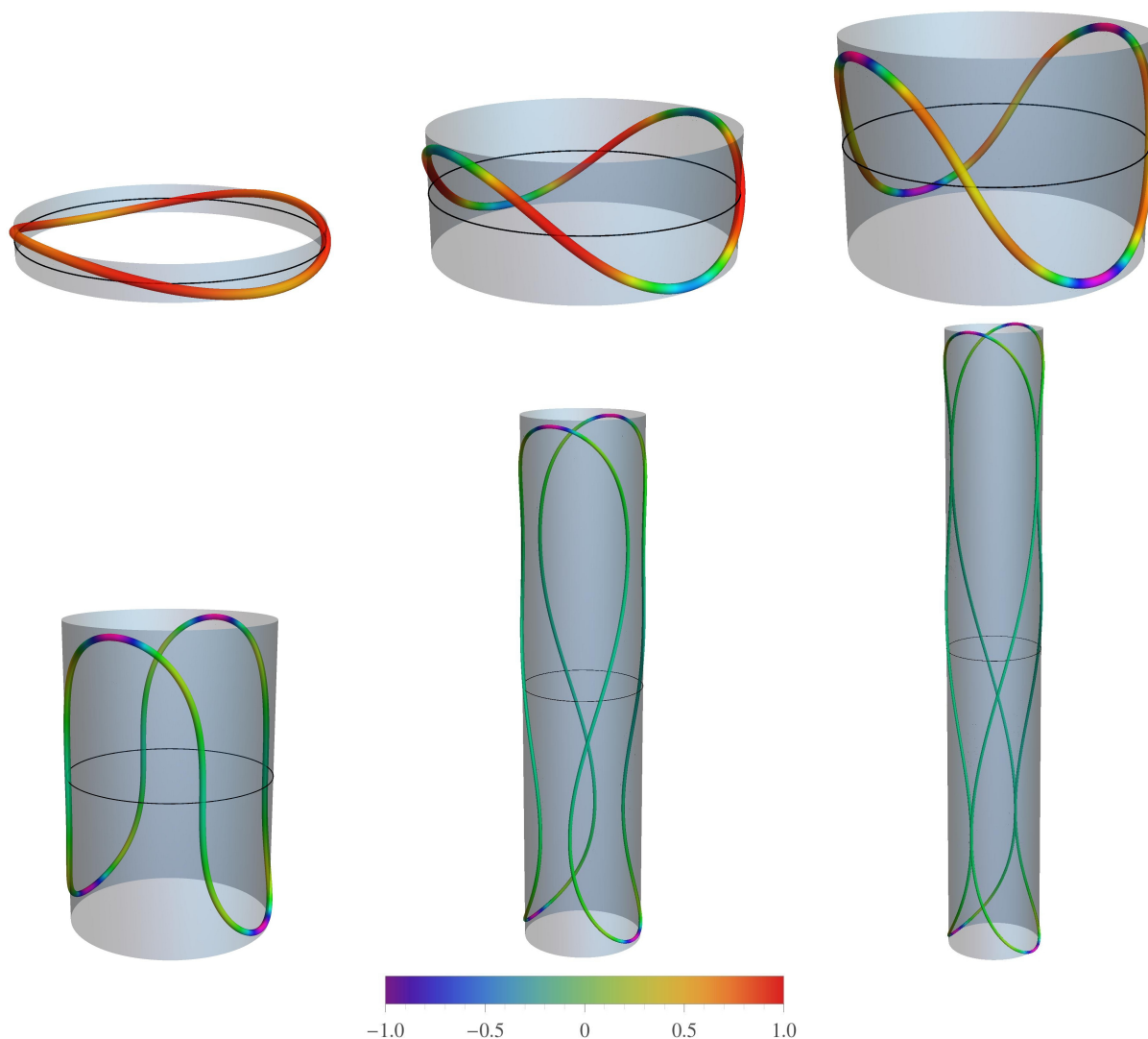


**Figure 5.9:** Closed curves in the  $L_{1,2}$  series. Each curve is colored by its normalized local force density  $\lambda$ .

some places and dilate it in others. However, the behavior of long filaments is mostly inaccessible analytically, even using perturbation theory. Instead, we must resort to numerical solutions of the Euler-Lagrange equations even for this simple case.

## 5.2 Dynamin as a surface-confined Kirchhoff rod

We would like to use our theory of surface confined elastic filaments to create a model for dynamin-mediated membrane fission. The dynamin family of proteins mediates fission during many distinct cellular processes, including cytokinesis, endocytosis, and vacuolar as well as mitochondrial fission [KIY94, JSBB10, LMR09, MGF04, MR13a, SF11a, SDS00a, WK14]. It has also been shown that some members of the dynamin family are able to form tubules from flat membranes [RKL<sup>+</sup>10, PM04, YPM01]. Proteins of this family appear in most phylogenetic branches, including plants, animals, yeast, and even prokaryotes [AT02, FDC12, LWKA02, vdB99].

To create a realistic model of dynamin in our framework, we must make a few important adjustments. Firstly, real dynamin polymers do not close back on them-

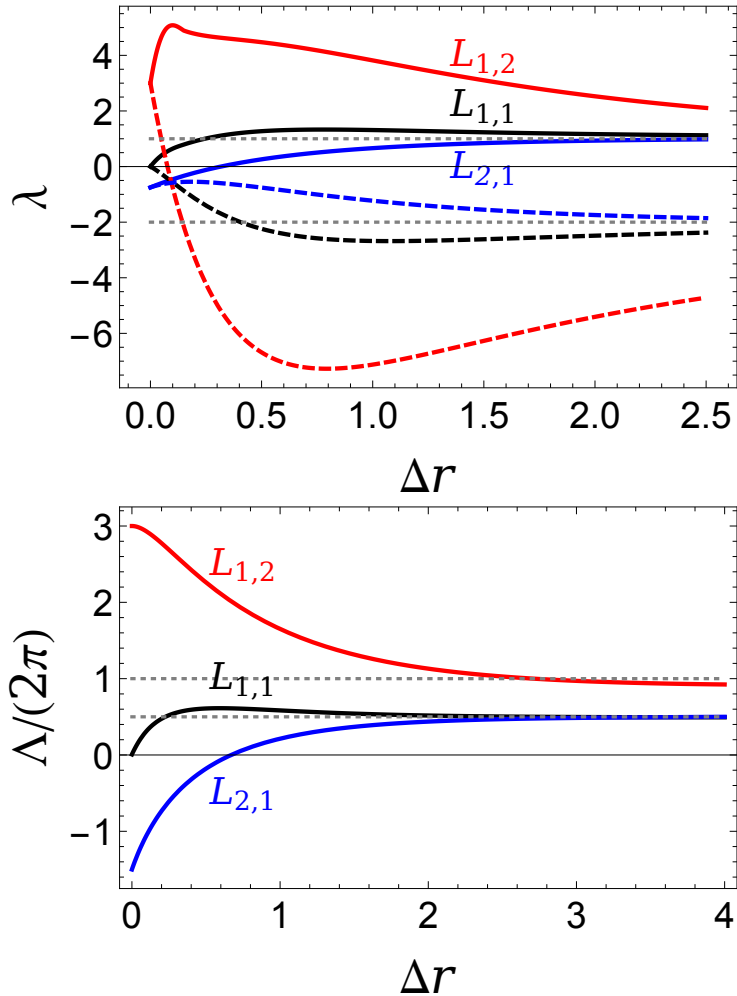


**Figure 5.10:** (Top) Maximum (solid lines) and minimum (dotted lines) force density  $\lambda$  exerted on the cylinder by closed curves as a function of  $\Delta r$ . If both have the same sign, the force on the cylinder is mono-directional. (Bottom) Net force  $\Lambda$  exerted on the cylinder as a function of  $\Delta r$ .

selves, making most of the last section inapplicable. Dynamin is also present at such high concentrations in cells that there is essentially an limitless supply for any given target, so it is more appropriate to treat the length of the filament as a dynamical variable, and fix a polymerization force or chemical potential which controls the length. Lastly, real dynamin polymers are helical, so we must consider polymers with preferred curvature and twist.

We therefore analyze open-ended, helical elastic filaments of variable length. In this case, we will consider only the lowest energy state for a given filament. First we will apply this to cylindrical substrates, as they are the most commonly studied *in vitro* [BAE<sup>+</sup>08a, DMH04a, PS08, RUFDC06a]. It turns out that the symmetries of the cylinder make this calculation analytically tractable, so it will also serve as a simple introduction to some of the concepts used later, as well as highlighting the importance of symmetries. Then, we will consider a more biologically relevant surface geometry, the catenoid, which represents the neck between two splitting membranes or organelles.

This neck shape must be constructed by other agents acting on the membrane, for instance clathrin in endocytosis or the ER in mitochondrial fission. Interestingly,

this can be performed by local constriction of the neck or dilation of the membrane at remote locations [BGVMS14]. We will find that our model provides insight into the desirable features of a fission machine that will lead us to important restrictions on the parameters of dynamin, and suggest physical explanations for recruitment and constriction.

Common features in the dynamin family include GTPase domains and pleckstrin homology domains used for membrane binding [vdB99]. As we have discussed, these proteins polymerize into helices that wind around their fission target [vdB99]. These features suggest a process by which these proteins mediate fission: after forming a helical scaffold around its target membrane, dynamin hydrolyzes GTP, and uses the associated energy to deform the target to its breaking point. However, this description glosses over certain subtleties. How exactly does dynamin deform the membrane [SDS00a]? How is dynamin recruited to the neck, or as van der Blik put it, “what keeps dynamin from turning all membranes into vesicles?” [vdB99]. What assistance does it need from other proteins [RUFDC06a]?

Van der Blik hypothesized that the answer to his question was that dynamin is recruited through a biochemical regulatory pathway. Contrarily, our goal in this section is to move toward a minimal model of a dynamin family protein’s elastic interactions with its target. As we will see, simple physical mechanisms are sufficient to explain dynamin’s recruitment. This will help us to understand both how real dynamin works and the restrictions under which evolution created this fission machine. Although it is an essential step in the fission process, we omit GTP hydrolysis. Our justification for this approach is that we seek to understand the passive aspects of fission before considering the active ones. What are the forces that more realistic elastic filaments can exert on surfaces whose curvature might not match their own, in particular, *under the constraint that they spontaneously polymerize onto that surface?* Even understanding this mechanical interaction turns out to be surprisingly informative.

This analysis will illustrate some of the connections between elasticity, geometry, and chemistry in the design of a polymerizing fission machine. For example, we find that the pitch of the helix is closely related to the range of neck radii onto which dynamin binds. We also show fundamental limitations on how much such a polymer can deform its target, and hence offer an explanation of why dynamin-mediated fission is an active process.

In the past few years, many theoretical approaches for modeling dynamin have been developed. Each of these imagines a different idealized form for the protein and is able to capture different aspects of the fission process. For instance, considering dynamin as a mean-field density functional on the membrane surface illustrated the role of dynamical instabilities in the fission process [SGR11]. A fluid dynamical analysis showed the limitations imposed by friction during constriction [LPJ08]. A model representing dynamin simply as a rigid sheath was able to show that dynamin’s recruitment can be connected to local membrane geometry [RKL<sup>+</sup>10]. Other theories imagined dynamin as a closed chain [FJK<sup>+</sup>16b] or as a system of insertions which agglomerate via membrane-mediated interactions [FgDG03].

However, we feel that a more detailed discussion of the elastic interaction between the dynamin polymer and the membrane is needed. As we will see, mismatch between the preferred geometries of the protein and its target produces the force on the membrane and inhibits polymerization.

Our model represents dynamin as a continuous, zero-thickness elastic filament. We begin with an energy functional which expresses the total energy of the filament as an integral over its length. In the case of dynamin, the orientation of the polymer relative to the surface is fixed: the protein must keep its pleckstrin homology domains in contact with the membrane in order to bind. We will therefore apply the calculations from section 4.3.

The key steps we make towards a more realistic model of dynamin are including twist rigidity, considering filaments with helical unstressed configurations, and introducing the effects of a polymerization force  $\mu$ . These generalizations impel us to use the Kirchhoff model of elastic rods with spontaneous curvature from equation (2.23). The energy functional is therefore given by

$$E = \frac{1}{2} \int_0^L ds \left\{ I_{ij} (\kappa_i - c_i) (\kappa_j - c_j) + \beta (\kappa_t - c_t)^2 \right\}, \quad (5.51)$$

where  $i$  and  $j$  serve as indices to refer to the normal and geodesic curvatures, and are implicitly summed over. The spontaneous curvatures  $c_g$  and  $c_n$  describe the filament's bending when unstressed, and the spontaneous twist  $c_t$  describes its twist (or, equivalently, geodesic torsion).

As shown in recent structural studies, dynamin's cross section is approximately symmetric under reflections through the plane defined by the filament's tangent and the local surface normal vector, implying that  $c_g \simeq 0$  [FPG<sup>+</sup>11, FJN11]. We will furthermore make the simplifying assumption that the cross section is isotropic, in which case  $I_{ij} = \alpha \delta_{ij}$ , where  $\alpha$  is the bending rigidity. This holds automatically if the cross section is symmetric with respect to rotations about its center. While the cross section is not quite circular, the width and height are comparable (both are about 10 nm), which also suggests that the two eigenvalues of  $I_{ij}$  are similar. As we will see, the model will indeed be able to describe many features of dynamin's behavior.

We can estimate the other spontaneous curvatures  $c_n$ , and  $c_t$  from the shape of dynamin filaments formed in the absence of any binding substrate. In the case of classical dynamin ("classical dynamin" refers to the prototypical dynamin molecule, dynamin 1), the protein forms helices of radius  $r \approx 15$  nm and pitch  $2\pi c \approx 10$  nm in low-salt, low pH solution [MR13a]. The curvature and torsion of a helix in terms of these parameters are

$$\kappa_n = \frac{r}{r^2 + c^2} \quad (5.52a)$$

$$\kappa_t = \frac{c}{r^2 + c^2}. \quad (5.52b)$$

Assuming that this is the stress-free configuration of the filament, we therefore estimate that classical dynamin has  $c_n = 1/15$  nm<sup>-1</sup>,  $c_t = 1/150$  nm<sup>-1</sup>.

We will use  $1/c_n$  as a reference length scale, so other lengths are measured in terms of  $1/c_n$ . The dimensionless ratio  $c_t/c_n = h/r$  is an especially important parameter in our analysis. We note here that it is small for classical dynamin, though it could vary throughout the dynamin family.

For isotropic filaments, the twist modulus  $\beta$  is related to the bending modulus by  $\beta = \alpha/(1+\nu)$ , where  $\nu$  is Poisson's ratio [LL59]. For ordinary materials,  $0 < \nu < 1/2$  so that  $2/3 \leq \beta/\alpha \leq 1$ . Test cases we have analyzed suggest that changing  $\beta$  in

this range has no qualitative effect on the behavior of the filament, so we take  $\beta = \alpha$ . This symmetry also has the advantage of permitting some level of analytical tractability. Because it is the more intuitively understandable quantity and the two terms are in this case interchangeable, we will use twist  $\kappa_t$  instead of geodesic torsion  $\tau_g$  throughout this section.

The bending rigidity  $\alpha$  can be estimated from the persistence length of the helix, or by assuming the Young modulus of dynamin is comparable to that of similar proteins, such as actin. For classical dynamin,  $\alpha \approx 10^5 k_B T \text{nm}$  [LPJ08, MR13a]. This is large enough that thermal fluctuations are unlikely to significantly perturb the shape of the filament, justifying their omission. We will use  $\alpha$  to set the energy scale.

Including our simplifications, the energy functional of the filament reduces to

$$E = \int_0^L ds \left\{ \frac{\alpha}{2} (\kappa_g^2 + (\kappa_n - c_n)^2 + (\kappa_t - c_t)^2) - \mu \right\}, \quad (5.53)$$

where  $\mu$  represents a combination of polymerization energy, adhesion energy, and the entropy lost by confining a monomer to a two-dimensional surface. This quantity has been called the “polymerization force”, and is estimated to be about  $\mu \approx 20 \text{ pN} = 5 k_B T / \text{nm}$  for classical dynamin at concentrations of  $10 - 15 \mu\text{M}$  [MR13a]. This is a larger concentration than what is expected *in vivo*, which is less than  $1 \mu\text{M}$ . But since the polymerization force depends only logarithmically on concentration, we believe this is still a good order-of-magnitude estimate. We point out that this value corresponds to  $\mu \approx 0.01 \alpha c_n^2$  in terms of our energy scale  $\alpha$  and length scale  $c_n$ , a relation which will be useful later on.

We will focus on the configuration with the lowest energy, i.e. the “ground state”. We write its energy as  $E(L, R)$ , which depends on the length of the polymer  $L$ , and a parameter  $R$  characterizing the size of the surface (e.g. the radius of the cylinder).

Equilibrium is achieved when

$$\left. \frac{\partial E}{\partial L} \right|_{(L,R)} = \mu. \quad (5.54)$$

This equation can be understood as prescribing an equilibrium length for a given value of  $\mu$ , or as giving the appropriate  $\mu$  for a given value of  $L$ . However, as we will see, the relationship between  $\mu$  and  $L$  is not always one-to-one; often, multiple different length polymers share the same  $\mu$ . In this case, we must check whether each state is stable, and compare their free energies  $E - \mu L$  to determine the ground state. The stability is determined by the second derivative of  $E$ : if

$$\left. \frac{\partial^2 E}{\partial L^2} \right|_{(L,R)} > 0, \quad (5.55)$$

then  $L$  will correspond to an energetic minimum, and hence a stable equilibrium. Stable states that are not the ground state are called “meta-stable”.

As we have seen, confining the filament to the surface prevents the filament from fully relaxing, thus inducing stress, leading to a local force density  $\boldsymbol{\lambda}(s)$  that is applied to the surface. Although  $\boldsymbol{\lambda}$  has components tangential to the surface, they are not transmitted to the surface, but balanced by the filament’s bending moment [GVVM14]. Because changes in the surface are a fundamental part of fission, we will

attempt to consider the surface’s response to these forces. However, we do not have a theory for the interaction between flexible surfaces and flexible rods; we therefore restrict to global changes in the surface, in which the scale parameter  $R$  is adjusted.

We are especially interested in finding the value of the surface size  $R$  in equilibrium. We introduce the net radial force

$$f_r(L, R) := - \left. \frac{\partial E}{\partial R} \right|_{(L, R)}, \quad (5.56)$$

will vanish at some equilibrium radius  $R_0$ . On the cylinder,  $f_r$  is equivalent to  $\int \boldsymbol{\lambda} \cdot \hat{\mathbf{r}} \, ds$ , but this is not true in general. On other surfaces  $\boldsymbol{\lambda} \cdot \hat{\mathbf{r}}$  includes contributions from the tangential components of  $\boldsymbol{\lambda}$ , which should not be transmitted to the surface. Although we use the symbol  $f_r$  and the term “force”, we should emphasize that  $f_r$  is not necessarily an actual force that is applied anywhere. Instead, it serves to keep track of how the energy changes with respect to the scale parameter  $R$ , and so we interpret it as a generalized force.

It is important to point out that classical dynamin is much stiffer than the substrate, though it is not obvious that this holds for all proteins in the dynamin family. One might argue it would be more appropriate to allow the surface, rather than the filament, to bend, as we did in section 3.2.4.

The bending moduli of the membrane and the filament can be compared (despite having different dimensions) using the membrane’s intrinsic length scale, which is defined in terms of its bending rigidity  $\kappa$  and applied tension  $\sigma$  as  $r_c = \sqrt{\kappa/2\sigma}$  [RKL<sup>+</sup>10]. In equilibrium, the membrane forms cylinders of radius  $r_c$ . Taking  $r_c = 15 \text{ nm}$ ,  $\kappa = 20 k_B T$ , we see that  $\kappa r_c / \alpha \approx 3 \times 10^{-3}$ , indicating that the filament is quite stiff.

However, it is somewhat curious that classical dynamin should be so stiff. By studying a more flexible filament, we can consider hypothetical designs for dynamin, and possibly other members of the dynamin family. Furthermore, this model will serve as a stepping stone to one that includes the elasticity of both objects. We expect the present model will correctly account for many qualitative properties, such as the approximate shape of the filament and binding phase diagrams determined by geometry and polymerization force.

### 5.2.1 Cylindrical substrate

In many *in vitro* experiments, dynamin is bound to cylindrical membrane tubules [RUFDC06a, BAE<sup>+</sup>08a]. The advantage of using cylindrical tubules is that the cylinder’s radius is determined by the membrane tension, and is thus easy to tune. We will now use this case to illustrate the concepts of our model without immediately getting bogged down in mathematics.

We begin by solving the shape equation for the filament. We can then calculate the total energy of the ground state as a function of  $L$  and cylinder radius  $R$ . This will allow us to determine whether it will bind at a given value of  $\mu$ . Supposing that it does, we can then calculate the total radial force  $f_r$  exerted on the surface.

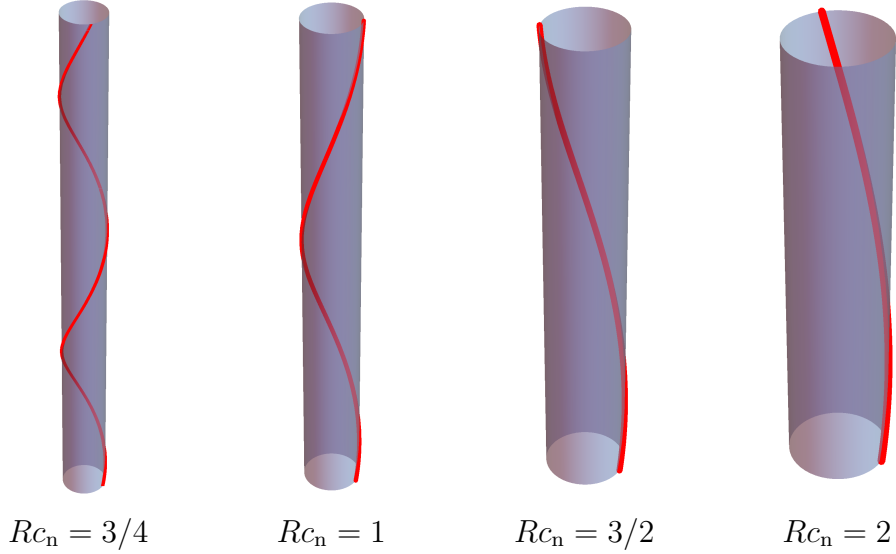


**Figure 5.11:** The equilibrium configuration of filaments confined to the surface of a cylinder is helical, with pitch angle  $\theta_0$ . The pitch of the filament in equilibrium depends on the radius of the cylinder.

Recall that the Darboux curvatures on a cylinder are given by

$$\kappa_g = \theta'(s) \quad (5.57a)$$

$$\kappa_n = \frac{\cos^2 \theta}{R} \quad (5.57b)$$

$$\kappa_t = \frac{\sin 2\theta}{2R} \quad (5.57c)$$

where  $\theta$  is the angle between the filament's tangent vector  $\mathbf{T}$  and the local horizontal  $\hat{\phi}$  (see figure 5.1).

Just as in section 5.1, the symmetries of the cylinder provide two integrals of the Euler-Lagrange equation, leading to a rigorous analogy to a particle in a potential. In this case, the Euler-Lagrange equation integrates to

$$\mathcal{H} = \frac{\theta'^2}{2} - \frac{1}{2} \left( \frac{\cos^2 \theta}{R} - c_n \right)^2 - \frac{1}{2} \left( \frac{\sin 2\theta}{2R} - c_t \right)^2 - f \sin \theta - \frac{m}{R} \cos \theta, \quad (5.58)$$

where  $f$  and  $m$  are the conserved stress and torque along the  $z$ -axis, respectively. Because the endpoints of the filament are free,  $f$  and  $m$  both vanish. As discussed above, in this case, we are interested in the lowest energy configuration of the filament. This occurs when  $\theta' = 0$ , and the remaining “potential energy” term is minimized. The minimum is at  $\theta_0$  such that

$$\tan(2\theta_0) = \frac{Rc_t}{Rc_n - 1/2}. \quad (5.59)$$

Since each point along the helix is identical,  $\theta_0$  completely characterizes the shape of the filament.

Inserting  $\theta(s) = \theta_0$  into the energy functional, we find the total energy of the ground state

$$E(L, R) = \frac{\alpha L}{2R^2} \left( \left[ \left( Rc_n - \frac{1}{2} \right)^2 + R^2 c_t^2 \right]^{1/2} - \frac{1}{2} \right)^2. \quad (5.60)$$

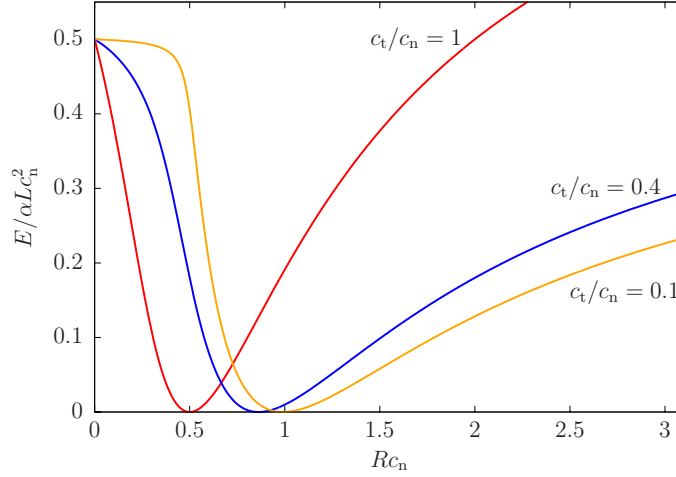


**Figure 5.12:** Energy  $E$  per unit length on the cylinder as a function of cylinder radius. Because  $E$  is linear in  $L$ , this has a second interpretation as a phase diagram.

Note that  $E$  is a linear function of  $L$ , and hence that  $E - \mu L$  is as well. If  $E - \mu L$  is increasing as a function of  $L$  (i.e.  $\mu < \partial E / \partial L$ ), the lowest energy state is realized at  $L = 0$ , so there is no polymerization at all. If  $E - \mu L$  is decreasing (i.e.  $\partial E / \partial L < \mu$ ), there is no minimum, and polymerization continues without bound. The equilibrium length is never finite! However, in experiments, it is possible to find finite polymers on cylinders. Our model hence suggests that these are not in equilibrium. Indeed, in Ref [RKL<sup>+</sup>10] it was found that, given enough time, cylindrical tubules will become completely coated with dynamin.

In figure 5.12, the energy density  $E/L$  is shown as a function of  $R$  for a few values of  $c_t/c_n$ . There is a minimum at  $R = R_0 = c_n / (c_n^2 + c_t^2)$ , corresponding to the radius the helix would have in the absence of a cylinder. Because  $E$  is exactly linear in  $L$ , the energy density  $E/L$  is equal to the binding threshold for  $\mu$ . Figure 5.12 can thus also be interpreted as a phase diagram with  $R$  on the horizontal axis and  $\mu$  on the vertical axis. Each energy density curve is then interpreted as a phase boundary for filaments with that ratio of  $c_t/c_n$ . If  $\mu \geq E/L$ , infinite binding occurs, while no binding occurs if  $\mu < E/L$ .

This concept is perhaps easier to understand by imagining a system at fixed  $\mu$ , with many tubules of different radius. By solving the inequality  $\partial E / \partial L < \mu$  for  $R$ , we can find which radii dynamin binds onto,

$$\frac{c_n - \sqrt{2\mu/\alpha}}{c_n^2 + c_t^2 - 2\mu/\alpha} < R < \frac{c_n + \sqrt{2\mu/\alpha}}{c_n^2 + c_t^2 - 2\mu/\alpha}. \quad (5.61)$$

This inequality shows directly how  $\mu$  relates to recruitment. At small  $\mu$ , the range is very narrow, so dynamin only binds on tubules with geometry similar to its own. The range of permissible radii widens as  $\mu$  increases. At  $\mu = \alpha(c_n^2 + c_t^2)/2$  (for classical dynamin  $\approx 220k_B T/\text{nm}$ ), the upper bound on  $R$  diverges, implying that dynamin polymerizes even on flat surfaces. This transition should be measurable in a lab environment, since for this polymerization force, dynamin should coat membranes regardless of their curvature. Although the transition  $\mu$  is too large to be accessible

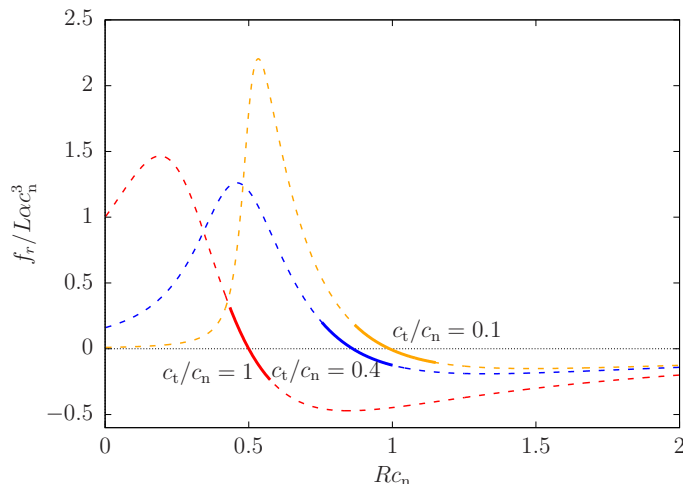


**Figure 5.13:** Force per unit length on the cylinder as a function of cylinder radius. Negative forces correspond to constricting the substrate. Solid lines indicate where binding would occur given a realistic polymerization force of  $5 k_B T/\text{nm}$ .

experimentally for classical dynamin, it would be much smaller for dynamin variants that have larger radii or softer bending rigidities.

When the polymerization force is more realistic, dynamin automatically polymerizes on tubules with radii close to  $R_0$ . If tubules in the limits set by Inequality (5.61) do not form spontaneously, other proteins have to partially constrict the membrane before dynamin can begin to bind and polymerize. Indeed, it appears that this role is played by clathrin in vesicle fission and the ER in mitochondrial fission.

The total radial force  $f_r$  is plotted in figure 5.13. The force vanishes on cylinders of radius  $R_0 = c_n/(c_n^2 + c_t^2)$ , as mentioned above. Intuitively, the filament pushes (or pulls) the surface towards this radius, so that the surface conforms to the polymer's preferred size.

Of course, whether any force is applied to the surface is contingent on the polymer's binding at all. For a given value of  $\mu$ , there is *no force at all* on tubules that do not satisfy inequality (5.61). In figure 5.12, solid lines indicate the radii at which binding would occur (and hence force would be applied) given  $\mu = .01\alpha c_n^2 \approx 5 k_B T/\text{nm}$ , while dashed lines indicate where it would not. For this value of  $\mu$ , the equilibrium radius  $R_0$  is only about 15% smaller than the maximum radius allowed by inequality (5.61).

Note that  $R_0$  decreases for increasing  $c_t$ . Thus the inner radius of the helix can be decreased by twisting as well as bending, suggesting one explanation for why dynamin twists during its conformational change [RUFDC06a].

## 5.2.2 Catenoidal substrate

We use a catenoid to represent the neck between two compartments undergoing fission. The surface is parametrized as

$$\mathbf{X}(\phi, z) = \begin{pmatrix} R \cosh(z/R) \cos \phi \\ R \cosh(z/R) \sin \phi \\ z \end{pmatrix}. \quad (5.62)$$

The catenoid is an ideal candidate for the neck because it has zero extrinsic curvature, and therefore minimizes the energy of a curvature elastic membrane. Indeed, it has been shown that as the neck between two vesicles becomes much smaller than the vesicle radius, it approaches this shape [FMR<sup>+</sup>94].

On the catenoid, the Darboux curvatures are given by

$$\kappa_g = \theta' - \frac{\sinh(z/R) \cos \theta}{R \cosh^2(z/R)} \quad (5.63a)$$

$$\kappa_n = \frac{\cos(2\theta)}{R \cosh^2(z/R)} \quad (5.63b)$$

$$\kappa_t = \frac{\sin(2\theta)}{R \cosh^2(z/R)} \quad (5.63c)$$

Clearly, the translational symmetry along the  $z$ -axis is broken. As a result, the Euler-Lagrange equation cannot be reduced to a quadrature.

The dependence of the ground state energy on  $L$  becomes non-trivial because not all points on the surface are equivalent. We emphasize this because it allows the possibility of finite length polymers in equilibrium. Theory and experiment suggest that these shorter polymers are better suited to mediating fission than very long ones [SBA<sup>+</sup>13, LPJ08, MLP<sup>+</sup>10].

Specifically, using equation (4.94), the Euler-Lagrange equation is given by

$$\begin{aligned} \kappa_g'' + c_t \kappa_n' - c_n \kappa_t' + \kappa_g \left( \frac{\kappa_g^2 + \kappa_n^2 - c_n^2 + \kappa_t^2 - c_t^2}{2} - \mathcal{H} \right) \\ + \kappa_t \left( \kappa_g \left[ \frac{c_n \kappa_t}{\kappa_n} - c_t \right] + \kappa_n' + \frac{\kappa_t \kappa_t'}{\kappa_n} \right) = \frac{\kappa_n^2 + \kappa_t^2}{\kappa_n} (\kappa_t' + c_n \kappa_g). \end{aligned} \quad (5.64)$$

The conserved torque is given by

$$\begin{aligned} m = -\kappa_g \tanh\left(\frac{z}{R}\right) + (\cos \theta (\kappa_n - c_n) + \sin \theta (\kappa_t - c_t)) \operatorname{sech}\left(\frac{z}{R}\right) \\ - R \cosh\left(\frac{z}{R}\right) \left( \cos \theta \left( \frac{\kappa_g^2 + \kappa_n^2 - c_n^2 + \kappa_t^2 - c_t^2}{2} - \mathcal{H} \right) - \sin \theta (\kappa_g' - c_n \kappa_t + c_t \kappa_n) \right) \end{aligned} \quad (5.65)$$

Using the results of section (4.3), filaments with free endpoints satisfy the boundary conditions (see Table 4.2)

$$m = 0 \quad (5.66a)$$

$$\kappa_g = 0 \quad (5.66b)$$

$$\kappa_g' + 2(c_t \kappa_n - c_n \tau_g) = 0. \quad (5.66c)$$

Unsurprisingly, this higher order shape equation is also much harder to solve. We will therefore have to seek perturbative solutions as well as numerical ones, for which we again use the Matlab routine BVP4C, in order to solve the problem for arbitrary  $\mu$  or  $L$ .

The parameter  $R$  now represents the radius of the neck. For surface coordinates, we use the azimuthal angle  $\phi$  and the height  $z$  above the catenoid's central plane.

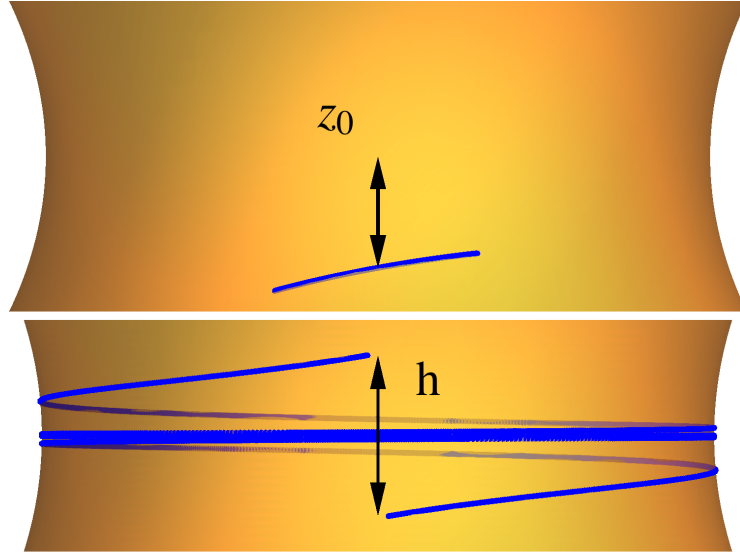


**Figure 5.14:** If  $R < R_c$ , short filaments bind away from the center, while on large catenoids they wind symmetrically about the neck's center.

### Perturbative regime

Since they are accessible analytically, we will first discuss the  $L \ll R$  and  $L \gg R$  limits. Then, we will move on to our numerical studies of intermediate length regime.

We begin our investigation of short polymers with the question whether, and, equally importantly, *where* they bind. Since they prefer to bind at the part of the catenoid that most closely matches their own geometry, they may bind a finite distance  $z_0$  away from the center of the neck, spontaneously breaking the up-down symmetry of the catenoid. We can calculate  $z_0$  for very short filaments with  $L \ll R$ . Again, we admit that in this case our continuum model does not really hold. However, we think this calculation paints an appropriate qualitative picture of dimer or oligomer binding. Let us assume that the filament approximately traces a geodesic on the surface. Then, the energy depends only on  $z(s)$  and  $\theta(s)$ . In the  $L \rightarrow 0$  limit, we can take  $z$  and  $\theta$  to be constant, so that only rigid motions of the dimer are included. In this approximation, the dimer is a directed point-like object. We can write its energy as

$$E = \frac{\alpha L}{2} \left[ \left( \frac{\cos(2\theta)}{R \cosh^2(z/R)} - c_n \right)^2 + \left( \frac{\sin(2\theta)}{R \cosh^2(z/R)} - c_t \right)^2 \right]. \quad (5.67)$$

Minimizing with respect to  $\theta$  and  $z$ , we find that short filaments should have

$$z_0 = \begin{cases} R \operatorname{arsinh} \left( \left[ \frac{R_c}{R} - 1 \right]^{1/2} \right) & R \leq R_c \\ 0 & R > R_c \end{cases} \quad (5.68a)$$

$$\theta_0 = \frac{1}{2} \arctan \frac{c_t}{c_n}, \quad (5.68b)$$

where we have defined the critical radius as

$$R_c := \frac{1}{\sqrt{c_n^2 + c_t^2}}. \quad (5.69)$$

Equation (5.68a) can be understood as follows. On necks with  $R < R_c$ , there are sites where the geometry of the surface and the polymer match exactly: the polymer can choose  $z$  and  $\theta$  so that  $\kappa_n$  and  $\kappa_t$  take their preferred values,  $c_n$  and  $c_t$ . However, on larger necks, the polymer prefers to be more strongly curved than any point on the catenoid, and so binds at the most curved site available, which is the center of the neck.

We can insert these results on the ground state of short filaments from equations (5.68a) and (5.68b) into the energy in equation (5.67) to find the elastic energy of short filaments. This is important because the competition between this and the binding energy determines whether binding occurs at all. Differentiating the total energy with respect to  $L$ , we find

$$\mu_0 = \begin{cases} 0 & R \leq R_c \\ \frac{1}{2}\alpha(R^{-1} - R_c^{-1})^2 & R > R_c. \end{cases} \quad (5.70)$$

Binding occurs for any  $\mu$  if  $R \leq R_c$ , again because if  $R < R_c$ , there are sites on the surface matching the preferred geometry of the polymer exactly. The non-zero binding threshold for  $R > R_c$  reflects the fact that it costs energy for polymers to form on large necks. At a given value of  $\mu$ , this threshold also implies an upper bound on  $R$ . Solving equation (5.70) for  $R$ , we see that binding will only occur on necks with

$$R \leq R_{\max} = \frac{R_c}{1 - R_c \sqrt{2\mu/\alpha}}. \quad (5.71)$$

When  $\mu > \alpha/2R_c^2 = \alpha(c_n^2 + c_t^2)/2$ , the upper bound diverges, and binding occurs on necks of any size. This is the same as the threshold for binding to cylinders of any size, implying it is the threshold for binding to planes.

In the opposite case of  $L \gg R$ , the behavior of the filament is determined by the spontaneous curvature  $c_n$  relative to the radius of the neck. If the filament is strongly curved, the polymer prefers to go towards the most curved parts of the catenoid, i.e. the center. In the weak curvature case, it rather prefers the flat parts above and below the neck. As the polymer grows, material is added to the preferred region, and the shape away from that region is left unchanged. The energetic cost of growing the polymer then becomes independent of  $L$ , so that the energy  $E(L, R)$  asymptotically grows linearly in  $L$ . It is therefore useful to define  $\mu_\infty(R) = \lim_{L \rightarrow \infty} \partial E / \partial L$ . When  $\mu > \mu_\infty$  the ground state becomes infinitely long.

To determine  $\mu_\infty$ , we will find the energetic cost of adding material either at the neck's center or in the flat regions of the catenoid. First, we consider the weak curvature case. Far away from the center of the neck, all curvatures are approximately zero. We calculate the energetic cost of adding material to this region by inserting  $\kappa_g = \kappa_n = \kappa_t = 0$  into equation (5.53), and see that the energy density is

$$\mu_\infty^{\text{weak}} = \frac{\alpha}{2} (c_n^2 + c_t^2). \quad (5.72)$$

On the other hand, strongly curved polymers add material at the center of the neck as they grow. At that point,  $\kappa_g = \kappa_t = 0$  and  $\kappa_n = 1/R$ . Inserting these values into the energy density gives

$$\mu_\infty^{\text{strong}} = \frac{\alpha}{2} \left[ \left( \frac{1}{R} - c_n \right)^2 + c_t^2 \right]. \quad (5.73)$$

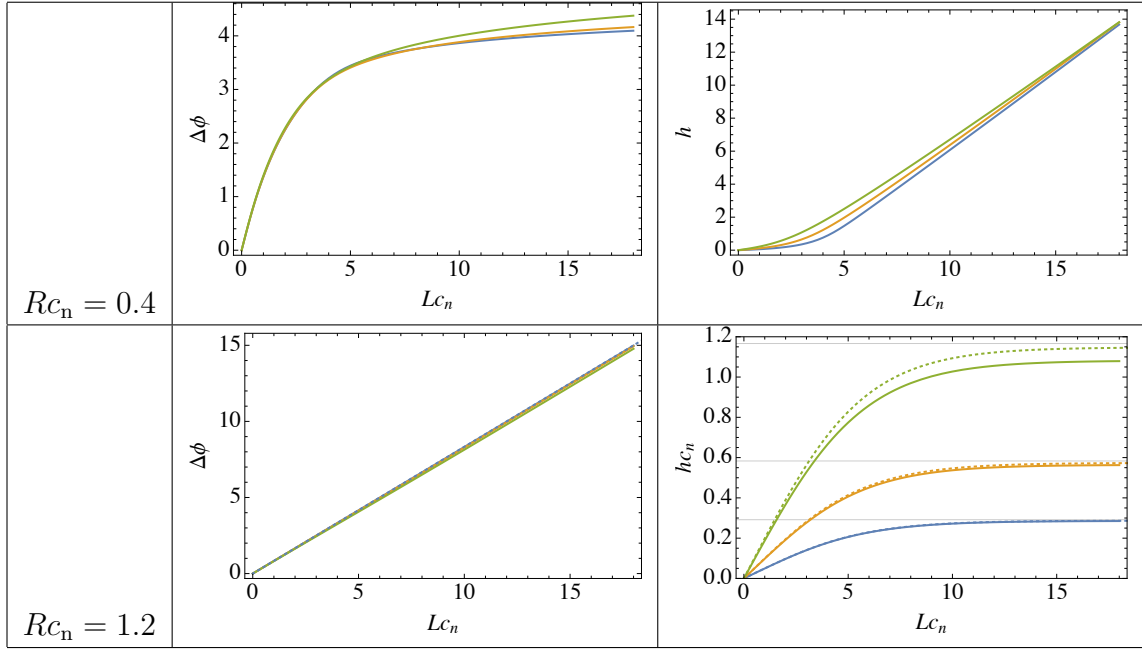


**Figure 5.15:**  $\Delta\phi$  and  $h$  in the weak and strong curvature regimes. Blue, orange, and green lines have  $c_t/c_n = 0.1$ ,  $c_t/c_n = 0.2$ , and  $c_t/c_n = 0.4$ , respectively. The solid and dotted lines correspond to numerical and perturbative results, respectively. In the bottom right panel, the asymptotic height for each value of  $c_t$  is indicated by the gray lines.

Comparing equations (5.73) and (5.72) allows us to make the distinction between strong and weak curvature more precise. If  $Rc_n < 1/2$ , the filament's energy is lower in the flat regions of the catenoid than at the neck. While the stress free state in the weak curvature regime is of course not a perfectly straight rod, even such a configuration is lower in energy than binding at the neck. Obviously, the ground state is not centered at the neck. This makes the regime  $Rc_n < 1/2$  quite unrealistic for dynamin, and so we will ignore it from now on.

Guided by this observation, we will assume the filament lies approximately at the ring with  $z = 0$  and  $\theta = 0$ , and therefore write  $z(s) = \epsilon z_1$ ,  $\theta(s) = \epsilon \theta_1$ . To lowest order, this implies

$$z' = \frac{\sin \theta}{\cosh(z/R)} \implies z'_1 = \theta_1, \quad (5.74)$$

$$\phi' = \frac{\cos \theta}{R \cosh(z/R)} \implies \phi_1 = \frac{s}{R}. \quad (5.75)$$

We will also assume that  $c_t$  is of order  $\epsilon$ ; physically, this is a valid limit for classical dynamin, for which  $c_t/c_n \approx 10^{-1}$ . This limit is also necessary from a mathematical perspective for our assumption that the filament is approximately circular to hold, and for the condition  $m = 0$  to be satisfied. At first order in  $\epsilon$ , the Euler-Lagrange equation (5.64) becomes

$$R^4 z_1^{(4)}(s) - 2(2Rc_n + 1)R^2 z_1''(s) + (2Rc_n - 1)z_1 = 0. \quad (5.76)$$

Measuring  $s$  from the center of the filament,  $z_1$  should be an odd function of  $s$ . It

is therefore given by

$$z_1 = A_1 \sinh(k_1 s) + A_2 \sinh(k_2 s), \text{ where} \quad (5.77)$$

$$k_1 = \frac{\sqrt{1 + 2Rc_n} + \sqrt{2 + 2Rc_n + 4R^2c_n^2}}{R}$$

$$k_2 = \frac{\sqrt{1 + 2Rc_n} - \sqrt{2 + 2Rc_n + 4R^2c_n^2}}{R}. \quad (5.78)$$

We can determine the coefficients  $A_1$  and  $A_2$  by enforcing the boundary conditions (5.66b)-(5.66c) at  $s = \pm L/2$ ,<sup>1</sup> leading to

$$A_1 = \frac{2R(1 - R^2k_2^2)c_t \sinh(k_2L/2)}{k_2(1 - k_1^2R^2)^2 \cosh(k_2L/2) \sinh(k_1L/2) - k_1(1 - k_2^2R^2)^2 \cosh(k_1L/2) \sinh(k_2L/2)} \quad (5.79a)$$

$$A_2 = \frac{2R(1 - R^2k_1^2)c_t \sinh(k_1L/2)}{k_1(1 - k_2^2R^2)^2 \cosh(k_1L/2) \sinh(k_2L/2) - k_2(1 - k_1^2R^2)^2 \cosh(k_2L/2) \sinh(k_1L/2)}. \quad (5.79b)$$

Let us define the amount the filament winds around the neck  $\Delta\phi(L) = \phi(L) - \phi(0)$ , and the height of the filament  $h(L)$  (see figure 5.14). For our perturbative calculations,  $\Delta\phi = L/R$ . At large  $L$ ,  $h(L)$  approaches a finite value

$$h_\infty = \lim_{L \rightarrow \infty} z(L/2) - z(-L/2)$$

$$= \frac{4R^3(k_2^2 - k_1^2)c_t}{k_1(1 - R^2k_2^2)^2 - k_2(1 - R^2k_1^2)^2}. \quad (5.80)$$

These perturbative results agree well with numerical solutions (see comparison in the bottom row Table 5.15). In the bottom left figure of Table 5.15, there is a dotted line indicating our perturbative results for  $\Delta\phi$ , though it is difficult to see. In the bottom right figure, we see that the agreement is poorer for larger values of  $c_t$ . We point out that at  $R = 1/c_n$ ,  $h_\infty$  is approximately  $h_\infty/R \approx \sqrt{2}c_t/c_n$ , reflecting that the ratio  $c_t/c_n$  controls the aspect ratio of the helix.

Because strongly curved polymers are confined within the  $h < h_\infty$  region, the density of polymer in this region becomes large as they grow longer. This build-up is not realistic because physical polymers have finite thickness and cannot overlap. This limits the applicability of our model in certain cases.

### Nonlinear regime

The regime where  $L \sim R$  is much more difficult analytically, and so in this case we rely on numerics. In this regime, a small increase in  $L$  can lead to *global* changes in the filament's shape. As a result,  $\partial E/\partial L$  is a non-trivial function of  $L$  and for certain values of  $\mu$ , there are *finite* values of  $L$  that satisfy equation (5.54). Our numerical solutions to the shape equation show that the energy of the filament increases monotonically with  $L$ . However, its derivative  $\partial E/\partial L$  is non-monotonic in

<sup>1</sup>This may seem to imply we have four equations for two variables. However, because of the symmetry of the filament, if each condition is satisfied at one end it is also satisfied at the other end. The additional condition  $m = 0$  simply becomes an equation for  $\mathcal{H}$ .

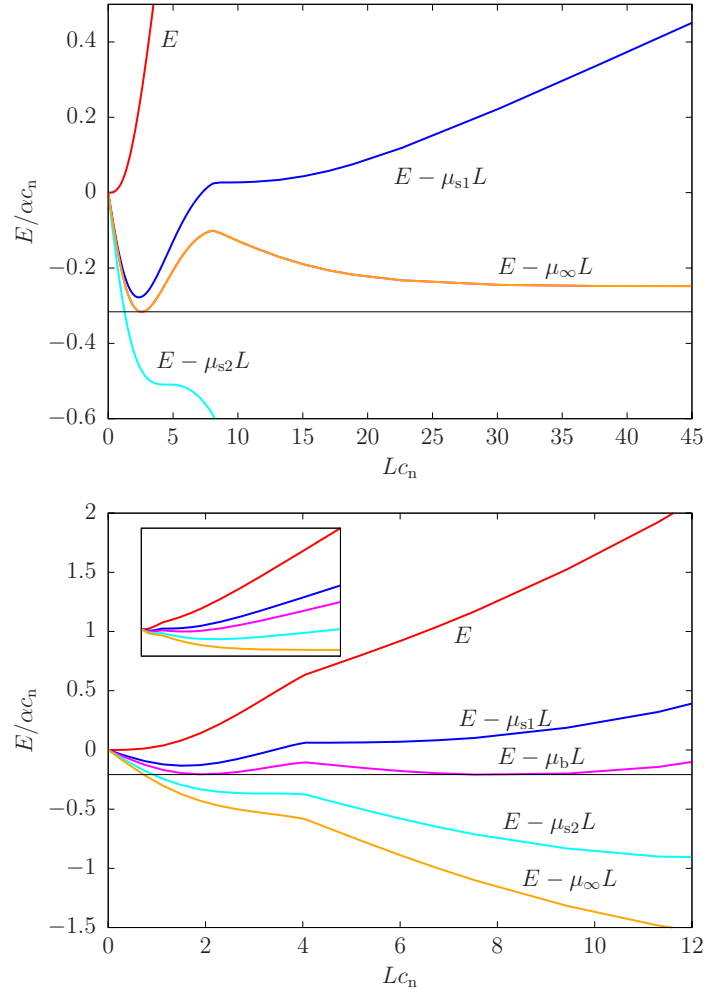


**Figure 5.16:** Total free energy as a function of  $L$  for special values of  $\mu$  explained in the text, with  $Rc_n = 0.6$ ,  $c_t/c_n = 0.1$  (top) and  $Rc_n = 0.6$ ,  $c_t/c_n = 0.4$  (bottom). In the  $c_t/c_n = 0.1$  case, the only transition is from asymmetric binding to infinite (symmetric) binding. The inset shows a zoomed out version.

$L$  if  $R$  is below  $R_c$ , leading to multiple equilibrium states at the same  $\mu$  and complex binding phase behavior.

Let us define a few useful values of  $\mu$  to help decipher the phase diagram in figure 5.17. In figure 5.16 we have plotted the free energy  $E - \mu L$  at these special values of  $\mu$  at  $Rc_n = 0.6$  (note this is still the strong curvature regime, since  $Rc_n > 1/2$ ) with  $c_t/c_n = 0.1$  and  $c_t/c_n = 0.4$ . For small  $\mu$ , the equilibrium state is a short filament centered away from the neck. Increasing  $\mu$  slightly,  $L$  increases and the filament moves towards the center of the catenoid. At  $\mu = \mu_{s1}$ , called the first spinodal, there is an additional state satisfying  $\partial E/\partial L = \mu$ . The higher  $L$  state is not a local minimum of  $E - \mu L$ , but only a saddle point. Interestingly, this state is symmetric under  $z \mapsto -z$ ,  $\phi \mapsto -\phi$ . Increasing  $\mu$  past  $\mu_{s1}$ , the symmetric state splits into two stationary states: one local minimum and one local maximum, both of which are symmetric. Eventually,  $\mu$  is large enough that the stable symmetric state and the asymmetric state have the same free energy. This is called the binodal, and this value of  $\mu$  is denoted  $\mu_b$ . The unstable symmetric state creates an energetic

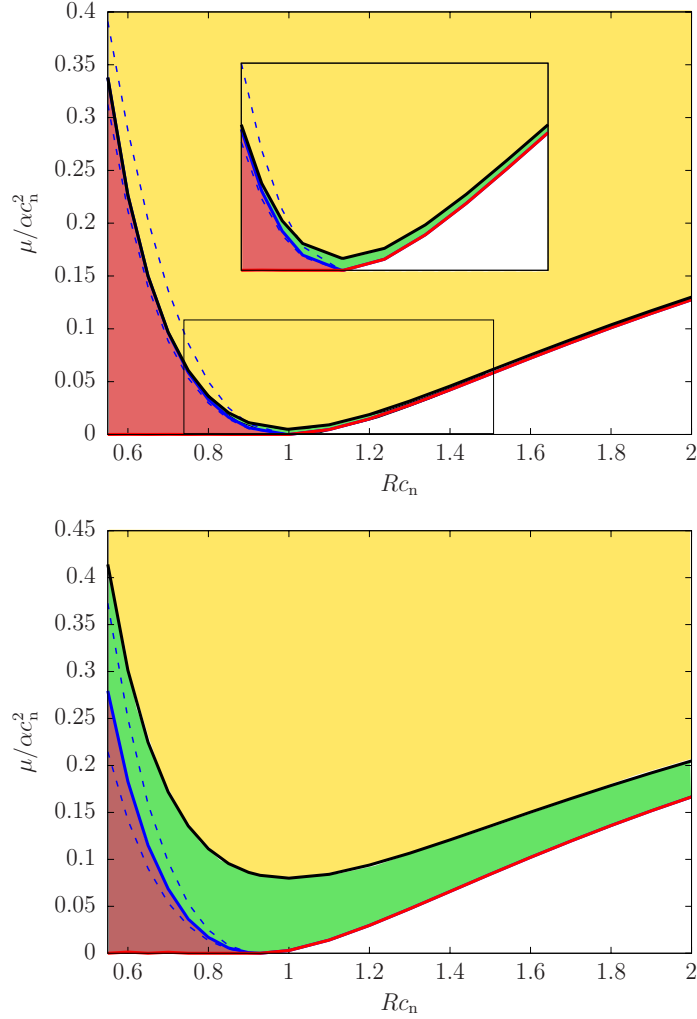


**Figure 5.17:** Phase diagrams for binding on a catenoid with (top)  $c_t/c_n = 0.1$ , (bottom)  $c_t/c_n = 0.4$ . Infinite binding occurs in the yellow region, asymmetric binding in the red region, and symmetric binding in the green region. The binding threshold  $\mu_0$  is shown in red, the binodal  $\mu_b$  in solid blue, the spinodals in dotted blue, and the asymptotic polymerization force  $\mu_\infty$  in black. The  $c_t/c_n = 0.4$  case is less realistic for classical dynamin, but better illustrates the difference between the binodal line and the two spinodal lines. The inset in the top graph zooms in on the boxed region.

barrier between the two stable states. For  $\mu > \mu_b$ , the symmetric state is the global minimum. However, the asymmetric state is still metastable until  $\mu$  reaches the second spinodal point,  $\mu = \mu_{s2}$ . Finally, for  $\mu > \mu_{s2}$  there is only one local minimum, and the ground state is symmetric. This state may or may not have infinite length, depending on whether  $\mu_{s2} > \mu_\infty$ . Indeed,  $\mu_{s2}$  does exceed  $\mu_\infty$  for small  $c_t/c_n$ , as shown in figure 5.17. In that case, the possibility arises that  $\mu_b = \mu_\infty$ , so that the onset of symmetric binding is simultaneous with that of infinite binding (shown in the top panel of figure 5.16).

Figure 5.17 illustrates how these values of  $\mu$  depend on  $R$ . The inset in the top panel shows the very narrow finite binding region when  $c_t/c_n = 0.1$ . We can quantify this narrowness by noting that the infinite binding threshold has a minimum

at  $R = 1/c_n$  given by  $\mu_{\infty, \min} = \alpha c_t^2/2$ . For classical dynamin, this corresponds to about  $2 k_B T/\text{nm}$ . The fact that this is very near the estimated actual value is intriguing, especially in light of studies showing that long polymers are ill-suited for fission. In inequality (5.71), we found the largest neck on which polymers form at a given  $\mu$ . Assuming that no infinite binding occurs, we can find an inequality that depends only on geometric features of the filament by requiring  $\mu < \alpha c_t^2/2$ ; one finds

$$R < \frac{R_c}{1 - R_c c_t} = \frac{1}{\sqrt{c_n^2 + c_t^2} - c_t}. \quad (5.81)$$

In figure 5.18, we show how the equilibrium length of the filament at fixed  $\mu$  depends on the radius of the neck, again with  $c_t/c_n = 0.1$  on the top and  $c_t/c_n = 0.4$  on the bottom. The symmetric-asymmetric binding transition has been omitted from the figure; it would manifest as a discontinuous drop in  $L$  at lower values of  $R$ . The violet curves illustrate what happens when  $\mu > \alpha c_t^2/2$ : if  $R$  lies within a certain finite interval (delimited by the dotted violet lines), the length diverges. The green curves have  $\mu = \alpha c_t^2/2$ , and hence diverge at  $R c_n = 1$ . At lower values of  $\mu$ , the length is always finite.

The dotted black line shows the radius for which the energy is minimal (which, in this case, depends on  $L$ ). At a given  $\mu$ , this plot thus also illustrates the energetic gradient flow. One imagines a pre-existing vesicle neck, for instance as created by clathrin. If this neck is small enough, dynamin binds, and in doing so, exerts forces constricting the neck. Energy minimization causes the system to flow along a fixed- $\mu$  curve toward  $R_0$ , i.e. the dotted line. As the radius decreases, the length of the polymer grows at first, reaching a maximum around  $R c_n \approx 1$ , when, surprisingly, the polymer actually shrinks again. Ultimately, equilibrium is reached at  $R = R_0$ . The filament cannot wrap entirely around the neck unless the length  $L$  is at least  $2\pi R$ . The solid black line in the figure shows this minimum length. If  $L$  is below this line at the equilibrium radius, adjacent rungs of the filament are unable to interact. Since such interactions are hypothesized to be essential for fission, this threshold could be very important [SBA<sup>+</sup>13].

Although we do not have an analytical expression for  $E(L, R)$ , we can determine  $R_0$  via perturbation theory when  $L \ll R$  and  $L \gg R$ . For very short filaments,  $E \approx \mu_0 L$ : minimizing the right hand side of equation (5.70) with respect to  $R$ , one finds  $R_0 = R_c$ . On the other hand, for long filaments,  $E \approx \mu_\infty L$ : minimization gives  $R_0 = 1/c_n$ . Interestingly,  $R_0$  is not monotonic in  $L$ , and does not depend on  $c_t$  if  $L$  is large. This suggests two advantages of shorter polymers: they have smaller equilibrium radii, and they enable the twisting motion of dynamin's conformational change to reduce the equilibrium radius further.

With knowledge of  $R_0$  and the maximum binding radius  $R_{\max}$  given by equation (5.71), we can estimate how much strain dynamin imposes on a neck without GTP hydrolysis. We define the maximum strain as

$$\gamma = \frac{R_{\max} - R_0}{R_{\max}} \approx \sqrt{\frac{2\mu}{\alpha}} R_c, \quad (5.82)$$

where we have ignored the slight decrease in  $R_0$  which occurs for low  $L$ . As one sees in the top panel of figure 5.18, for realistic values of  $c_t$  and  $\mu$  the radius of the neck only decreases by about 10-15%. It has been estimated that to induce fission, a much more dramatic decrease from 15 nm to 3 nm would be necessary [KK03].

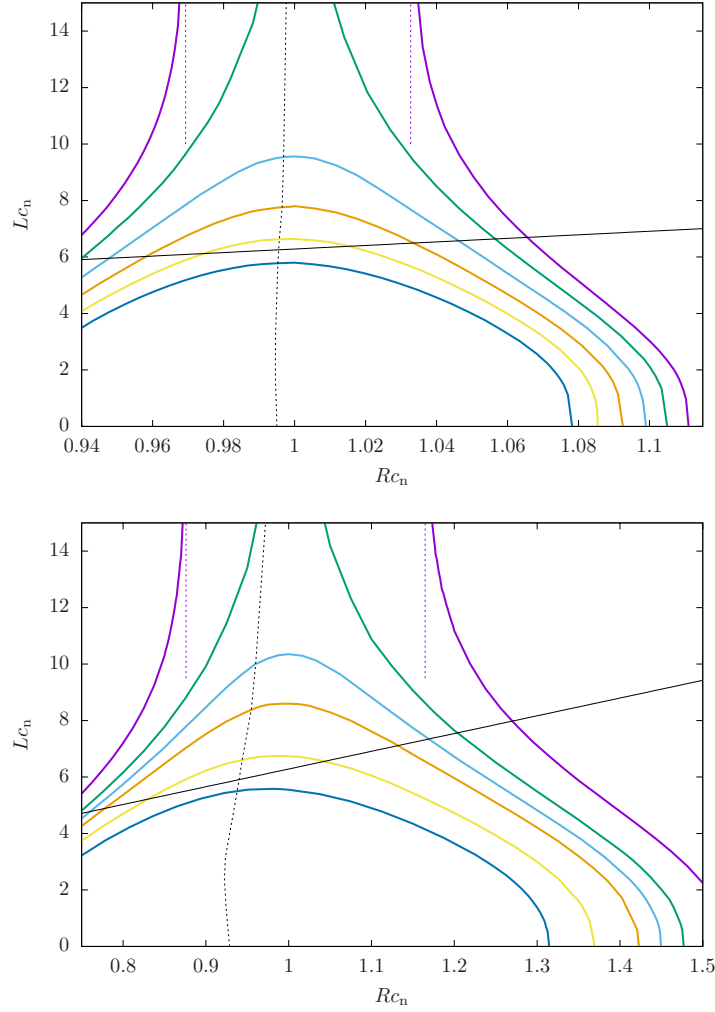


**Figure 5.18:** Equilibrium length as a function of  $R$  at fixed  $\mu$  with  $c_t/c_n = 0.1$  (top), and  $c_t/c_n = 0.4$  (bottom). The solid black line is  $L = 2\pi R$ , which of course indicates the threshold for winding once around the neck. The dotted black line shows where the energy is minimized with respect to  $R$ . In the top figure, the curves are  $\mu/\alpha c_n^2 \times 10^3 = 5.5, 5, 4.5, 4, 3.5, 3$ , going from top to bottom. In the bottom figure, they are  $\mu/\alpha c_n^2 \times 10^3 = 90, 80, 75, 70, 60, 50$ .

As in the cylindrical case, the fact that the neck must be of similar size to the filament's rest state in order for polymerization to occur inhibits passive constriction of the neck.

### 5.2.3 Conclusions

We have analyzed the binding of a curved polymer with constant polymerization force to cylindrical and catenoidal substrates with the aim of constructing a minimal model of dynamin and similar proteins. This model is a substantial jump in realism from our previous analysis of cylindrical confinement of semi-flexible polymers in section 5.1. Here, we include helical rest configurations and a more realistic surface geometry. We also allow the length of the polymer to vary and remove the constraint that the polymer close back on itself.

On the cylinder, the energy of the filament is linear in  $L$ , hence it is minimized at either  $L = 0$  or  $L = \infty$ , eliminating a finite binding phase. This suggests a limitation of experiments using only cylindrical substrates: membrane bound dynamin polymers will tend to be very long, but shorter polymers may be more efficient fission machines [SBA<sup>+</sup>13]. Experiments on cylindrically bound dynamin can be useful for studying intermediate stages in the fission process or dynamin’s conformational change (for example), but are not likely to accurately reflect the dynamics of *in vivo* fission.

It is possible that there is a finite binding phase on cylinders which we overlooked by omitting membrane deformations from our analysis. However, no such phase was found in [RKL<sup>+</sup>10], in which Roux et al. studied dynamin binding onto cylindrical tubules at many different concentrations. If such a phase does exist, it seems to occur over a very narrow range in  $\mu$ .

On the catenoid, however,  $E$  depends non-trivially on  $L$ , creating the possibility for equilibrium finite length polymers. In fact, all polymers have finite length if  $\mu < \alpha c_t^2/2$ . Intriguingly, experimental estimates of  $\mu$  are very close to this bound, suggesting that dynamin may indeed have evolved to avoid this transition. The significant difference between the binding phase diagram on the cylinder and the catenoid suggests that dynamin’s behavior depends strongly on the shape of the substrate, a fact which to our knowledge has not been explored experimentally.

We must point out, though, that the infinite polymerization presented in our model is incomplete, because we allow the polymer to wind infinitely densely around the center of the neck. It is clear that, in reality, as more dynamin binds, more of the surface is occupied. The actual behavior of very long filaments depends on how the polymer rigidity  $\alpha$  compares to the membrane bending rigidity, usually called  $\kappa$ . If  $\kappa$  is sufficiently small, dynamin could begin to tubulate the membrane before infinite binding becomes relevant.

The equilibrium cylinder radius  $R_0$  decreases as a function of  $c_t$ . This reflects the fact that twisting of the polymer can lead to constriction. For catenoidally bound polymers,  $R_0$  depends additionally on the polymer’s length. For large  $L$ ,  $R_0 \approx 1/c_n$  is independent of  $c_t$ . If  $L$  is small,  $R_0 \approx R_c$ . The twisting motion of dynamin’s conformational change is therefore put to best use by short polymers. Though if the polymers are too short, they may just detach from the membrane when stressed, rather than induce any geometric change. Detachment is more difficult if they are long enough to wind completely around the neck. Furthermore, longer polymers are able to exert larger forces on the membrane. Understanding the balance between these considerations would require a model of the dynamin-membrane interaction far from equilibrium.

The adhesion energy or polymerization force  $\mu$  limits the range of surfaces on which filaments will bind, and hence the extent to which the filament can deform the surface. Because we do not allow the surface to deform locally, we expect that in reality this range is wider than our model predicts. On cylindrical membranes, dynamin only binds if the radius is near the equilibrium radius  $R_0$ . In the catenoidal case, dynamin is only drawn to the central neck if the latter is larger the critical radius  $R_c$ . This competition of binding energy and elastic deformation leads to a physical explanation for recruitment: polymerization only occurs if the substrate is already geometrically similar to the polymer. This offers a mechanical answer to the question, “what prevents dynamin from turning all membrane into vesicles”

[vdB99]. However, mismatch in the geometries of the filament and the substrate also induces stress in the filament, and therefore force on the substrate. Thus the easier it is for dynamin to bind, the less useful it is for constricting, presenting something of a catch-22. This is perhaps why dynamin-mediated fission relies on a conformational change in the protein [BAE<sup>+</sup>08a, PS08, RUFDC06a]: without such a reconfiguration, very little constriction is possible.

We conclude that elasticity alone probably does not account for dynamin's fission capacity. According to our model, fission requires an equilibrium-breaking active process. However, we have of course only examined the region of parameter space we believe to be most relevant, and we cannot totally rule out the possibility of a passive fission mechanism.

# Chapter 6

## Conclusion and summary

Throughout this thesis, we have seen many applications of the elasticity of low-dimensional continua to soft matter and biological problems. Evidently, a top down view can be very informative about biological systems, even in cases where the effects of chemistry are also essential. Let us review our findings, and discuss some potentially interesting avenues of inquiry for the future.

In Chapter 2, we briefly reviewed the geometry of curves and surfaces in three dimensional space. We also introduced energy functionals for filaments and sheets, endowing them with mechanical as well as geometric properties.

In Chapter 3, we focused on surfaces. In section 3.1, we discussed the buckling of membranes, to which we applied a novel extension of the Helfrich model. This extension is very simple; the energy density is both continuous and smoothly differentiable. It is therefore surprising that the system exhibits anomalous and pathological behavior, including negative compressibility and faceting. To date, the predictions of the model have not been compared with the kinks formed in simulated membranes. Does the model accurately capture the transition from smooth to kinked, that is, does it predict the right phase diagram? Can it predict the change in the membrane's tangent angle across a kink? Another interesting question that remains open is how this model behaves in different topologies, such as those of spherical vesicles or cylindrical tubules. Perhaps an analytical study of the faceting of gel phase vesicles is feasible.

Then in section 3.2, we considered helicoidally symmetric surfaces. Using an elegant parametrization first applied by Do Carmo [DCD82], we were able to easily study helicoidal minimal surfaces, which we found have a singular transition from a regime with two solutions to a regime with no solutions, exactly like that of axially symmetric minimal surfaces. This parametrization also facilitated an analysis of the conservation laws emerging from the helicoidal symmetry. A conserved stress associated with translation and rotation invariance of the energy functional emerged. Interestingly, the scale invariance of the conformally symmetric Willmore functional was broken because of the fixed length scale implicit in helicoidal symmetry, i.e. the pitch. Therefore the conserved quantity associated with the scale invariance of the Willmore functional is not conserved on helicoidal Willmore surfaces. This is reminiscent of the concept of an *anomaly* in quantum field theory, and would be interesting to examine in those terms.

Our analysis of helicoidal soap films raised the possibility of an interesting explanation for how the membrane ultimately breaks during dynamin-mediated mem-

brane fission, previously considered by Kozlov [Koz01]. Could membrane fission be explained by a similar instability to that occurring in soap films? If so, fission could be understood entirely at the level of Helfrich theory. Unfortunately, we found that, because the membrane shape equation is higher order than that of a soap film, membranes have a larger space of solutions, and as a consequence do not exhibit a similar instability. The hope for a model of fission at the level of Helfrich theory is significantly diminished, but not gone: it is still possible that a second variation analysis will show that the membrane in fact *does* become unstable, but not in the same way that a soap film does. However, in view of the growing experimental evidence supporting the catalytic model of fission, we are inclined to give it more credence.

In Chapters 4 and 5, we studied elastic filaments confined to rigid surfaces. Chapter 4 reviewed and expanded on the theoretical fundamentals originally found by Guven and Vázquez-Montejo. That group originally devised a powerful method of analysis for surface-confined filaments, which they first applied to Euler rods confined to spheres [GVM12], then generalizing the theory with Valencia to any rod with a cross section fixed relative to the surface normal [GVVM14]. Our contribution was to expand their theory to filaments with freely rotating cross sections; this also elucidated certain aspects of the theory with fixed cross sections that were previously unclear. Unfortunately, we were unable to extend the theory to include the elasticity of the substrate. As it turns out, the interaction between a flexible one-dimensional object and a flexible two-dimensional object is analytically quite difficult. At a heuristic level, we can anticipate a form for the Euler-Lagrange equations. The Euler-Lagrange equations for each of the membrane and the filament separately state that the forces on the object in question vanish; rendering this statement in geometrical language makes finding equilibrium configurations possible. It seems that coupling the surface and filament together should require simply that the forces on each object are balanced by those of the other at the places where they are in contact. Regrettably, a proof for this statement turns out to be elusive.

Chapter 5 contained applications of the results of Chapter 4. First, in section 5.1, we considered Bernoulli-Euler rods confined to a cylinder. Despite being one of the simplest possible examples of a confined elastic filament, this problem turned out to be surprisingly rich, illustrating the mathematical complexity exhibited by confined filaments. This analysis led to the counter-intuitive result that it is possible for closed elastic loops to constrict cylinders, depending on the topology of the loop. Specifically, the loop must wind more than once around the cylinder to impart constrictive forces at every point. Though this is far from a realistic description of dynamin’s constriction of a membrane neck, it qualitatively illustrates how such constriction can be possible. If the dynamin helix wraps multiple times around the membrane neck, it can be “topologically” prevented from disassociating from the membrane, similarly to these loops.

Lastly, in section 5.2, we pursued a model of dynamin-mediated fission from another perspective: one in which the filament is flexible, and the surface is fixed. The theory of surface-confined elastic rods with *fixed* cross sections was perfect for this task, as dynamin’s membrane binding is localized to one domain. Competition between the energetic costs of elastic deformation and the energetic gain of binding emerged naturally from the model. This competition suggests a potential explanation for how dynamin is recruited to membrane necks. The model also

provides evidence that a passively constricting filament would not be capable of initiating membrane fission. The local membrane deformations that would result from the forces exerted on the membrane by the polymer were notably absent from our model. However, in light of our analysis of helicoidal membranes (indicating that helicoidal membranes are mechanically stable), pursuing a complete continuum theory of polymer-membrane interactions would, in our view, not be especially useful for understanding dynamin. Including these features in our model would probably lead only to a quantitative change in our binding phase diagrams. Rather, dynamical questions are much more important at this stage. For example, what keeps dynamin from disassembling after the GTP-hydrolysis step? In the language of our model, the GTP-hydrolysis induced conformational change results in an increase of the spontaneous curvature,  $c_n$ . At this stage, equilibrium is likely broken in two ways: firstly, mechanical equilibrium between the protein and the membrane is disturbed; secondly, the dynamin polymer is not at its equilibrium length. Associated with each of these disequilibria, the system can move toward equilibrium either by decreasing the membrane radius or depolymerizing the dynamin. Which happens first determines whether the membrane achieves fission.

# Appendix A

## Illustration of numerical methods

For many problems in this thesis, we have had to solve differential equations with boundary conditions at both the initial point and the final point of the problems domain; such problems are known as *boundary value problems*, as opposed to *initial value problems*, where there are only boundary conditions at one end of the domain. In cases where analytical solutions were not possible, we have used the Matlab routine `bvp4c` to solve these problems. It is worthwhile to discuss our procedure for using `bvp4c` in depth. In this appendix, we will present an illustration of `bvp4c`, applied to the buckling problem from section 3.1. Although we do not use `bvp4c` to solve it in the main text, that problem is just difficult enough to be a useful illustration.

Detailed documentation on `bvp4c` is available online from Mathworks, the creators of Matlab; see reference [Mat].

Before we demonstrate how to put our problem into code, we must discuss a few mathematical details. Namely, the program requires a differential equation of the form

$$\mathbf{y}'(x) = \mathbf{F}(\mathbf{y}, x, \lambda_1, \lambda_2, \dots), \quad (\text{A.1})$$

where  $x$  is the independent variable taking values on the interval  $x \in [x_a, x_b]$ , the vector  $\mathbf{y}$  contains the functions we want to solve for, and the  $\lambda_i$  are some unknown parameters, which the program also solves for. The differential equations we are interested in solving are in every case the Euler-Lagrange equations corresponding to some Lagrangian, and are therefore *not* first order. Whichever problem we want to solve must be rendered in this form before we can use `bvp4c`. Furthermore, the program needs a set of boundary conditions (one for each component of  $\mathbf{y}$  and one for each parameter  $\lambda_i$ ), and a guess for what the solution looks like. Once these have been provided, the routine attempts to minimize the residual  $|\mathbf{y}'(x) - \mathbf{F}(\mathbf{y}(x), x, \lambda_1, \lambda_2, \dots)|$  over a discretization of the domain  $x \in [x_a, x_b]$  [Mat]. In this appendix, we emphasize how to write higher order equations in the appropriate form, find appropriate boundary conditions, and construct clever guesses for the solution.

## A.1 Finding the differential equations

Recall that in that section 3.1 we sought to minimize the functional

$$\frac{\mathcal{E}}{\kappa} = \int dA \left\{ \frac{1}{\ell^2} \left( \sqrt{1 + \ell^2 K^2} - 1 \right) \right\}, \quad (\text{A.2})$$

for a buckled planar membrane. In our original discussion, we solved the Euler-Lagrange equation for this Lagrangian analytically. Here, of course will use a numerical method.

Again, we describe the surface using an angle arc-length parametrization. We add a system of Lagrange multipliers to the functional to both enforce this parametrization and incorporate information about the embedding of the surface in space,

$$\frac{\mathcal{E}}{\kappa} = \int_0^{L_y} dy \int_0^L ds \left\{ \frac{1}{\ell^2} \left( \sqrt{1 + \ell^2 \dot{\psi}^2} - 1 \right) - \frac{f_x}{\kappa} (\dot{x} - \cos \psi) - \frac{f_z}{\kappa} (\dot{z} - \sin \psi) \right\}. \quad (\text{A.3})$$

As it turns out, the multiplier  $f_z$  is always zero for the present problem; it is hence omitted in the text. For the sake of completeness, though, we include it here. Treating  $\mathcal{E}/\kappa L_y$  as the Lagrangian, we can at this stage calculate the Euler-Lagrange equation for the membrane. However, recall that we are looking for a set of *first order* equations to describe the surface; the Hamilton equations for the membrane are obvious candidates that have a few useful extra features.

Varying with respect to  $f_x$  and  $f_z$  returns the constraints defining  $\psi$  and guaranteeing our arc-length parametrization,

$$\dot{x} = \cos \psi \quad (\text{A.4a})$$

$$\dot{z} = \sin \psi. \quad (\text{A.4b})$$

Varying with respect to  $x$  and  $z$  then gives us that  $f_x$  and  $f_z$  are conserved,

$$\dot{f}_x = 0 \quad (\text{A.5a})$$

$$\dot{f}_z = 0. \quad (\text{A.5b})$$

The interesting physics happens around  $\psi$ . The momentum conjugate to  $\psi$  (physically, this is the bending moment of the membrane) is given by

$$p_\psi := \frac{1}{\kappa L_y} \frac{\partial \mathcal{E}}{\partial \dot{\psi}} = \frac{\dot{\psi}}{\sqrt{1 + \ell^2 \dot{\psi}^2}}. \quad (\text{A.6})$$

This is essentially our differential equation for  $\psi$ . However, recall that `bvp4c` requires the equations to be in the form of equation (A.1). We must therefore solve equation (A.6) for  $\dot{\psi}$ ,

$$\dot{\psi} = \frac{p_\psi}{\sqrt{1 - \ell^2 p_\psi^2}}. \quad (\text{A.7})$$

Lastly, the Hamilton equation for  $p_\psi$  is

$$\dot{p}_\psi = \frac{1}{\kappa L_y} \frac{\partial \mathcal{E}}{\partial \psi} = -\frac{f_x}{\kappa} \sin \psi + \frac{f_z}{\kappa} \cos \psi. \quad (\text{A.8})$$

We have a set of six equations to solve, requiring six boundary conditions. In sections 3.2.4, 4.2.1, and 4.3.1, we saw that boundary conditions emerge from the requirement that boundary terms in a variation vanish. For a given coordinate, this requirement can be satisfied by either of two options: either the coordinate must be fixed at the boundary, or its conjugate momentum must vanish at the boundary. This is one the advantages of using Hamilton's equations: boundary conditions usually take a very simple form. In this case, we want to fix all of the coordinates at both ends of the buckle. The boundary conditions are therefore given by

$$x(0) = 0 \tag{A.9a}$$

$$x(L) = L_x \tag{A.9b}$$

$$z(0) = 0 \tag{A.9c}$$

$$z(L) = 0 \tag{A.9d}$$

$$\psi(0) = 0 \tag{A.9e}$$

$$\psi(L) = 0. \tag{A.9f}$$

Of course, if we wanted some coordinate to be free rather than fixed at the endpoints, we would instead require its conjugate momentum to vanish. For example, if we wanted hinged boundary conditions, where  $\psi$  is free, we would require  $p_\psi(0) = p_\psi(L) = 0$ .

## A.2 Making a good guess

When  $L_x \approx L$ , the membrane will be approximately flat. We can therefore assume that  $\psi$  and  $z$  are small in that case. Naïvely, we might therefore guess that the membrane is totally flat, described by

$$x(s) = s \tag{A.10a}$$

$$z(s) = 0 \tag{A.10b}$$

$$\psi(s) = 0 \tag{A.10c}$$

$$p_\psi(s) = 0. \tag{A.10d}$$

However, a totally flat buckle is not a good enough guess; in particular, the membrane could buckle either upward or downward, and the program has no way to choose a direction<sup>1</sup>, and so fails to find a solution. We must provide a better approximation of the solution, one which also chooses an orientation for the buckle, breaking the symmetry by hand. This suggests that we can use perturbation theory to create our guess. This is usually the most reliable method: a good perturbative guess is often enough for the program to find the correct answer even well outside the linear regime. In many cases though, this is unnecessary, and simply providing a guess function with approximately the right qualitative shape will suffice.

Instead of assuming  $z$ ,  $\psi$ , and  $p_\psi$  vanish, let us assume that they are simply

---

<sup>1</sup>A perfect illustration of the ‘‘Buridan’s ass’’ thought experiment; unfortunately, Matlab is not capable of meta-reasoning.

*small.* To first order, Hamilton's equations then become

$$\dot{x} = \cos \psi \approx 1 \quad (\text{A.11a})$$

$$\dot{z} = \sin \psi \approx \psi \quad (\text{A.11b})$$

$$\dot{\psi} = \frac{p_\psi}{\sqrt{1 - \ell^2 p_\psi^2}} \approx p_\psi \quad (\text{A.11c})$$

$$\dot{p}_\psi = -\frac{f_x}{\kappa} \sin \psi + \frac{f_z}{\kappa} \cos \psi \approx -\frac{f_x}{\kappa} \psi + \frac{f_z}{\kappa}. \quad (\text{A.11d})$$

Because the membrane is up-down symmetric, we make the ansatz that  $f_z$  vanishes. Equation (A.11a) and the boundary conditions (A.9a) and (A.9b) immediately give us  $x(s) = L_x s/L$ . Differentiating equation (A.11c) and inserting equation (A.11d), we see that

$$\ddot{\psi} = -\frac{f_x}{\kappa} \psi, \quad (\text{A.12})$$

which is of course the equation of a harmonic oscillator with frequency  $\sqrt{f_x/\kappa}$ . Considering the boundary condition (A.9e), we conclude that  $\psi$  is given by

$$\psi = \psi_i \sin \left( \sqrt{\frac{f_x}{\kappa}} s \right). \quad (\text{A.13})$$

This equation sets our guess for  $\psi$ ; by applying our boundary conditions, it will also give us a guess for  $f_x$ . In order for  $\psi$  to vanish at  $s = L$ , it must be the case that

$$\begin{aligned} \psi(L) &= \psi_i \sin \left( \sqrt{\frac{f_x}{\kappa}} L \right) = 0 \\ \implies \sqrt{\frac{f_x}{\kappa}} L &= \arcsin(0) = n\pi, \end{aligned} \quad (\text{A.14})$$

where  $n$  is an integer. Since we are interested in buckles that complete one full period, we take the  $n = 2$  solution, so that

$$\begin{aligned} \sqrt{\frac{f_x}{\kappa}} L &= 2\pi \\ f_x &= \kappa \left( \frac{2\pi}{L} \right)^2. \end{aligned} \quad (\text{A.15})$$

This should look familiar: it's our old friend the critical buckling threshold from equation (3.24)! That  $f_x$  takes this value should come as no surprise, since we assumed that the membrane is only slightly buckled. The force  $f_x$  should therefore be approximately the minimum force needed to create a buckle.

For our guess to be useful, we of course must estimate the actual amplitude of the oscillations, i.e. the inflection angle  $\psi_i$ . We can find  $\psi_i$  to lowest order by calculating the strain in terms of our solution,

$$\begin{aligned} \gamma &= 1 - \frac{L_x}{L} = 1 - \frac{1}{L} \int_0^L ds \cos \psi = 1 - \frac{1}{L} \int_0^L ds \cos \left( \psi_i \sin \left[ \frac{2\pi}{L} s \right] \right) \\ &= 1 - J_0(\psi_i) \approx \frac{\psi_i^2}{4} \end{aligned} \quad (\text{A.16})$$

$$\implies \psi_i = 2\sqrt{\gamma}. \quad (\text{A.17})$$

It is only now that we have broken the up-down symmetry of the buckle by choosing the positive branch of the square root.

We can calculate  $z(s)$  using equation (A.11b),

$$z(s) = \int_0^s \psi(s) ds = \int_0^s 2\sqrt{\gamma} \sin\left(\frac{2\pi}{L}s\right) ds = 2\sqrt{\gamma} \frac{L}{2\pi} \left[1 - \cos\left(\frac{2\pi}{L}s\right)\right]. \quad (\text{A.18})$$

Lastly, we obtain  $p_\psi$  by differentiating  $\psi(s)$ ,

$$p_\psi = \psi'(s) = 2\sqrt{\gamma} \frac{2\pi}{L} \cos\left(\frac{2\pi}{L}s\right). \quad (\text{A.19})$$

In summary, for a given  $L$  and  $L_x$  (or equivalently, a given  $L$  and  $\gamma$ ), we use the guess functions

$$x = \frac{L_x}{L} s \quad (\text{A.20a})$$

$$z = \frac{L}{\pi} \sqrt{1 - \frac{L_x}{L}} \left[1 - \cos\left(\frac{2\pi}{L}s\right)\right] \quad (\text{A.20b})$$

$$\psi = 2\sqrt{1 - \frac{L_x}{L}} \sin\left(\frac{2\pi}{L}s\right) \quad (\text{A.20c})$$

$$p_\psi = \frac{4\pi}{L} \sqrt{1 - \frac{L_x}{L}} \cos\left(\frac{2\pi}{L}s\right) \quad (\text{A.20d})$$

$$f_x = \kappa \left(\frac{2\pi}{L}\right)^2 \quad (\text{A.20e})$$

$$f_z = 0. \quad (\text{A.20f})$$

### A.3 Implementation

We now have all the theoretical ingredients necessary to implement this problem in `bvp4c`. We choose a unit system such that  $\kappa = \ell = 1$ . The only parameters necessary to specify a solution are its total length  $L$  and projected length  $L_x$ .

The solution is represented by a vector

$$\mathbf{y} = \begin{pmatrix} x \\ z \\ \psi \\ p_\psi \end{pmatrix}, \quad (\text{A.21})$$

along with a pair of parameters,  $f_x$  and  $f_z$ . In equilibrium,  $\mathbf{y}$  satisfies the differential equation

$$\frac{d\mathbf{y}}{ds} = \mathbf{F}(\mathbf{y}, f_x, f_z) = \begin{pmatrix} \cos \psi \\ \sin \psi \\ \frac{p_\psi}{\sqrt{1-p_\psi^2}} \\ -f_x \sin \psi + f_z \cos \psi \end{pmatrix} \quad (\text{A.22})$$

In our computer implementation of this problem, we will actually parametrize the buckle by its *normalized arclength*  $t = s/L$  rather than the arclength  $s$ . This has

a few advantages: firstly, it means that every solution to the Hamilton equations has the same domain,  $t \in [0, 1]$ . Secondly, it allows us to include the length explicitly as a parameter for the differential equation. Using this parametrization, the Hamilton equations become

$$\begin{aligned} \frac{d\mathbf{y}}{ds} &= \frac{1}{L} \frac{d\mathbf{y}}{dt} = \mathbf{F}(\mathbf{y}, f_x, f_z) \\ \implies \frac{d\mathbf{y}}{dt} &= L\mathbf{F}(\mathbf{y}, f_x, f_z). \end{aligned} \tag{A.23}$$

Of course, the domain  $t \in [0, 1]$  must be discretized on the computer. This discretization is called the *mesh*, and need not be uniform. The routine will adjust the mesh so that it is finer in regions where  $\mathbf{y}$  changes more quickly. Just as the program requires an initial guess for the solution, it also must be provided with an initial mesh; giving a uniform discretization is the simplest choice.

To use the routine, we must make calls to two functions: `bvpinit` and `bvp4c`. The function `bvpinit` creates the object containing our initial guess. Its arguments are, in order: our initial mesh, our initial guess (as a matrix  $\mathbf{y}(t)$ ), and our guess for the input parameters. The function `bvp4c` then attempts to solve the differential equations by minimizing the residual  $|\mathbf{y}'(t) - L\mathbf{F}(\mathbf{y}(t), f_x, f_z)|$ . It takes three arguments: the function handle for a (user-defined) function describing the differential equations to be solved, the function handle for a (user-defined) function describing the boundary conditions, and our guess solution in the form of a object created by `bvpinit`. The function describing the differential equation (called `hamilton_eq` in our code) takes three arguments: the independent variable (in our case,  $t$ ), the dependent variable (the vector  $\mathbf{y}$ ), and the parameters ( $f_x$ ,  $f_z$ , and  $L$ ). The function encoding the boundary conditions (called `bc_func` in our code) takes three arguments as well: the dependent variable at the initial point ( $\mathbf{y}(0)$ , called `ya` in the code below), the dependent variable at the final point ( $\mathbf{y}(L)$ , called `yb` in the code), and the parameters.

Once we have found a solution for a given set of parameters  $L_x$  and  $L$ , we can use it as our initial guess for a different set of parameters. This method is necessary for finding solutions far from the linear regime. As long as the qualitative features of the solution do not change too quickly as the parameters change, this method is very effective. This will not always be true, though. For example, in our study of helicoidal membranes in section 3.2.4, we found solutions to the membrane shape equation that differed significantly on either side of a phase boundary.

## A.4 Example scripts

Below, we present two scripts written for Matlab version R2015a. The first, given a total length  $L$  and projected length  $L_x$ , finds a profile curve for the membrane buckling problem using our perturbative solution as its initial guess. The second rather uses an already existing solution for the initial guess.

```

function sol = guess_solve(L, Lx)
% This function takes two inputs: the overall length of the buckle,
% and its projected length along the x-axis. It returns a
% solution object, which contains the functions x(s), z(s), psi(s),
% and p_psi(s), as well as the parameters f_x, f_z, and L.

% Coordinates:
% y(1) = x
% y(2) = z
% y(3) = psi
% y(4) = momentum conjugate to psi
% Parameters:
% C(1) = stress fx
% C(2) = stress fz
% C(3) = length L

% Guess the parameters:
fxg = (2*pi/L)^2;
fzg = 0;
PARAM_GUESS = [ fxg fzg L];

% Prepare the mesh:
t = 0 : 0.001 : 1.0;

% Guess the actual solution:
psi0 = 2*sqrt(1 - Lx/L);
SOL_GUESS = [ t*Lx
              psi0*L/(2*pi)*(1 - cos(2*pi*t))
              psi0*sin(2*pi*t)
              psi0*(2*pi/L)*cos(2*pi*t)];

% Create initial guess object using the function bvpinit
solinit = bvpinit(t, SOL_GUESS, PARAM_GUESS);

% Solve:
sol = bvp4c(@hamilton_eq, @bc_func, solinit);

%%%%%%%%%%%%%%%%%%%%%%%%%%%%%%%%%%%%%%%%%%%%%%%%%%%%%%%%%%%%%%%%%%%%%%%%
% BOUNDARY CONDITION FUNCTION
%%%%%%%%%%%%%%%%%%%%%%%%%%%%%%%%%%%%%%%%%%%%%%%%%%%%%%%%%%%%%%%%%%%%%%%%
function zero = bc_func(ya, yb, params)
% This function returns a vector that should vanish when the
% boundary conditions are satisfied
zero = [ ya(1)
         yb(1) - Lx
         ya(2)
         yb(2)
         ya(3)
         yb(3)
         params(3) - L ];
end
    
```

---

```
%%%%%%%%%%%%%%%%%%%%%%%%%%%%%%%%%%%%%%%%%%%%%%%%%%%%%%%%%%%%%%%%%%%%%%%%%
% HAMILTON EQUATIONS FUNCTION
%%%%%%%%%%%%%%%%%%%%%%%%%%%%%%%%%%%%%%%%%%%%%%%%%%%%%%%%%%%%%%%%%%%%%%%%%
function dydt = hamilton_eq(t, y, params)
% This function returns a vector that should vanish when
% Hamilton's equations are satisfied
    psi = y(3);
    p_psi = y(4);
    FX = params(1);
    FZ = params(2);
    Ltemp = params(3);

    dydt = [ Ltemp*cos(psi)
             Ltemp*sin(psi)
             Ltemp*p_psi/sqrt(1 - p_psi^2)
             Ltemp*(-FX*sin(psi) + FZ*cos(psi)) ];
end
%%%%%%%%%%%%%%%%%%%%%%%%%%%%%%%%%%%%%%%%%%%%%%%%%%%%%%%%%%%%%%%%%%%%%%%%%
end
```

---

```

function sol = seed_solve(L, Lx, solinit)
% This function takes three inputs: the overall length of the buckle,
% its projected length along the x-axis, and a solution object to use
% as an initial guess. It returns a solution object, which contains the
% functions x(s), z(s), psi(s), and p_psi(s), as well as the parameters
% f_x, f_z, and L.

% Solve using solinit as guess:
sol = bvp4c(@hamilton_eq, @bc_func, solinit);

%%%%%%%%%%%%%%%%%%%%%%%%%%%%%%%%%%%%%%%%%%%%%%%%%%%%%%%%%%%%%%%%%%%%%%%%
% BOUNDARY CONDITION FUNCTION
%%%%%%%%%%%%%%%%%%%%%%%%%%%%%%%%%%%%%%%%%%%%%%%%%%%%%%%%%%%%%%%%%%%%%%%%
function zero = bc_func(ya, yb, params)
% This function returns a vector that should vanish when the
% boundary conditions are satisfied
zero = [ ya(1)
        yb(1) - Lx
        ya(2)
        yb(2)
        ya(3)
        yb(3)
        params(3) - L ];
end

%%%%%%%%%%%%%%%%%%%%%%%%%%%%%%%%%%%%%%%%%%%%%%%%%%%%%%%%%%%%%%%%%%%%%%%%
% HAMILTON EQUATIONS FUNCTION
%%%%%%%%%%%%%%%%%%%%%%%%%%%%%%%%%%%%%%%%%%%%%%%%%%%%%%%%%%%%%%%%%%%%%%%%
function dydt = hamilton_eq(t, y, params)
% This function returns a vector that should vanish when
% Hamilton's equations are satisfied
psi = y(3);
p_psi = y(4);
FX = params(1);
FZ = params(2);
Ltemp = params(3);

dydt = [ Ltemp*cos(psi)
        Ltemp*sin(psi)
        Ltemp*p_psi/sqrt(1 - p_psi^2)
        Ltemp*(-FX*sin(psi) + FZ*cos(psi)) ];
end
%%%%%%%%%%%%%%%%%%%%%%%%%%%%%%%%%%%%%%%%%%%%%%%%%%%%%%%%%%%%%%%%%%%%%%%%
end

```

---

# Bibliography

- [ABDC<sup>+</sup>16] Bruno Antonny, Christopher Burd, Pietro De Camilli, Elizabeth Chen, Oliver Daumke, Katja Faelber, Marijn Ford, Vadim A Frolov, Adam Frost, Jenny E Hinshaw, et al. Membrane fission by dynamin: what we know and what we need to know. *The EMBO journal*, 35(21):2270–2284, 2016.
- [ALSP97] Cristina R Artalejo, Mark A Lemmon, Joseph Schlessinger, and H Clive Palfrey. Specific role for the ph domain of dynamin-1 in the regulation of rapid endocytosis in adrenal chromaffin cells. *The EMBO Journal*, 16(7):1565–1574, 1997.
- [Ant74] Stuart S Antman. Kirchhoff’s problem for nonlinearly elastic rods. *Quarterly of applied mathematics*, 32(3):221–240, 1974.
- [Ant05] Stuart S Antman. *Nonlinear Problems of Elasticity*. Springer New York, 2005.
- [AT02] S. Arimura and Nobuhiro Tsutsumi. A dynamin-like protein ADL2b, rather than FtsZ, is involved in arabidopsis mitochondrial division. *Proc. Natl. Acad. Sci.*, 99(8):5727–5731, 2002.
- [B<sup>+</sup>84] Robert L Bryant et al. A duality theorem for willmore surfaces. *Journal of differential geometry*, 20(1):23–53, 1984.
- [BAE<sup>+</sup>08a] P. Bashkirov, Sergey A. Akimov, Alexey I. Evseev, Sandra L. Schmid, Joshua Zimmerberg, and Vadim A. Frolov. GTPase cycle of dynamin is coupled to membrane squeeze and release, leading to spontaneous fission. *Cell*, 135(7):1276 – 1286, 2008.
- [BAE<sup>+</sup>08b] Pavel V Bashkirov, Sergey A Akimov, Alexey I Evseev, Sandra L Schmid, Joshua Zimmerberg, and Vadim A Frolov. Gtpase cycle of dynamin is coupled to membrane squeeze and release, leading to spontaneous fission. *Cell*, 135(7):1276–1286, 2008.
- [Ber90] Michael Berry. Anticipations of the geometric phase. *Physics Today*, 43(12):34–40, 1990.
- [BG79] AE Blaurock and RC Gamble. Small phosphatidylcholine vesicles appear to be faceted below the thermal phase transition. *Journal of Membrane Biology*, 50(2):187–204, 1979.

- [BGVMS14] B. Božič, Jemal Guven, Pablo Vázquez-Montejo, and Saša Svetina. Direct and remote constriction of membrane necks. *Phys. Rev. E*, 89:052701, May 2014.
- [BM00] Claude Bouchiat and Marc Mezard. Elastic rod model of a supercoiled dna molecule. *The European Physical Journal E*, 2(4):377–402, 2000.
- [BMS99] Alexander Balaeff, L Mahadevan, and Klaus Schulten. Elastic rod model of a dna loop in the lac operon. *Physical Review Letters*, 83(23):4900, 1999.
- [BPA99] Arezki Boudaoud, Pedro Patricio, and Martine Ben Amar. The helioid versus the catenoid: geometrically induced bifurcations. *Physical review letters*, 83(19):3836, 1999.
- [BWD14] Tristan Bereau, Zun-Jing Wang, and Markus Deserno. More than the sum of its parts: Coarse-grained peptide-lipid interactions from a simple cross-parametrization. *The Journal of chemical physics*, 140(11):03B615\_1–11220, 2014.
- [Can70] Peter B Canham. The minimum energy of bending as a possible explanation of the biconcave shape of the human red blood cell. *Journal of theoretical biology*, 26(1):61IN777–76IN881, 1970.
- [CD05] Ira R Cooke and Markus Deserno. Solvent-free model for self-assembling fluid bilayer membranes: stabilization of the fluid phase based on broad attractive tail potentials. *The Journal of chemical physics*, 123(22):224710, 2005.
- [CG02] Riccardo Capovilla and Jemal Guven. Stresses in lipid membranes. *Journal of Physics A: Mathematical and General*, 35(30):6233, 2002.
- [CGS03] Riccardo Capovilla, Jemal Guven, and Jose’Antonio Santiago. Deformations of the geometry of lipid vesicles. *Journal of Physics A: Mathematical and General*, 36(23):6281, 2003.
- [CIFC<sup>+</sup>11] Belle Chang-Ileto, Samuel G Frere, Robin B Chan, Sergey V Voronov, Aurélien Roux, and Gilbert Di Paolo. Synaptojanin 1-mediated pi (4, 5) p 2 hydrolysis is modulated by membrane curvature and facilitates membrane fission. *Developmental cell*, 20(2):206–218, 2011.
- [COL<sup>+</sup>15] Corentin Coulais, Johannes TB Overvelde, Luuk A Lubbers, Katia Bertoldi, and Martin van Hecke. Discontinuous buckling of wide beams and metabeams. *Physical review letters*, 115(4):044301, 2015.
- [DC76] Manfredo Perdigao Do Carmo. *Differential geometry of curves and surfaces*. Prentice-hall Englewood Cliffs, 1976.
- [DCD82] Manfredo P Do Carmo and Marcos Dajczer. Helicoidal surfaces with constant mean curvature. *Tohoku Mathematical Journal, Second Series*, 34(3):425–435, 1982.

- [DDG08] Anna Dall'Acqua, Klaus Deckelnick, and H Christoph Grunau. Classical solutions to the Dirichlet problem for Willmore surfaces of revolution. *Adv. Calc. Var.*, 1(4):379–397, 2008.
- [DEK<sup>+</sup>97] H-G Döbereiner, Evan Evans, Martin Kraus, Udo Seifert, and Michael Wortis. Mapping vesicle shapes into the phase diagram: a comparison of experiment and theory. *Physical Review E*, 55(4):4458, 1997.
- [Des15] Markus Deserno. Fluid lipid membranes: From differential geometry to curvature stresses. *Chemistry and physics of lipids*, 185:11–45, 2015.
- [DGBWQ13] Pierre-Gilles De Gennes, Françoise Brochard-Wyart, and David Quéré. *Capillarity and wetting phenomena: drops, bubbles, pearls, waves*. Springer Science & Business Media, 2013.
- [DH76] HJ Deuling and W Helfrich. The curvature elasticity of fluid membranes: a catalogue of vesicle shapes. *Journal de Physique*, 37(11):1335–1345, 1976.
- [DHKW92] Ulrich Dierkes, Stefan Hildebrandt, Albrecht Küster, and Ortwin Wohlrab. *Minimal surfaces*. Springer, 1992.
- [DI16] Patrick Diggins IV. *Investigation of elastic properties of lipids and proteins using computer simulations*. PhD thesis, Carnegie Mellon University, 2016.
- [DIMD15] Patrick Diggins IV, Zachary A McDargh, and Markus Deserno. Curvature softening and negative compressibility of gel-phase lipid membranes. *Journal of the American Chemical Society*, 137(40):12752–12755, 2015.
- [DM93] MA Davies and FC Moon. 3-d spatial chaos in the elastica and the spinning top: Kirchhoff analogy. *Chaos: An Interdisciplinary Journal of Nonlinear Science*, 3(1):93–99, 1993.
- [DMH04a] D. Danino, Kwan-Hoon Moon, and Jenny E. Hinshaw. Rapid constriction of lipid bilayers by the mechanochemical enzyme dynamin. *J. Struct. Biol.*, 147(3):259 – 267, 2004.
- [DMH04b] Dganit Danino, Kwan-Hoon Moon, and Jenny E Hinshaw. Rapid constriction of lipid bilayers by the mechanochemical enzyme dynamin. *Journal of structural biology*, 147(3):259–267, 2004.
- [DSWM98] Jianwu Dai, Michael P Sheetz, Xiaodong Wan, and Catherine E Morris. Membrane tension in swelling and shrinking molluscan neurons. *Journal of Neuroscience*, 18(17):6681–6692, 1998.
- [EHA14] David A Ehrhardt, Ryan B Harris, and Matthew S Allen. Numerical and experimental determination of nonlinear normal modes of a circular perforated plate. In *Topics in Modal Analysis I, Volume 7*, pages 239–251. Springer, 2014.

- [FDC12] S. M. Ferguson and Pietro De Camilli. Dynamin, a membrane-remodelling GTPase. *Nat. Rev. Mol. Cell Biol.*, 13:75–88, 2012.
- [FEAS15] Vadim A Frolov, Artur Escalada, Sergey A Akimov, and Anna V Shnyrova. Geometry of membrane fission. *Chemistry and physics of lipids*, 185:129–140, 2015.
- [FgDG03] J. Fournier, Paul g. Dommersnes, and Paola Galatola. Dynamin recruitment by clathrin coats: a physical step? *C.R. Biologies*, 326:467–476, 2003.
- [FJK<sup>+</sup>16a] Julien Fierling, Albert Johner, Igor M Kulić, Hervé Mohrbach, and Martin Michael Müller. How bio-filaments twist membranes. *Soft matter*, 12(26):5747–5757, 2016.
- [FJK<sup>+</sup>16b] Julien Fierling, Albert Johner, Igor M Kulić, Hervé Mohrbach, and Martin Michael Müller. How bio-filaments twist membranes. *Soft matter*, 12(26):5747–5757, 2016.
- [FJN11] M. G. J. Ford, Simon Jenni, and Jodi Nunnari. The crystal structure of dynamin. *Nature*, 477(7366):561–566, 09 2011.
- [FLDB<sup>+</sup>03] Vadim A Frolov, Vladimir A Lizunov, Antonina Ya Dunina-Barkovskaya, Andrey V Samsonov, and Joshua Zimmerberg. Shape bistability of a membrane neck: a toggle switch to control vesicle content release. *Proceedings of the National Academy of Sciences*, 100(15):8698–8703, 2003.
- [FM86] Gary Felsenfeld and James D. McGhee. Structure of the 30 nm chromatin fiber. *Cell*, 44(3):375–377, 02 1986.
- [FMR<sup>+</sup>94] B. Fourcade, Ling Miao, Madan Rao, Michael Wortis, and Royce Zia. Scaling analysis of narrow necks in curvature models of fluid lipid-bilayer vesicles. *Phys. Rev. E*, 49:5276–5286, Jun 1994.
- [FPG<sup>+</sup>11] K. Faelber, York Posor, Song Gau, Martin Held, Yvette Roske, Dennis Schulze, Volker Haucke, Frank Noe, and Oliver Daumke. Crystal structure of nucleotide-free dynamin. *Nature*, 477:566 – 560, 2011.
- [Fra11] Theodore Frankel. *The geometry of physics: an introduction*. Cambridge University Press, 2011.
- [GPL05] Sachin Goyal, Noel C Perkins, and Christopher L Lee. Nonlinear dynamics and loop formation in kirchhoff rods with implications to the mechanics of dna and cables. *Journal of Computational Physics*, 209(1):371–389, 2005.
- [GPS02] Herbert Goldstein, Charles Poole, and John Safko. *Classical mechanics*. AAPT, 2002.
- [GR14] Izrail Solomonovich Gradshteyn and Iosif Moiseevich Ryzhik. *Table of integrals, series, and products*. Academic press, 2014.

- [Guv04] Jemal Guven. Membrane geometry with auxiliary variables and quadratic constraints. *Journal of Physics A: Mathematical and General*, 37(28):L313, 2004.
- [Guv05] Jemal Guven. Conformally invariant bending energy for hypersurfaces. *Journal of Physics A: Mathematical and General*, 38(37):7943, 2005.
- [GVM12] Jemal Guven and Pablo Vázquez-Montejo. Confinement of semiflexible polymers. *Physical Review E*, 85(2):026603, 2012.
- [GVVM14] Jemal Guven, Dulce María Valencia, and Pablo Vázquez-Montejo. Environmental bias and elastic curves on surfaces. *Journal of Physics A: Mathematical and Theoretical*, 47(35):355201, 2014.
- [GWB12] Raymond E Goldstein, Patrick B Warren, and Robin C Ball. Shape of a ponytail and the statistical physics of hair fiber bundles. *Physical review letters*, 108(7):078101, 2012.
- [HCV52] David Hilbert and Stephan Cohn-Vossen. *Geometry and the Imagination*, volume 87. American Mathematical Soc., 1952.
- [HDID13] Mingyang Hu, Patrick Diggins IV, and Markus Deserno. Determining the bending modulus of a lipid membrane by simulating buckling. *The Journal of chemical physics*, 138(21):214110, 2013.
- [Hel73] Wolfgang Helfrich. Elastic properties of lipid bilayers: theory and possible experiments. *Zeitschrift für Naturforschung C*, 28(11-12):693–703, 1973.
- [HS95] Jenny E Hinshaw and Sandra L Schmid. Dynamamin self-assembles into rings suggesting a mechanism for coated vesicle budding. *Nature*, 374(6518):190, 1995.
- [HSDS96] FM Hochmuth, Jin-Yu Shao, Jianwu Dai, and Michael P Sheetz. Deformation and flow of membrane into tethers extracted from neuronal growth cones. *Biophysical journal*, 70(1):358–369, 1996.
- [Hud78] John V Huddleston. The compressible elastica in three dimensions. *International Journal of Mechanical Sciences*, 20(4):229–236, 1978.
- [HWM02] Gerald Lim HW, Michael Wortis, and Ranjan Mukhopadhyay. Stomatocyte–discocyte–echinocyte sequence of the human red blood cell: Evidence for the bilayer–couple hypothesis from membrane mechanics. *Proceedings of the National Academy of Sciences*, 99(26):16766–16769, 2002.
- [HYZC99] Zhou Haijun, Zhang Yang, and Ou-Yang Zhong-Can. Bending and base-stacking interactions in double-stranded dna. *Physical review letters*, 82(22):4560, 1999.
- [JS94] Frank Jülicher and Udo Seifert. Shape equations for axisymmetric vesicles: a clarification. *Physical Review E*, 49(5):4728, 1994.

- [JSBB10] R. Jain, Shiteshu Shrimal, Sudha Bhattacharya, and Alok Bhattacharya. Identification and partial characterization of a dynamin-like protein, EhDLP1, from the protist parasite *Entamoeba histolytica*. *Eukaryotic Cell*, 9(1):215–223, 2010.
- [JSL93] Frank Jülicher, Udo Seifert, and Reinhard Lipowsky. Conformal degeneracy and conformal diffusion of vesicles. *Physical review letters*, 71(3):452, 1993.
- [Kam02] Randall D Kamien. The geometry of soft materials: a primer. *Reviews of Modern physics*, 74(4):953, 2002.
- [KB04] Teun Koetsier and Hendrik Blauwendraat. The archimedean screw-pump: A note on its invention and the development of the theory. In *International symposium on history of machines and mechanisms*, pages 181–194. Springer, 2004.
- [KCdKB03] Edgar E Kooijman, Vladimir Chupin, Ben de Kruijff, and Koert NJ Burger. Modulation of membrane curvature by phosphatidic acid and lysophosphatidic acid. *Traffic*, 4(3):162–174, 2003.
- [KIY94] H. Kojima, A. Ishiura, and T. Yanagida. Direct measurement of stiffness of single actin filaments with and without triptomyosin by *in vitro* nanomanipulation. *Proc. Natl. Acad. Sci.*, 91:12962–12966, 1994.
- [KK03] Yonathan Kozlovsky and Michael M Kozlov. Membrane fission: model for intermediate structures. *Biophysical journal*, 85(1):85–96, 2003.
- [Kle86] H Kleinert. The membrane properties of condensing strings. *Physics Letters B*, 174(3):335–338, 1986.
- [KNNS13] Shuhei Kawamoto, Takenobu Nakamura, Steven O Nielsen, and Wataru Shinoda. A guiding potential method for evaluating the bending rigidity of tensionless lipid membranes from molecular simulation. *The Journal of chemical physics*, 139(3):07B613.1, 2013.
- [Koz99] Michael M Kozlov. Dynamin: possible mechanism of “pinchase” action. *Biophysical journal*, 77(1):604–616, 1999.
- [Koz01] Michael M Kozlov. Fission of biological membranes: interplay between dynamin and lipids. *Traffic*, 2(1):51–65, 2001.
- [Kre68] Erwin Kreyszig. *Introduction to differential geometry and Riemannian geometry*, volume 16. Dover, 1968.
- [Lei86] S Leibler. Curvature instability in membranes. *Journal de Physique*, 47(3):507–516, 1986.
- [Lev08] Ralph Levien. The elastica: a mathematical history. *University of California, Berkeley, Technical Report No. UCB/EECS-2008-103*, 2008.

- [Lip91] Reinhard Lipowsky. The conformation of membranes. *Nature*, 349(6309):475, 1991.
- [LL59] Lev Davidovich Landau and Eugin M Lifshitz. *Course of Theoretical Physics Vol 7: Theory and Elasticity*. Pergamon press, 1959.
- [LMR09] M. Lenz, Sandrine Morlot, and Aurélien Roux. Mechanical requirements for membrane fission: Common facts from various examples. *FEBS Letters*, 583:3839–3846, 2009.
- [LPJ08] M. Lenz, Jacques Prost, and Jean-François Joanny. Mechanochemical action of the dynamin protein. *Phys. Rev. E*, 78:011911, 2008.
- [LS96] Joel Langer and David A Singer. Lagrangian aspects of the kirchhoff elastic rod. *SIAM review*, 38(4):605–618, 1996.
- [LWKA02] D.D. Leipe, Yuri I Wolf, Eugene V Koonin, and L Aravind. Classification and evolution of P-loop GTPases and related ATPases. *J. Mol. Biol.*, 317(1):41 – 72, 2002.
- [LY82] Peter Li and Shing-Tung Yau. A new conformal invariant and its applications to the willmore conjecture and the first eigenvalue of compact surfaces. *Inventiones mathematicae*, 69(2):269–291, 1982.
- [MAGP16] Thomas Machon, Gareth P Alexander, Raymond E Goldstein, and Adriana I Pesci. Instabilities and solitons in minimal strips. *Physical Review Letters*, 117(1):017801, 2016.
- [Mat] Mathworks. bvp4c documentation. <https://www.mathworks.com/help/matlab/ref/bvp4c.html#bt5uooc-27>. Accessed: 2017-07-19.
- [MGF04] G. W. Morgan, David Goulding, and Mark C. Field. The single dynamin-like protein of *Trypanosoma brucei* regulates mitochondrial division and is not required for endocytosis. *J. Biol. Chem.*, 279(11):10692–10701, 2004.
- [MGL<sup>+</sup>11] Ira Milosevic, Silvia Giovedi, Xuelin Lou, Andrea Raimondi, Chiara Collesi, Hongying Shen, Summer Paradise, Eileen O’Toole, Shawn Ferguson, Ottavio Cremona, et al. Recruitment of endophilin to clathrin-coated pit necks is required for efficient vesicle uncoating after fission. *Neuron*, 72(4):587–601, 2011.
- [MH88] Alexander Mielke and Philip Holmes. Spatially complex equilibria of buckled rods. *Archive for rational Mechanics and Analysis*, 101(4):319–348, 1988.
- [MH01] CE Morris and Ulrike Homann. Cell surface area regulation and membrane tension. *Journal of Membrane Biology*, 179(2):79–102, 2001.
- [MLAR14] JT Miller, A Lazarus, B Audoly, and PM Reis. Shapes of a suspended curly hair. *Physical review letters*, 112(6):068103, 2014.

- [MLP<sup>+</sup>10] S. Morlot, Martin Lenz, Jacques Prost, Jean-François Joanny, and Aurélien Roux. Deformation of dynamin helices damped by membrane friction. *Biophys. J.*, 99(11):3580–3588, 2010.
- [MMTK04] Seyed Ali Mousavi, Lene Malerød, Berg Trond, and Rune Kjekken. Clathrin-dependent endocytosis. *Biochemical Journal*, 377(1):1–16, 2004.
- [MR13a] S. Morlot and Aurélien Roux. Mechanics of dynamin mediated membrane fission. *Annu. Rev. Biophys.*, 42:629–649, 2013.
- [MR13b] Sandrine Morlot and Aurélien Roux. Mechanics of dynamin-mediated membrane fission. *Annual review of biophysics*, 42:629–649, 2013.
- [MRY<sup>+</sup>07] Siewert J Marrink, H Jelger Risselada, Serge Yefimov, D Peter Tieleman, and Alex H De Vries. The martini force field: coarse grained model for biomolecular simulations. *The journal of physical chemistry B*, 111(27):7812–7824, 2007.
- [MSV<sup>+</sup>01] Bruno Marks, Michael HB Stowell, Yvonne Vallis, Ian G Mills, Adele Gibson, Colin R Hopkins, and Harvey T McMahon. Gtpase activity of dynamin and resulting conformation change are essential for endocytosis. *Nature*, 410(6825):231–235, 2001.
- [Mül07] Martin Michael Müller. *Theoretical studies of fluid membrane mechanics*. PhD thesis, Johannes Gutenberg-Universität Mainz, 2007.
- [MVMGD16] Zachary A McDargh, Pablo Vázquez-Montejo, Jemal Guven, and Markus Deserno. Constriction by dynamin: Elasticity versus adhesion. *Biophysical Journal*, 111(11):2470–2480, 2016.
- [NG99] Michel Nizette and Alain Goriely. Towards a classification of euler–kirchhoff filaments. *Journal of mathematical physics*, 40(6):2830–2866, 1999.
- [NM88] Emeritus HK Nickerson and Gerald S Manning. Intrinsic equations for a relaxed elastic line on an oriented surface. *Geometriae Dedicata*, 27(2):127–136, 1988.
- [Nog11] Hiroshi Noguchi. Anisotropic surface tension of buckled fluid membranes. *Physical Review E*, 83(6):061919, 2011.
- [OD16] Oz Oshri and Haim Diamant. Properties of compressible elastica from relativistic analogy. *Soft matter*, 12(3):664–668, 2016.
- [OO74] Ada L Olins and Donald E Olins. Spheroid chromatin units ( $\nu$  bodies). *Science*, 183(4122):330–332, 1974.
- [PM04] G. J. K. Praefcke and Harvey T. McMahon. The dynamin superfamily: universal membrane tubulation and fission molecules? *Nat. Rev. Mol. Cell Biol.*, 5(2):133–147, 02 2004.
- [Poi14] Siméon Denis Poisson. *Mémoire sur les surfaces élastiques*. 1814.

- [Pol86] A Polyakov. Fine structure of strings. *Nuclear Physics B*, 268(2):406–412, 1986.
- [PS08] T. J. Pucadyil and Sandra L. Schmid. Real-time visualization of dynamin-catalyzed membrane fission and vesicle release. *Cell*, 135(7):1263 – 1275, 2008.
- [QQF<sup>+</sup>12] François Quéméneur, Catherine Quilliet, Magalie Faivre, Annie Viallat, and Brigitte Pépin-Donat. Gel phase vesicles buckle into specific shapes. *Physical review letters*, 108(10):108303, 2012.
- [RAL<sup>+</sup>11] Vyas Ramanan, Neeraj J Agrawal, Jin Liu, Sean Engles, Randall Toy, and Ravi Radhakrishnan. Systems biology and physical biology of clathrin-mediated endocytosis. *Integrative Biology*, 3(8):803–815, 2011.
- [Ram11] Rajesh Ramachandran. Vesicle scission: dynamin. In *Seminars in cell & developmental biology*, volume 22, pages 10–17, 2011.
- [RBN83] Y Rotenberg, Lr Boruvka, and AW Neumann. Determination of surface tension and contact angle from the shapes of axisymmetric fluid interfaces. *Journal of colloid and interface science*, 93(1):169–183, 1983.
- [RC05] V Riva and J Cardy. Scale and conformal invariance in field theory: a physical counterexample. *Physics Letters B*, 622(3):339–342, 2005.
- [RGL<sup>+</sup>99] Niels Ringstad, Helge Gad, Peter Löw, Gilbert Di Paolo, Lennart Brodin, Oleg Shupliakov, and Pietro De Camilli. Endophilin/sh3p4 is required for the transition from early to late stages in clathrin-mediated synaptic vesicle endocytosis. *Neuron*, 24(1):143–154, 1999.
- [RKL<sup>+</sup>10] A. Roux, Gerbrand Koster, Martin Lenz, Benoît Sorre, Jean-Baptiste Manneville, Pierre Nassoy, and Patricia Bassereau. Membrane curvature controls dynamin polymerization. *Proc. Nat. Acad. Sci.*, 107(9):41414146, March 2010.
- [Rou14] Aurélien Roux. Reaching a consensus on the mechanism of dynamin? *F1000prime reports*, 6, 2014.
- [RPL<sup>+</sup>09] Rajesh Ramachandran, Thomas J Pucadyil, Ya-Wen Liu, Sharmistha Acharya, Marilyn Leonard, Vasyl Lukiyanchuk, and Sandra L Schmid. Membrane insertion of the pleckstrin homology domain variable loop 1 is critical for dynamin-catalyzed vesicle scission. *Molecular biology of the cell*, 20(22):4630–4639, 2009.
- [RS08] Rajesh Ramachandran and Sandra L Schmid. Real-time detection reveals that effectors couple dynamin’s GTP-dependent conformational changes to the membrane. *The EMBO journal*, 27(1):27–37, 2008.
- [RT95] Leo Radzihovsky and John Toner. A new phase of tethered membranes: tubules. *Physical review letters*, 75(26):4752, 1995.

- [RUFDC06a] A. Roux, Katherine Uyhazi, Adam Frost, and Pietro De Camilli. GTP-dependent twisting of dynamin implicates constriction and tension in membrane fission. *Nature*, 441(7092):528–531, 05 2006.
- [RUFDC06b] Aurélien Roux, Katherine Uyhazi, Adam Frost, and Pietro De Camilli. Gtp-dependent twisting of dynamin implicates constriction and tension in membrane fission. *Nature*, 441(7092):528–531, 2006.
- [SBA<sup>+</sup>13] A. V. Shnyrova, Pavel V. Bashkirov, Sergey A. Akimov, Thomas J. Pucadyil, Joshua Zimmerberg, Sandra L. Schmid, and Vadim A. Frolov. Geometric catalysis of membrane fission driven by flexible dynamin rings. *Science*, 339(6126):1433–1436, 2013.
- [SBQ<sup>+</sup>96] Kamran Salim, Matthew J Bottomley, E Querfurth, MJ Zvelebil, I Gout, R Scaife, RL Margolis, R Gigg, CI Smith, PC Driscoll, et al. Distinct specificity in the recognition of phosphoinositides by the pleckstrin homology domains of dynamin and bruton’s tyrosine kinase. *The EMBO journal*, 15(22):6241, 1996.
- [SdlC12] Rastko Sknepnek and Monica Olvera de la Cruz. Nonlinear elastic model for faceting of vesicles with soft grain boundaries. *Physical Review E*, 85(5):050501, 2012.
- [SDS00a] Sanja Sever, Hanna Damke, and Sandra L Schmid. Garrotes, springs, ratchets, and whips: putting dynamin models to the test. *Traffic*, 1(5):385–392, 2000.
- [SDS00b] Sanja Sever, Hanna Damke, and Sandra L Schmid. Garrotes, springs, ratchets, and whips: putting dynamin models to the test. *Traffic*, 1(5):385–392, 2000.
- [Sev02] Sanja Sever. Dynamin and endocytosis. *Current opinion in cell biology*, 14(4):463–467, 2002.
- [SF11a] S. L. Schmid and Vadim A. Frolov. Dynamin: functional design of a membrane fission catalyst. *Annu. Rev. Cell Dev. Biol.*, 27:79–105, 2011.
- [SF11b] Sandra L Schmid and Vadim A Frolov. Dynamin: functional design of a membrane fission catalyst. *Annual review of cell and developmental biology*, 27:79–105, 2011.
- [SFH<sup>+</sup>14] Anna C Sundborger, Shunming Fang, Jürgen A Heymann, Pampa Ray, Joshua S Chappie, and Jenny E Hinshaw. A dynamin mutant defines a superconstricted prefission state. *Cell reports*, 8(3):734–742, 2014.
- [SGR11] R. Shlomovitz, Nir Gov, and Aurélien Roux. Membrane mediated interactions and the dynamics of dynamin oligomers on membrane tubes. *New J. Phys.*, 13:065008, 2011.

- [SH94] Yaoming Shi and John E Hearst. The kirchhoff elastic rod, the non-linear schrödinger equation, and dna supercoiling. *The Journal of chemical physics*, 101(6):5186–5200, 1994.
- [Sin08] David A Singer. Lectures on elastic curves and rods. In *AIP Conference Proceedings*, volume 1002, pages 3–32. AIP, 2008.
- [SMS99] Sanja Sever, Amy B Muhlberg, and Sandra L Schmid. Impairment of dynamin’s gap domain stimulates receptor-mediated endocytosis. *Nature*, 398(6727):481–486, 1999.
- [SMWM99] Michael HB Stowell, Bruno Marks, Patrick Wigge, and Harvey T McMahon. Nucleotide-dependent conformational changes in dynamin: evidence for a mechanochemical molecular spring. *Nature cell biology*, 1(1):27–32, 1999.
- [SS85] Yosio Suzuki and Kunio Shimbori. Ice core drills usable for wet ice. *Memoirs of National Institute of Polar Research. Special issue*, 39:214–218, 1985.
- [SWT<sup>+</sup>99] Anne Schmidt, Michael Wolde, Christoph Thiele, Werner Fest, Hartmut Kratzin, Alexandre V Podtelejnikov, Walter Witke, Wieland B Huttner, and Hans-Dieter Soëling. Endophilin mediates synaptic vesicle formation by transfer of arachidonate to lysophosphatidic acid. *Nature*, 401(6749):133–141, 1999.
- [TOY08] ZC Tu and ZC Ou-Yang. Elastic theory of low-dimensional continua and its applications in bio-and nano-structures. *Journal of Computational and Theoretical Nanoscience*, 5(4):422–448, 2008.
- [TSK<sup>+</sup>13] Mark Terasaki, Tom Shemesh, Narayanan Kasthuri, Robin W Klemm, Richard Schalek, Kenneth J Hayworth, Arthur R Hand, Maya Yankova, Greg Huber, Jeff W Lichtman, et al. Stacked endoplasmic reticulum sheets are connected by helicoidal membrane motifs. *Cell*, 154(2):285–296, 2013.
- [Tu11] ZC Tu. Geometry of membranes. *arXiv preprint arXiv:1106.2370*, 2011.
- [vdB99] A. M. van der Blik. Functional diversity in the dynamin family. *Trends Cell Biol.*, 9(3):96 – 102, 1999.
- [VdH01] GHM Van der Heijden. The static deformation of a twisted elastic rod constrained to lie on a cylinder. In *Proceedings of the Royal Society of London A: Mathematical, Physical and Engineering Sciences*, volume 457, pages 695–715. The Royal Society, 2001.
- [VDM14] Vassil M Vassilev, Petar A Djondjorov, and Ivailo M Mladenov. Lie group analysis of the willmore and membrane shape equations. In *Similarity and Symmetry Methods*, pages 365–376. Springer, 2014.

- [VMMDG15] Pablo Vázquez-Montejo, Zachary McDargh, Markus Deserno, and Jemal Guven. Cylindrical confinement of semiflexible polymers. *Physical Review E*, 91(6):063203, 2015.
- [WD15] Xin Wang and Markus Deserno. Determining the pivotal plane of fluid lipid membranes in simulations. *The Journal of chemical physics*, 143(16):164109, 2015.
- [WD16] Xin Wang and Markus Deserno. Determining the lipid tilt modulus by simulating membrane buckles. *The Journal of Physical Chemistry B*, 120(26):6061–6073, 2016.
- [Wil65] Thomas J Willmore. Note on embedded surfaces. *An. Ştiinţ. Univ. “Al. I. Cuza” Iaş Sect. I a Mat.*, 11:493–496, 1965.
- [WK14] M. Williams and Kyoungtae Kim. From membranes to organelles: Emerging roles for dynamin-like proteins in diverse cellular processes. *Eur. J. Cell Biol.*, 93(7):267 – 277, 2014.
- [WS96] Dale E Warnock and Sandra L Schmid. Dynamin gtpase, a force-generating molecular switch. *Bioessays*, 18(11):885–893, 1996.
- [YKM05] Jie Yan, Ryo Kawamura, and John F Marko. Statistics of loop formation along double helix dnas. *Physical Review E*, 71(6):061905, 2005.
- [YPM01] Y. Yoon, Kelly R Pitts, and Mark A McNiven. Mammalian dynamin-like protein DLP1 tubulates membranes. *Mol. Biol. Cell*, 12(9):2894–2905, 09 2001.
- [ZCH87] Ou-Yang Zhong-Can and Wolfgang Helfrich. Instability and deformation of a spherical vesicle by pressure. *Physical review letters*, 59(21):2486, 1987.
- [ZCH89] Ou-Yang Zhong-Can and Wolfgang Helfrich. Bending energy of vesicle membranes: General expressions for the first, second, and third variation of the shape energy and applications to spheres and cylinders. *Physical Review A*, 39(10):5280, 1989.
- [ZCL<sup>+</sup>96] Jie Zheng, Sean M Cahill, Mark A Lemmon, David Fushman, Joseph Schlessinger, and David Cowburn. Identification of the binding site for acidic phospholipids on the ph domain of dynamin: implications for stimulation of gtpase activity. *Journal of molecular biology*, 255(1):14–21, 1996.
- [ZMT17] YH Zhang, Zachary McDargh, and ZC Tu. First integrals of the axisymmetric shape equation of lipid membranes. *Unpublished work*, 2017.

# Glossary

- $2\pi c$  pitch of helicoidal surface. 35
- $I_{ij}$  inertia tensor of rod. 13
- $K$  extrinsic or mean curvature of a surface. 22
- $P$  local pressure across a surface. 39
- $R_0$  equilibrium radius for a surface constricted by a filament. 86
- $U(\theta)$  potential energy function in analogy between a cylindrically confined filament and a particle in a potential. 72
- $K_{\mathbf{G}}$  Gaussian or intrinsic curvature of a surface. 22
- $K_{\mathbf{s}}$  spontaneous extrinsic curvature of a surface. 24
- $\alpha$  bending rigidity of a filament. 12
- $\alpha_i$  bending rigidities of a filament along eigenvectors of the inertia tensor  $I_{ij}$ . 14
- $c_{\mathbf{g}}$  spontaneous geodesic curvature of a filament. 84
- $c_{\mathbf{n}}$  spontaneous normal curvature. 84
- $c_{\mathbf{t}}$  spontaneous twist. 15, 84
- $\delta$  dimensionless measure of crossover length  $\ell$ . 31
- $\delta_b^a$  Kronecker delta. 20
- $\ell$  crossover length for gel phase membranes. 28
- $\gamma$  dimensionless strain for membrane buckles. 30
- $\kappa$  Frenet curvature. 10
- $\kappa$  surface bending rigidity. Note that this symbol is also used for the Frenet curvature. The reader should easily be able to tell which is the intended meaning based on context. 24
- $\kappa_{\mathbf{g}}$  geodesic curvature. 16
- $\kappa_{\mathbf{n}}$  normal curvature. 16
- $\lambda$  normal component of force density in a filament. 60

- $\mathcal{E}$  energy density for elastic filament. 55
- $\mathcal{F}_i$  components of bending moment of a filament. 56
- $\mathcal{H}$  curvature independent part of filament stress. 53
- $\mu$  polymerization force controlling a filament's length on a surface. 64
- $\phi$  dimensionless stress for gel phase membranes. 29
- $\psi_i$  inflection angle for membrane buckles. 29
- $\sigma$  surface tension. 19
- $\tau$  Frenet torsion. 11
- $\tau_{\mathbf{g}}$  geodesic torsion. 16
- $\theta$  angle between filament tangent vector and local  $\hat{\phi}$  direction. 71
- $\mathbf{B}$  binormal vector to a curve. 10
- $\mathbf{F}$  stress in a filament. 53
- $\mathbf{M}$  torque in a filament. 55
- $\mathbf{N}$  principal normal vector to a curve. 10
- $\mathbf{S}$  bending moment in a filament. 55
- $\mathbf{T}$  tangent vector to a curve. 10
- $\mathbf{X}(u^1, u^2)$  embedding function for a surface. 17
- $\mathbf{Y}(s)$  embedding function for a curve. 10
- $\lambda$  force density in a filament. 59
- $\omega$  angular velocity vector of a filament. 11
- $d_i$  Darboux frame basis vectors. 60
- $e_a$  tangent vectors to a surface. 18
- $f_i$  material frame basis vectors. 55
- $\mathbf{L}$  conormal or transverse vector to a curve. 16
- $\mathbf{m}_i$  material frame normal vectors. 12
- $\mathbf{n}$  unit normal vector to a surface. 21
- $c_i$  spontaneous curvature of a filament in material direction  $i$ . 15
- $f$  conserved stress in cylindrically bound filament. 72
- $f_r$  total radial force transmitted to a surface by a filament. 86

$g_{ab}$  metric tensor. 18

$m$  conserved torque in cylindrically bound filament. 72

$m$  elliptic parameter. Easily distinguished from torque on a confined filament in context. 31

$n$  number of oscillatory periods in closed cylindrically confined filaments. 75

$u$  coordinate parametrizing motion along symmetry of helicoidal surface. 35

$u^a$  coordinates on a surface. 17

$v$  arclength along generatrix of helicoidal surface. 35

$w$  winding number of closed cylindrically confined filaments. 75